

PONTIFÍCIA UNIVERSIDADE CATÓLICA  
DO RIO DE JANEIRO



**Pedro Alcides Lobo Penna Firme**

**Salt geomechanics applied to strategic engineering  
projects**

**Tese de Doutorado**

Thesis presented to the Programa de Pós-graduação em Engenharia Civil of PUC-Rio in partial fulfillment of the requirements for the degree of Doutor em Ciências – Engenharia Civil.

Advisor: Prof<sup>a</sup>. Deane de Mesquita Roehl  
Co-advisor: Prof. Celso Romanel

Rio de Janeiro  
May 2022



**Pedro Alcides Lobo Penna Firme**

**Salt geomechanics applied to strategic engineering  
projects**

Thesis presented to the Programa de Pós-graduação em Engenharia Civil of PUC-Rio in partial fulfillment of the requirements for the degree of Doutor em Engenharia Civil. Approved by the Examination Committee:

**Prof<sup>a</sup>. Deane de Mesquita Roehl**

Advisor

Departamento de Engenharia Civil e Ambiental – PUC-Rio

**Prof. Celso Romanel**

Co-advisor

Departamento de Engenharia Civil e Ambiental – PUC-Rio

**Prof. Luiz Fernando Campos Ramos Martha**

Departamento de Engenharia Civil e Ambiental – PUC-Rio

**Prof. Raul Rosas e Silva**

Departamento de Engenharia Civil e Ambiental – PUC-Rio

**Dr. Leonardo Cabral Pereira**

Cenpes – Petrobras

**Prof. Hans Joakim Skadsem**

UIS

Rio de Janeiro, May 3rd, 2022

All rights reserved.

### **Pedro Alcides Lobo Penna Firme**

Pedro A. L. P. Firme holds a bachelor's (2010) and a master's (2013) degrees in Civil Engineering from the Pontifical Catholic University of Rio de Janeiro (PUC-Rio), Brazil. Pedro is a researcher in the Multiphysics Modeling and Simulation Group at Tecgraf Institute – PUC-Rio. His research is focused on numerical modelling and simulation of the multiphysical behavior of salt in wells, caverns, among others, besides topics related to reservoir geomechanics. His doctoral thesis, defended on May 3rd, 2022 consolidates a comprehensive research on salt geomechanics applied to strategic engineering projects.

#### Bibliographic data

Firme, Pedro Alcides Lobo Penna

Salt geomechanics applied to strategic engineering projects / Pedro Alcides Lobo Penna Firme ; advisor: Deane de Mesquita Roehl ; co-advisor: Celso Romanel. – 2022.

248 f. : il. color. ; 30 cm

Tese (doutorado)–Pontifícia Universidade Católica do Rio de Janeiro, Departamento de Engenharia Civil e Ambiental, 2022.

Inclui bibliografia

1. Engenharia Civil e Ambiental - Teses. 2. Sal. 3. Fluência. 4. Abandono de poços. 5. Caverna de sal. 6. Comportamento termomecânico. I. Roehl, Deane de Mesquita. II. Romanel, Celso. III. Pontifícia Universidade Católica do Rio de Janeiro. Departamento de Engenharia Civil e Ambiental. IV. Título.

CDD: 624

## Acknowledgments

To God, in whom is the fountain of life, who has given me all the skills and the conditions necessary to carry out this work.

To my parents, Maria Margarida and José Alcides, my wife, Débora, my grandmother, Maria Teresa (in memoriam) – she would certainly be very happy with this achievement –, my father-in-law, Paulo, my relatives and my friends. Thank you all for the great encouragement to my professional and academic activities and for the understanding in the moments of absence.

To my advisor, Prof<sup>a</sup>. Deane Roehl, for the encouragement, availability to supervise this thesis, and valuable contributions to the research on salt geomechanics. Thanks also for the opportunity to work as a researcher in the Multiphysics Modeling and Simulation Group at Tecgraf Institute, which has provided an excellent technical infrastructure and the research environment propitious to the development of this thesis.

To my co-advisor, Prof. Celso Romanel, for the encouragement, availability to co-supervise this thesis and valuable discussions and contributions to the research on salt geomechanics.

To Dr. Eleazar Cristian Mejia Sanchez, for the constant assistance in GeMA framework, the simulation tool adopted in the applications of the thesis. This support was essential for the new developments on salt geomechanics.

To the members of the examination committee, Prof. Luiz Fernando Campos Ramos Martha, Prof. Raul Rosas e Silva, Dr. Leonardo Cabral Pereira and Prof. Hans Joakim Skadsem, for taking time to analyze this work and for valuable considerations and suggestions that added value to the final version of the thesis.

To my friends at the Multiphysics Modeling and Simulation Group at Tecgraf Institute for fruitful discussions on geomechanics and numerical simulations that contributed to the work in the context of the thesis.

This study was financed in part by the Coordenação de Aperfeiçoamento de Pessoal de Nível Superior - Brasil (CAPES) - Finance Code 001 and in part by the R&D project registered as ANP no. 20234-1, “SONAR” (PUC-Rio/Petrobras/ANP), sponsored by Petrobras under the ANP R&D levy, Brazil as “Compromisso de Investimentos com Pesquisa e Desenvolvimento”.

## Abstract

Firme, Pedro Alcides Lobo Penna; Roehl, Deane de Mesquita (Advisor); Romanel, Celso (Co-advisor). **Salt geomechanics applied to strategic engineering projects**. Rio de Janeiro, 2022. 248p. Tese de Doutorado - Departamento de Engenharia Civil e Ambiental, Pontifícia Universidade Católica do Rio de Janeiro.

The importance of salt in many human activities has accompanied the main phases of civilization. Strategic and innovative applications in salt rocks are planned until the present day, such as geological barriers for well abandonment and storage caverns for new energy sources or decarbonization. This thesis focuses on the geomechanical behavior of salt with special regards to creep, dilation, thermal effects and their impact on the hydraulic behavior. Models have supported the development of methodologies to assess integrity and tightness conditions of strategic projects in the context of energy. These include Pre-salt well abandonment, salt caverns and salt as caprock of carbonate reservoirs. Advanced numerical simulations using the framework GeMA have investigated representative scenarios of each project. To this end, creep constitutive models, customized boundary conditions and specific output variables have been implemented. Among the creep models, the EDTM has been developed in the context of this doctoral research, focusing on Brazilian salt. The case studies have led to important findings. A Pre-salt well can close completely by creep after casing removal. Pressure reduction and well heating have accelerated closure significantly. In the most critical scenario, the final permeability was slightly higher than 100 times the initial value. A salt cavern can mechanically support pressure cycles caused by a contingency hydrocarbon supply scheme; however, a final permeability of 6.5 times the initial value has been noticed. In reservoir geomechanics, the caprock creep contribution in the subsidence is small and irreversible even if the reservoir pressure is recovered. Permeability changes have been subtle despite the creep contribution and the reservoir pressure variation. The literature review, the creep models, the analysis methodologies, the capabilities incorporated into the framework and the discussions motivated by the case studies represent the added value of the thesis to the scientific community and industry regarding the strategic use of salt rocks.

## Keywords

Salt rock; halite; creep; dilatancy; Pre-salt well; salt cavern; well abandonment; thermomechanical behavior.

## Resumo

Firme, Pedro Alcides Lobo Penna; Roehl, Deane de Mesquita; Romanel, Celso. **Geomecânica de rochas salinas aplicada a projetos estratégicos de engenharia**. Rio de Janeiro, 2022. 248p. Tese de Doutorado - Departamento de Engenharia Civil e Ambiental, Pontifícia Universidade Católica do Rio de Janeiro.

A importância do sal em diversas atividades humanas tem acompanhado as fases principais da civilização. Aplicações estratégicas e inovadoras envolvendo rochas salinas são planejadas até os dias atuais, tais como barreiras geológicas para abandono de poços e cavernas de estocagem para novas fontes de energia ou descarbonização. Esta tese foca no comportamento geomecânico do sal com atenção especial à fluência, dilatação, efeitos térmicos e seus impactos no comportamento hidráulico. Modelos deram suporte ao desenvolvimento de metodologias para avaliação de condições de integridade e estanqueidade de projetos estratégicos no contexto de energia. Eles incluem o abandono de poços do pré-sal, cavernas de sal e sal como rocha capeadora de reservatórios carbonáticos. Simulações numéricas avançadas utilizando o *framework* GeMA investigaram cenários representativos de cada projeto. Para tanto, modelos constitutivos de fluência, condições de contorno customizadas e variáveis de saída específicas foram implementados. Dentre os modelos de fluência, o EDMT foi desenvolvido no contexto desta pesquisa de doutorado, com foco no sal brasileiro. Os estudos de caso conduziram a observações importantes. Um poço do pré-sal pode fechar completamente por fluência após a remoção do revestimento. A redução da pressão e o aquecimento do poço aceleraram seu fechamento de modo significativo. No cenário mais crítico, a permeabilidade final foi ligeiramente superior a 100 vezes o valor inicial. Uma caverna de sal pode suportar mecanicamente ciclos de pressão causados por um esquema contingencial de fornecimento de hidrocarbonetos, embora uma permeabilidade final de 6,5 vezes o valor inicial tenha sido observada. Na geomecânica de reservatórios, a contribuição da fluência da rocha capeadora na subsidência é pequena e irreversível mesmo que a pressão do reservatório seja recuperada. As mudanças na permeabilidade foram sutis apesar da contribuição da fluência do sal e da variação de pressão do reservatório. A revisão da literatura, os modelos de fluência, as metodologias de análise, as funcionalidades incorporadas ao *framework* e as discussões motivadas pelos estudos de caso representam o valor

agregado da tese para a comunidade científica e para a indústria no que tange ao aproveitamento estratégico de rochas salinas.

### **Palavras-chave**

Sal; halita; fluência; dilatância; poço do pré-sal; caverna de sal; abandono de poços; comportamento termomecânico.

# Table of contents

1	Introduction .....	22
1.1.	Motivation .....	22
1.2.	Big picture of salt geomechanics in Brazil .....	23
1.3.	Context of the thesis: the Multiphysics Modeling and Simulation Group at Tecgraf Institute – PUC-Rio.....	25
1.4.	Thesis goals and structure .....	26
2	Salt multiphysics .....	29
2.1.	Mechanical behavior (M) .....	30
2.1.1.	Creep behavior.....	31
2.1.1.1.	Power law (PL).....	33
2.1.1.2.	Double-mechanism creep law (DM).....	35
2.1.1.3.	Multi-mechanism deformation creep model (MD) .....	37
2.1.1.4.	Enhanced double-mechanism creep law (EDMT).....	41
2.1.1.5.	Comparative performance of the creep constitutive models ....	42
2.1.2.	Dilation behavior .....	44
2.1.2.1.	Spiers' boundary .....	46
2.1.2.2.	Ratigan's boundary .....	46
2.1.2.3.	Hunsche's boundary .....	46
2.1.2.4.	DeVries' boundary .....	47
2.1.2.5.	Comparative performance of the dilatancy boundaries.....	48
2.2.	Thermomechanical behavior (TM).....	50
2.3.	Hydromechanical behavior (HM) .....	54
2.4.	Long-term behavior of salt.....	60
2.5.	Formulations in the scope of the thesis .....	62

2.5.1.	Thermo-viscoelastic behavior of salt and repercussion on the hydraulic behavior (TM+H approach) .....	63
2.5.2.	Constitutive behavior of non-salt materials.....	70
2.5.3.	Summary of properties .....	70
2.5.4.	Contributions of the thesis in modelling and simulation.....	73
3	Strategic engineering projects involving salt rocks .....	76
3.1.	Salt creep as an allied mechanism in the formation of geological barriers for well P&A.....	76
3.1.1.	Overview on P&A .....	76
3.1.2.	P&A numbers and concepts.....	78
3.1.3.	A brief review on materials for P&A and introduction to geological barriers 82	
3.1.3.1.	Shales as geological barrier.....	84
3.1.3.2.	Salt as geological barrier.....	87
3.1.3.3.	Granular salt as backfilling (plug) material .....	90
3.2.	Salt caverns for strategic underground storage .....	93
3.2.1.	Overview on salt caverns .....	93
3.2.2.	A brief historic review of salt caverns opened by solution mining	94
3.2.3.	Geomechanical aspects and cases of interest .....	97
3.2.4.	Introduction to solution mining.....	100
3.2.5.	Cavern construction (opening) by solution mining.....	104
3.2.6.	Cavern destination and operation .....	105
3.2.7.	Cavern abandonment.....	107
3.3.	Salt caprock of Pre-salt reservoirs.....	110
3.3.1.	Overview on reservoir compaction and subsidence .....	110
3.3.2.	A brief historic review of subsidence due to hydrocarbon exploration	112

3.3.3.	The influence of salt caprock creep on subsidence.....	116
3.4.	Relevance of the strategic engineering projects in the Brazilian context.....	120
4	Validation and reference examples.....	124
4.1.	Triaxial creep tests .....	124
4.1.1.	Brazilian halite.....	124
4.1.2.	Gulf of Mexico halite.....	128
4.1.2.1.	West Hackberry .....	129
4.1.2.2.	Big Hill.....	130
4.2.	Hydrostatic compaction test .....	132
4.3.	Brazilian mine gallery .....	134
4.4.	Pre-salt well closure .....	138
4.4.1.	Isothermal Pre-salt well.....	138
4.4.2.	Thermomechanical Pre-salt well .....	144
4.4.2.1.	Well models considering homogenous halite (A1) .....	145
4.4.2.2.	Well models considering homogenous tachyhydrite (B3) .....	147
4.4.2.3.	Models with halite-tachyhydrite-halite intercalation (C3) .....	148
4.5.	Closing remarks related to the validation and reference examples	
	151	
5	Case study of well abandonment using salt as geological barrier....	152
5.1.	Objective .....	152
5.2.	Lithology and geomechanical model .....	152
5.3.	Initial and boundary conditions .....	153
5.4.	Hypotheses, methodology and alignment with international literature	
	155	
5.5.	Results and discussions .....	159
5.5.1.	Displacements and temperatures.....	159

5.5.2.	Stresses and strains.....	161
5.5.3.	Porosity and permeability .....	164
5.6.	Partial conclusions.....	169
6	Case study of salt cavern.....	171
6.1.	Objective .....	171
6.2.	Lithology and geomechanical model .....	171
6.3.	Initial and boundary conditions .....	172
6.4.	Hypotheses, methodology and alignment with international literature 173	
6.4.1.	Cavern construction .....	174
6.4.2.	Cavern operation.....	176
6.5.	Results and discussions .....	177
6.5.1.	Construction period .....	177
6.5.2.	Operation period .....	182
6.6.	Partial conclusions.....	191
7	Case study of salt as caprock of Pre-salt reservoir.....	193
7.1.	Objective .....	193
7.2.	Lithology and geomechanical model .....	193
7.3.	Initial and boundary conditions .....	195
7.4.	Hypotheses, methodology and alignment with international literature 196	
7.5.	Results and discussions .....	199
7.5.1.	Hydrocarbon production period .....	199
7.5.2.	CO <sub>2</sub> injection period .....	203
7.6.	Partial conclusions.....	213
8	Conclusions and suggestions for future work .....	215

8.1. General conclusions .....	215
8.2. Specific conclusions from the simulations .....	215
8.3. Final remarks .....	217
8.4. Suggestions for future work .....	217
9 References .....	219

## List of figures

Figure 1. Thesis structure. The chapters are indicated in parentheses, in italics. ....	27
Figure 2. Schematic summary of the multiphysical behavior of salt. The thermal, hydraulics, mechanics, and chemical physics are respectively denoted by “T”, “H”, “M” and “C”.....	29
Figure 3. Typical creep curve. The values in parenthesis provide an order of magnitude of the curve applied for salt rocks. ....	32
Figure 4. Analogy between the “multiple mechanism viscoplastic law” and the double-mechanism creep law. Figure adapted from Firme et al. (2018a). ....	36
Figure 5. Deformation mechanism map for salt adapted from Munson (1979). Figure adapted from Firme et al. (2016b).....	38
Figure 6. Triaxial creep test: numerical simulation workflow. ....	43
Figure 7. Triaxial creep test: comparison of the creep curves (a) and creep rate curves (b) obtained using each of the constitutive models previously discussed. Experimental data from Costa et al. (2005). ....	44
Figure 8. Dilatancy boundaries according to Spiers et al. (dark blue), Ratigan et al. (light blue), Hunsche (green), Hunsche Modified – lower boundary (light green), Hunsche Modified – upper boundary (yellow) and DeVries et al. (tension/extension in red, isochoric in dark red and compression in purple). Modified from Firme et al. (2019). ....	49
Figure 9. Schematic representation of the coupled thermomechanical behavior of salt. ....	53
Figure 10. Conceptual representation of the phenomena involved in the hydromechanical behavior of salt. Adaptation from figures presented by Urai et al. (2008) (1) and Schulze et al. (2001) (2).....	56
Figure 11. Schematic representation of the coupled hydromechanical behavior of salt. ....	58

Figure 12. Application of Stokes flow to Pre-salt well-related simulations. Adaptation from figures presented by Weijermars et al. (2014b) (1) and Weijermars et al. (2014a) (2)..... 62

Figure 13. Workflow of the TM+H finite element analysis..... 68

Figure 14. Graphical abstract of the main contributions of the thesis in the workflow for numerical simulation of strategic projects involving salt rocks. .... 74

Figure 15. Conventional methods for well P&A. Adaptation from figures presented in <https://energynorthern.com/2019/08/05/abrado-wins-major-multi-well-pa-contract-from-chevron/> (1), <https://decomnorthsea.com/news/32-time-savings-on-cut-pull-operation> (2) and Khalifeh and Saasen (2020) (3)..... 77

Figure 16. Well closure towards casing in an uncemented interval. Adapted from Firme et al. (2016b), based on a former simulation carried out by Fossum and Fredrich (2007). .... 84

Figure 17. Schematic illustration of the shale as geological barrier in the context of numerical modelling. .... 86

Figure 18. Schematic illustration of formation of a geological barrier by salt creep. .... 89

Figure 19. Schematic illustration of formation of a geological barrier by granular salt backfilling. .... 93

Figure 20. Potential scenarios for casing damage in washout intervals. 101

Figure 21. Sketch of salt cavern opening by solution mining (Evans et al., 2008). .... 104

Figure 22. Sketch of solution mining technique: direct (a) and reverse (b) circulation (Kazemi and Jessen, 1964)..... 105

Figure 23. Schematic illustration of the subsidence delay (Hettema et al., 2002). .... 117

Figure 24. Subsidence in the center of the depleted radius in function of reservoir depletion. Representation of the subsidence delay due to elastic-plastic transition (a) and salt caprock creep (b). Adapted from Firme et al. (2014a) and Firme et al. (2021)..... 118

Figure 25. Results of triaxial creep tests carried out in Brazilian halite. Simulations considering PL (a), DM (b), MD (c) and EDMT (d) creep constitutive models.....	126
Figure 26. Results of triaxial creep tests carried out in West Hackberry salt. ....	130
Figure 27. Results of a multistage triaxial creep test carried out in Big Hill salt.....	131
Figure 28. Results of a multistage triaxial creep test carried out in Big Hill salt – thermal strain contribution.....	132
Figure 29. Results of a hydrostatic compaction test carried out in Rothbach sandstone – porosity-dependent permeability (a) and mean stress-dependent permeability (b).....	134
Figure 30. 2D plane strain finite element model of the Brazilian mining gallery. Elevations and dimensions in meters.....	135
Figure 31. Contours maps of deviatoric stress ( $\sigma_d$ ) and vertical displacements ( $uv$ ) in the Brazilian mining gallery surroundings.....	136
Figure 32. Vertical convergence (a) and vertical convergence rate (b) of the Brazilian mining gallery. Convergence measurements from D'Élia (1991). ....	137
Figure 33. Axisymmetric finite element model of the Brazilian Pre-salt well. Elevations and dimensions in meters. ....	139
Figure 34. Validation of the numerical simulations carried out in the Brazilian Pre-salt well. The caliper logs presented by Medeiros (1999) have been post-processed by the author of the thesis to reflect the well closure by creep between 0 and 10 hours after well drilling. ....	141
Figure 35. Contour maps of horizontal displacements and the strength indicator (ratio) after 10 hours of simulation in the Brazilian Pre-salt well. ....	142
Figure 36. Well diameter (a) and the strength indicator (b) evolution over 30 days of simulation in the Brazilian Pre-salt well.....	143
Figure 37. Axisymmetric and 2D plane strain models A1. Elevations and dimensions in meters. ....	146
Figure 38. Horizontal displacement (radial closure) of point P in models A1: axisymmetric (a) and 2D plane strain (b).....	147

Figure 39. Axisymmetric and 2D plane strain models B3. Elevations and dimensions in meters. ....	147
Figure 40. Horizontal displacement (radial closure) of point P in models B3: axisymmetric (a) and 2D plane strain (b).....	148
Figure 41. Axisymmetric and 3D models C3. Elevations and dimensions in meters. ....	149
Figure 42. Horizontal displacement (radial closure) of point P in models C3: axisymmetric (a) and 3D (b). ....	150
Figure 43. Horizontal displacement (radial closure) of point P (a) and temperature at 720 hours (b) of models C3: comparison of results using different 3D elements (8-node and 20-node bricks, and 4-node and 10-node tetrahedrons).....	151
Figure 44. 2D plane strain model of the Pre-salt well. Elevations and dimensions in meters (unless otherwise stated).....	153
Figure 45. Workflow for the well abandonment simulations considering salt as barrier. ....	155
Figure 46. Comparison between the stress paths obtained using Abaqus™ and GeMA. ....	156
Figure 47. Simplified workflow for the well abandonment simulations considering salt as barrier. ....	157
Figure 48. Workflow of the TM+H approach applied to the well abandonment. ....	158
Figure 49. Well diameter evolution (a) and temperature evolution (b) over time. ....	160
Figure 50. Mean stresses (solid lines), deviatoric stresses (dashed lines) and Lode angle (dotted lines) (a) and dilation indicator (b) over time.....	162
Figure 51. Stress paths (p-q diagram) from section milling to well complete closure – model A0 (a), model A1 (b), model A2 (c) and model A3 (d). .	163
Figure 52. Volumetric strain (a) and porosity-dependent permeability (b) over time.....	165
Figure 53. Mean stress-dependent permeability results over time (a) and along the segment A-A' when the well is completely closed (b). ....	166

Figure 54. Mean stress-dependent permeability in function of the mean stress (“Permeability” paths) of models A0 (a), A1 (b), A2 (c) and A3 (d).  
 ..... 168

Figure 55. Axisymmetric finite element model of the salt cavern. Elevations and dimensions in meters. .... 172

Figure 56. Cavern construction steps. Adapted from Firme et al. (2019).  
 ..... 175

Figure 57. Cavern operation scheme workflow. Adapted from Firme et al. (2019). .... 176

Figure 58. Cavern operation scheme applied to this study. Adapted from Firme et al. (2019). .... 177

Figure 59. Internal pressure and deviatoric stress over the construction period: interval between pseudo-equilibrium and leaching out (a); and interval between leaching out and first filling (b). .... 178

Figure 60. Lode angle over the construction period: interval between pseudo-equilibrium and leaching out (a); and interval between leaching out and first filling (b). .... 178

Figure 61. Dilation indicator over the construction period: interval between pseudo-equilibrium and leaching out (a); and interval between leaching out and first filling (b). .... 179

Figure 62. Volumetric strain over the construction period: interval between pseudo-equilibrium and leaching out (a); and interval between leaching out and first filling (b). .... 179

Figure 63. Stress paths of the cavern wall over the construction period. 180

Figure 64. Porosity over the construction period: interval between pseudo-equilibrium and leaching out (a); and interval between leaching out and first filling (b). .... 181

Figure 65. Porosity-dependent permeability over the construction period: interval between pseudo-equilibrium and leaching out (a); and interval between leaching out and first filling (b). .... 181

Figure 66. Mean stress-dependent permeability over the construction period: interval between pseudo-equilibrium and leaching out (a); and interval between leaching out and first filling (b). .... 182

Figure 67. Displacement magnitude (a) and equivalent von Mises strain (b) of the cavern wall over the cavern lifespan. ....	183
Figure 68. Equivalent von Mises strain rate (a) and Lode angle (b) of the cavern wall over the lifespan. ....	183
Figure 69. Dilation indicator of the cavern wall over the lifespan (a) and stress paths over the operation period (b). ....	185
Figure 70. Contour maps of the dilation and shear failure indicators of the cavern over the lifespan. ....	186
Figure 71. Dilation and shear failure indicators along the vertical segments A-F-A' (a) and E-E' (b) in the cavern model. ....	187
Figure 72. Dilation indicator along the vertical segment C-C' in the cavern model. ....	188
Figure 73. Volumetric strain (a) and porosity (b) of the cavern wall over the lifespan. ....	189
Figure 74. Porosity-dependent (a) and mean stress-dependent (b) permeability of the cavern wall over the lifespan. ....	189
Figure 75. Mean stress-dependent permeability along the vertical segments A-F-A' (a) and E-E' (b) in the cavern model. ....	191
Figure 76. Mean stress-dependent permeability along the horizontal segment C-C' in the cavern model. ....	191
Figure 77. Axisymmetric finite element model of the Pre-salt section. Elevations and dimensions in meters. ....	194
Figure 78. Initial conditions (a) and pore pressure variation (b) assigned to the geomechanical model. ....	195
Figure 79. Schemes of reservoir depletion and injection. ....	196
Figure 80. Center reservoir compaction (a) and surface subsidence (b) – linear depletion scheme. ....	200
Figure 81. Center reservoir compaction (a) and surface subsidence (b) – nonlinear depletion scheme. ....	201
Figure 82. Reservoir compaction (a) and surface subsidence (b) in the end of the linear depletion (30 years). ....	202
Figure 83. Reservoir compaction (a) and surface subsidence (b) in the end of the nonlinear depletion (30 years). ....	202

Figure 84. Center reservoir compaction (a) and surface subsidence (b) over time – linear depletion/injection scheme..... 204

Figure 85. Center reservoir compaction (a) and surface subsidence (b) over time – nonlinear depletion/injection scheme..... 205

Figure 86. Reservoir compaction (a) and surface subsidence (b) in the end of depletion (30 years) and in the end of injection (60 years) – linear depletion/injection scheme. .... 206

Figure 87. Reservoir compaction (a) and surface subsidence (b) in the end of depletion (30 years) and in the end of injection (60 years) – nonlinear depletion/injection scheme. .... 206

Figure 88. Vertical displacements along the vertical segment H-H' in the end of depletion (30 years) and in the end of injection (60 years) – linear (a) and nonlinear (b) depletion/injection scheme. .... 207

Figure 89. Countour maps of the vertical displacements in the end of depletion (30 years) and in the end of injection (60 years) – linear depletion/injection scheme. .... 208

Figure 90. Countour maps of the vertical displacements in the end of depletion (30 years) and in the end of injection (60 years) – nonlinear depletion/injection scheme. .... 208

Figure 91. Stress paths (p-q diagram) of salt bottom (a) and top (b) – linear depletion/injection scheme. .... 209

Figure 92. Stress paths (p-q diagram) of salt bottom (a) and top (b) – nonlinear depletion/injection scheme. .... 210

Figure 93. Stress paths (p'-q diagram) of seafloor (model top) – linear (a) and nonlinear (b) depletion/injection scheme. .... 210

Figure 94. Mean stress-dependent permeability at salt bottom (a) and top (a) over time – linear depletion/injection scheme. .... 211

Figure 95. Mean stress-dependent permeability at salt bottom (a) and top (a) over time – nonlinear depletion/injection scheme. .... 212

Figure 96. Mean stress-dependent permeability at seafloor (model top) over time – linear (a) and nonlinear (b) depletion/injection scheme. .... 213

## List of tables

Table 1. Comparative summary of the capabilities of the constitutive models to represent creep phases.....	42
Table 2. Permeability ranges of salt rocks (Bérest et al., 2001; Cosenza and Ghoreychi, 1996).....	55
Table 3. TM+H approach – thermomechanical problem and changes in the hydraulic behavior. ....	69
Table 4. Thermal and elastic properties adopted for the Brazilian halite (References: 1: Poiate Jr. (2012), 2: Pudewills and Droste (2003), 3: Bérest et al. (2014) and 4: Firme et al. (2016b)).....	71
Table 5. Creep properties adopted in the PL model (rate formulation) for the Brazilian halite, assuming stresses in kPa, times in seconds and temperatures in Kelvin (Lomenick and Bradshaw, 1969). ....	71
Table 6. Transient creep properties adopted in the MD and EDTM models for the Brazilian halite (References: 1: Firme et al. (2016b) and 2: Munson (2004)).....	71
Table 7. Steady-state creep properties adopted in the DM and EDTM models for the Brazilian halite (Poiate Jr., 2012).....	71
Table 8. Steady-state creep properties adopted in the MD model for the Brazilian halite (References 1: Firme et al. (2016b) and 2: Munson (1999)). .....	72
Table 9. Geomechanics-flow correlation parameters adopted for the Brazilian halite (David et al., 2001).....	72
Table 10. Mechanical properties adopted for non-salt rocks – Part 1 of 3. .....	72
Table 11. Mechanical properties adopted for non-salt rocks – Part 2 of 3. .....	73
Table 12. Mechanical properties adopted for non-salt rocks – Part 3 of 3. .....	73

Table 13. Comparative summary of the salt and shale characteristics of interest for geological barriers. ....	84
Table 14. Specifications of the triaxial creep tests carried out in Brazilian halite (Costa et al., 2005; Poiate Jr., 2012; Poiate Jr. et al., 2006). Identifications (A-D) attributed by the author of the thesis. ....	124
Table 15. Specifications of triaxial creep tests carried out in West Hackberry salt (Munson, 1999).....	129
Table 16. Specifications of the multi-stage triaxial creep test carried out in Big Hill salt (BH01). ....	130
Table 17. Summary of the scenarios of boundary conditions. ....	154
Table 18. Summary of the times for well closure. ....	160

# 1 Introduction

## 1.1. Motivation

The importance of salt in many industrial and subsistence human activities has accompanied the main phases of civilization. As examples of that, one of the oldest known salt mines is the mine of Hallstatt (Austria), that dates from the Middle Bronze Age (Grabner et al., 2021). A number of salt caverns and wells crossing salt rocks have been opened in the last century for many purposes. Recently innovative applications involving salt rocks have been planned, such as using salt creep as an allied mechanism to seal abandoned wells and using salt caverns for strategic energy storage (Evans et al., 2021; Wollenweber et al., 2018). More than a mineral commodity, salt has come to be seen as a rock formation of strategic value for hydrocarbon accumulation and as a host for the storage of energy sources or waste disposal.

Salt rocks exhibit distinguished properties such as creep deformation, high ductility and very low permeability. The presence of salt as reservoir caprocks is evidence of trapped hydrocarbons below them. For the same reason, salt openings such as caverns are expected to be tight geological environments for strategic storage or waste disposal. Observing these characteristics, salt environments are likely adequate for carbon capture and storage (CCS) operations, being storage caverns and/or as caprocks of a reservoir for CO<sub>2</sub> injection. More so, the combined effect of significant creep behavior without undergoing damage and very low permeability also suggests that salt rocks are propitious to form geological barriers for well abandonment. This topic has been suggested in the context of North Sea for shales (often referred to as “shale as barrier” in the literature). With this multiplicity of possible uses of salt rocks – some of them still innovative, particularly in the Brazilian context –, there is the need to develop workflows and enhance the existing ones for the analysis of mechanical integrity and tightness of salt strategic environments. Many of these applications are generally not accessible for on-site observations making predictions and mitigations challenging.

The recent events related to the Russo-Ukrainian War (since February 2022) have indirectly demonstrated the importance of the strategic use of salt rocks in basic circumstances of life. Brazil has shown a certain fragility regarding fertilizers in face of the risk of interruption or reduction of supply from abroad. The country is not yet self-sufficient in potash, obtained from sylvinite<sup>1</sup>, which is an important element for the production of fertilizers. There are potash mining projects to be implemented in the future in addition to the already existing Taquari-Vassouras potash mine (Farias et al., 2021). These developments would reduce Brazil's need for potash importation. On the other hand, the United States has demonstrated the advantages of the strategic use of salt rocks. In March 2022, this country has committed to release 30 million barrels of crude oil from the Strategic Petroleum Reserves (SPR) in order to mitigate the reduction in oil supply due to this war (U.S. Energy Information Administration, 2022). These reserves are in a complex of salt caverns for petroleum strategic storage. Recent information in non-official papers indicate that this amount has increased to about 180 million barrels within a six-month period (one million barrels per day). In Brazil, there is still no strategic storage in these proportions, so the country remains without more relevant alternatives to mitigate the effects of global fluctuations in the oil and gas supply.

Considering this complexity and the current world facts, there is much room for technological advances in strategic engineering projects involving salt rocks, particularly in the context of well abandonment and strategic storage for energy or CCS purposes. This thesis aims at filling some gaps in these areas.

## **1.2. Big picture of salt geomechanics in Brazil**

Hydrocarbon production triggers significant stress changes, reservoir compaction and surface subsidence. This can be even more critical in the Brazilian Pre-salt with the construction of wells crossing thick salt layers to reach heterogeneous carbonates, very often naturally fractured, karstified and overpressured. Brazilian Pre-salt fields (such as Santos basin) are typically overlain by more than 2,000 meters of stratified evaporites (Mohriak and Leroy, 2012). In this context, there is still a gap in the subsidence analyses considering the creep contribution of the caprock, that may be being overlooked. Adequate predictions of the seafloor subsidence evolution in offshore fields are of utmost importance for safe production and decommissioning. Moreover, high pressure

---

<sup>1</sup> Type of salt rock.

and high temperature (HPHT) environments are challenging for reservoir geomechanics and well integrity. In wells, it tends to reduce the operational window and to damage the cement sheath (Ruiz, 2018; Shadravan and Amani, 2012).

Salt geomechanics shall also be influenced by the current environmental concern with the trend towards zero emissions of carbon and greenhouse gases in the near future (Evans et al., 2021). The production of the Brazilian Pre-salt reservoirs often deals with high gas-oil ratio (GOR) hydrocarbons. Taking Libra field reservoirs as an example, the initial GOR is about 440 Sm<sup>3</sup>/Sm<sup>3</sup>, and 44% of the associated gas is carbon dioxide (CO<sub>2</sub>) (Anjos et al., 2019). The CO<sub>2</sub> produced together with the hydrocarbons cannot be released into the atmosphere. To this end, CO<sub>2</sub> injection methods in depleted carbonate reservoirs or in salt caverns would be a strategic alternative to enhance field production while promoting a safe CO<sub>2</sub> destination. In this sense, depleted reservoirs and salt caverns have pros and cons in terms of implantation and usability. The Pre-salt carbonates are naturally fractured and exhibit a complex pore/fracture network. This can be troublesome to avoid CO<sub>2</sub> leakage through the overburden layers. Nevertheless, using depleted Pre-salt reservoirs has the advantage that these spaces are readily available, while the caverns would have yet to be opened. On the other hand, Brazil has abundance of salt formations, and this type of rock has proven worldwide to be adequate for strategic storage. The salt openings are ideally free of the major complexities related to the pore network and natural fractures, typical of carbonates. Furthermore, the use of salt caverns for decarbonization purposes have been currently mentioned in the literature (Costa et al., 2019a; Evans et al., 2021). Both considering CO<sub>2</sub> injection in a depleted reservoir or in a salt cavern, analyzing the impact of the salt creep behavior on subsidence is important to foresee the long-term impact on the ground or on the seafloor and anticipate environmental and structural threats. Furthermore, advances in salt computational geomechanics for salt mining are strategic considering the projects to be implemented in Brazil in the future (Carnallite and Autazes projects), that involve solution mining and room-and-pillar mining techniques. The ore extraction from these sites should be carried out in such a way to allow subsequent use of the resulting caverns for energy-related sources or decarbonization purposes.

Besides these challenges, another issue to be considered for all the wells is the future abandonment. Well plug and abandonment (P&A) consists of a wide decommissioning process in fields where hydrocarbon production is no longer economically advantageous or feasible. Each well permanent abandonment may

cost a few million dollars considering standard P&A methods and this is an expense with no return to the operator. Some of the Brazilian onshore and offshore post-salt fields are reaching maturity (Souza, 2019). There are more than 60 offshore installations and more than 165 wells to be decommissioned in the next years (Furtado et al., 2018; Soares, 2017), besides a significant number of wells temporarily abandoned that need to turn into permanent P&A (França, 2020). In the future, Pre-salt wells will have to be abandoned. Considering this recent reality, P&A is a still growing topic in the Brazilian industry and academia. The abundance of salt rock formations in the Pre-salt fields and the advantageous salt properties encourage the use of geological barriers formed by salt creep. The previous experience in integrity and stability analyses of Pre-salt wells supports the expectation that Brazilian salt would be able to meet requirements from standard regulations on P&A and to close around the casing (filling the annulus space) or around the entire well section. This technique is preceded by what has already been tested in North Sea shales and is mentioned in the guidelines for P&A developed by the Brazilian Petroleum and Gas Institute (IBP, 2017).

An important and continuous research effort focused on Brazilian salt rocks has been made by means of laboratory testing and computational modelling since the potash exploration and especially since the discovery of the enormous hydrocarbon reserves in the Pre-salt reservoirs. This large scale research has promoted a great development in terms of methodologies and computational tools for the simulation of wells crossing salt formations (Costa, 1984; Poiate Jr., 2012). Recently, this experience has been extended to possible future offshore salt caverns for underground storage and decarbonization purposes (Costa et al., 2015, 2019a, 2019b; Firme et al., 2018b, 2019). A preliminary assessment on well abandonment using salt as geological barrier has been carried out by the author of the thesis and is under continuous development.

Having this big picture of the salt geomechanics in mind, the research in up-to-date salt-related strategic projects is a contribution to better positioning Brazil in face of the energy and environmental challenges in the coming decades.

### 1.3.

#### **Context of the thesis: the Multiphysics Modeling and Simulation Group at Tecgraf Institute – PUC-Rio**

The Multiphysics Modeling and Simulation Group at Tecgraf Institute of the Pontifical Catholic University of Rio de Janeiro (PUC-Rio) has been developing

computational solutions for challenges of the oil and gas (O&G) industry since the 1990's. Several methodologies for numerical simulations have been developed under research initiatives, projects and partnerships with the industry and university. The main topics addressed are reservoir geomechanics, Pre-salt well stability and integrity, geological fault reactivation, hydraulic fracturing, flow through porous and fractured media, salt caverns, karstification, geochemistry, coupled multiphysics/multiscale simulations, among others.

A mature research and development (R&D) area in strategic projects involving salt rocks has been developed since then. This area includes conceptual and numerical developments on salt rock constitutive modelling with special regards to: i) creep, dilation and damage; ii) thermomechanical and hydromechanical coupled approaches; and iii) deterministic, probabilistic and artificial intelligence methods. These capabilities have been applied to well and cavern modelling, scenarios of local dissolution, reservoir simulations considering the salt behavior in the caprock, among other related applications. As academic production on salt geomechanics and related topics, several journal/conference papers and postgraduate papers have been produced by members of the group in the recent years (Brandão, 2016; Brandão et al., 2017; De Simone, 2016; De Simone et al., 2017; Firme et al., 2016a, 2015a, 2015b, 2014b; Firme, 2013; Firme et al., 2019, 2018a, 2018b, 2017, 2016b; Peña et al., 2019; Pereira et al., 2018; Quevedo et al., 2019; Santos, 2018; Santos et al., 2017; Teófilo et al., 2018).

This thesis is inserted in the research area of salt geomechanics with a view of contributing to the Brazilian expertise and technology in current applications related to energy and decarbonization. It consolidates a series of advances and developments in the area after the master's research of the author (Firme, 2013) and during his involvement in salt geomechanics and multiphysics research partnerships with industry as a researcher in the group.

#### **1.4. Thesis goals and structure**

This thesis intends to address strategic engineering problems that involve salt rocks, more particularly in the Brazilian energy and decarbonization R&D contexts. As specific goal, the mechanical and thermomechanical behaviors of salt with regards to creep and dilation in scenarios of wells, caverns and as caprocks of Pre-salt reservoirs are analyzed. The changes in the hydraulic properties provoked by the geomechanical response is investigated. To this end, the thesis

provides a conceptual basis, workflows for numerical simulations of relevant applications and a critical discussion of the results. As an additional goal, the thesis aims at applying workflows and developing the attributes needed for advanced simulations in salt rocks using an existing in-house finite element framework fully developed in the context of the university (Mendes, 2016; Mendes et al., 2016).

The engineering applications seek to ensure that the salt structure (e.g., well, cavern or caprock) remains sound and tight, in order to obtain the greatest advantage of the ductility and impermeability of salt. The findings of the research shall serve as a guide for further advanced or specific analyses.

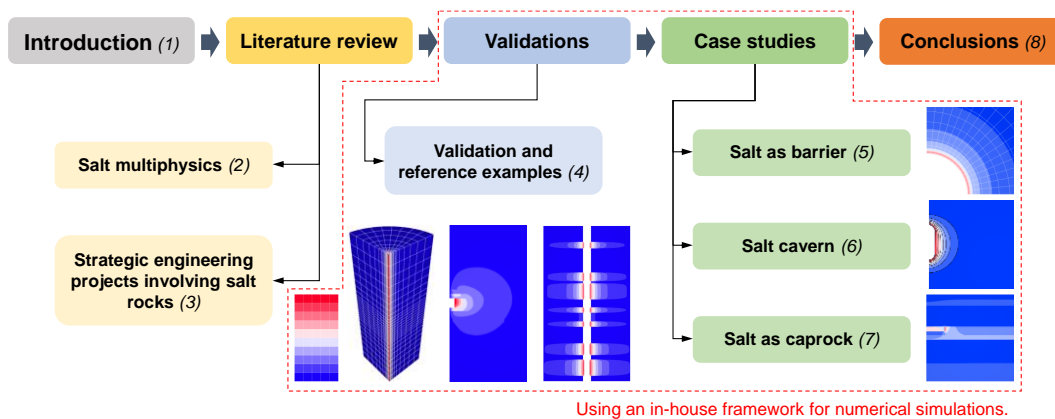


Figure 1. Thesis structure. The chapters are indicated in parentheses, in italics.

The thesis is structured as shown in Figure 1, following five major topics: introduction, literature review, validations, case studies and conclusions. The manuscript is divided into eight chapters with contents briefly described below.

Following this Introduction (Chapter 1), Chapter 2 (Salt multiphysics) consists of the literature review on the multiphysical behavior of salt. Essential aspects of the mechanical behavior of salt are analyzed – particularly those related to creep and dilation, as well as the thermomechanical and hydromechanical coupled behaviors. The governing equations, numerical methods, constitutive models adopted for salt and non-salt rocks and the main contributions of the thesis in the context are presented. Moreover, Chapter 3 (Strategic engineering projects involving salt rocks) consists of the review on the state of the art and innovative strategic engineering projects involving salt rocks. Among them, the thesis has focused on: i) the permanent P&A of Pre-salt wells using the salt as geological barrier; ii) the use of salt caverns for strategic underground storage; and iii) salt as caprock of a Pre-salt reservoir during hydrocarbon production or CO<sub>2</sub> injection.

Next, Chapter 4 (Validation and reference examples) presents a number of reference simulations adopted to validate the implementations of the creep constitutive models and the workflows for mechanical and thermomechanical finite element analyses with repercussions on the hydraulic behavior in the in-house framework adopted as the simulation tool adopted in the thesis.

In the case studies section, Chapter 5 (Case study of well abandonment using salt as geological barrier) presents a case study of a conceptual Pre-salt well to analyze the salt creep behavior as an allied mechanism to form a geological barrier for permanent well abandonment. Mechanical and thermomechanical analyses are carried out and the repercussion on the hydraulic behavior of salt is analyzed as the barrier is formed. Next, Chapter 6 (Case study of salt cavern) shows a case study of a synthetic salt cavern to analyze its mechanical behavior and the hydraulic changes from construction to the end of operation. More so, Chapter 7 (Case study of salt as caprock of Pre-salt reservoir) presents a case study of a synthetic Pre-salt section to analyze the effect of the reservoir pressure changes on the salt caprock creep deformation and how this combined effect affects the geomechanical behavior and triggers permeability changes. Partial conclusions follow in each of the case studies.

Finally, the conclusions section, Chapter 8 (Conclusions and suggestions for future work) presents general and specific conclusions of the thesis. Limitations are discussed and suggestions for future work are given.

## 2 Salt multiphysics

Day-to-day rock mechanics often assumes salt rocks as creeping and impermeable materials. This approach is acceptable in mining, well and cavern practical applications as long as isolation from unsaturated water is fairly ensured. In these cases, the time-dependent deformation behavior – the creep – is one of the most important issues to be assessed to monitor the integrity and serviceability of engineering projects.

Typical salt properties such as creep deformation and essentially null permeability are widely recognized as useful in strategic engineering projects. Examples include casting competent hydrocarbon traps and underground storage media, in addition to possibly being useful for P&A and as caprocks of reservoirs for CO<sub>2</sub> storage. As more complex applications are planned, salt should be analyzed in a more comprehensive perspective, considering a sophisticated representation of the mechanical behavior and a multiphysical approach.

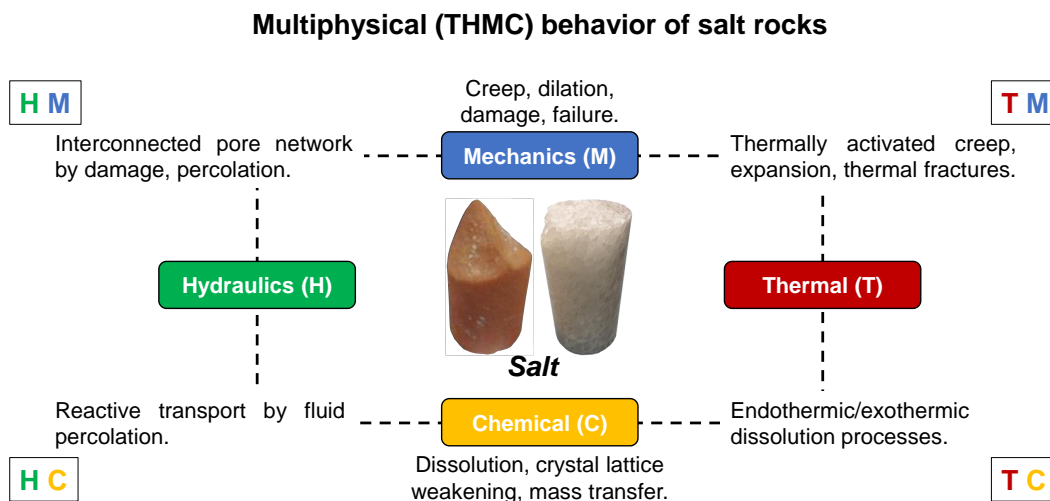


Figure 2. Schematic summary of the multiphysical behavior of salt. The thermal, hydraulics, mechanics, and chemical physics are respectively denoted by “T”, “H”, “M” and “C”.

This chapter is devoted to discussing the multiphysical behavior of salt, i.e., the mechanical and the main coupled behaviors which are relevant in the short- and long-term considering strategic projects involving salt rocks. Figure 2 shows a schematic summary of the multiphysical behavior of salt, where the main coupled

phenomena are indicated. Each of these physics and couplings are described below. Similar schemes have also been presented in the literature, see for instance the work of Cosenza and Ghoreychi (1996).

## 2.1. Mechanical behavior (M)

The mechanical behavior of salt has been widely studied over the last decades especially from the 1970's on. Generally, solely mechanical studies focus on the time dependent deformation. A viscoelastic behavior using a linear-elastic model superimposed by empirical creep laws is often idealized. The creep behavior is ideally isochoric and salt accumulates considerable creep deformation without undergoing macroscopic failure (Schulze et al., 2001). According to this hypothesis, salt remains in a compressive regime and does not undergo significant changes in volume despite the changes in geometry. However, when high stress levels and strain accumulation are reached, salt undergoes dilation and it provokes the opening of microcracks and the generation of new ones. Percolation paths become effective and connected as microcracks open; therefore, the salt tightness hypothesis may be no longer valid. Although undergoing dilation does not properly mean rock failure, this is an undesirable condition in engineering projects. That said, a literature review on the mechanical behavior of salt should address at least creep and dilation behaviors.

An in-depth assessment on the salt creep micromechanics goes beyond the scope of the thesis (which is more engineering oriented) and has been carried out by the author during his master's degree and subsequent work (Firme, 2013; Firme et al., 2016b, 2018a, 2019). Here, the salt creep phases and their corresponding micromechanisms are briefly addressed. The general formulation of the salt creep mechanical problem is presented, which will facilitate the presentation of the constitutive models in the following sections. The mechanical behavior of salt is formulated based on the additive decomposition of the total strain tensor ( $\varepsilon_{ij}$ ) assuming a thermo-viscoelastic behavior, equation (1).

$$\varepsilon_{ij} = \varepsilon_{ij}^{el} + \varepsilon_{ij}^{cr} + \varepsilon_{ij}^{th} \quad (1)$$

where  $\varepsilon_{ij}^{el}$ ,  $\varepsilon_{ij}^{cr}$  and  $\varepsilon_{ij}^{th}$  are respectively the elastic, creep and thermal contributions to the total strain tensor. The creep contribution to the total strain tensor is calculated from the creep strain rate tensor ( $\dot{\varepsilon}_{ij}^{cr}$ ), equation (2):

$$\dot{\varepsilon}_{ij}^{cr} = \frac{3}{2} \frac{\dot{\varepsilon}_{cr}}{\sigma_d} s_{ij} \quad (2)$$

in which  $\sigma_d$  is the uniaxial equivalent stress (scalar) generalized by the von Mises flow rule to the multiaxial problem (deviatoric stress) and  $s_{ij}$  is the deviatoric stress tensor. The deviatoric stress is a function of the second invariant of the deviatoric stresses ( $J_2$ ), equation (3):

$$\sigma_d = \sqrt{3J_2} \quad (3)$$

Still in equation (2),  $\dot{\varepsilon}_{cr}$  is the uniaxial equivalent creep strain rate (scalar) corresponding to the multiaxial problem. Its formulation depends on the creep constitutive model. Section 2.1.1 addresses some of these models. The thermal contribution ( $\dot{\varepsilon}_{ij}^{th}$ ) refers to the instantaneous thermal expansion, which couples the thermal and the mechanical physics, to be discussed in section 2.2. Lastly, dilation and damage are analyzed in an uncoupled way using a dilatancy boundary – this is addressed in more detail in section 2.1.2.

### 2.1.1. Creep behavior

Studies on salt creep are often focused on micromechanisms and the theoretical background for that originates from plasticity applied to metals. Creep micromechanics is closely related to dislocations, which are defects in the crystal lattice of the material. The concept of dislocation has been introduced by Taylor (1935) apud Odqvist (1974), explaining why the crystal lattice of metals undergoes plastic deformations when subjected to stress levels in the elastic regime. Most of the deformation mechanisms in salt rocks are related to dislocation motions (Pouya, 2000), which are propagated by means of creep mechanisms. These mechanisms are influenced by the stress state, temperature, chemical composition, among other factors. Moreover, diffusion can contribute to salt creep in certain circumstances.

Mechanically, creep occurs in order to dissipate the strain energy from stress changes provoked in an undisturbed viscous material. In the case of engineering projects involving salt rocks, stress changes are usually caused by excavation or drilling procedures and creep is observed as a non-instant response to them. More so, salt creep is also thermally-activated. Generally speaking, the higher the increase in the deviatoric stress or temperature, the higher the creep rate. The

examples shown in Chapter 4 highlight this creep sensitivity to deviatoric stress and temperature.

Theoretically, creep behavior is divided into three phases: transient (primary), steady-state (secondary) and accelerative (tertiary). Figure 3 shows typical creep ( $\epsilon$ ) and creep rate ( $\dot{\epsilon}$ ) curves represented by solid and dashed lines respectively. This curve is ideally applicable for any creeping material. The values in parenthesis provide an order of magnitude of the curve applied for salt rocks.

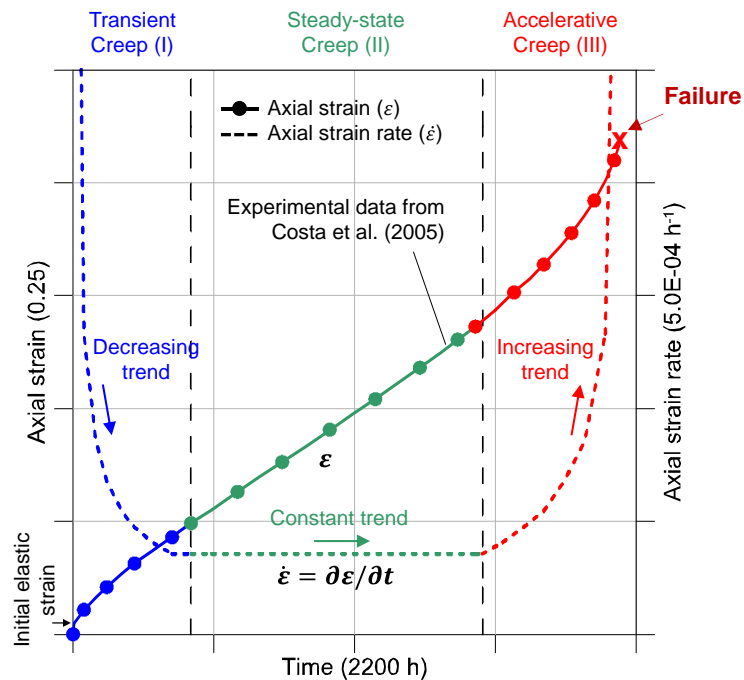


Figure 3. Typical creep curve. The values in parenthesis provide an order of magnitude of the curve applied for salt rocks.

The transient creep phase (I) is represented by the blue curves. It begins after an initial elastic strain that represents an instantaneous response to a perturbation in the undisturbed formation. The creep rate begins with a high value and decreases until a virtually constant value is reached. Micromechanically, this phase exhibits hardening behavior caused by an internal dislocation motion. The nature of this hardening is usually postulated in two ways. The first way is the time-hardening concept, in which stress states present small variation over time, so that time remains as the relevant parameter for creep strain evolution. The second way is the strain-hardening concept, in which stress states vary significantly over time. Hence, strains are relevant to the creep strain evolution. Next, the steady-state creep (II) is represented by the green curves. In this creep phase, the strain rate is constant. Steady-state is possibly the most well-known creep phase, and several constitutive models have been formulated based on it. Micromechanically, this

phase represents the equilibrium condition in the density of dislocations when dislocation growth and piling up are balanced. Different micromechanisms that govern the steady-state creep have been identified, generally related to dislocation motions (glide, climb, cross-slip, among others). Lastly, the accelerative creep (III) is represented by the red curves. The strain rate increases and the material experiences relevant volumetric deformation (dilation). Because of the dilation behavior, the rock accumulates damage until it undergoes failure.

Regarding salt creep constitutive modelling for geomechanical analyses, empirical power and/or Arrhenius expressions are often adopted to account for the contribution of dislocation micromechanisms such as those mentioned in the previous paragraph (Hansen, 2014; Urai and Spiers, 2007). Several creep constitutive models have been developed and enhanced over the last decades. Among these models, one mentions the power law (Lomenick and Bradshaw, 1969; Yao et al., 2007), the double-mechanism creep law (Costa et al., 2000; Dusseault, 1989; Dusseault et al., 1987), the multi-mechanism deformation creep model (Munson, 2004; Munson and Dawson, 1979) and the Lubby2 model (Heusermann et al., 2003). Recently, a hybrid model that joins the steady-state creep rate of the double-mechanism creep law to the transient function of the multi-mechanism creep model has been proposed and demonstrating good results. This constitutive model, which is a contribution of the current doctoral research, is called “Enhanced double-mechanism creep law using a transient function” (EDMT model). A dedicated paper to introduce the model and to present validation examples has been published (Firme et al., 2018a). The next sections describe briefly some of these models. None of them account for accelerative (tertiary) creep; however, salt damage is indirectly analyzed by means of dilation envelopes.

#### **2.1.1.1. Power law (PL)**

The power law (PL model) is a classic creep constitutive model formerly applied to metals and subsequently widely adopted in salt rock studies. This model has been formerly presented by Norton (1929) apud Yao et al. (2007) and considered only the effect of the stress state (deviatoric stress) in the creep deformation. Next, the contribution of time has been included using another power term (Bailey, 1935 apud Yao et al., 2007). Subsequently, the contribution of the temperature has been added by an Arrhenius expression (Dorn, 1955 apud Yao et al., 2007). The effect of the temperature is an important aspect when dealing with

salt rocks since salt creep is thermally activated. This generalized form of the power law that considers the creep strain ( $\varepsilon_{cr}$ ) as function of deviatoric stress, time and temperature is given by equation (4):

$$\varepsilon_{cr} = A\sigma_d^n t^m \exp\left(\frac{-Q}{RT}\right) \quad (4)$$

where  $A$ ,  $n$  and  $m$  are empirical constants calibrated using experimental data,  $\sigma_d$  is the deviatoric stress (uniaxial equivalent),  $t$  is the time,  $T$  is the temperature,  $Q$  is the thermal activation energy and  $R$  is the universal gas constant.

This empirical model has been adopted for salt in the past in waste disposal and mining contexts (Costa, 1984; Lomenick and Bradshaw, 1969). However, the temperature contribution was regarded as a power law term rather than an Arrhenius expression. In these cases, the formulation is presented by equation (5):

$$\varepsilon_{cr} = A\sigma_d^n t^m T^k \quad (5)$$

in which  $k$  is an empirical constant.

Although equations (4) and (5) are presented in terms of creep strain, salt creep constitutive models are often defined in terms of creep strain rate ( $\dot{\varepsilon}_{cr}$ ) in the numerical simulators. Hence, taking the power law from equation (5), the creep strain rate is given by equation (6). After time differentiation, equation (6) is reshaped as shown in equation (7).

$$\dot{\varepsilon}_{cr} = \frac{\partial \varepsilon_{cr}}{\partial t} = (Am)\sigma_d^n t^{m-1} T^k \quad (6)$$

$$\dot{\varepsilon}_{cr} = \bar{A}\sigma_d^n t^{\bar{m}} T^k \quad (7)$$

where  $\bar{A}$  and  $\bar{m}$  are constants so that  $\bar{A} = Am$  and  $\bar{m} = m - 1$ , respectively.

In general, using the power law with the proper empirical constants leads to good fittings for the transient phase. However, the strain curve tends to become horizontal over time. It means that the strain rate converges to an almost null value (see Figure 7). This is not physically coherent with the fact that the steady-state creep rate is represented by a constant value (non-zero). Since the steady-state creep is the most important phase in typical salt rock-related geomechanical analyses, the power law should not be adopted in this context, except in short-term analyses where transient creep dominates.

### 2.1.1.2. Double-mechanism creep law (DM)<sup>2</sup>

The double-mechanism creep law (DM model) is an empirical creep model widely employed in the Brazilian research on salt geomechanics. It originates from the mining research, from a “multiple mechanism viscoplastic law” (Dusseault, 1989; Dusseault et al., 1987; Mraz et al., 1991). These authors point out that salt rocks exhibit purely steady-state creep behavior in the typical mining context due to its ionic structure that makes possible constant deformation rates. The premise of this constitutive model is that the salt formation is subjected mainly to two deformation regimes: viscoelastic and viscoplastic. The viscoelastic regime is composed by slow deformations associated to diffusion processes and to dislocation motions, originally called “solution precipitation” and “dislocation glide”, respectively. The viscoplastic regime involves plastic flow, crack generation, fissures and healing processes; it was originally called “steady-state cracking”.

Physically, the DM model considers a governing mechanism responsible for the steady-state creep behavior depending on the stress level of the engineering problem. Two main mechanisms have been noticed for the Brazilian salt rocks: dislocation creep and steady-state cracking. The dislocation creep refers to the slow and continuous dislocation slippage in the viscoelastic regime under lower stress levels. This mechanism occurs in the salt crystal lattice (Urai and Spiers, 2007). Steady-state cracking consists of the balance between cracking through the salt grain contacts and annealing by pressure solution along the microcracks (Dusseault, 1989; Poiate Jr., 2012; Urai and Spiers, 2007). For the sake of clarity, this thesis adopts “steady-state cracking” instead of “pressure solution” as often referred to in works using the DM model (Costa et al., 2015; Poiate Jr., 2012). Nonetheless, “pressure solution”, within the meaning expressed in those works, is understood as an essential mechanism for steady-state cracking.

The analogy between the “multiple mechanism viscoplastic law” and the DM model is graphically illustrated by Figure 4. The threshold between the dominance of one mechanism and the other is a reference deviatoric stress – the former model adopts Prandtl’s limit ( $K$ ) as such, while the latter uses a reference stress ( $\sigma_0$ ). These stresses are related to corresponding creep strain rates ( $\dot{\epsilon}_K$  and  $\dot{\epsilon}_0$ ,

---

<sup>2</sup> This section was updated for presentation from the article “Enhanced double-mechanism creep laws for salt rocks” written by the author and advisors of the thesis (Firme et al., 2018a) and published in *Acta Geotechnica*.

respectively). Prandtl's limit is considered twofold since it is presented in terms of deviatoric stresses instead of shear stresses.

The DM model formulates the steady-state creep rate ( $\dot{\epsilon}_{ss}$ ) as follows in equation (8),

$$\dot{\epsilon}_{ss} = \dot{\epsilon}_0 \exp\left(\frac{Q}{RT_0} - \frac{Q}{RT}\right) \left(\frac{\sigma_d}{\sigma_0}\right)^{n_i} \quad (8)$$

where  $\dot{\epsilon}_0$ ,  $\sigma_0$  and  $T_0$  are the threshold strain rate, deviatoric stress and temperature respectively – they are related to the transition of governing mechanism noticed in laboratory. The stress power  $n_i$  indicates that the mechanism  $i$  is dominant ( $n_1$  for dislocation creep and  $n_2$  for steady-state cracking). These powers are given by the curve inclinations illustrated in Figure 4 (right plot), where reference values are indicated. Other parameters have already been introduced (see equation (4)).

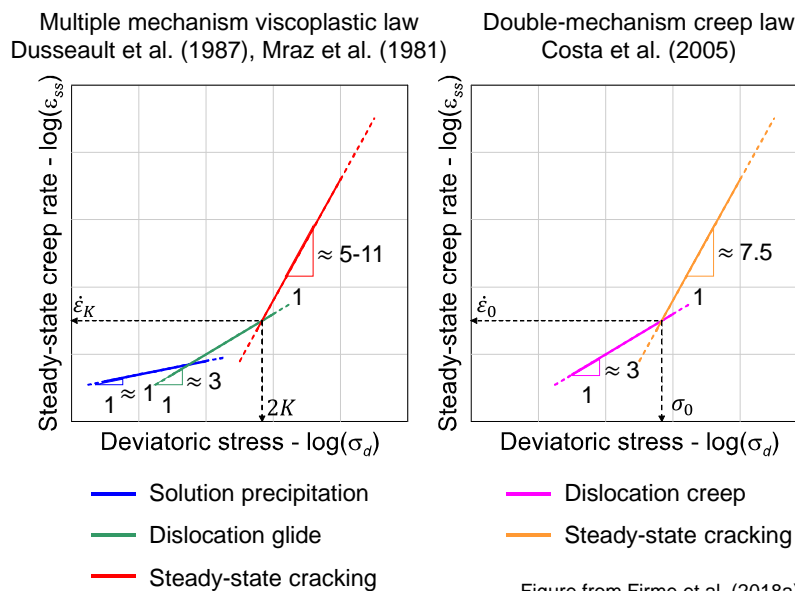


Figure from Firme et al. (2018a)

Figure 4. Analogy between the “multiple mechanism viscoplastic law” and the double-mechanism creep law. Figure adapted from Firme et al. (2018a).

The DM model does not account for transient creep; therefore, the steady-state phase is directly coupled to the initial elastic strain. For this reason, the creep curve (strain versus time) remains lagged (see Figure 7). Neglecting salt transient creep is at first an acceptable simplification in reservoir geomechanics and in long-term well simulations without major changes in stresses and/or temperatures. However, whenever early creep deformation estimates are necessary, the contribution of transient creep is relevant. An example of this is the early-stage creep prediction, which is important to monitor Pre-salt well closure since a minimum diameter to allow casing running and minimum cement sheath thickness

are mandatory. Another example are salt caverns for hydrocarbon storage or waste disposal, in which tightness is an essential condition. These media can be subject to cyclic internal pressures, resulting in cyclic stress changes; therefore, a comprehensive creep modelling is fundamental to forecast stress states prone to cause damage by dilation and, in turn, leakage. Apart from these limitations, the DM model is a straightforward creep constitutive model that has been extensively adopted over the last decades in well geomechanical analyses involving Brazilian salt rocks. Data calibrated against the DM model have proven to be reliable and good fittings for the steady-state creep rate are often obtained (Costa et al., 2019a, 2010, 2005, 2000; Poiate Jr., 2012; Poiate Jr. et al., 2006).

Lastly, a creep model similar to the DM model, often referred to as “Norton-Hoff” law in the salt cavern literature, is widely adopted (Bérest et al., 2001; Sicsic and Bérest, 2014; L. Wang et al., 2015).

### **2.1.1.3. Multi-mechanism deformation creep model (MD)<sup>3</sup>**

The multi-mechanism deformation creep model (MD model) is one of the most sophisticated salt creep constitutive models. It originates from work on the historical Waste Isolation Pilot Plant (WIPP, see Section 3.2.2) as a legacy from the large-scale program of research and testing conducted in the context. The MD model stands out in the simulation of both the transient and the steady-state phases of creep. A superposition of up to three micromechanical creep mechanisms composes the steady-state creep. The transient creep phase is calculated using the steady-state creep rate and a transient function with a hardening parameter.

The MD model requires an in-depth understanding of salt creep micromechanics. The various conditions for the occurrence of creep can be cast in a deformation mechanism map, Figure 5, introduced by Ashby (1972) and applied to salt rocks by Munson (1979). According to this map, creep is governed by dislocation mechanisms or diffusion processes depending on the deviatoric stress and the temperature. In this abacus,  $G$  is the elastic shear modulus and  $T_m$  is the salt melting temperature, adopted as 1077 K (Fossum and Fredrich, 2002;

---

<sup>3</sup> Parts of this section come from excerpts from the articles “An assessment of the creep behaviour of Brazilian salt rocks using the multi-mechanism deformation model” (Firme et al., 2016b) published in *Acta Geotechnica* and “Multi-mechanism deformation creep model applied to Brazilian salt rocks” (Firme et al., 2015b) published in the proceedings of the Mechanical Behavior of Salt VIII Conference (Salt Mech 8). Both articles were written by the author and advisors of the thesis.

Munson, 1979). The mechanisms of interest for geomechanical purposes are dislocation glide, dislocation climb and undefined mechanisms. They are briefly analyzed below.

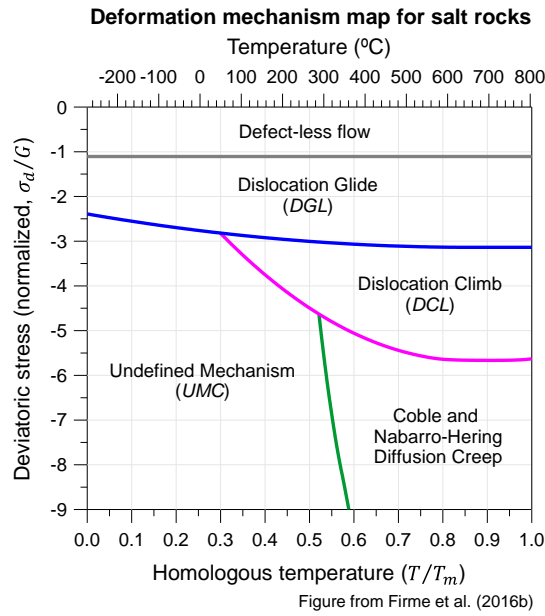


Figure 5. Deformation mechanism map for salt adapted from Munson (1979). Figure adapted from Firme et al. (2016b).

The dislocation glide (DGL) is a slow creep mechanism arising from several slip modes in the crystal lattice of the material. At the microscopic scale, this mechanism occurs at any stress level unbalanced by a deviatoric stress. The successive migration of crystal grains through slip planes tends to generate tangles of dislocations. There is an increase in the density and in the amount of dislocations at the grain boundaries, leading to an obstruction in the dislocation motion – the hardening behavior (Fossum and Fredrich, 2002; Jeremic, 1994). Above a critical deviatoric stress, the transposition of the barriers for dislocation motion is once again enabled (Hambley et al., 1998). In this case, the contribution of dislocation glide for the steady-state creep rate ( $\dot{\epsilon}_{ss,DGL}$ ) is given by equation (9):

$$\dot{\epsilon}_{ss,DGL} = |H(\sigma_d - \sigma_{0,DGL})| \left[ B_1 \exp\left(\frac{-Q_1}{RT}\right) + B_2 \exp\left(\frac{-Q_2}{RT}\right) \right] \sinh\left[\frac{q(\sigma_d - \sigma_{0,DGL})}{G}\right] \quad (9)$$

where  $|H(\sigma_d - \sigma_{0,DGL})|$  is a Heaviside step function that limits the occurrence of dislocation glide for a deviatoric stress ( $\sigma_d$ ) higher than the reference stress of the mechanism ( $\sigma_{0,DGL}$ ). Additionally,  $B_1$  and  $B_2$  are structure factors of the mechanism,  $Q_1$  and  $Q_2$  are thermal activation energies and  $q$  is a stress constant. The other parameters have already been introduced.

Based on the works of Fossum and Fredrich (2002) and Hansen (2014), the author of the thesis understands that even in cases with deviatoric stress levels ( $\sigma_d$ ) lower than  $\sigma_0$ , the glide mechanism is active and implicitly regarded as plastic deformations in climb. When  $\sigma_d$  is higher than  $\sigma_{0,DGL}$ , the contribution of equation (9) refers to the energy that allows the dislocations to transpose the tangles formed by the migration of crystal grains through slip planes – the concept of Peierl's stress, from Hambley et al. (1998) and Hirth and Lothe (1982).

The dislocation climb (DCL) is a dynamic recovery mechanism, controlled by a thermal activation phenomenon, and its contribution is very significant at high temperatures (Fossum and Fredrich, 2002; Jeremic, 1994). The high deformation energy generated by the dislocations during slip motion triggers plastic deformation and hardening. The climb mechanism acts by allowing the movement of the dislocations. In this sense, it is implicit that climb occurs in a context where dislocations are on the verge of moving. According to Fossum and Fredrich (2002), “glide with climb is often called just climb because the climb process actually controls the deformation rate even though the plastic deformation results from glide (...).”<sup>4</sup> This definition is considered here. The contribution of dislocation climb to the steady-state creep rate ( $\dot{\epsilon}_{ss,DCL}$ ) is given by a typical Arrhenius expression, equation (10):

$$\dot{\epsilon}_{ss,DCL} = A_1 \exp\left(\frac{-Q_1}{RT}\right) \left(\frac{\sigma_d}{G}\right)^{n_1} \quad (10)$$

where  $A_1$  and  $n_1$  are the structure factor and the stress power of the mechanism, respectively. The other parameters have already been introduced.

Not only are undefined mechanisms expected to be distinct from the dislocation-based mechanisms, but they also contribute to salt creep. However, the association of these mechanisms to micromechanical models is not at all clear. The interpretation of such mechanisms is not unanimous among researchers and among the characteristics of each salt formation. Some researchers associate this mechanism to a pressure solution mechanism, which acts on the salt grain contacts (Costa et al., 2005; Poiate Jr., 2012). Other researchers consider a mass transfer by solution and precipitation in the viscoelastic regime (Dusseault, 1989; Dusseault et al., 1987). Additionally, an association between this undefined mechanism and dislocation cross-slip has been suggested (Hansen, 2014); this last definition is considered here. The undefined mechanism (UMC) is usually

---

<sup>4</sup> Excerpt from page 35 of the work of Fossum and Fredrich (2002).

taken into account empirically by an Arrhenius expression, analogous to the Dislocation Climb. Its rate ( $\dot{\epsilon}_{ss,UMC}$ ) is given by equation (11):

$$\dot{\epsilon}_{ss,UMC} = A_2 \exp\left(\frac{-Q_2}{RT}\right) \left(\frac{\sigma_{eq}}{G}\right)^{n_2} \quad (11)$$

where  $A_2$  and  $n_2$  are the structure factor and the stress power of the mechanism, respectively. The other parameters have already been defined.

Finally, the steady-state creep rate ( $\dot{\epsilon}_{ss}$ ) is given by the superposition of the three micromechanical creep mechanisms previously presented (equations (9) to (11)), as shown in equation (12):

$$\dot{\epsilon}_{ss} = \dot{\epsilon}_{ss,DGL} + \dot{\epsilon}_{ss,DCL} + \dot{\epsilon}_{ss,UMC} \quad (12)$$

The creep strain rate in the MD model is formulated as follows, equation (13):

$$\dot{\epsilon}_{cr} = F \dot{\epsilon}_{ss} \quad (13)$$

where  $F$  is the transient function given by equation (14):

$$F = \begin{cases} \exp\left[\Delta \left(1 - \frac{\zeta}{\epsilon_t^*}\right)^2\right] & , \quad \zeta \leq \epsilon_t^* \\ \exp\left[-\delta \left(1 - \frac{\zeta}{\epsilon_t^*}\right)^2\right] & , \quad \zeta > \epsilon_t^* \end{cases} \quad (14)$$

in which  $\Delta$  is a hardening parameter (equation (15)),  $\delta$  is a softening parameter,  $\epsilon_t^*$  is the intersect of the steady-state creep rate with the ordinate axis in a strain versus time creep curve (equation (16)), and  $\zeta$  is an internal isotropic hardening variable subject to an evolutionary equation (equation (17)).

$$\Delta = \alpha_h + \beta_h \log\left(\frac{\sigma_d}{G}\right) \quad (15)$$

$$\epsilon_t^* = K_0 \exp(cT) \left(\frac{\sigma_d}{G}\right)^l \quad (16)$$

$$\dot{\zeta} = (F - 1) \dot{\epsilon}_{ss} \quad (17)$$

In the above equations,  $\alpha_h$  and  $\beta_h$  are fitting parameters,  $K_0$  is a transient parameter and  $c$  and  $l$  are a theoretical constant and power, respectively. The evolutionary equation (17) for the parameter  $\zeta$  is solved explicitly by Euler's forward scheme. A null initial value is assumed for  $\zeta$ . One notices that when  $\zeta$  reaches  $\epsilon_t^*$ ,  $F$  is equal to one and  $\dot{\zeta}$  is null. It represents that the steady-state creep rate has been reached.

The MD model stands out as a powerful model for the simulation of the transient and the steady-state phases of salt creep (see Figure 7). Very good results are often observed. In general, calculations using the MD model are quite cumbersome and short time increments must be adopted especially in the transient phase when hardening plays an important role in the nonlinear analysis. As the steady-state is reached, computational cost tends to be comparable with those of other steady-state creep models.

Dealing with sophisticated constitutive models has the side effect of the necessity of numerous parameters – and frequently only few data are available for calibration. One of the main contributions of the master's research of the author was to calibrate the sensitive parameters of the Brazilian halite to use the MD model (Firme, 2013; Firme et al., 2016b). The calibration based on the experimental data has led to structure factors and stress powers quite distinct from the typical range of steady-state parameters of WIPP and Gulf of Mexico salts. The transient parameter ( $K_0$ ) has also been calibrated and its value was in the typical range. Nonetheless, validation examples based on Brazilian scenarios have presented very good agreement between numerical analyses and experimental data. Both the transient and the steady-state creep phases have been adequately simulated.

#### **2.1.1.4. Enhanced double-mechanism creep law (EDMT)**

The enhanced double-mechanism creep law using a transient function (EDMT model) is a hybrid model that joins the steady-state creep rate of the DM model to the transient function of the MD model. This model is a contribution of this doctoral research, and a comprehensive description and validation examples are found in the work of Firme et al. (2018a). Considering that the steady-state creep formulation in the MD model is independent of the transient one, the EDMT model assumes that the standard DM model is validated for main Brazilian salt rocks and can be adopted “as is”. The transient phase is back-analyzed using MD model's transient function ( $F$ ) that multiplies the steady-state creep rate.

The formulation of the EDMT model revisits the transient/steady-state creep rate formulation of the MD model, equation (13). However, the steady-state creep rate from the DM model is adopted rather than that from MD model. It means to replace equation (8) in equation (13). Therefore, the constitutive equation of the creep strain rate is given by equation (18):

$$\dot{\epsilon}_{cr} = F \left( \dot{\epsilon}_0 \exp \left( \frac{Q}{RT_0} - \frac{Q}{RT} \right) \left( \frac{\sigma_d}{\sigma_0} \right)^{n_i} \right) \quad (18)$$

where the transient function  $F$  is the same of that of the MD model. Therefore, it is calculated using equations (14) to (17)). The other parameters have already been introduced.

Using the EDMT model for Brazilian salt rocks is preferable to using the MD model since the price one pays to consider more sophisticated models is the lack of available information for calibration requiring assumptions or correlations that might be subjective. The calibrated data for the DM model have been producing adequate results and should continue to be adopted in creep analyses in Brazilian salt rocks. Moreover, the EDMT model holds the “strain-based transient creep response with nonlinear work-hardening and recovery processes”<sup>5</sup> (van Sambeek et al., 1993a) developed for the MD model. This is a more intrinsic approach for transient creep (in comparison to mathematical fittings) since the parameter  $K_0$  is determined from experimental curves. This model has been adopted in simulations of triaxial creep tests, wells, mining galleries and salt caverns. Very good agreement with experimental data and physically coherent numerical results have been observed (Firme et al., 2018a, 2018b, 2019).

#### 2.1.1.5.

#### Comparative performance of the creep constitutive models

Four relevant creep constitutive models have been briefly presented in sections 2.1.1.1 to 2.1.1.4 and their capabilities in terms of representing the creep phases are summarized in Table 1.

Table 1. Comparative summary of the capabilities of the constitutive models to represent creep phases.

Creep constitutive model	Creep phase		
	Transient (primary)	Steady-state (secondary)	Accelerative (tertiary)
PL	Yes	No	No
DM	No	Yes*	No
MD	Yes	Yes	No
EDMT	Yes	Yes	No

\*Only creep rate.

<sup>5</sup> Excerpt from page 131 of the work of van Sambeek et al. (1993a).

This section shows numerical simulations of a triaxial creep test carried out using Brazilian halite samples to compare the performance of these models. The in-house framework GeMA (to be introduced in Section 2.5) is adopted. The simulations are based on the experimental work presented by Costa et al. (2005). In laboratory, the salt (halite) samples are 17.6 cm high by 8.8 cm in diameter (Poiate Jr., 2012). Considering the axisymmetry and the symmetry at the half of the sample, the numerical models have 8.8 cm high by 4.4 cm in radius. The axisymmetric finite element model has 181 nodes and 50 8-node quadratic elements with reduced integration (elements type “Q8”). Figure 6 illustrates the workflow for the simulations. The sample is initially subjected to a confinement stress that simulates a geostatic stress state. In this case, a confinement stress ( $\sigma_c$ ) of 10 MPa is adopted. The test temperature is of 86°C. Next, an axial load is instantaneously applied to the sample. A deviatoric stress ( $\sigma_d$ ) of 14 MPa is considered. The new stress state is held during the simulation time, while the creep behavior is monitored. The test is carried out by 1,000 hours and the axial strain is measured at the top of the numerical models.

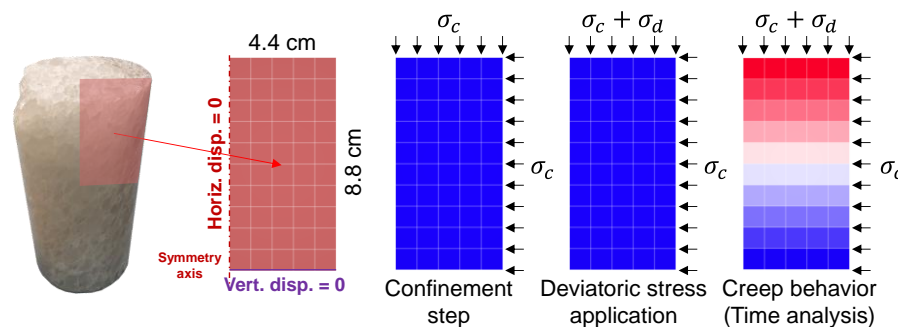


Figure 6. Triaxial creep test: numerical simulation workflow.

Figure 7 (a) depicts the performance of the creep constitutive models. The black dotted line represents the experimental curve of the triaxial creep test. Furthermore, Figure 7 (b) presents the corresponding creep rate curves. Although not originally available, the author of the thesis calculated the experimental rate based on the experimental creep curve points. The scattered rate points in the graph may be related to the discrete time differentiation ( $\dot{\epsilon} = \partial\epsilon/\partial t \approx \Delta\epsilon/\Delta t$ ). Both EDMT (red curves) and MD (orange curves) models present a very good agreement with the experimental curve. This is expected as these models simulate the transient and the steady-state creep phases and the material sensitive parameters have been calibrated for the Brazilian halite. The strain rates obtained are in the range of the experimental rate calculated from the experimental creep curve. The DM model (green curves) shows good agreement with the experimental

creep curve in terms of strain rate, i.e., comparing curve inclinations. The constant creep rate obtained with the DM model is conceptually coherent since both deviatoric stress and temperature are constant during the test. The PL model (blue curves) presents a creep curve that tends to become horizontal with time, while the creep rate tends to a null value. The steady-state creep is not adequately represented by the PL model; therefore, this model should not be adopted in typical salt rock-related geomechanical analyses, except in the short-term, when transient creep dominates, or for comparison with other creep models.

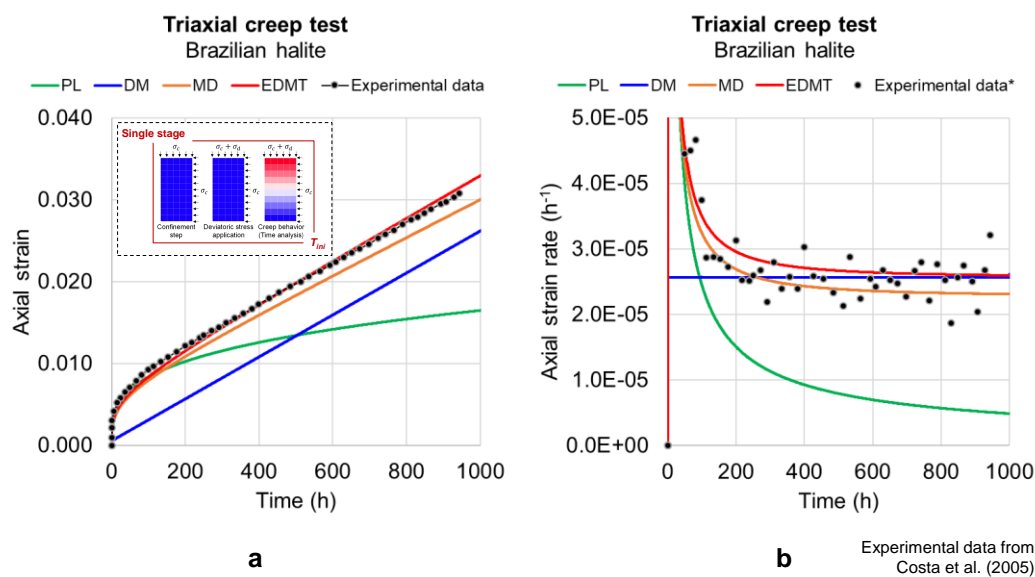


Figure 7. Triaxial creep test: comparison of the creep curves (a) and creep rate curves (b) obtained using each of the constitutive models previously discussed. Experimental data from Costa et al. (2005).

### 2.1.2. Dilation behavior<sup>6</sup>

In the mining industry, ore exploration is a target; therefore, the controlled fragmentation of the rock mass is an objective and not properly a risk to be avoided. The concern in covering the excavation walls is present only where there are critical instability threats. In hydrocarbon wells, drilling thick salt layers to access the Pre-salt reservoirs is a need, and boreholes are often cased and cemented. These components ensure not only structural stability but also hydraulic isolation. The scenario is more adverse in storage caverns. Cavern walls lie exposed in direct contact with the stored material. The access to the cavern is restricted and

<sup>6</sup> This section comes from excerpts from the article "Salt caverns history and geomechanics towards future natural gas strategic storage in Brazil" written by the author and advisors of the thesis (Firme et al., 2019) and published in Journal of Natural Gas Science and Engineering, with minor modifications.

direct visual inspection is impossible. A salt cavern for underground storage is subjected to several stress scenarios during its lifespan, especially considering cyclic schemes of internal pressure during the operation phase, and significant percolation through the walls cannot be allowed. In this context, the maintenance of integrity and tightness is of utmost importance in the short- and long-term.

As previously mentioned, the salt creep behavior is ideally isochoric and salt accumulates significant creep deformation without undergoing failure. It is often associated to a compressive domain. However, once a threshold stress state is exceeded, the material reaches a dilation domain – volumetric deformation becomes relevant and microcracks open. This provokes damage accumulation, leading to strain hardening and rock strength decrease until failure happens (Schulze et al., 2001). Besides that, the opening of microcracks generates interconnected pore networks that enhance the permeability of the medium. Percolation paths are formed (or expanded) and leaching and/or dissolution may enlarge the paths. In such condition, analyses should consider the hydraulic behavior of the surroundings. If dissolution becomes relevant, geometry changes may also happen. The transition between compressive and dilation domains occurs over a band. In practice, this is stated as an envelope – the dilatancy boundary (DeVries et al., 2005b, 2005a; Hunsche, 1993; Hunsche and Hampel, 1999; Schulze et al., 2001; van Sambeek et al., 1993b). The delimitation of this boundary is of utmost importance in the analysis of salt behavior. Dilatancy boundaries have been fitted on results of laboratory tests and the stress states influence them significantly. Schulze et al. (2001) postulate a small contribution of the load geometry and lithology. In general, the influence of the salt type, temperature and strain rate is considered small.

Four widely known salt dilatancy boundaries are briefly introduced – they take the names of the respective researchers who developed them: Spiers', Ratigan's, Hunsche's and DeVries' boundaries. These criteria are useful to constrain the admissible domain for the stress paths in geomechanical analyses. The dilatancy boundaries are formulated here in terms of the mean stresses and the critical deviatoric stresses on the envelope. This methodology to account for dilation is a stress-based approach<sup>7</sup> (Labaune et al., 2018). Since this thesis

---

<sup>7</sup> According to Labaune et al. (2018), an alternative for the stress-based approach for dilation is the strain-based approach. In this case, one establishes the norm of the viscoplastic strain or strain rate as limiting criterion. The analyses carried out by these authors in the context of salt caverns have shown that the strain-based approach presented more conservative results for the dilation zones.

considers the von Mises flow rule<sup>8</sup>, the corresponding dilation envelopes are presented in such a way to be easily coded in numerical simulators.

### 2.1.2.1. Spiers' boundary

Spiers' boundary (Spiers et al., 1989) derives from tests carried out in salt samples from the Asse mine (north of Germany). Triaxial tests were carried out under a temperature range from 20 to 200°C, a confinement pressure range from 0 to 50 MPa and a constant strain rate range from  $10^{-7}$  to  $10^{-4}$  s<sup>-1</sup>. Results obtained with samples from the salt dome of Avery Island and bedded salt from southeast New Mexico were added. The temperature and the strain rate of the test did not influence the results, even assuming comprehensive ranges. The critical deviatoric stress to trigger dilation ( $\sigma_{d,cr}$ ) is given by a linear function of the mean stress ( $\sigma_m$ ) that best fitted the experimental data, equation (19):

$$\sigma_{d,cr} = (a\sigma_m + b)\sqrt{3} \quad (19)$$

where  $a = 0.83$  and  $b = 1.9$ , assuming stresses in MPa. This envelope assumes a residual strength below which the material remains in a compressive regime even when it is totally unconfined ( $\sigma_m = 0$ ).

### 2.1.2.2. Ratigan's boundary

Ratigan's boundary (van Sambeek et al., 1993b) derives from triaxial tests performed on WIPP bedded salt and Avery Island dome salt. This dilatancy boundary is often adopted in the Brazilian halite in numerical simulations of wells and caverns (Costa et al., 2015; Firme et al., 2018a; Poiate Jr., 2012). Its formulation is similar to Spiers' boundary, but does not consider a residual unconfined strength, equation (20):

$$\sigma_{d,cr} = (a\sigma_m)\sqrt{3} \quad (20)$$

in which  $a = 0.81$ .

### 2.1.2.3. Hunsche's boundary

Hunsche's boundary (Hunsche, 1993) derives from a series of laboratory tests to identify salt failure under several conditions. Uniaxial and triaxial tests were

---

<sup>8</sup> The von Mises flow rule is adopted only for the multi-axial space generalization.

carried out on high-purity salt samples from the Asse mine, sited in Zechstein 3 formation. True triaxial tests were conducted in pure samples obtained from five deep wells drilled in the Gorleben salt dome (north of Germany). A quadratic function of the mean stress best fitted the experimental data, equation (21):

$$\sigma_{d,cr} = (f_1 \sigma_m^2 + f_2 \sigma_m) \left( \frac{3}{\sqrt{2}} \right) \quad (21)$$

in which  $f_1 = -0.0168$  and  $f_2 = 0.86$ , assuming stresses in MPa.

By plotting Hunsche's envelope (see Figure 8), one observes that the curve crosses the mean stress axis by a little over 50 MPa. This should be interpreted as a mathematical implication of the parabolic function since it is not expected that the material would be in the imminence of dilation at a confinement (mean) stress of 50 MPa. Popp et al. (2001) have observed this peculiarity and pointed out that this boundary is defined as such "to emphasize that the microcracks are closed under hydrostatic pressures higher than this value [about 50 MPa] after a short time."<sup>9</sup> Those authors proposed a modification in this model by replacing the downward trend of the parabola by a band of low slope (see Figure 9 of their work). This band has been retrofitted by Firme et al. (2019) using the Matlab toolbox and two dilatancy boundaries have been derived – upper and lower boundaries. These dilatancy boundaries are so called "Hunsche Modified" and are respectively given by equations (22) and (23):

$$\sigma_{d,cr} = A_1 \exp(B_1 \sigma_m) - C_1 \exp(G_1 \sigma_m) \quad (22)$$

$$\sigma_{d,cr} = A_2 \exp(B_2 \sigma_m) - C_2 \exp(G_2 \sigma_m) \quad (23)$$

where the fitting parameters are  $A_1 = 25.02$ ,  $B_1 = 0.004636$ ,  $C_1 = 17.9$ ,  $G_1 = -0.1285$ ,  $A_2 = 19.06$ ,  $B_2 = 0.005629$ ,  $C_2 = 19.23$  and  $G_2 = -0.1139$ , assuming stresses in MPa. In these parameters, indexes "1" refer to the upper boundary and indexes "2" refer to the lower boundary.

#### 2.1.2.4. DeVries' boundary

DeVries' boundary (DeVries et al., 2005a, 2005b) derives from a series of laboratory tests carried out on high-purity salt samples from a bedded salt formation near Cayuta, New York (Nieland et al., 2001). These authors considered a dilation criterion based on the Mohr-Coulomb constitutive model. Not only the

---

<sup>9</sup> Excerpt from page 4070 of the work of Popp et al. (2001).

role of the mean stresses in suppressing brittle deformation but also the effect of the intermediate stress on the rock strength and the different mechanical responses to compression and extension have been taken into account. The formulation depends on the mean stress ( $\sigma_m$ ) and on the Lode angle ( $\theta$ ), as presented in equation (24):

$$\sigma_{d,cr} = \left( \frac{D_1(|3\sigma_m|)^k + T_0}{\sqrt{3} \cos \theta - D_2 \sin \theta} \right) \sqrt{3} \quad (24)$$

where  $D_1 = 0.773$ ,  $D_2 = 0.524$ ,  $T_0 = 1.95$  and  $k = 0.693$  for stresses in MPa. Note that equation (24) provides different boundaries for different loading conditions. Generally, the Lode angle is defined by (25):

$$\theta = \frac{1}{3} \operatorname{asin} \left( \frac{-3\sqrt{3} J_3}{2J_2^{3/2}} \right) \quad (25)$$

in which  $J_2$  and  $J_3$  are respectively the second and the third invariants of the deviatoric stresses.

Since this criterion derives from a Mohr-Coulomb criterion defined in terms of stress invariants, the triaxial compression and extension cast the limits, in which Lode angle is  $+30^\circ$  ( $\pi/6$ ) and  $-30^\circ$  ( $-\pi/6$ ) respectively<sup>10</sup>.

#### 2.1.2.5.

#### Comparative performance of the dilatancy boundaries

Figure 8 compares the dilatancy boundaries briefly presented in sections 2.1.2.1 to 2.1.2.4 in the same stress space (p-q) diagram. Spiers' and Ratingan's boundaries (dark blue and light blue curves respectively) are linear envelopes so that the higher the mean stress, the proportionally higher the critical deviatoric stress for dilation. Hunsche's boundary (green curve) is a parabola that crosses the mean stress axis by a little over 50 MPa as a mathematical implication of the equation (21). This is the only envelope (among those considered) that assumes that dilation can occur under hydrostatic loading besides deviatoric loading. The lower and the upper modified versions of Hunsche's boundary (light green and yellow curves respectively) present a nonlinear behavior with the critical deviatoric stress for dilation increasing with the mean stress. Finally, DeVries' boundaries are presented. The purple curve represents the DeVries' boundary considering triaxial compression ( $\theta = \pi/6$ ), the dark red curve represents the boundary for isochoric

<sup>10</sup> The solid mechanics signal convention is considered.

shear ( $\theta = 0$ ) and the red curve represents the boundary for triaxial extension ( $\theta = -\pi/6$ ). The curves are nonlinear and quite similar to those of the modified versions of Hunsche's boundary. One observes that the higher the mean stress, the higher the critical deviatoric stress for dilation, but not in a proportional way. In summary, with the exception of Hunsche's boundary, all dilatancy boundaries indicate that the higher the mean stress, the higher the critical deviatoric stress for dilation. This is generally expected since the strength of the geotechnical materials tends to increase with confinement. The possibility of a well-consolidated salt (natural salt for instance) presenting an envelope analogous to a cap model such as that from Hunsche's boundary – typical of poorly consolidated materials such as some carbonates and sandstones –, should be better analyzed. On the other hand, DeVries' envelope has the advantage of making it possible to consider different loading conditions, better representing the particular conditions of the engineering problem analyzed.

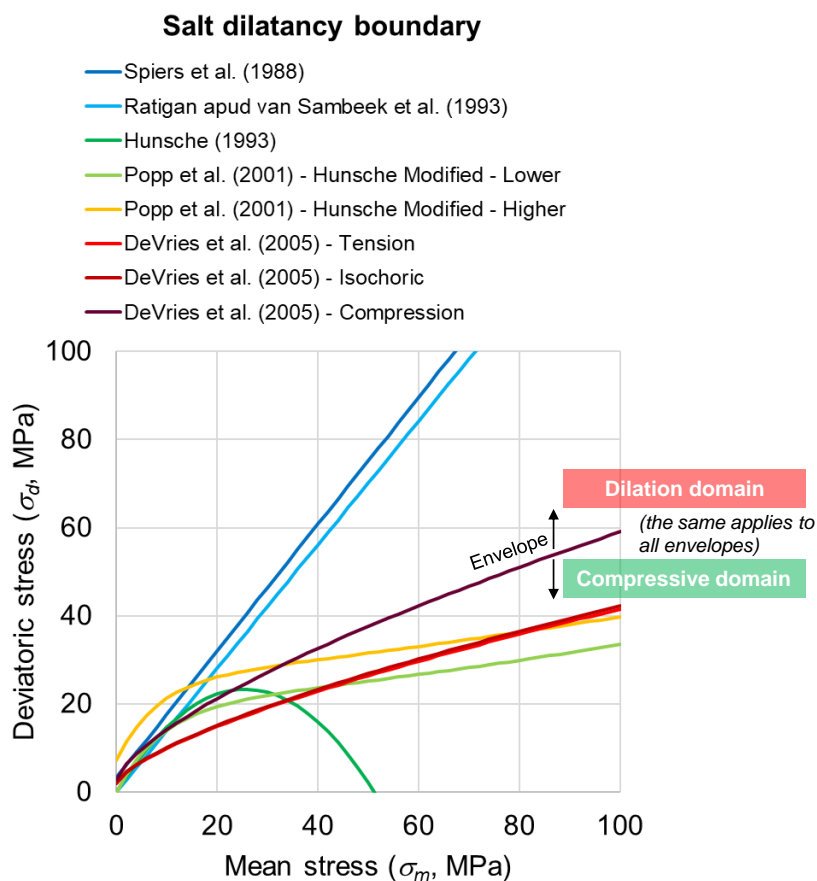


Figure 8. Dilatancy boundaries according to Spiers et al. (dark blue), Ratigan et al. (light blue), Hunsche (green), Hunsche Modified – lower boundary (light green), Hunsche Modified – upper boundary (yellow) and DeVries et al. (tension/extension in red, isochoric in dark red and compression in purple). Modified from Firme et al. (2019).

More so, these widely known dilatancy boundaries were calibrated from tests carried out on salt samples with a high overall purity level. Consequently, the conclusions about the variables of influence on the dilation behavior have derived from these tests and presuppose pure salt. Using these envelopes for more heterogeneous salt such as Brazilian ones (due to the lack of data) should be done with caution since a different mineralogy may reflect on a different mechanical behavior.

So far, the mechanical behavior of salt has been analyzed in isolation from other physics; however, its behavior is multiphysical. In the next sections, the main couplings of interest to strategic engineering problems are addressed.

## **2.2. Thermomechanical behavior (TM)**

The thermal behavior of salt is very important not only regarding heat transfer aspects but also because temperature has great influence on rock mechanics, especially on strength and deformability (Zhu and Arson, 2014). As seen in section 2.1.1, salt creep constitutive models depend on stress and temperature, besides time. It means that the mechanical behavior of salt is intrinsically a coupled thermomechanical behavior even if the temperature field is known in advance and attributed to the model as a parameter. Furthermore, the micromechanical approach for creep using deformation mechanism maps also depends on temperature (Ashby, 1972; Munson, 1979). In this representation, the stress level, the shear modulus and the temperature of the salt formation dictate the dominance of some creep micromechanisms over others (see Figure 5). Regarding the macroscopic behavior of salt, Fossum and Fredrich (2002) point out that thermal changes influence the creep behavior, not only considering the stress changes, but also because salt creep is thermally-activated and shall also trigger stress changes including shear stresses. This may be critical at rock interfaces, especially between salt and non-salt rocks or weak materials, where interlayer slippage can occur.

According to Cosenza and Ghoreychi (1996), undisturbed salt presents a high thermal diffusivity of about  $3.0E-06$  m<sup>2</sup>/s. This value is approximately three times higher than other geotechnical materials. The thermal convection is negligible for low porosity scenarios, i.e., undisturbed or slightly disturbed salt and well-compacted granular salt. On the other hand, it is significant in crushed or granular salt (high porosity scenarios, about 0.35). The thermal conductivity can

be ten times lower than that of undisturbed salt. Still according to these authors, salt rocks exhibit a high thermal linear expansion (about  $4.0E-05^{\circ}C^{-1}$ ), which is often three times higher than other geomaterials. More so, the salt viscosity is the thermally activated term of solid mechanics-based constitutive models for creep. The viscosity, in turn, depends on the temperature so that the higher the temperature, the lower the viscosity. The halite effective viscosity is in the range of  $1.0E+15$  to  $1.0E+19$  Pa.s depending not only on the temperature but also on the composition, moisture content and grain size (Weijermars and Jackson, 2014).

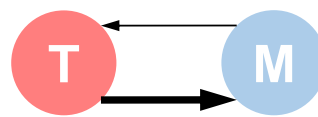
Considering wells, Guenot and Santarelli (1989) point out that the temperature of the well fluids is a very important parameter. Rock properties may be modified by cyclic temperature variations. Cooling the well wall creates a stiffer zone around it due to contraction, generating a high stress concentration. This stiffer zone enhances the strength of the material as long as confinement generally enhances the strength of geotechnical materials. Thermal stresses are generated by non-uniform temperature distribution around the well, and this is the case of fluid circulation that cools or warms the well walls. Temperature changes provoke volumetric deformation in the formation and fluid expansion or contraction. Since creep/swelling mechanisms of rocks such as shale and salt depend on temperature, the changes in the reservoir temperature during production affect the behavior of the well vicinity. In general, cooling the well leads to wall stress reduction. These authors have commented that a cooling temperature gradient stabilizes wells with drilling muds of low density. However, up to a certain level, cooling may trigger unstable conditions regarding shear or fracturing. The thermal effects are of particular importance when considering shallow intervals subjected to significant heating and intervals without drilling fluid, with low friction angles and high Young's moduli. Amaral et al. (2017) have presented an application of cold water injection in reservoirs for hydrocarbon recovery in the context of the Brazilian Pre-salt. In this scenario, caprocks are mainly evaporites. One-way coupled thermomechanical numerical simulations have been carried out considering a scenario of injection of water at  $29^{\circ}C$  for 16 years. Cold-water injection causes contraction and horizontal stress reduction, reducing also the pressure to initiate and propagate a fracture. Horizontal stresses have shown a significant decrease in the carbonate reservoir while no significant impact has been observed in the integrity of the salt rocks. The relevance of the cooling effect was such that reservoir underwent compaction even though it was subjected to water injection. The water-cooling effect prevailed over the poroelastic effect of the injection.

The literature related to salt caverns for underground storage presents physical similarities with well problems and in-depth aspects on rock mechanics. Sriapai et al. (2012) have carried out laboratory tests in pure halite samples from Khorat basin, northeast Thailand. The samples have been collected in depths from 70 and 100 m and the tests have adopted temperatures compatible with underground storage caverns for gas or compressed air. Assuming isothermal conditions for a number of testing temperatures, these authors have observed a decrease in salt short-term strength as the temperature increases. The temperature effect is larger under higher mean stresses. The effect of temperature on rock strength may be intensified in a salt cavern operation considering a number of loading/unloading cycles over its lifespan. The maximum temperature due to injection and the maximum shear stress during fluid withdrawal should be determined. In the end, these critical values should be used to define the maximum and minimum working pressures in the cavern. Sicsic and Bérest (2014) have mentioned two scenarios in which thermal fractures showed up in wells and gas caverns (see figures 1 and 2 of their work). The first scenario was by heating due to the circulation of diesel-burned gases at 315°C and the second scenario was by cooling due to the circulation of liquefied nitrogen at -196°C. These events demonstrated the influence of the temperature on the mechanical behavior of the formation regardless of the internal pressure. These authors have highlighted that intense heating may generate spalling in caverns while intense cooling may generate fractures perpendicular to the cavern wall. Furthermore, Bérest et al. (2014, 2016) have analyzed the thermomechanical effects of depressurization of compressed air energy storage (CAES) caverns. They have observed that a rapid internal pressure decrease induces a significant temperature decrease and tensile stresses are prone to develop. However, the thermal contrast is superficial since that caverns operate in cycles and occurs over a short period. Hence, tensile stresses are developed but are superficial. Fractures emerge perpendicularly to the cavern wall and the blocks between fractures continue strongly bounded to the rock mass. These findings are likely extensible to any gas storage cavern (Bérest et al., 2016). More so, temperature reduction leads to tensile stresses proportional to Young's modulus – usually one observes a stress reduction of 1 MPa/°C. Since the salt tensile strength is lower than 2 MPa, sudden salt cooling may trigger tensile cracks and enhanced permeability (Cosenza and Ghoreychi, 1996).

While the mechanical behavior strongly depends on the thermal behavior, the opposite does not happen in the same intensity. According to Cosenza and

Ghoreychi (1996), the thermal behavior shows small sensitivity to the mechanical behavior (stresses and strains) in undisturbed or slightly disturbed salt. However, the stress state may have a significant effect on the thermal properties of crushed salt since in this case porosity decreases as confinement increases – the grain package gradually consolidates forming a monolithic solid (and its properties tend to those of intact salt). The reduction on thermal conductivity is very important when the pores are filled with gas. Figure 9 presents a schematic representation of the coupled thermomechanical behavior of salt.

Impact on the thermal properties in granular salt. Granular salt progressively turns into a solid salt – properties comparable to those of intact/little disturbed salt. *(Limited and small impact)*



Impact on the thermally activated creep (viscosity), expansion, thermal fractures, spalling. *(Big impact)*

Figure 9. Schematic representation of the coupled thermomechanical behavior of salt.

Lastly, regarding heating generation under brine percolation, pure salt solution in water is endothermal in a mining room temperature while anhydrite solution is very exothermal; therefore, a solution of halite with anhydrite impurities is expected to be exothermal.

In terms of formulation for numerical simulations, the thermal behavior of salt is accounted for in three instances. Firstly, revisiting the additive decomposition of the total strain tensor ( $\varepsilon_{ij}$ ), equation (1), the thermal strain contribution ( $\varepsilon_{ij}^{th}$ ) is given by equation (26):

$$\varepsilon_{ij}^{th} = \alpha \Delta T \delta_{ij} \quad (26)$$

where  $\alpha$  is the thermal expansion,  $\Delta T$  is the temperature change and  $\delta_{ij}$  is the Kronecker delta. This equation provides the coupling term between the thermal and the mechanical physics. Secondly, the mechanical behavior is also influenced by the thermal physics since the creep constitutive models (section 2.1.1) depend on the temperature. Thirdly, the thermal contribution to the multiphysical behavior of salt is related to heat transfer and is formulated by means of the transient Fourier law, equation (27)<sup>11</sup>.

<sup>11</sup> Source/sink terms are not considered in equation (27).

$$\rho c_p \dot{T} - \nabla(\lambda \nabla T) = 0 \quad (27)$$

in which  $T$  and  $\dot{T}$  are the temperature and the temperature rate respectively,  $\rho$  is the density,  $c_p$  is the specific heat and  $\lambda$  is the thermal conductivity.

### 2.3. Hydromechanical behavior (HM)

The hydraulic behavior of salt is usually neglected in many engineering applications since intact (undisturbed/natural) salt is essentially impermeable. In fact, salt rocks are among the less permeable rocks if compared to rocks such as granite, claystone and dolomite (Schulze et al., 2001). However, salt hydraulics may become relevant when it undergoes dilation, microcracks open and there is a permeability enhancement. Depending on the chemical compatibility between the salt and the permeating fluid, dissolution may occur over the flow paths, affecting the integrity of the engineering work. For a better understanding, the hydraulic behavior of salt is addressed first and then the interaction with the mechanical (and thermomechanical) behavior is discussed.

According to Cosenza and Ghoreychi (1996), the initial hydraulic state in salt is not well known. In the case of salt saturated with brine, flow is not necessarily triggered by a pressure gradient as usual in flow approaches. Brine and gas flow through salt is generally influenced by three factors: the pore structure (porosity and permeability), the fluid properties and the transport mechanisms. In the case of brine, a pressure gradient and chemical osmotic effects drive the flow. The gas transport, in turn, is mainly governed by convection and diffusion – macroscopic and molecular processes respectively. As reference values, the permeability of intact salt is by  $1.0\text{E-}21 \text{ m}^2$  (reference from WIPP<sup>12</sup>) and  $6.0\text{E-}20 \text{ m}^2$  (reference from SMRI<sup>13</sup> well 1-year test) (Bérest et al., 2001; Cosenza and Ghoreychi, 1996). Salt rocks exhibit a very low permeability even when heterogeneities are present. Based on laboratory and field tests, Cosenza et al. (1999) point out that salt can present very low permeability, although measurable, when it undergoes damage and in the presence of impurities since both represent preferential paths for fluid percolation. Observations made on high purity halite (halite mineral content higher than 90%) have identified the ductility of halite minerals as the most important reason for the low permeability values (Schulze et al., 2001). On the other hand, disturbed or mined salt rocks present higher permeability. Disturbed salt exhibits

<sup>12</sup> Waste Isolation Pilot Plant.

<sup>13</sup> Solution Mining Research Institute.

values between  $1.0\text{E-}11$  to  $1.0\text{E-}21$   $\text{m}^2$ , compacted salt shows values between  $1.0\text{E-}11$  to  $1.0\text{E-}09$   $\text{m}^2$  and crushed salt presents values higher than  $1.0\text{E-}09$   $\text{m}^2$  (Cosenza and Ghoreychi, 1996). This calls attention to the salt tightness hypothesis generally taken by engineering when one gets close to excavations and drillings where salt is disturbed or even damaged. Table 2 summarizes the permeability ranges mentioned in this paragraph.

Table 2. Permeability ranges of salt rocks (Bérest et al., 2001; Cosenza and Ghoreychi, 1996)

Salt rock condition	Permeability range ( $\text{m}^2$ )
Intact / natural	$1.0\text{E-}21$ to $6.0\text{E-}20$
Disturbed	$1.0\text{E-}21$ to $1.0\text{E-}11$
Compacted	$1.0\text{E-}11$ to $1.0\text{E-}09$
Crushed / granular	$> 1.0\text{E-}09$

The work of Gloyna and Reynolds (1961) is a very important milestone on the topic of permeability in salt rocks. According to these authors, the possibility of salt rock formations becoming toxic waste disposal media has boosted hydraulic studies in this material. It was necessary to understand how salt encompasses the waste material and prevents its release into the environment. Permeability tests were carried out with dome and bedded salt samples. Several permeating fluids were adopted, such as kerosene, mineral oil, pure brine (sodium chloride solution), brine mixed with aluminum nitrate and helium gas. Based on these tests, important observations and conclusions were made: i) the flow occurs only through the grain contacts (boundaries). There is no flow through salt grains; ii) the bedded salt permeability is lower than that of dome salt. This is possibly due to bedded salt exhibits a higher impurity content; and iii) the permeability in field is expected to be significantly lower than that in laboratory since there is a stress relief when salt is collected from the field, and it induces the opening of fissures and cracks. Laboratory cannot reconsolidate the sample in such a manner that the formation consolidation in field over the geological periods is restored.

The orientation of the discontinuities in salt formations also influences permeability. Muhammad et al. (2015) have presented permeability results of three types of salt samples composed by halite and glauberite separated by one discontinuity. In the first sample, the discontinuity is vertical; in the second, it is inclined; and in the third, the discontinuity is horizontal. The permeability change after loading the samples was more significant in the sample with the vertical discontinuity – the final permeability was 13 times the initial value. The final

permeability of the samples with the horizontal and the inclined discontinuities was of two and 0.12 times the initial values, respectively. Such observations highlight the role played by the discontinuities in the permeability, especially when the discontinuities are parallel to the flow direction. These findings are of particular interest for Brazilian salt formations since they are frequently in stratification with other evaporitic or sedimentary rocks such as anhydrite and shale.

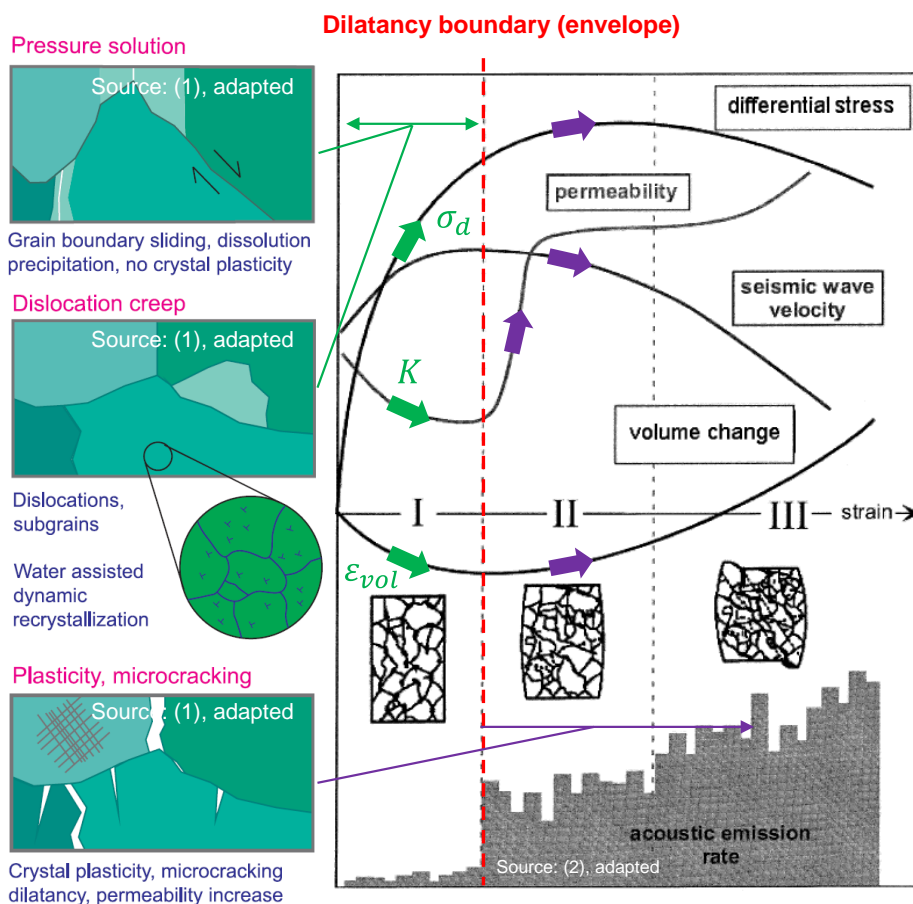


Figure 10. Conceptual representation of the phenomena involved in the hydromechanical behavior of salt. Adaptation from figures presented by Urai et al. (2008) (1) and Schulze et al. (2001) (2).

Figure 10 represents conceptually the hydromechanical behavior of salt. According to Cosenza and Ghoreychi (1996), salt hydraulics is influenced by the mechanical behavior since the loads trigger porosity and flow changes. As confinement increases, pore interconnection reduces, microcracks are closed and therefore permeability decreases (see stage I in Figure 10). Moreover, deviatoric stresses can also affect the flow dynamics by the generation of damaged and/or disturbed rock zones in mining room walls for instance. If the dilatancy boundary is exceeded, salt dilation may trigger damage that in turn enhances permeability (see stages II and III in Figure 10). The interaction between geomechanics and flow in salt rocks is better understood considering their crystalline structure. Alkan

(2009) points out that salt rocks are polycrystalline materials with grains of different shapes and textures. When natural salt is undisturbed, the cracks (grain contacts or fissures) are almost fully closed, casting an inactive microcrack network that results in very low permeability. The activation of the microcrack network occurs when cohesive forces are exceeded, as postulated by classical reservoir geomechanics (Zoback, 2010). This is represented by the stress state of the salt rock exceeding the dilatancy boundary so that the material undergoes volumetric expansion (dilation). The newly opened cracks and fissures generate interconnected pore networks and propagate, increasing the permeability. Well fluids, gases and internal brine percolate over these networks. Therefore, the delimitation of the dilatancy boundary is fundamental for assessing the hydromechanical behavior of salt (Alkan, 2009).

Considering excavated regions – and, in particular, a Pre-salt well wall – dilation behavior is likely observed and hydrogeological contrasts are then expected. The technical literature refers to these regions as “disturbed rock zone” or “excavation damage zone” (DRZ and EDZ respectively) (Alkan, 2009; Stormont and Daemen, 1992). In openholes and storage caverns, DRZs may represent regions that allow some degree of fluid percolation. Estimating the internal extension of a DRZ in a formation is a challenge although it is fundamental for understanding the hydraulic behavior. According to Finley et al. (1994), the extent of a permeability-enhanced disturbed zone in fractured well surroundings varies with depth, host rock properties and stress state. Increases in natural salt permeability may be of six orders of magnitude for volumetric strains up to 1% (Finley et al., 1994 apud Peach, 1991). Stormont et al. (1991) have noticed in field tests carried out in WIPP site that the hydraulic disturbed radius was up to 1.5 times the radius of the well wall. Furthermore, laboratory tests have been carried out to compare the mechanical performance of salt samples with and without fluid percolation. The damage criteria are more restrictive in samples with fluid percolation (Cosenza et al., 2002) – these samples represent DRZs. Geophysical and hydraulic field tests allow estimating the DRZ extent and correlating the results with the material structure. It allows identifying the existence of interconnected fissure networks, i.e., the porosity and permeability enhancement due to dilation behavior. In geophysical tests, electrical resistivity and acoustic wave velocity are measured. Permeability increase is indicated when there is a decrease in the wave velocities, which is correlated with a change in the material pore structure (see Figure 10). In the hydraulic tests, one measures the pore pressure and the

permeability related to the injection of gas, brine and other fluids. According to Stormont and Daemen (1992), the gas permeability of the intact salt is essentially null. Therefore, if the gas permeability is measurable, it means that a new pore structure has emerged due to rock damage. Hydraulic conductivity is then correlated with the pore structure of the formation. More so, the type of permeating fluid also influences the mechanical strength. Cosenza et al. (2002) have observed that samples subjected to brine percolation exhibited lower strength than those subjected to oil percolation. These authors have suggested that the nucleation and propagation of fissures expands the salt-brine contact surface, enhancing chemical activity and leading to rock weakening. Figure 11 shows a schematic representation of the coupled hydromechanical behavior of salt.

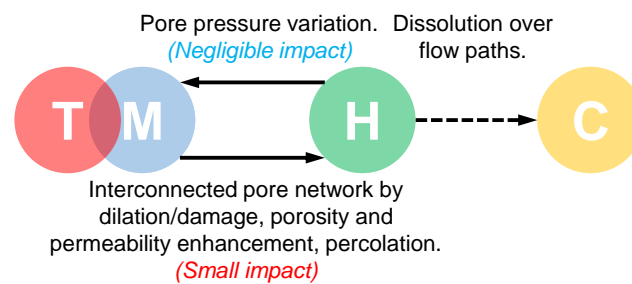


Figure 11. Schematic representation of the coupled hydromechanical behavior of salt.

Although the relation between salt hydraulics and mechanics is conceptually notorious, proper quantification of the hydromechanical behavior is challenging. Typical coupled flow-geomechanics reservoir analyses considers that flow affects geomechanics due to pore pressure evolution, which in turn triggers changes in the effective stresses. On the other hand, geomechanics affects flow due to the volumetric deformation, impacting porosity and permeability. Generally speaking, this is the concept of “stress-dependent permeability” (Chin et al., 2000). Considering aspects regarding thermally-activated salt creep, stress-related dilation, excavated regions (DRZs or EDZs) and the corresponding hydraulic consequences, the author of the thesis believes that this concept is valid for salt rocks, not so much for the porous medium itself, but due to the opening of microcracks creating and interconnected pore network. A major challenge is the proper choice of mathematical coupling expressions between these two physics. David et al. (2001) have presented experimental studies on the Rothbach sandstone (from Eastern France) in order to investigate the effect of stresses on rock permeability. They carried out hydrostatic and triaxial compaction tests – the hydrostatic tests are of particular interest in the context of the thesis. These authors have derived empirical relations (presented below) for the permeability evolution

in function of the effective stresses and porosity. Kuhlman and Matteo (2018) have presented a literature review on the relation between porosity and permeability with special regards to salt rocks. The authors have pointed out that there are a number of porosity and permeability correlations from the hydrocarbon-related rocks while salt-related information is still scarce. The salt creep behavior may be responsible for significant differences between salt rocks and sandstones with respect to variations in porosity and permeability. Still according to these authors, the excavation/drilling surroundings are DRZs and the pore network also includes microfractures and microcracks. The fracture porosity is sensitive to the effective stress (mean stress), and therefore a hydromechanical coupling expression that relates permeability and effective stresses is more representative.

In terms of formulation for numerical simulations, the changes in the hydraulic behavior of salt are accounted for in two ways. Firstly, the permeability is related to porosity by means of the power-law shown in equation (28) (Chin et al., 2000; David et al., 2001):

$$K_{t+\Delta t} = K_t \left( \frac{\phi_{t+\Delta t}}{\phi_t} \right)^\chi \quad (28)$$

where  $K$  is the permeability (area unit),  $\phi$  is the porosity and  $\chi$  is an empirical power. Note that  $t$  and  $t + \Delta t$  are two consecutive time steps. According to David et al. (2001), the empirical power  $\chi$  ranges from 1 to 25, in which the higher values correspond to the high porosity rocks. Equation (28) requires a flow-geomechanics coupling relation between the permeability and the porosity. The porosity evolution is calculated based on the volumetric strain evolution, as shown in equation (29) (Chin et al., 2000; Otto and Kempka, 2015):

$$\phi_{t+\Delta t} = 1 - (1 - \phi_t) \exp(-\Delta \varepsilon_{vol_{t \rightarrow t+\Delta t}}) \quad (29)$$

in which  $\Delta \varepsilon_{vol}$  is the volumetric strain increment between the time steps  $t$  and  $t + \Delta t$ . The permeability calculated in function of the porosity is so called “porosity-dependent permeability” ( $K, f(\phi)$ ). Secondly, the permeability is related to the mean stress variation through the exponential expression shown in equation (30) (David et al., 2001; Kuhlman and Matteo, 2018):

$$K_{t+\Delta t} = K_t \exp(-\omega \Delta \sigma_{m_{t \rightarrow t+\Delta t}}) \quad (30)$$

where  $\Delta \sigma_m$  is the mean stress increment between the time steps  $t$  and  $t + \Delta t$  and  $\omega$  is an empirical parameter. According to David et al. (2001), the empirical parameter  $\omega$  ranges from 0.023 to 0.11 MPa<sup>-1</sup> for low porosity and crystalline rocks

and from 0.001 to 0.020 for high porosity and granular rocks. The permeability calculated in function of the mean stress is so called “mean stress-dependent permeability” ( $K, f(\sigma_m)$ ).

Moreover, the hydraulic behavior of salt is considered in terms of flow through a microfracture/microcrack network. Although one expects a low velocity flow that does not generate relevant pore pressure, the flow velocity field is an important input for reactive transport analyses. In this context, Darcy’s law likely provides pragmatic solutions although its applicability in salt rocks is questionable (Cosenza and Ghoreychi, 1996).

## **2.4. Long-term behavior of salt**

The creep constitutive models presented in sections 2.1.1.1 to 2.1.1.4 are widely employed in salt structure analyses for engineering purposes. These models have been inherited either from metallurgy or from mining with the main purpose of predict strains and displacements following a solid mechanics framework. Although the most frequent way to simulate salt rock creep in engineering applications adopts solid mechanics models – typically linear-elasticity superimposed by an empirical creep constitutive model –, there is some concern if this approach represents properly the far-field rock formation and the long-term. The long-term perspective is very important when dealing with strategic projects involving salt rocks, such as well abandonment, salt caverns for mining, hydrocarbon storage or carbon capture and storage (CCS), and salt as caprocks of reservoirs.

According to Bérest et al. (1979), researchers in the context of salt caverns agree that salt presents an elastic-ductile behavior in short-term compression, when creep is highly nonlinear and depends on deviatoric stress, temperature and time; an elastic-fragile behavior in short-term tension; and a fluid behavior in long-term (flowing even at very lower deviatoric stresses). In the same sense, Urai et al. (2008, 1986) have called attention to the presence of relatively high creep rates in field in long-term under low deviatoric stresses. The standard creep constitutive models generally underestimate these long-term rates since they depend strongly on the deviatoric stresses. In a petroleum geology perspective (Mohriak and Szatmari, 2009), salts “are not exactly rocks – they are soluble, they came from

liquids and they return to them as soon as possible.”<sup>14</sup> Analogously, in a fluid mechanics view oriented to well P&A (Vrålstad et al., 2019), salt “behaves essentially like a highly viscous fluid and will in the end always close the annulus given reduced annulus pressure and sufficient time.”<sup>15</sup> Therefore, salt can be understood as a geomaterial that exhibits a hybrid character, which is considered as a rock or as a highly viscous fluid depending on the context. That said, there is a need to model salt as a viscous fluid rather than a solid material for long-term predictions.

Typically, the knowledge area of geodynamics follows a “backward” long-term perspective. Broadly and among other applications, geodynamics studies the evolution of the salt deformation in the crust over a geological timescale and the repercussions of this on the geological structures observed today. Salt is often regarded as high viscous fluid rather than a viscoelastic/viscoplastic solid. One of the main ideas in geodynamics is that “the flow of geomaterials over geological timescales is calculated by solving the momentum equation neglecting inertial terms (Stokes equations)”<sup>16</sup> (Lobanov et al., 2014). Among other works in the area, Thieulot (2011) has simulated an extensional sandbox experiment with a viscous layer in the central bottom of the model considering 2D and 3D lithospheric extension models. Stokes’ equations have been adopted for the viscous layers. More so, the work of Popov et al. (2014) is recommended for a more extensive list of applications of Stokes solution in geodynamics.

More specifically in salt rocks, according to Weijermars and Jackson (2014), salt behaves as an elastoplastic solid in short-term (up to 1,000 hours) and as viscoelastic (fluid) in long-term tectonic times (up to 100 million years). Viscous creep triggered by deviatoric stresses does not cease since salt tectonic flow continues. Salt may migrate in a horizontal direction for hundreds of kilometers due to creep flow. That generates a lateral pressure gradient (Poiseuille flow) and/or an overburden downslope horizontal movement (Couette flow) depending on the boundary conditions. In this sense, it ideally casts a creeping flow than can be simulated using Stokes’ equations. In the context of Pre-salt wells, Weijermars et al. (2014b) have presented an assessment on the closure of openholes. Salt wells are subjected to both elastic and viscous stresses imposed by surroundings until the elastic stresses are fully released by creep into the well. These authors have

---

<sup>14</sup> Excerpt from page 19 of the work of Mohriak and Szatmari (2009), freely translated from Portuguese.

<sup>15</sup> Excerpt from page 486 of the work of Vrålstad et al. (2019).

<sup>16</sup> Excerpt from page 18 of the work of Lobanov et al. (2014).

adopted a Rankine flow model (sink flow) to describe salt creep towards the well. This methodology has the advantage of considering the effect of the far-field creep on well closure while typical solid mechanics-based well analyses do not. Regarding cased wells, Weijermars et al. (2014a) discussed about drag forces acting on casings. The pre-existent flow prior well drilling is described by a combination of Couette and Poiseuille flows. Once the well is cased, a typical Stokes' creeping flow past a cylinder (the casing) applies exerting drag forces upon the casing. Analogously, in a P&A context, the plug integrity should be checked against the drag forces triggered by salt flow. These simulations have highlighted the relevance of Stokes' equations in the context of Pre-salt wells. Figure 12 sketches the application of Stokes flow to Pre-salt-related simulations.

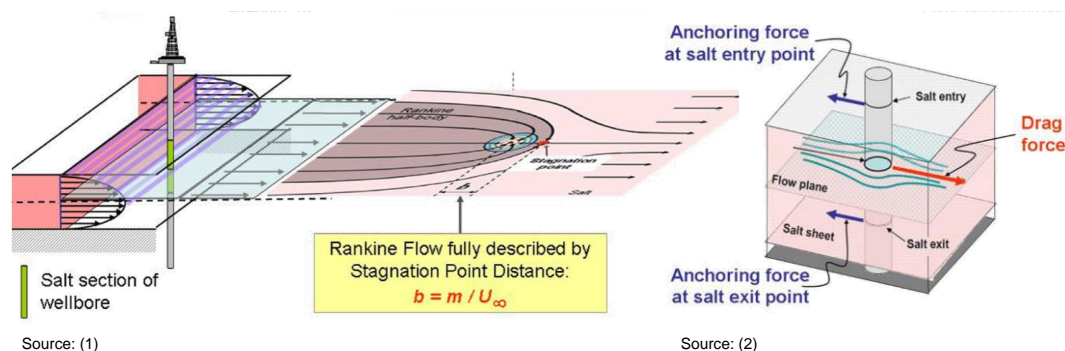


Figure 12. Application of Stokes flow to Pre-salt well-related simulations. Adaptation from figures presented by Weijermars et al. (2014b) (1) and Weijermars et al. (2014a) (2).

In a parallel development to the main theme of the thesis, the author has implemented the weak form of the Stokes-Brinkman equations (Brinkman, 1949) in the context of flow through karstified porous media. This implementation can be adopted in future simulations of the Pre-salt well scenarios mentioned in the previous paragraph. However, considering the broad scope of this doctoral research, this research line has been regarded for future studies.

## 2.5. Formulations in the scope of the thesis

This section presents the relevant formulations for this research line and, more in particular, the computational tool and the formulation adopted in the applications presented in the thesis. The results of the thesis are based on numerical simulations using the coupled temperature-displacement and/or the displacement-based finite element method.

As computational tool, the thesis adopts the in-house multiphysics and multiscale framework Geo Modelling Analysis – GeMA<sup>17</sup> (Mendes, 2016; Mendes et al., 2016). This framework holds a number of powerful solvers for a wide range of multiphysical problems and also works as an interactive environment for in-house and external solvers by means of orchestrated procedures. GeMA framework has been adopted with success in related contexts such as mechanical and hydromechanical simulations in natural fractured reservoirs (Mejia Sanchez et al., 2019; Rueda et al., 2018), dual-porosity/dual-permeability models for flow through fractured media (Rueda et al., 2019), and extended finite elements (XFEM) to simulate hydraulic fracturing (Escobar et al., 2019). GeMA adopts the open-source solver Armadillo (Sanderson and Curtin, 2018, 2016). The solid mechanics signal convention is considered.

### 2.5.1.

#### **Thermo-viscoelastic behavior of salt and repercussion on the hydraulic behavior (TM+H approach)**

The approach adopted for salt in the applications of the thesis is to assume it as a thermo-viscoelastic material. A coupled thermomechanical behavior is considered to properly account for the temperature distribution over the model when there is a localized temperature variation (well heating for instance) in addition to the displacement, stress and strain fields. More specifically, this idealization consists of the linear thermoelasticity superimposed by a creep constitutive model coupled to the heat transfer equation (transient Fourier law). As previously seen, the thermal changes influence the mechanical behavior by means of thermal stresses and thermally-activated creep deformation.

Furthermore, plasticity is regarded *sensu lato* through the dilatancy boundary in a stress-based approach<sup>18</sup>. Unless otherwise stated, the applications of the thesis adopt the EDMT creep constitutive model (Section 2.1.1.4) and DeVries' dilatancy boundary (Section 2.1.2.4). Once the thermomechanical problem is solved (displacements, temperatures, stresses and strains), the repercussion on the hydraulic behavior is analyzed, i.e., the changes in porosity and permeability. In the thesis, this methodology is so-called TM+H approach (to be detailed below).

---

<sup>17</sup> The in-house framework GeMA has been developed in the Multiphysics Modeling and Simulation Group at Tecgraf Institute of the Pontifical Catholic University of Rio de Janeiro (PUC-Rio). GeMA website: <https://web.tecgraf.puc-rio.br/gema/gema/doxygen/html/index.html>

<sup>18</sup> See note 7.

The coupled thermomechanical finite element formulation is recurrent in commercial programs and finite element textbooks – see Potts and Zdravkovic (1999) for instance. Gonçalves (2011) and Lira et al. (2015) have presented a formulation focused on the context of salt creep thermomechanical analyses. From a combined approach of the works above, the thermo-viscoelasticity is considered in the stress incrementation between the time steps  $t$  and  $t + \Delta t$  as (31):

$$\{\Delta\sigma^{el}\} = [D]\{\Delta\varepsilon^{el}\} \quad (31)$$

where  $\{\Delta\sigma^{el}\}$  is the (elastic) stress tensor increment,  $[D]$  is the elasticity (constitutive) matrix and  $\{\Delta\varepsilon^{el}\}$  is the elastic strain tensor increment. Considering the additive decomposition of the total strain tensor into the elastic, creep (viscous) and thermal components, it follows that (incrementally) (32):

$$\{\Delta\varepsilon^{el}\} = \{\Delta\varepsilon\} - \{\Delta\varepsilon^{cr}\} - \{\Delta\varepsilon^{th}\} \quad (32)$$

in which  $\{\Delta\varepsilon\}$ ,  $\{\Delta\varepsilon^{cr}\}$  and  $\{\Delta\varepsilon^{th}\}$  are respectively the total, the creep (viscous) and the thermal strain increments. Therefore, the elastic stress tensor in the next step ( $t + \Delta t$ ) is given by (33):

$$\{\sigma^{el}\}_{t+\Delta t} = \{\sigma^{el}\}_t + [D]\{\Delta\varepsilon - \Delta\varepsilon^{cr} - \Delta\varepsilon^{th}\}_{t+\Delta t} \quad (33)$$

where  $\{\sigma^{el}\}_t$  is the stress tensor of the previous step  $t$  or, if one deals with the initial step, it represents the initial stress state (geostatic).

Expressing the equilibrium of the body in terms of the Principle of Virtual Displacements, it follows that (34):

$$\delta W_{int}|_{t+\Delta t} = \delta W_{ext}|_{t+\Delta t} \quad (34)$$

where  $\delta W_{int}|_{t+\Delta t}$  is the internal virtual work given by (35):

$$\delta W_{int}|_{t+\Delta t} = \int_V \{\sigma^{el}\}^T \delta\{\varepsilon\} dV \Big|_{t+\Delta t} \quad (35)$$

and  $\delta W_{ext}|_{t+\Delta t}$  is the virtual work of the loads given by (36):

$$\delta W_{ext}|_{t+\Delta t} = \int_V \{F_b\}^T \delta\{U\} dV \Big|_{t+\Delta t} + \int_\Gamma \{F_\Gamma\}^T \delta\{U\} d\Gamma \Big|_{t+\Delta t} \quad (36)$$

in which  $V$  and  $\Gamma$  are respectively the volume and the surface of the body. Moreover,  $U$  is the displacement of the body,  $F_b$  are the body forces and  $F_\Gamma$  are the surface loads.

According to equation (33) and considering the virtual deformation of an arbitrary change in the volume configuration as  $\delta\{\varepsilon\} = \delta\{\Delta\varepsilon\}$ , the internal virtual work generated is (37):

$$\delta W_{int}|_{t+\Delta t} = \delta\{\Delta\varepsilon\}^T \int_V \{\sigma^{el}\}_t + [D]\{\Delta\varepsilon - \Delta\varepsilon^{cr} - \Delta\varepsilon^{th}\}|_{t+\Delta t} dV \quad (37)$$

Assuming a von Mises flow rule and an explicit time integration of the creep rate, the creep strain increment is calculated by (38):

$$\{\Delta\varepsilon^{cr}\}_{t+\Delta t} = \Delta t \{\dot{\varepsilon}^{cr}\}_{t+\Delta t} = \Delta t \frac{3}{2} \frac{\dot{\varepsilon}_{cr}}{\sigma_d} \{s\} \Big|_{t+\Delta t} \quad (38)$$

where  $\dot{\varepsilon}_{cr}$  is the uniaxial equivalent creep strain rate and  $\sigma_d$  is the uniaxial equivalent stress generalized by von Mises flow rule (deviatoric stress, equation (3)) – both are scalar quantities that represent the multiaxial problem. Since the EDMT creep constitutive model is adopted,  $\dot{\varepsilon}_{cr}$  is given by equation (18). However, for the sake of generality, neither  $\dot{\varepsilon}_{cr}$  nor  $\sigma_d$  has been replaced in equation (38). By default, GeMA adopts an explicit time integration for creep. The explicit integration is conditionally stable and the time increment should not exceed a critical value. For more details on stable time incrementation in creep models, see section 4.9 of Stone (1997). Advances in the use of explicit integration methods in the context of creep of geomaterials are presented by Quevedo et al. (2019).

Besides that, the thermal strain increment is calculated by (39):

$$\{\Delta\varepsilon^{th}\}_{t+\Delta t} = \{I\}\alpha\{\Delta T\}|_{t+\Delta t} \quad (39)$$

in which  $\{\Delta T\}$  is the temperature change between steps  $t$  and  $t + \Delta t$ ,  $\{I\}$  is an auxiliary vector to consider only the volumetric component of the tensor and  $\alpha$  is the thermal expansion (scalar).

Discretizing the entire volume into finite elements of domain  $\Omega_e$ , the primary variables of the problem are the element displacement field ( $U_e$ ) and incremental temperatures ( $\Delta T_e$ ). Polynomial functions ( $N$ ) are adopted to interpolate the displacement field inside the element so that  $\{U_{\Omega_e}\} = [N]\{u_e\}$  and a differential operator ( $B$ ) composed by the derivatives of the interpolation functions is adopted considering the strain-displacement compatibility relation so that  $\{\varepsilon\} = [B]\{u_e\}$ . Having in mind a coupled thermomechanical problem, polynomial functions ( $N_T$ ) are adopted to interpolate the change in the temperature field so that  $\{\Delta T_{\Omega_e}\} = [N_T]\{\Delta T_e\}$ . Thus, the element equilibrium is given by equation (40):

$$\begin{aligned}
& \left[ \int_{\Omega_e} [B]^T [D] [B] d\Omega_e \right] \{u_e\} \Big|_{t+\Delta t} - \left[ \int_{\Omega_e} [B]^T [D] \{I\} \alpha \{N_T\} d\Omega_e \right] \{\Delta T_e\} \Big|_{t+\Delta t} \\
&= \left\{ \int_{\Omega_e} [B]^T [D] \Delta t \frac{3 \dot{\epsilon}_{cr}}{2 \sigma_d} \{s\} d\Omega_e \right\} \Big|_{t+\Delta t} \\
&- \left\{ \int_{\Omega_e} [B]^T \{\sigma^{el}\} d\Omega_e \right\} \Big|_t + \left\{ \int_{\Omega_e} [B]^T [D] \{\varepsilon\} d\Omega_e \right\} \Big|_t \\
&+ \left\{ \int_{\Omega_e} [N]^T \{F_{b_e}\} d\Omega_e \right\} \Big|_{t+\Delta t} + \left\{ \int_{\Gamma_e} [N]^T \{F_{\Gamma_e}\} d\Gamma_e \right\} \Big|_{t+\Delta t}
\end{aligned} \tag{40}$$

In a compact form, equation (40) is reshaped into (41):

$$[\mathbb{K}_{uu_e}] \{u_e\} + [\mathbb{K}_{uT_e}] \{\Delta T_e\} = \{f_{u_e}\} \tag{41}$$

where  $[\mathbb{K}_{uu_e}]$  is the local (element) stiffness matrix of the mechanical problem,  $[\mathbb{K}_{uT_e}]$  is the local thermomechanical coupling matrix and  $\{f_{u_e}\}$  is the consistent force vector respectively given by (42), (43) and (44).

$$[\mathbb{K}_{uu_e}] = \left[ \int_{\Omega_e} [B]^T [D] [B] d\Omega_e \right] \tag{42}$$

$$[\mathbb{K}_{uT_e}] = \left[ - \int_{\Omega_e} [B]^T [D] \{I\} \alpha \{N_T\} d\Omega_e \right] \tag{43}$$

$$\begin{aligned}
\{f_{u_e}\} = & \left\{ \int_{\Omega_e} [B]^T [D] \Delta t \frac{3 \dot{\epsilon}_{cr}}{2 \sigma_d} \{s\} d\Omega_e \right\} \Big|_{t+\Delta t} - \left\{ \int_{\Omega_e} [B]^T \{\sigma^{el}\} d\Omega_e \right\} \Big|_t \\
& + \left\{ \int_{\Omega_e} [B]^T [D] \{\varepsilon\} d\Omega_e \right\} \Big|_t + \left\{ \int_{\Omega_e} [N]^T \{F_{b_e}\} d\Omega_e \right\} \Big|_{t+\Delta t} \\
& + \left\{ \int_{\Gamma_e} [N]^T \{F_{\Gamma_e}\} d\Gamma_e \right\} \Big|_{t+\Delta t}
\end{aligned} \tag{44}$$

The global matrices and vectors consist of the accumulation of the local matrices and vectors of all elements of the domain, so that (45):

$$[\mathbb{K}_{uu}] \{U\} + [\mathbb{K}_{uT}] \{\Delta T\} = \{f_u\} \tag{45}$$

where  $[\mathbb{K}_{uu}] = \sum_{j=1}^{\# elem.} [\mathbb{K}_{uu_e}]$ ,  $[\mathbb{K}_{uT}] = \sum_{j=1}^{\# elem.} [\mathbb{K}_{uT_e}]$  and  $\{f_u\} = \sum_{j=1}^{\# elem.} \{f_{u_e}\}$ .

Furthermore, a second equation stands for the thermal problem which is governed by the transient Fourier law. A weak formulation of equation (27) is

assumed. Applying the weighed residual method using a set of weighting functions for temperature ( $W_T$ ) as shown in equation (46) for a 2D plane model (the thickness is unity), one gets:

$$\int_V [W_T]^T \left[ \rho c_p \frac{\partial T}{\partial t} - \lambda \left( \frac{\partial^2 T}{\partial x^2} + \frac{\partial^2 T}{\partial y^2} \right) \right] dV = 0 \quad (46)$$

The temperature field is obtained by solving the weighted integral formulation given by equation (46). Considering the entire volume discretized into finite elements of domain  $\Omega_e$ , using the interpolation functions previously defined ( $N_T$ ) so that the element temperature  $\{T_{\Omega_e}\} = [N_T]\{T_e\}$  and the adopting the Galerkin method ( $[W_T] = [N_T]$ ), it follows that (47):

$$[S_{TT_e}]\{\dot{T}_e\} + [K_{TT_e}]\{T_e\} = \{f_{T_e}\} \quad (47)$$

in which  $S_{TT_e}$  is the local (element) heat capacity matrix,  $K_{TT_e}$  is the local conduction matrix and  $f_{T_e}$  is the local thermal consistent forcing function respectively given by (48), (49) and (50).

$$S_{TT_e} = \left[ \int_{\Omega_e} \rho c_p [N_T]^T [N_T] d\Omega_e \right] \quad (48)$$

$$K_{TT_e} = \left[ \int_{\Omega_e} \lambda \left\{ \frac{\partial [N_T]^T}{\partial x} \frac{\partial [N_T]}{\partial x} + \frac{\partial [N_T]^T}{\partial y} \frac{\partial [N_T]}{\partial y} \right\} d\Omega_e \right] \quad (49)$$

$$f_{T_e} = \left\{ \int_{\Gamma_e} [N_T]^T \lambda \left\{ \frac{\partial [N_T]}{\partial x} T_e + \frac{\partial [N_T]}{\partial y} T_e \right\} d\Gamma_e \right\} \quad (50)$$

The global matrices and vectors consist of the accumulation of the local matrices and vectors of all elements of the domain, so that (51):

$$[S_{TT}]\{\dot{T}\} + [K_{TT}]\{T\} = \{f_T\} \quad (51)$$

where  $[S_{TT}] = \sum_{j=1}^{\# elem.} [S_{TT_e}]$ ,  $[K_{TT}] = \sum_{j=1}^{\# elem.} [K_{TT_e}]$  and  $\{f_T\} = \sum_{j=1}^{\# elem.} \{f_{T_e}\}$ .

The time integration in the transient analysis follows using the finite difference method. Assuming that the temperature rate can be approximated by the temperature variations in a time increment  $\Delta t$ , equation (52),

$$\{\dot{T}\} = \frac{\partial \{T\}}{\partial t} = \frac{\{T\}_{t+\Delta t} - \{T\}_t}{\Delta t} \quad (52)$$

and a typical theta-method for time integration, equation (53),

$$\{T\} = (1 - \theta)\{T\}_t + \theta\{T\}_{t+\Delta t} \quad (53)$$

one gets equation (54) by replacing (52) and (53) in equation (51):

$$\begin{aligned} ([S_{TT}] + \theta\Delta t[\mathbb{K}_{TT}])\{T\}_{t+\Delta t} \\ = ([S_{TT}] - (1 - \theta)\Delta t[\mathbb{K}_{TT}])\{T\}_t \\ + \Delta t((1 - \theta)\{f_T\}_t + \theta\{f_T\}_{t+\Delta t}) \end{aligned} \quad (54)$$

In the above equations,  $\theta$  is a factor between 0 and 1 that indicates the finite difference scheme adopted<sup>19</sup>. By default, GeMA adopts an implicit time integration for the thermal problem.

Finally, the thermomechanical problem is solved simultaneously for displacements and temperatures in GeMA through a fully coupled approach. Alternatively, the problem could be solved by calculating the temperature field for each time step using equation (54) and applying the results to calculate the displacement field using equation (45). This thermomechanical problem represents a one-way coupling since the thermal physics affects the mechanical physics by means of the thermal strains and the thermally activated creep behavior. On the other hand, the mechanical physics generally does not affect the thermal physics, except for the case of consolidating granular salt (see Section 2.2).

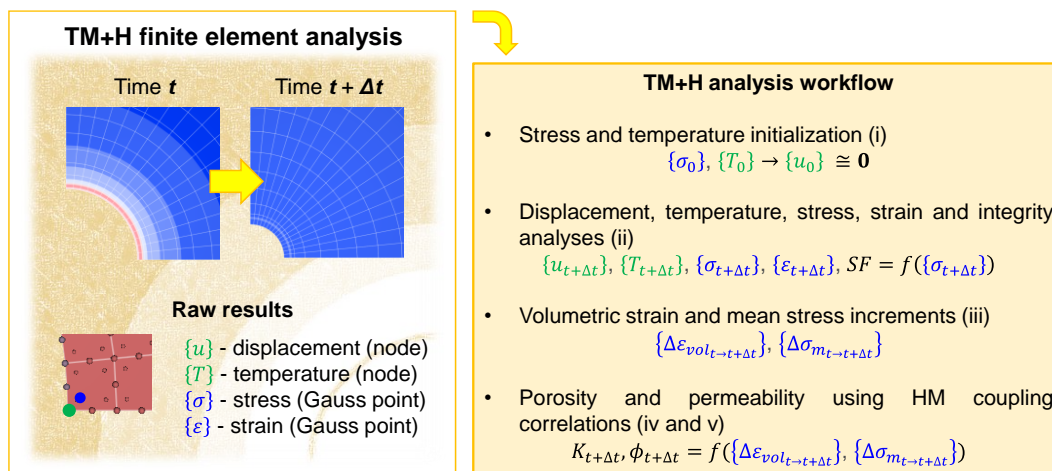


Figure 13. Workflow of the TM+H finite element analysis.

Having the solution of the thermomechanical problem, the next step is to calculate the repercussion on the hydraulic behavior of the salt, i.e., the porosity and permeability changes as the stress state of salt rock evolve. In the numerical analyses, the repercussion of the thermomechanical behavior on the salt hydraulics is calculated in each time step following this workflow: i) the initial

<sup>19</sup> The finite difference schemes typically employed in this context are the Explicit Euler or Forward Euler ( $\theta = 0$ ), Central or Crank-Nicolson ( $\theta = 1/2$ ), Implicit Euler or Backward Euler ( $\theta = 1$ ) and Galerkin method ( $\theta = 2/3$ ).

stresses and temperatures are assigned in time  $t = 0$ ; ii) the displacement, stress, strain and temperature fields are calculated for time step  $t + \Delta t$  by means of the thermomechanical finite element simulation. Integrity analyses using dilatancy boundaries (see Section 2.1.2) can be carried out in this step; iii) the increments of volumetric strain and mean stress are calculated between the time steps  $t$  and  $t + \Delta t$ ; iv) the porosity is calculated in time step  $t + \Delta t$  using equation (29); and v) the porosity-dependent permeability and the mean stress-dependent permeability in time  $t + \Delta t$  are calculated using equations (28) and (30) respectively. In the end, two permeability values are obtained and compared in order to identify the most critical scenario. Figure 13 illustrates the workflow of the TM+H finite element analysis. More so, this methodology assumes that both porosity and mean stress are relevant quantities that influence salt permeability during creep of openings in salt. These dependencies have been discussed in Section 2.3.

This TM+H approach has been inspired by Otto and Kempka (2015) in geomechanics although not applied to salt rocks. These authors have carried out simulations in the context of underground coal gasification, in which high temperature increases occur around the excavation. The porosity evolution has been calculated based on the volumetric deformation (equation (29)) and the influence of the porosity evolution on the permeability has been calculated based on equation (28). This thesis, however, sought to adapt this methodology to salt geomechanical analyses in strategic engineering projects. The contribution of the thesis to the existing approach is indicated in Table 3.

Table 3. TM+H approach – thermomechanical problem and changes in the hydraulic behavior.

Source – material	TM problem			Hydraulic problem <sup>20</sup>		
	Coupled	Creep	Dilation	$\phi$	$K, f(\phi)$	$K, f(\sigma_m)$
Otto and Kempka (2015) – coal	X	-	-	X	X	-
This thesis – salt	X	X	X <sup>21</sup>	X	X	X

<sup>20</sup> Variables defined in Section 2.3.

<sup>21</sup> Dilation is analyzed in an uncoupled way using a dilatancy boundary.

### 2.5.2. Constitutive behavior of non-salt materials

The mechanical behavior of the non-salt (standard elastoplastic) rocks is included in most of the applications of the thesis due to the interaction of these rocks with salt. As examples of the non-salt rocks considered in the thesis, one mentions: anhydrite<sup>22</sup>, basalt, calcirudite, carbonate (limestone), conglomerate, sandstone and shale<sup>23</sup>. The mechanical behavior of these rocks is described using a typical elastoplastic geotechnical constitutive model, Mohr-Coulomb. This section briefly presents the formulation adopted.

The Mohr-Coulomb is a mean stress-sensitive frictional failure criterion for geomaterials. The critical deviatoric stress to trigger shear failure ( $\sigma_{d,cr}$ ) depends on the mean effective stress ( $\sigma'_m$ ) and on the Lode angle, as expressed in Equation (55) – see, for instance, Souza Neto et al. (2008):

$$\sigma_{d,cr} = \left( \frac{c \cdot \cos \varphi - \sigma'_m \sin \varphi}{\cos \theta - (1/\sqrt{3}) \cdot \sin \theta \sin \varphi} \right) \sqrt{3} \quad (55)$$

where  $\varphi$  is the friction angle,  $c$  is the cohesion and  $\theta$  is the Lode angle (see Equation (25)). Since this criterion is formulated in terms of stress invariants, it is limited to Lode angles between  $+30^\circ$  ( $\pi/6$ ) and  $-30^\circ$  ( $-\pi/6$ ).

### 2.5.3. Summary of properties

Unless otherwise stated, the properties adopted in the applications of the thesis are summarized in this section. For the Brazilian halite, the thermal and the elastic properties are shown in Table 4. The properties of the PL model in a creep rate formulation are given by Table 5. Furthermore, the transient creep properties of the MD model are summarized in Table 6. The steady-state creep properties of the DM model are presented in Table 7. Note that the properties summarized in Table 6 and Table 7 also apply to the EDMT model. The steady-state creep properties of the MD model are presented in Table 8. In those tables, the properties indicated with an asterisk were calibrated specifically for the Brazilian halite.

<sup>22</sup> Anhydrite is an evaporitic rock without relevant creep behavior. It is generally modeled as an elastoplastic material.

<sup>23</sup> Although some shale groups exhibit creep behavior and are candidates for geological barriers, this thesis focuses on Brazilian Pre-salt scenarios in which shales are typically modelled an elastoplastic material without relevant creep behavior.

Table 4. Thermal and elastic properties adopted for the Brazilian halite (References: 1: Poiate Jr. (2012), 2: Pudewills and Droste (2003), 3: Bérest et al. (2014) and 4: Firme et al. (2016b)).

Parameter	Description	Value	Ref.
$\rho$ (kg/m <sup>3</sup> )	Density	2170.0 *	1
$c_p$ (J/(kg.K))	Specific heat capacity	879.63	2
$\lambda$ (W/m.K)	Thermal conductivity	6.0	3
$\alpha$ (K <sup>-1</sup> )	Thermal expansion	4.2E-05	2
$E$ (GPa)	Young's modulus	25.37 *	1, 4
$\nu$	Poisson's ratio	0.36 *	1

Table 5. Creep properties adopted in the PL model (rate formulation) for the Brazilian halite, assuming stresses in kPa, times in seconds and temperatures in Kelvin (Lomenick and Bradshaw, 1969).

Parameter	Description	Value
$A$	Empirical power law multiplier	1.01924E-41
$n$	Empirical stress power	3.0
$\bar{m}$	Empirical time power	-0.7
$k$	Empirical temperature power	9.5

Table 6. Transient creep properties adopted in the MD and EDMT models for the Brazilian halite (References: 1: Firme et al. (2016b) and 2: Munson (2004)).

Parameter	Description	Value	Ref.
$K_0$	Transient parameter	7.75E+04 *	1
$c$ (K <sup>-1</sup> )	Theoretical constant	9.198E-03	2
$m$	Theoretical power	3.0	2
$\alpha_h$	Fitting parameter for hardening	-17.37	2
$\beta_h$	Fitting parameter for hardening	-7.738	2
$\delta$	Softening parameter	0.58	2

Table 7. Steady-state creep properties adopted in the DM and EDMT models for the Brazilian halite (Poiate Jr., 2012).

Parameter	Description	Value
$Q$ (J/mol)	Thermal activation energy	50,160.0
$R$ (J/mol.K)	Universal gas constant	8.314
$\dot{\epsilon}_0$ (h <sup>-1</sup> )	Threshold creep rate	1.888E-06 *
$\sigma_0$ (MPa)	Threshold deviatoric stress	9.91 *
$T_0$ (K)	Threshold temperature	359.15 *
$n_1$	Stress power for dislocation creep	3.36 *
$n_2$	Stress power for steady-state cracking	7.55 *

Table 8. Steady-state creep properties adopted in the MD model for the Brazilian halite (References 1: Firme et al. (2016b) and 2: Munson (1999)).

Parameter	Description	Value	Ref.
$A_1$ (s <sup>-1</sup> )	Structure factor of the DCL	1.638E+27 *	1
$Q_1$ (J/mol)	Thermal activation energy of the DCL	104,500	2
$n_1$	Stress power of the DCL	7.2 *	1
$A_2$ (s <sup>-1</sup> )	Structure factor of the UMC	1.924E+06 *	1
$Q_2$ (J/mol)	Thermal activation energy of the UMC	41,800	2
$n_2$	Stress power of the UMC	3.2 *	1
$\sigma_{0,DGL}$ (MPa)	Reference stress of the DGL	20.57	2
$q$	Stress constant	5,335	2
$B_1$ (s <sup>-1</sup> )	Structure factor 1 of the DGL	9.981E+06	2
$B_2$ (s <sup>-1</sup> )	Structure factor 2 of the DGL	4.976E-02	2

In order to analyze the changes in the hydraulic behavior of salt, the parameters of the geomechanics-flow correlations are given in Table 9.

Table 9. Geomechanics-flow correlation parameters adopted for the Brazilian halite (David et al., 2001).

Parameter	Description	Value
$\chi$	Power in the porosity-permeability relation, equation (28)	1.00
$\omega$	Parameter in the mean stress-permeability relation, equation (30)	0.11

Lastly, the mechanical properties of the non-salt rocks are given by Table 10, Table 11 and Table 12.

Table 10. Mechanical properties adopted for non-salt rocks – Part 1 of 3.

Parameter	Description	Anhydrite	Basalt	Calcurudite
$\rho$ (kg/m <sup>3</sup> )	Density	2,918.43	2,762.49	2,710.5
$E$ (GPa)	Young's modulus	55.11	33.28	40.56
$\nu$	Poisson's ratio	0.36	0.32	0.23
$c$ (MPa)	Cohesion (MC <sup>**</sup> )	0.9	66.20	11.08
$\varphi$ (deg)	Friction angle (MC <sup>**</sup> )	37	31	15.08
$\psi$ (deg)	Dilation angle	17*	11*	8.9
References: (see below)		6, 7	4	1-3

Table 11. Mechanical properties adopted for non-salt rocks – Part 2 of 3.

Parameter	Description	Carbonate	Sandstone	Shale
$\rho$ (kg/m <sup>3</sup> )	Density	2,604.49	2,200	2,299.69
$E$ (GPa)	Young's modulus	40.56	20.7	19.34
$\nu$	Poisson's ratio	0.23	0.15	0.15
$c$ (MPa)	Cohesion (MC <sup>**</sup> )	11.08	1.1	4.8
$\varphi$ (deg)	Friction angle (MC <sup>**</sup> )	15.08	32	22
$\psi$ (deg)	Dilation angle	8.9	12*	2*
References: (see below)		2, 3	5, 8	5

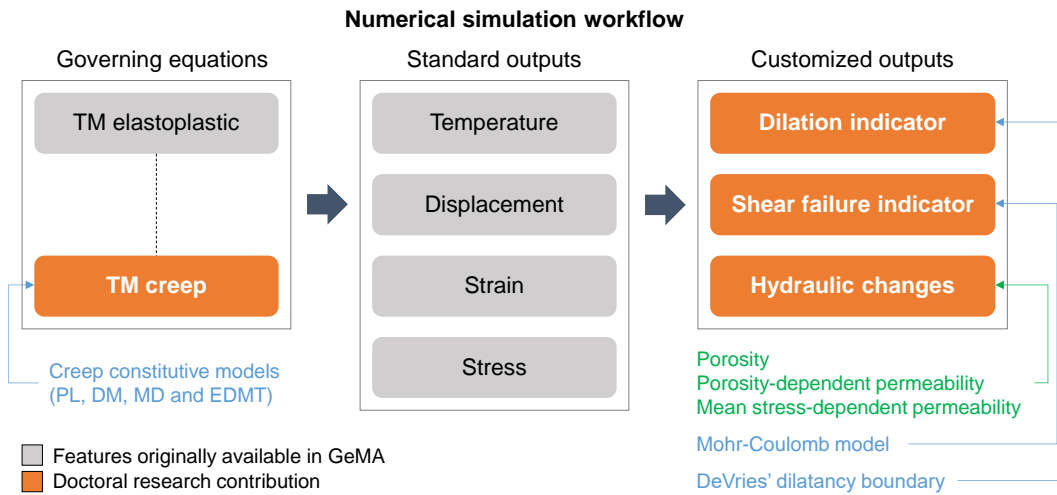
Table 12. Mechanical properties adopted for non-salt rocks – Part 3 of 3.

Parameter	Description	Conglomerate
$\rho$ (kg/m <sup>3</sup> )	Density	2,710.5
$E$ (GPa)	Young's modulus	15.82
$\nu$	Poisson's ratio	0.25
$c$ (MPa)	Cohesion (MC <sup>**</sup> )	1.1
$\varphi$ (deg)	Friction angle (MC <sup>**</sup> )	32
$\psi$ (deg)	Dilation angle	12*
References: (see below)		1, 5

The references in Table 10, Table 11 and Table 12 are: 1: Oliveira et al. (2014), 2: Domingues (2011), 3: Corrêa (2016), 4: Goodman (1989), 5: Costa et al. (2019a), 6: Firme et al. (2018a), 7: Poiate Jr. (2012) and 8: Otto and Kempka (2015). More so, when unavailable, the dilation angle was assumed as the friction angle minus 20 degrees (Alejano and Alonso, 2005) or null if the friction angle is lower than 20 degrees (indicated with an “\*” in the tables). The abbreviation “MC” stands for Mohr-Coulomb (indicated with an “\*\*” in the tables).

#### 2.5.4. Contributions of the thesis in modelling and simulation

The governing equations and the simulation methodology established as the workplan of the thesis have required a number of adjustments and developments to be carried out using the existing in-house framework GeMA. These developments – mainly implementations –, represent part of the contribution of the thesis to this research area and to the framework.



#### Creep constitutive models (PL, DM, MD, EDTM)\*

```

1  #include <gpMaterialCreep.h>
2
3  **
4  ** Copyright (C) 2014 by Carlos Augusto Teixeira Mendes
5  ** All rights reserved.
6
7  ** This file is part of the "GeMA" software. It's use should respect
8  ** the terms in the license agreement that can be found together
9  ** with this source code.
10 ** It is provided AS IS, with NO WARRANTY OF ANY KIND,
11 ** INCLUDING THE WARRANTY OF DESIGN, MERCHANTABILITY AND FITNESS FOR
12 ** A PARTICULAR PURPOSE.
13 **
14
15
16
17 * \file gmpMaterialEDMTCreep.h
18 * \brief Declaration of the GmpMaterialEDMTCreep class
19
20 * \author Pedro Firme
21 * \author Cristian Mejia Sanchez
22 * \date February, 2020
23 */
24
25 #ifndef _GEMA_PLUGIN_MECHANICALMATERIAL_EDMTCREEP_H_
26 #define _GEMA_PLUGIN_MECHANICALMATERIAL_EDMTCREEP_H_
27
28 #include "gmpMechanicalConfig.h"
29 #include <gmpFemPhysics.h>
    
```

#### Customized boundary conditions\*

```

-- Govern functions
--
-- function to interpolate in a tabular time function
function interpTabularData(StepTime, TabularData)
--
CellFunction { id = 'TrPressPseudoGeostatic',
parameters = { (src = 'time', unit = 's'),
method = function(t,y)
--
}
CellFunction { id = 'TrPressLeachingOut',
parameters = { (src = 'time', unit = 's'),
method = function(t,y)
--
}
CellFunction { id = 'TrPressDebrine',
parameters = { (src = 'time', unit = 's'),
method = function(t,y)
--
}
CellFunction { id = 'TrPressFirstFill',
parameters = { (src = 'time', unit = 's'),
method = function(t,y)
--
}
CellFunction { id = 'TransientPressOperation',
parameters = { (src = 'time', unit = 's'),
method = function(t,y)
    
```

#### Customized outputs: integrity indicators and changes in the hydraulic behavior\*

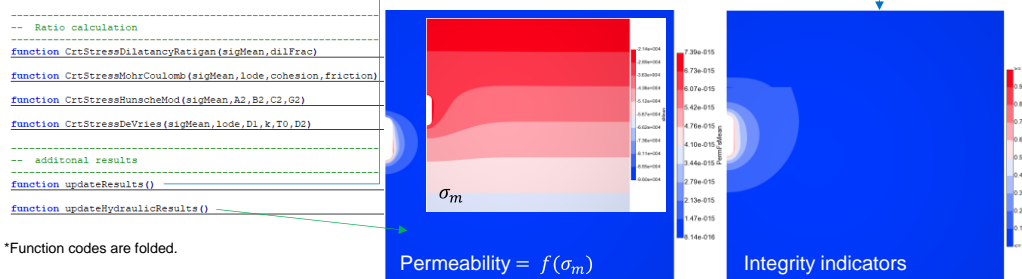


Figure 14. Graphical abstract of the main contributions of the thesis in the workflow for numerical simulation of strategic projects involving salt rocks.

Figure 14 shows a graphical abstract of the contributions. More specifically, the implementations in the context of thesis were<sup>24</sup>:

- Creep constitutive models (PL, DM, MD, EDTM), subsequently validated in the workflow for coupled thermomechanical problems.

<sup>24</sup> Many developments in GeMA framework related to this research area have been made possible from fruitful discussions and code reviews with Dr. Eleazar Cristian Mejia Sanchez. His assistance is sincerely acknowledged.

- Customized boundary conditions, such as transient pressure schemes to simulate solution mining, change of well fluids over time, gas operation cycles and pore pressure variation schemes.
- Post-processing strength indicators regarding dilation and shear failure, and the corresponding output variables to be visualized in contour maps.
- Hydromechanical coupling correlations, i.e., the porosity and permeability changes in function of the geomechanical response, and the corresponding output variables to be visualized in contour maps.

Besides that, the workflow followed in the in-house framework and some example models for validation have also been added to the program content in order to guide future users and developments.

### 3 Strategic engineering projects involving salt rocks

In the previous chapter, the essential fundamentals of the behavior of salt have been addressed. In this chapter, the continuation of the literature review is presented, focusing on more specific aspects of strategic engineering projects involving salt rocks, which are the scenarios of the thesis.

Among the current projects worldwide, this research emphasizes the permanent P&A of wells crossing salt rocks using the creep behavior as an allied mechanism in the formation of geological barriers, the use of salt caverns for strategic underground storage of hydrocarbons, CO<sub>2</sub> (CCS) or energy elements (compressed air energy system, CAES) and the salt caprock behavior in the context of Pre-salt reservoirs during hydrocarbon production or for CO<sub>2</sub> storage. Each of these areas is discussed in the following sections.

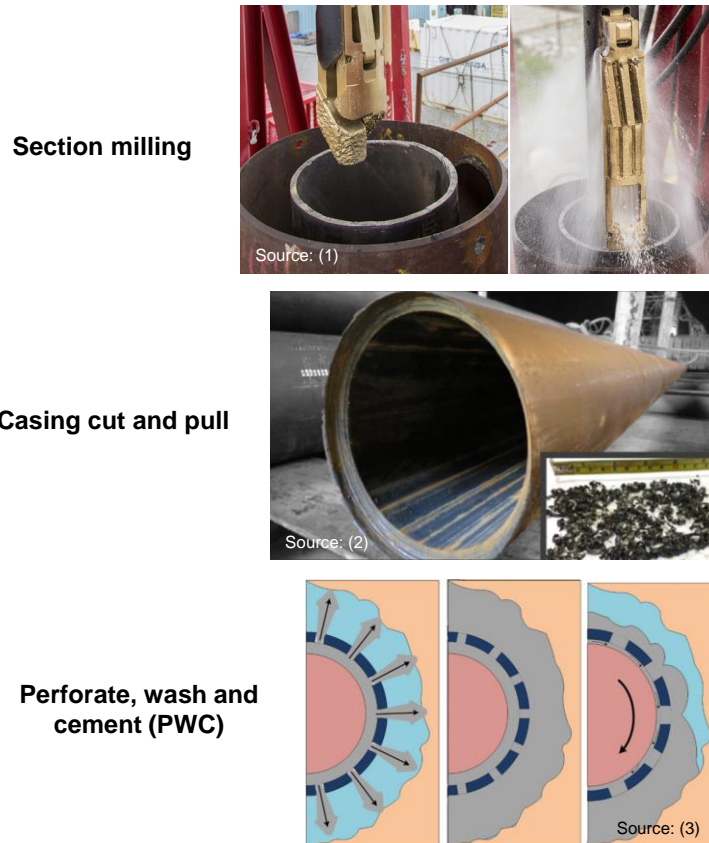
#### **3.1. Salt creep as an allied mechanism in the formation of geological barriers for well P&A**

##### **3.1.1. Overview on P&A**

Unproductive wells and those with irreparable damage have to be abandoned for economic and environmental reasons (Abshire et al., 2012; Khalifeh et al., 2013). Several fields in the North Sea and in the Gulf of Mexico, the largest mature oil fields in the world, are in the end of lifespan (Vrålstad et al., 2019) and the large number of wells to be abandoned in the next years is a concern for the O&G industry. P&A is a wide decommissioning process that, added to the structure removal, represents the major part in the decommissioning cost (Myrseth et al., 2017). This cost is high and also of no return to the operator. Therefore, the O&G industry, assisted by the academy, faces the challenge of finding the best ways to plug and abandon wells at an efficient cost, while ensuring safety and reliability.

P&A often consists of hydraulic isolation and protection of three key regions: reservoir zones (reservoir abandonment), freshwater zones such as aquifers

(intermediate abandonment) and future exploration zones, preventing them from leakage from/into the well. Ideally, surface equipment is removed. To this end, one has to remove wellhead, conductor and casings (if possible), and plug the wellhead with quality materials, usually cement (Abshire et al., 2012; Hallak, 2017).



- (1) <https://energynorthern.com/2019/08/05/abrado-wins-major-multi-well-pa-contract-from-chevron/>  
 (2) <https://decomnorthsea.com/news/32-time-savings-on-cut-pull-operation>  
 (3) Khalifeh and Saasen (2020).

Figure 15. Conventional methods for well P&A. Adaptation from figures presented in <https://energynorthern.com/2019/08/05/abrado-wins-major-multi-well-pa-contract-from-chevron/> (1), <https://decomnorthsea.com/news/32-time-savings-on-cut-pull-operation> (2) and Khalifeh and Saasen (2020) (3).

There are a number of methods for well P&A considering different abandonment concepts, regulations around the world, geological scenarios, types of wells, the need for optimizing processes and budget. The conventional methods for P&A are didactically divided here into three groups: “section milling”, “casing cut and pull” and “perforate, wash and cement” (PWC), Figure 15. The “section milling” has been the most adopted P&A method. It is indicated specially when casing cannot be cut and pulled (Hallak, 2017; Halvorsen, 2016), the cementation behind the casing is not sufficient quality to cast an barrier with the proper hydraulic isolation (Khalifeh et al., 2013; Wang et al., 2016) or when the section is not able to be perforated, washed and cemented (Nelson et al., 2018). This method consists

of milling the casing, cement and part of the well along an interval in such a way to create an openhole to be plugged. The “casing cut and pull” is a method that consists of cutting casing above an uncemented interval and pulling it out of the well. This method is ideally applicable in intervals where well annulus is not sufficiently cemented or is not cemented. The casing uncemented intervals are detected via cement logs and stretch tests (Hallak, 2017). The casing cutting operations follow by explosives, abrasive, mechanical or chemical cutters, or also by thermal methods (Myrseth et al., 2017). The action on retrieving the casing cut is quite complex due to the uncertainties related to integrity of the formation and annulus cementation. To circumvent these difficulties, casing can be segmented to be pulled out in parts (Khalifeh and Saasen, 2020). Finally, PWC is an alternative and recent method for the conventional cut and pull and section milling methods (Delabroy et al., 2017; Hallak, 2017). Generally speaking, it consists of perforating an uncemented casing interval, washing the annular space with a modified water-based mud (WBM) (Khalifeh and Saasen, 2020) and injecting cement behind the casing by the perforations and across the section, forming a plug. Although casing is perforated, it is neither removed nor milled. Thus, no significant amounts of debris and swarf are generated and there is no need to transport these fragments to the surface. The final plug comprises the perforations and the inner section of the casing (both cemented) besides the perforated casing.

### **3.1.2. P&A numbers and concepts**

Some of the largest hydrocarbon provinces over the world are in the North Sea (Norwegian Continental Shelf and United Kingdom sector), Gulf of Mexico (United States), British Columbia (Canada) and Brazil. These regions host an enormous number of wells and therefore are important scenarios to illustrate the discussions on the topic of well P&A.

According to Khalifeh et al. (2013), the first hydrocarbon well in onshore Norway dates from 1966. Until 2012, more than 3,800 wells have been constructed. Among them, 170 wells are permanently abandoned, 800 are temporarily abandoned and the others are producing. Abshire et al. (2012) present a structure quantitative of the Norwegian Continental Shelf in which there are more than 350 platforms and more than 3,700 wells to be abandoned. The United Kingdom (UK) sector of North Sea has more than 500 structures and nearly 3,000 wells to be permanently abandoned in the next years. Recently, Vrålstad et al.

(2019) have indicated that nearly 2,000 wells in the North Sea are planned to be plugged and abandoned in the next decade. In the same context, Myrseth et al. (2017) point out approximately 3,000 wells are to be permanently abandoned the in Norwegian Continental Shelf. Laterly, Strand and Corina (2019) have mentioned that more than 1,900 wells that are classified as P&A in this hydrocarbon province.

In parallel, the Gulf of Mexico is mentioned as the “largest and the most active decommissioning market in the world”<sup>25</sup> (Kaiser, 2017) and hosts nearly 12,000 unproductive wells, which are candidates for P&A (Abshire et al., 2012). Between 2004 and 2014, about 3,000 wells have been temporarily abandoned and 8,000 wells have been permanently abandoned (Kaiser, 2017).

In British Columbia (Canada), the earliest reported well for hydrocarbon production dates from 1919 (Trudel et al., 2019). Public data from Western Canada shows that 24,802 wells have been drilled and nearly 7,614 wells have been already abandoned until December 2016. Among these wells, 6,070 have records. More so, there are more than 200 structures are to be abandoned in offshore Netherlands, Denmark, Ireland, Spain and Germany (Abshire et al., 2012).

The cost of the P&A operations reflects the materials and methods needed to meet the requirements of the regulators and to cope with the geomechanical and flow context of the well site. As reference, P&A is responsible for 25% of the costs of drilling offshore exploration wells in Norway and North Sea (Khalifeh et al., 2013; Strand and Corina, 2019). According to Abshire et al. (2012), the general cost of well P&A in the UK sector is US\$ 1-2 million per well considering water depths lower than 100 meters and using a fixed platform, while it costs US\$ 5-6 million per well using a semisubmersible or dynamically positioned floating drilling unit. Adopting a support vessel-based abandonment has an intermediate cost. Still according to these authors, abandoning a Norwegian well is more expensive than a Middle East well due to the different requirements that have to be met.

Regarding P&A concepts, different procedures reflect the many geological scenarios, wells types and different regulations around the world. Trudel et al. (2019) have presented a comparison among the P&A goals in important hydrocarbon provinces. The UK Oil and Gas Industry Association Limited (OGUK) considers P&A as a “rock to rock” sealing – the concept of caprock restoration. Two well barrier elements (WBEs) are required for each permeable interval, and 30 meter-length plugs are required. The Norwegian oil and gas industry standards

---

<sup>25</sup> Excerpt from page 94 of the work of Kaiser (2017).

for operations (NORSOK) considers P&A in terms of permanent well abandonment by plugging it to prevent any chemical and geological complications in an eternal perspective. Two WBEs are also required for each permeable interval and 100 meter-length plugs are required in openhole intervals. More so, according to Hou et al. (2012), the standards for well abandonment in Germany require a 100 meter-length cement plug above perforations and water aquifers and a cement plug of same length ending in the well top. Kaiser (2017) has presented the view of the United States regulators in the context of the Gulf of Mexico. According to this author, the goal is to “to keep fluid isolated in the zones in which they naturally occur until the conditions that exist within the formation return to the well.”<sup>26</sup> The standards are managed by the Bureau of Ocean Energy Management (BOEM) and by the Bureaus of Safety and Environmental Enforcement (BSEE). Some wells are temporarily abandoned when the field reaches exploration maturity. In this case, it is required two independent WBEs or at least a plug isolating the perforated intervals. The wells to be permanently abandoned must isolate openhole intervals, perforated intervals, casing ends and the annular spaces, and place a surface plug. When the WBEs are tested and casings are removed, temporary abandonment turns into permanent abandonment. According to Trudel et al. (2019), the Alberta Energy Regulator (AER) in the Western Canada considers the hydraulic isolation of the non-saline groundwater and of the porous zones as the objective of well P&A. In that context, it is not common to mill or to cut and pull casing. The use of two WBEs by permeable interval is not mandatory. The regulations are similar to those of onshore North America standards. Nevertheless, they would not meet offshore UK and Norwegian P&A regulations in some design aspects.

Considering offshore applications such as those from North Sea, P&A has to be developed in an eternal perspective since re-entering a well in such conditions is highly challenging and costly. UK and Norwegian P&A regulations require to plug the well over its entire section, promoting the caprock restoration (Vrålstad et al., 2019). On the other hand, Canadian wells are typically onshore and therefore accessible if necessary. This is an advantageous scenario since even the best sealing materials may undergo damage in very long timescales such as those of permanent abandonment (Trudel et al., 2019).

When looking at the Brazilian scenario, P&A is a still growing topic in the industry and academia. The expertise in well P&A in Brazil is still being formed and

---

<sup>26</sup> Excerpt from page 94 of the work of Kaiser (2017).

there is a large room for technological advance this area. The large-scale oil production has begun in Brazil in the 1980's (Furtado et al., 2018) and some of the onshore and post-salt hydrocarbon fields are reaching maturity (Souza, 2019). Brazil has about 30,000 wells and 7,000 among them are offshore. From these numbers, 20% of the wells are producing, and only about 8% are permanently abandoned (França, 2020)<sup>27</sup>. There are more than 60 offshore installations and more than 165 wells to be decommissioned in the next years (Furtado et al., 2018; Soares, 2017). More so, there is a significant number of wells (by 49%) temporarily abandoned waiting to turn into permanent P&A (França, 2020). Each offshore well abandonment is estimated in above 24 million dollars plus labor, services and materials expenses (Furtado et al., 2018). Regarding P&A methods, the use of two permanent WBEs (cement plugs) is a frequent choice. PWC procedure is not commonly employed in Brazilian onshore wells (França, 2020). According to Matos (2021)<sup>28</sup>, through-tubing abandonment procedures are widely employed by the industry, and the use of PWC tools would be welcome to reduce the decommissioning time of the wells. P&A removing casing is exceptional.

The regulations for O&G activities in force in Brazil are provided by the National Agency for Petroleum, Natural Gas and Biofuels (ANP). More specifically, ANP's resolutions no. 25/2002 and the latest no. 46/2016 apply to well integrity and abandonment. Hallak (2017) observes that the number of WBEs required by the Brazilian resolution is similar that of NORSOK (D-010). This author highlights that the length of the WBEs is specified in the ANP's former resolution (no. 25/2002) but not in the latter (no. 46/2016) and therefore has taken NORSOK D-010 and OGUK (issue 5) recommendations as reference. A guide that links the Brazilian regulations under ANP's resolution no. 46/2016 to NORSOK and OGUK best practices is presented by the Brazilian Petroleum and Gas Institute (IBP, 2017). Among the materials allowed as WBE, NORSOK D-010 recommendations also mention shale (abundant in the North Sea O&G provinces) as long as it exhibits creep behavior to close the annulus space around an uncemented casing interval and meets the integrity and tightness conditions expected from a WBE. IBP's guide (IBP, 2017) also mentions this particular situation of using creeping formations such as some shales and salt rocks to seal the annulus between

---

<sup>27</sup> Information from the technical presentation at Webinar in Decommissioning and P&A Section – Brazil Norway held on December 09<sup>th</sup>, 2020.

<sup>28</sup> Information from the technical presentation at SPE Brazil Tech Tuesday held on March 30<sup>th</sup>, 2021.

formation and casing. In this case, each geological barrier casing a WBE has to be at least 30 meter-length and exhibit satisfactory integrity and tightness.

From this brief literature review, one realizes that the number of candidate wells for P&A in the main hydrocarbon provinces around the world is worrying, highlighting the current relevance of this theme. Despite some divergences among the references, there are a few thousands wells to be abandoned in the most important hydrocarbon provinces. When not considered in the well construction period, the abandonment can be even more challenging. The records of old wells, candidates for P&A, are generally limited, bad, or even unavailable. This lack of information requires investigation especially about the condition of the cementation before plugging. The long-term isolation is also a concern since one has to avoid as much as possible the need for reentering a leaking well for further repair (Wang et al., 2016). Having that in mind, a strategic well design accounts for the abandonment period in advance and recognizes the importance of the first cementation for a successful P&A (Khalifeh et al., 2013).

### **3.1.3.**

#### **A brief review on materials for P&A and introduction to geological barriers**

Quality sealing materials for plugs are of utmost importance for an effective and safe well abandonment. According to Finley et al. (1994), a sealing system is more than choosing a long-life and low permeability material. Permanent seals (or plugs) require a high-quality emplacement and chemical compatibility with the host formation. Excavated structures (such as a well drilled in the rock formation) exhibit mechanical and hydraulic changes in the surroundings. Without the proper remediation, permanent flow paths caused by the rock damage around the plug likely persist regardless the properties of the isolation material. This concept in relation to sealing calls attention to the importance of an adequate choice of isolation materials, although other aspects related to host formation may also influence the (success of the) abandonment process.

In the past, hydrocarbon wells were backfilled and abandoned using brush, wood, paper sacks, linen and other materials to form a basis for a cement plug (Strand and Corina, 2019). Fortunately, a stricter group of materials that qualifies as sealing material has nowadays been defined. As reference, the Norwegian oil and gas industry standards for operations (NORSOK) establishes that plugging materials have to be of very low permeability (or be impermeable), non-shrinking,

ductile, chemical resistant and maintain long-term integrity, besides presenting adequate surface-to-surface bonding (Khalifeh and Saasen, 2020). The main materials currently available for this purpose are Portland cement, materials derived from cement, and rock, grouts, thermally-activated materials, gels and metals (Khalifeh et al., 2013). Cement plugs are often the standard choice in P&A. Moreover, geomaterials such as a creeping rock formation (mainly shales and salt rocks) may qualify as WBEs. More specifically, one idealizes a geological barrier spontaneously formed by a creeping formation. In the case of wells crossing salt layers, the openhole could be backfilled using granular salt. The backfilling is followed by the consolidation of the granular package by the creep of the host formation, forming a virtually homogeneous well barrier.

Using creeping formations to form a geological barrier either embracing the casing along uncemented intervals or closing completely an openhole is a recent trend in P&A. According to Orlic et al. (2019),

“using the same caprock material for well (...) (P&A) is therefore an attractive option as the initial sealing capacity of caprocks penetrated by wells could be restored by well plugs made of the native caprock lithology.”<sup>29</sup>

The topic is relatively latter-day and most of the literature on using formations as geological barriers for P&A is oriented to shales. Anyway, the shale-oriented literature provides useful insights for the potential use of salt in the same context.

Firstly, it is important to identify the similar and the distinct characteristics of salt and shale. Consolidation is normally neglected when dealing with natural salt rocks that present essentially null pore pressure. This may be relevant in shales. Aspects related to creep behavior, more specifically with stimulation by reducing pressure and/or heating the rock, are similar for them. As seen before, salt creep behavior depends on the deviatoric stresses and is thermally-activated (see Section 2.1.1). Besides that, the fact that there are stress levels that trigger dilation followed by damage and permeability enhancement (see Section 2.1.2) and the attenuation by self-healing are another similar aspect between salt and shale. In a solid mechanics view, standard salt rocks exhibit ductile behavior and develop higher strain rates, suggesting the ability to close by creep an openhole forming a geologic barrier. In a fluid mechanics view, salt is seen as a highly viscous fluid which is expected to creep and to encompass the casing by closing an uncemented annulus space (Vrålstad et al., 2019). The salt capability to close by creep towards

---

<sup>29</sup> Excerpt from page 1 of the work of Orlic et al. (2019).

casing along uncemented intervals has also been addressed in the literature (Firme et al., 2016a, 2016b; Fossum and Fredrich, 2007; Willson et al., 2003), Figure 16.

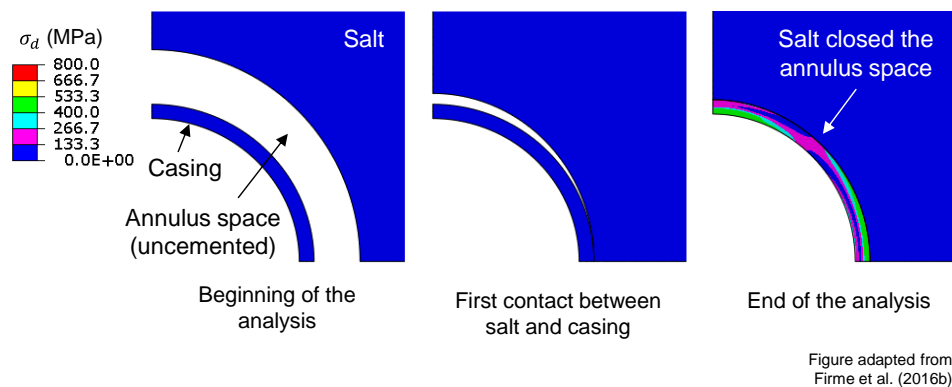


Figure 16. Well closure towards casing in an uncemented interval. Adapted from Firme et al. (2016b), based on a former simulation carried out by Fossum and Fredrich (2007).

On the other hand, not all shales are capable of forming geological barriers. Those who qualifies as so are normally consolidated and exhibit high clay content and lower uniaxial compressive strength. As a consequence, this shale group exhibits ductile failure and develop large plastic deformation (Holt et al., 2020), and are potentially capable of closing an openhole or a drift. Lastly, a disadvantage of salt over shale is the high solubility of salt in contact with water or water-based fluids, introducing some challenges for the P&A operations. Table 13 summarizes the salt and shale characteristics of interest for geological barriers. In the following sections, the characteristics of each rock material are discussed in more detail.

Table 13. Comparative summary of the salt and shale characteristics of interest for geological barriers.

Characteristic / property	Salt rock	Shale
Consolidation	No*	Yes
Thermally-activated creep	Yes**	Yes**
Damage / self-healing	Yes	Yes
Ductile behavior	Yes	Yes***
Solubility in water	Yes	No
Low permeability	Yes	Yes

\*If intact or little disturbed; \*\*Salt often exhibits higher creep rates; \*\*\* If normally consolidated.

### 3.1.3.1. Shales as geological barrier

Using shales as geological barriers is an alternative which has been studied due to the great demand for P&A in the North Sea wells, where shale formations

are abundant. A brief summary of the state of the art follows. Fjær et al. (2016) have presented an assessment on using creeping shales as well barriers. According to them, a geological barrier candidate shale has to exhibit a low creep/plastic deformation threshold. Shales with low quartz content are prone to present a low threshold and a high capacity to absorb meaningful deformation without undergoing failure (breakout). Moreover, a significant reduction in the annulus pressure needs to be induced to stimulate creep along the interval to be plugged. As a consequence, this triggers deviatoric stresses and reduces the mean effective stresses. The stress changes around the well, if significant, may provoke dilation and this is undesirable for rock integrity, resulting in a damaged and permeable barrier unable for P&A. On the other hand, if the geological barrier forms adequately, significant financial savings related to well P&A are made. The authors, however, have pointed out that there are some open issues regarding the shale barrier development. Stavland (2017) has analyzed the thermal stimulation of shales to induce the formation of the geological barrier. This author has carried out numerical simulations adopting the Mohr-Coulomb criterion with tensile cutoff as the mechanical model for shale. Heating the shale triggers a pore pressure increase due to the expansion of the pore fluids. Consequently, the effective stresses decrease and the rock may undergo failure and plastic deformation closing the annular space. If the rock has undergone failure, the barrier may not be tight enough. Next, Kristiansen et al. (2018) have observed wells in which the uncemented annulus space in shale intervals has been found spontaneously closed by creep. These authors have made some considerations about the time-dependent behavior of shales, especially consolidation and creep. The deformation related to consolidation results from the dissipation of the pore pressure excess when there is a stress change. It depends on shale permeability and often produces a low deformation level. Creep, in turn, depends significantly on the deviatoric stress and is thermally-activated. Thus, as the well is heated during the production period, creep rates increase; and the opposite occurs if the well is cooling during injection periods. The steady-state creep and especially the tertiary (accelerative) creep may lead shale to failure. More so, even if the strain rate increases and the shale embraces the casing, fractures may develop in the deformed rock, affecting tightness. According to Vrålstad et al. (2019), the shale behaves as solid with finite shear strength. Under a moderate stress level, it keeps a stable arch around the well. If this arch is broken, the formation undergoes fracturing instead of deforming uniformly, enhancing permeability. Although the porosity and permeability of the deformed shale are higher than those of

undisturbed shale, it is still a valuable alternative to cement. These authors believe that a self-sealing behavior (analogous to self-healing in salt) improves the sealing capacity of the shale over time. Holt et al. (2020) have studied the mechanical behavior of shale with regards to geological barriers. They have distinguished two groups of shales. The first group is the “sloughing shales”, which consists of overconsolidated or slightly cemented shales. These rocks exhibit brittle failure such as breakouts, releasing rock fragments inside the well. The second group is the “gumbo shales”, which is composed by normally consolidated shales with high clay content and lower uniaxial compressive strength. They exhibit ductile failure and develop large plastic deformation, promoting well closure. This last group is a preferable candidate for natural barriers using shale. Lastly, Xie et al. (2020) have analyzed the shale creep stimulated by heating using laboratory experiments and numerical simulations. In short, they have observed that heating the shale led to a pore pressure increase due to fluid expansion and it induced plastic deformation and failure. On the other hand, shale was able to embrace the casing casting a geological barrier due to the plastic deformation. According to the simulations, considering a well with 12.25 inches in diameter, temperature of 46°C and vertical stress of 28.3 MPa, the wall should be heated by 220°C during 100 hours for the shale embraces casing. However, there are still doubts about the sealing capacity of the barrier since tensile and shear failure are expected in this scenario. Furthermore, the interested reader is referred to other recent works in the area for additional information (Halvorsen, 2016; Skjerve, 2013; Vignes, 2011).

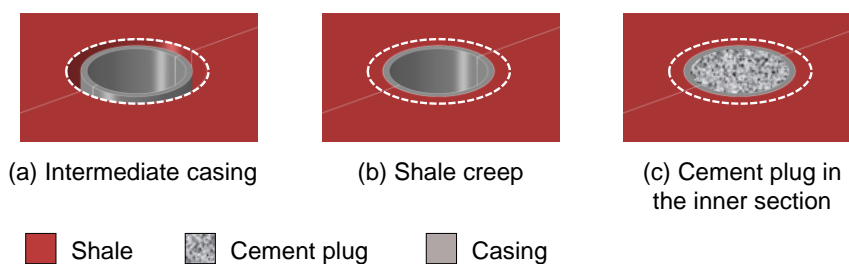


Figure 17. Schematic illustration of the shale as geological barrier in the context of numerical modelling.

A schematic illustration of the formation of shale barriers is presented in Figure 17. The complete cross section may not be closed by creep, although this mechanism can be effective to embrace the casing forming a tight annulus barrier. If the annulus is closed by creep and the barrier adequately isolates the interval, only the casing inner section needs to be plugged with cement (Xie et al., 2020).

### **3.1.3.2. Salt as geological barrier**

Using salt rocks as geological barriers is a natural alternative for the permanent abandonment of wells crossing salt layers. Salt properties such as creep deformation and essentially null permeability have been recognized for a long time as useful for casting competent hydrocarbon traps and strategic storage environments. Among the strategic storage purposes, the toxic waste disposal is one of the most important. The storage of these elements in subsurface salt caverns is a safe way to avoid their release into the environment. According to Finley et al. (1994), environments dedicated to toxic waste disposal have to meet severe regulatory standards. In this context, the long-term sealing performance of the cement is worrying considering the degradation of the properties with time.

The possibility of salt rock formations becoming toxic or nuclear waste disposal media has boosted hydraulic studies in salt rocks (Gloyna and Reynolds, 1961). Hansen (2011) has listed a number of advantages of using salt as disposal environment for heat generating high-level waste (HLW) and waste disposal in general. Five projects for disposal of dangerous waste were proposed in Texas (USA) in the early 1980's (Brassow and Thoms, 2000). Among them, the Waste Isolation Pilot Plant (WIPP) in New Mexico (USA) is probably the best known. This is going to be dealt in more detail in Section 3.2.2. Promoting salt rock environments for the toxic waste disposal has demonstrated the strategic capacity of this material to encapsulate waste by creep and form competent hydraulic barriers in the short- and the long-term. Linking this to well abandonment, Orlic and Buijze (2014) have pointed out that the research on nuclear waste disposal in salt rock environments has been the basis for conceiving P&A by means of salt creep to close and seal a well. This highlights the relevance of the intention to adopt salt rocks as geological barriers in the context of well P&A.

As previously mentioned, the salt capability to creep towards casing along uncemented intervals has also been recognized (see Figure 16). In a solid mechanics view, standard salt rocks exhibit ductile behavior and often develop higher strain rates. In parallel, in a fluid mechanics view, salt behaves as highly viscous fluid that ideally flows towards the openhole in a sink flow or Rankine flow scenario (Weijermars et al., 2014b). While integrity problems can occur especially in casings non-uniformly embraced by salt, the high creep rates developed by salt indicate that the annulus space and even the entire section can be naturally sealed.

Meanwhile, regarding P&A methods, UK and Norway regulations require plugging the well over its entire cross section, promoting a caprock restoration (“rock to rock” sealing) (Vrålstad et al., 2019). To this end, the background on salt rocks indicates that these formations can ideally cast a geological barrier that restores the pre-existent condition of the caprock before the existence of the well. In addition, there is the guarantee of short- and long-term chemical compatibility between the host rock and the sealing material since they are of same nature.

Although still incipient, some applications have been carried out in the context of salt as geological barriers and contribute with insights and findings. A brief summary of the state of the art follows. Hou et al. (2012) have presented a case of a well abandonment in a depleted gas reservoir in Altmark area (Germany). To this end, conventional methods and a salt creep have been considered. In that context, the depleted reservoirs have been reused as CO<sub>2</sub> storage media. These authors have pointed out that the injected CO<sub>2</sub> in contact with the reservoir fluids generates carbonic acid that, in turn, affects the integrity of the cement plug under certain conditions. In parallel, the salt formation has exhibited strength and impermeability under HPHT conditions, evidenced by entrapped CO<sub>2</sub> and hydrocarbons inclusions in the rock. The well abandonment procedure has involved section milling using a heavy water-based mud (WBM) as fluid. Posteriorly, the fluid has been replaced with a lighter mud (salt brine and nitrogen) to let the openhole wall release stresses and creep. The well closure around the milled section has been successfully verified, which conveys an idea of the effectiveness of the method. In parallel, the strength, creep behavior, porosity and permeability of the salt barrier are to be evaluated in laboratory. More so, a recent study of well sealing (abandonment) by salt rock has been developed in the Netherlands (Wollenweber et al., 2018), but it is yet to be implemented in the field.

Numerical simulations have also been performed in this context. Furthermore, Orlic and Buijze (2014) have carried out simulations of well closure by salt creep with special regards to well abandonment. These authors have mentioned as criteria for evaluating the geological barrier: i) the time it takes for the salt to close the well; and ii) the maintenance of the barrier tightness (i.e., the evolution of the porosity and permeability). Conceptual 2D plane strain models have been considered and their results may be applicable to real-field cases such as the well P&A of a gas field in offshore the Netherlands. For the sake of reference, their application has considered a milled openhole of 9.45 inches in diameter and typical halite properties. Among the scenarios studied, the shortest

time for well closure was 500 days for a well sited at a depth of 3,500 meters. Subsequently, Orlic et al. (2019) have continued the studies on salt as geological barriers. They have presented conceptual axisymmetric and 2D plane strain models to analyze the openhole closure by creep. Similar to the previous work, their application has considered a milled openhole of 11 inches in diameter and typical halite properties. An internal pressure of 1 MPa inside the well has triggered a strong stress deviation in relation to the in-situ stresses, enhancing salt creep behavior. An internal monitoring pipe of 3 inches in diameter has been inserted inside the openhole; therefore, an effective closure of 8 inches is needed to close the well. The authors have noticed closure times from 2 to 4.5 weeks for a 3,100 meter-depth well, from 2.5 to 6 months for a 2,500 meter-depth well and from 1 to 3 years for a 2,000 meter-depth well. In the axisymmetric models, the openhole interval was of 1 meter and 10 meters – the longest interval avoids overconstraining the creep behavior. Creep stimulation techniques such as reducing internal pressure and/or increasing temperature have been mentioned.

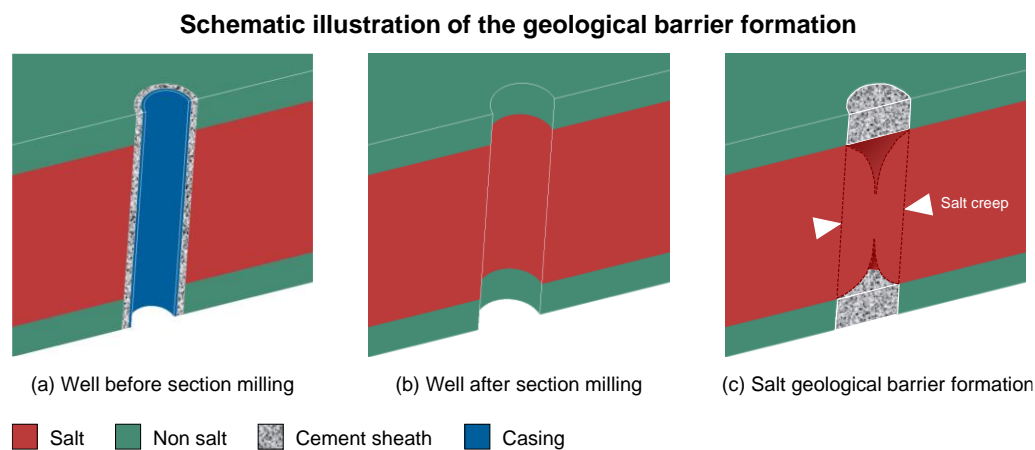


Figure 18. Schematic illustration of formation of a geological barrier by salt creep.

The formation of geological barrier by salt creep ideally follows the schematic illustration<sup>30</sup> shown in Figure 18. A well interval is considered before P&A, Figure 18 (a). When the lifespan of the well is reached, the intervals to be isolated are milled (or casing is cut and pulled) leaving an openhole, Figure 18 (b). The openhole is cleaned and salt is free to creep and gradually closes the well section, Figure 18 (c). There are stimulation procedures to enhance the creep rate such as

<sup>30</sup> The figures that schematically illustrate the P&A methods presented throughout this thesis intend to illustrate the changes in the numerical models that represent the steps of each method. Since the thesis is oriented to numerical modeling and simulation, technical details related to equipment and processes have been disregarded in these representations. Although the figures represent a section milling, they apply for casing cut and pull with minor modifications.

reducing the internal pressure of the well and/or heating the well. When the entire well section is closed by the salt, the barrier borders are expected to reconsolidate by self-healing and form a tight barrier. The background of the area of backfilling with granular salt for further consolidation forming a solid barrier seems to support this expectation (see Section 3.1.3.3).

Conversely, the casing may not be removed, just like the P&A using shale as barrier. In this case, salt creep is expected to close completely the annulus space forming a tight barrier, and the inner section of the casing needs to be plugged (see Figure 17). Having this scenario, the interface between salt and casing needs to be monitored in terms of tightness in order to not behave as a flow channel.

### **3.1.3.3. Granular salt as backfilling (plug) material**

One of the essential questions regarding the use of salt as a geological barrier is the time that creep takes to close the well. Proof of concept analyses support that salt creep is able to close the openhole; however, the time required to this end is still much longer than that of conventional methods take to plug a well (see Chapter 5). Stimulation methods for creep such as reducing the internal pressure and heating the well accelerate the closure time; however, time may still be long considering reasonable values for pressure reduction and well heating. According to Orlic and Buijze (2014), as the well radius decrease as consequence of salt creep, the creep rate decreases exponentially. This is expected since deviatoric stresses decrease as strain energy is dissipated by creep.

In the case of salt rocks, the formation of the geological barrier could be enhanced and accelerated by backfilling the openhole with granular salt. The granular package is subsequently encapsulated and consolidated by the host salt formation. As the grain boundaries merge due to the self-healing behavior, a tight seal (plug) is formed. The consolidation of granular (crushed) mined salt forming a solid and tight barrier has been studied over the last decades in the context of nuclear waste repository isolation (Bauer et al., 2015; Finley et al., 1994; Mills et al., 2018; Stormont et al., 2017). Additionally, Hou et al. (2012) have pointed out that DRZs (well surroundings for instance) can be sealed using granular (crushed) salt and presented simulations in the context. That said, granular salt is likely an ideal sealing material in wells drilled in salt if the barrier is not expected to form in a feasible time in terms of engineering.

According to the works cited in the previous paragraph, there are experimental evidences that granular/crushed salt consolidates under certain conditions, with porosity and permeability reduction over time, reaching similar values to those of the host rock. To this end, conditions for high quality density and for the self-healing capacity over time have to be ensured. In this scenario, the granular rock consolidation is driven by the creep behavior of the host formation. Cement bridge plugs are adopted to provide confinement for the granular salt. Small amounts of water accelerate consolidation and permeability reduction in comparison to a dry granular salt package. Regarding hydraulic properties, the immediate permeability of granular salt depends on the emplacement density. It usually varies from  $1.0E-16$  to  $1.0E-18$  m<sup>2</sup> considering a careful emplacement, and tends to approximate to that of the host formation (lower than  $1.0E-21$  m<sup>2</sup>) with time (Finley et al., 1994). A high compatibility level between the materials of plug and host formation is expected when using a granular salt backfilling into a well drilled in salt since they are materials of same nature. It represents a significant advantage over cement plugs since the permanent chemical compatibility between cement (and other sealing materials) and salt is not easily demonstrated. More so, using a chemically/mechanically incompatible seal material may be troublesome in terms of the barrier integrity and then tightness.

Recent experimental studies have been developed in this area. Bauer et al. (2015) have carried out an experimental assessment of gas permeability of consolidating granular (crushed) salt. The experiment reported in this work aimed at measuring the deformation and the permeability evolution of a consolidating granular salt sample. It was carried out at a temperature of 250°C, confinement stress of 20 MPa and took just under 500 hours. The material tested was granular salt mined from WIPP salt, whose formation is generally bedded and presents about 5% of impurities. The initial porosity of the sample was about 0.40. An inert gas was adopted as the permeating fluid to estimate permeability of the sample during consolidation. The authors have noticed that the apparent permeability strongly decreases to values lower than  $1.0E-21$  when porosities lower than 0.01 and fractional densities<sup>31</sup> higher than 0.995 are reached (see Figures 10 and 11 of their work). The consolidation of granular salt likely happened following similar mechanisms to those that drive self-healing. Thereby, the very low permeability of salt is recovered. Next, Stormont et al. (2017) have carried out gas permeability

---

<sup>31</sup> In this case, the fractional density is the ratio between the densities of the consolidating salt package and the standard WIPP salt in an intact condition.

experiments in granular salt. The material tested was mined from WIPP salt (bedded formation) and Avery Island salt (domal formation). The tests were performed at temperatures ranging from 90°C to 250°C, confinement stresses from 20 MPa to 40 MPa and samples exhibited initial porosities by 0.40. The experiments have presented important findings. Firstly, the permeability of the consolidating salt is directly affected by the evolution of the porosity so that it decreases as porosity decreases due to consolidation. Secondly, apart from a combined effect with porosity, other variables such as stress, the temperature and time seem not to affect the permeability. Thirdly, the relation between permeability and porosity presents three regions (see Figures 2 and 3 of their work). In the first region, the sample has a large interconnected pore network since it is actually a grain package. The test loading compacts the sample and the pore dimensions reduce. The reduction in permeability is not very significant. This region is represented in a power law porosity-permeability relation (such as equation (28)) using a power (such as variable  $\chi$ ) about 3. In the second region, the ongoing consolidation process reduce the pore network connectivity. As a critical value for porosity is reached and exceeded, the permeability reduction is more significant. These authors have indicated values of 0.02-0.05 for this critical porosity. This region is represented in a power law porosity-permeability relation using a power higher than 10. Lastly, in the third region, the consolidation of the sample closes the interconnection of the pores almost entirely. From this moment on, the permeability becomes too low and cannot be measured. The authors have suggested this so-called threshold for the virtual impermeability happen for porosities lower than 0.01. In conclusion, while the expectation on the capacity of a consolidating granular salt sample to turn into an essentially impermeable sample is satisfied, a sufficiently low porosity value has to be reached for an impermeability condition (in terms of engineering) be verified. More so, according to Mills et al. (2018), the consolidation of granular salt depends fundamentally on the stress state, moisture availability, temperature, time and grain impurities. These authors have investigated the micromechanical processes in granular salt by means of experimental tests using material from WIPP and Avery Island salt. They have pointed out that granular salt consolidation follows brittle processes, grain rearrangement and cataclastic flow. As the void spaces are virtually eliminated, grain boundary processes and crystal-plastic mechanisms control additional porosity reduction. Without the adequate moisture, higher stresses are needed to consolidate granular salt as long as the void spaces reduce. Granular salt was consolidated in laboratory hydrostatic creep tests at a temperature of

250°C and a confinement (hydrostatic) stress of 38 MPa. The authors have pointed out that a better understanding on the consolidated salt micromechanics and how it affects the constitutive models and the long-term porosity is still needed to the application of granular salt as sealing material.

The formation of geological barrier by salt creep and backfilling with granular salt ideally follows the schematic illustration<sup>32</sup> shown in Figure 19. A well interval with a cemented casing is considered before P&A, Figure 19 (a). When the lifespan of the well is reached, the intervals to be isolated are milled (or casing is cut and pulled) leaving an openhole, Figure 19 (b). After the openhole is cleaned and backfilled with granular salt, the host formation (also salt) is free to creep and it drives the consolidation of the granular salt, Figure 19 (c). With time, the grain boundaries merge by self-healing and a solid is progressively formed.

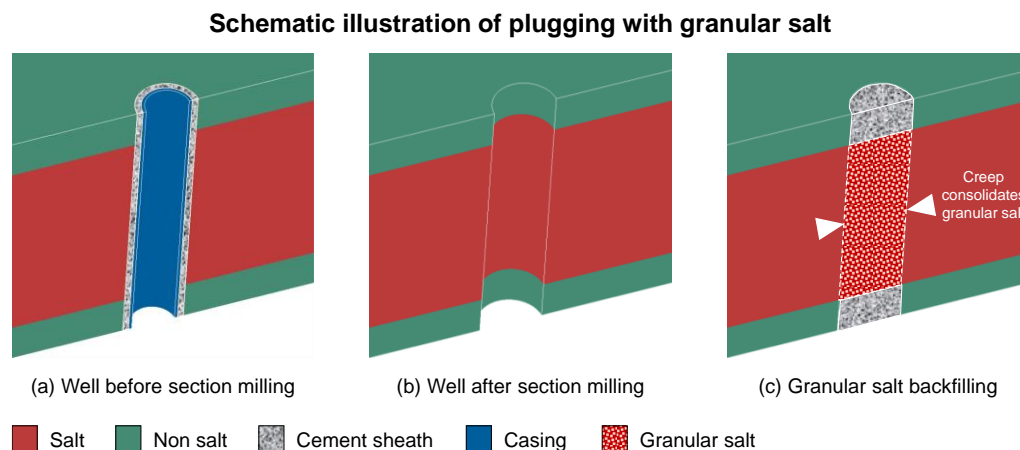


Figure 19. Schematic illustration of formation of a geological barrier by granular salt backfilling.

## 3.2. Salt caverns for strategic underground storage

### 3.2.1. Overview on salt caverns<sup>33</sup>

Salt rocks stand out in the mining and energy industries by playing an important role as potential ore sources and barriers for fluids and gases. Distinguished characteristics such as creep deformation and essentially null permeability make these rocks useful as underground storage media.

<sup>32</sup> See note 30.

<sup>33</sup> Sections 3.2.1, 3.2.2 and 3.2.3 were updated and expanded for presentation from the article "Salt caverns history and geomechanics towards future natural gas strategic storage in Brazil" written by the author and advisors of the thesis (Firme et al., 2019) and published in Journal of Natural Gas Science and Engineering.

The underground storage in salt caverns is a strategic initiative that dates from the 1940's, almost always related to energy purposes. In the past, abandoned brine production wells were used as storage facilities. Therefore, there is a certain link between salt caverns and solution mining since the latter is the typical construction process of the former. Comprehensive knowledge on solution mining has been consolidated especially since the 1960's. Reference papers approaching solution mining based on fluid mechanics formulations date from this decade (Durie and Jessen, 1964a, 1964b; Kazemi and Jessen, 1964; Sears and Jessen, 1966). These works have been responsible for the "beginning of a quick development of modelling software used for salt cavern leaching"<sup>34</sup> (Kunstman and Urbanczyk, 2000). On the other hand, open literature generally does not provide abundant information about solution mining on a more scientific basis. Nevertheless, a considerable number of papers approaching the main aspects related to hydrocarbon storage in salt caverns have been published. Using salt caverns as toxic or nuclear waste disposal media, for energy purposes and for CCS have proven to be additional fields of interest.

The geomechanics research applied to salt caverns focuses on assessing the integrity of caverns and wells concerning the solution mining process, i.e., the construction period, the internal pressure cycles or schemes during the operation period and the abandonment period. A literature review of the overall history of salt caverns, a state of the art and other aspects of interest for salt geomechanics are presented in the following sections. It is followed by the fundamentals of the mechanical behavior of salt applicable to underground caverns during construction, operation and abandonment.

### **3.2.2.**

#### **A brief historic review of salt caverns opened by solution mining<sup>35</sup>**

The histories of salt caverns and of the solution mining technique link to each other – very often, hydrocarbon storage is a later use of abandoned brine production wells or caverns. According to Kostick (2006), the first records of using solution mining are from China, around 250 BC. Bamboo tubes were adopted at that time as the circulation pipes adopted today. Still according to this author, the current technology on solution mining originates from France, by 858. Possibly the

---

<sup>34</sup> Excerpt from page 279 of the work of Kunstman and Urbanczyk (2000).

<sup>35</sup> See note 33.

first record of the solution mining method at production scale is associated to the Spanish in 1752 (Jeremic, 1994).

The storage of fluids and gases in underground salt caverns was first conceived in Canada during the 1940's, in the context of World War II (Bays, 1962). In the early 1950's, the storage of liquefied petroleum gas (LPG) and light hydrocarbons (LHC) spread out over the United States (USA) and Europe. The use of salt caverns to store natural gas began in the 1960's. These caverns have been opened and explored for more than 50 years in Germany (Lux and Düsterloh, 2015). Currently, salt caverns are the most growing alternative for gas storage (Barajas and Civan, 2014). Thoms and Gehle (2000) list some of the former gas storage caverns. Those caverns were constructed in Kansas (USA, by the 1960's), Michigan (USA, 1961), Saskatchewan (Canada, 1963), Mississippi (USA, 1970), Tersanne (France, 1970) and Kiel (Germany, 1971). Additionally, the Jintan salt cavern (China, 2002-2010) is mentioned as the first one for gas storage in China (Wang et al., 2018). A well-known application in this context is the Strategic Petroleum Reserve (SPR), sited in the American states of Texas and Louisiana. In the mid 1970's, the American government decided to create a reserve of crude oil in existing salt caverns. Subsequently, new caverns were opened. Currently, these caverns make up an authorized storage capacity of 714 thousand barrels<sup>36</sup> (U. S. Department of Energy, 2022). The United States Department of Energy (DoE) supports that such geological hydrocarbon repositories have proven to be reliable and economically viable worldwide. The salt caverns "offer the best security and are the most affordable means of storage, costing up to 10 times less than aboveground tanks and 20 times less than hard rock mines."<sup>37</sup> The existence of these strategic reserves has proven to be very important in mitigating the reduction in oil supply due to the Russo-Ukrainian war (since February 2022) (U.S. Energy Information Administration, 2022).

A next step is to consider salt caverns constructed offshore. The Gateway project (by 2007/2008) is possibly the precursor project in this way, which envisages the creation of 20 offshore salt caverns for strategic gas storage in the Irish Sea (Evans et al., 2008; Gateway, 2007). This region has also been

<sup>36</sup> Public data from January 31th, 2022 (<https://www.energy.gov/fe/services/petroleum-reserves/strategic-petroleum-reserve/spr-storage-sites>).

<sup>37</sup> Excerpt from the U.S. Department of Energy (2022) (<https://www.eia.gov/todayinenergy/detail.php?id=51538>).

considered for compressed air energy storage (CAES) and currently for hydrogen processing and storage (Evans et al., 2021; Lee, 2021).

In addition, there has long been the intention of using salt caverns for toxic or nuclear waste disposal. This initiative takes advantage of the salt tightness to isolate such materials and avoid their release in the atmosphere. As introduced before (see Section 3.1.3.2), there are many advantages to using salt formations as host medium for heat generating high-level waste (HLW) and waste disposal in general (Hansen, 2011). According to this author, salt formations are: i) geologically stable by millenniums; ii) easy mining and essentially tight (impermeable); iii) exhibit high thermal conductivity and self-healing behavior; and iv) show wide geographic distribution. In the early 1980's, five distinct projects for disposal of dangerous waste were proposed in Texas (USA) (Brassow and Thoms, 2000). One of the well-known engineering works in this kind of application is the Waste Isolation Pilot Plant (WIPP). This is the first licensed geological repository for nuclear wastes in the world. The development of this repository has mobilized a significant program in characterization and modelling in salt rock mechanics. The WIPP caverns were opened by standard room-and-pillar underground mining.

With the intensification of environmental awareness, there is need for alternatives to overcome the greenhouse effect. Decarbonization and CCS are now on the agenda of new developments. Salt caverns can be used as permanent storage for greenhouse gases such as carbonic gas and methane ( $\text{CO}_2$  and  $\text{CH}_4$  respectively). Dusseault et al. (2004, 2001a) point out the options for this kind of storage or geologic sequestration, emphasizing the storage in salt caverns and showing that this is feasible in the Canadian context.

In Brazil, possibly the main enterprise involving salt caverns is the Taquari-Vassouras potash mining, sited in the state of Sergipe. This is the unique national source of potash for fertilizers. The salt-related geological peculiarities of the region such as the existence of high-mobility salt such as tachyhydrite and carnallite besides halite, sylvinitite and non-salt layers have created a number of geomechanics challenges for the ore exploration. A large background on the Brazilian salt geomechanics have been inherited from there (Costa, 1984). The mine has started operation in 1985 (Farias et al., 2021) and adopts the standard room-and-pillar underground mining process. There are plans (to be implemented in the future) to increase the domestic production of potash by solution mining carnallite layers in the state of Sergipe (Carnallite Project) and by room-and-pillar

potash mining in the state of Amazonas (Autazes Project) (Farias et al., 2021). Hydrocarbon strategic storage is still under study; however, the main challenge to open and maintain offshore caverns has been the high cost involved in mobilizing equipment to deep waters. Solution mining has been employed in brine extraction in Alagoas (city of Maceió) and Recôncavo (Matarandiba Island) basins<sup>38</sup>. In both cases, the production started in the 1970's and the cavity shapes have been controlled by sonar (Florêncio, 2009; Melo et al., 2008). The future conversion of onshore mined cavities into hydrocarbon storage caverns could serve as prototype for new caverns for this purpose. The major use of natural gas is quite recent since this source has progressively been taking part of the national energy mix only after a crisis in this sector in the late 1990's. The extension of the expertise acquired over the potash and the Pre-salt hydrocarbon exploration to support offshore cavern applications in Brazil is a strategic step further in the state of the art of salt caverns worldwide. The works of Costa et al. (2015, 2012) have presented fundamentals and synthetic applications of that in Brazilian salt formations. This type of project has almost no precedent, with the exception of the Gateway project. In the context the ever-increasing decarbonization trend, Costa et al. (2019a, 2019c, 2020) and Goulart et al. (2020) have proposed a "hybrid subsea CCS system", through which the CO<sub>2</sub> separation (from the fluid and the gas produced) would occur offshore in such a way that the residual CO<sub>2</sub> steam is directly injected in offshore salt caverns at the field vicinity instead of being handled on the surface and injected in a supercritical state in the reservoir. An experimental salt cavern to be opened by solution mining using seawater has been proposed by these authors.

### **3.2.3. Geomechanical aspects and cases of interest<sup>39</sup>**

Bays (1962) summarizes the essential conditions for a salt formation to qualify as host for a storage cavern. The formation must be sufficiently thick in order to prevent crushing due to stress transfer caused by cavern development. In parallel, the formation must be pure to avoid subsurface movements due to significant intercalations with impurities. The formation also has to be impermeable and insoluble to the stored material. The cavern must develop at a depth to allow efficient well construction, i.e., good cementing job and sufficient geostatic loads to confine the stored material. Additionally, the cavern roof or the caprock must present support capacity considering the fluctuation of the storage material

---

<sup>38</sup> The continuity of brine production in 2022 in these regions needs to be confirmed.

<sup>39</sup> See note 33.

(consequently, variation in the internal pressure). Finally, efficient surface infrastructure for cavern construction and operation must be available. More so, recent geological incidents/accidents involving salt caverns in operation or abandoned have shown that the structural geology context of the region is extremely relevant – caverns constructed close to fault regions or dome edges are disadvantaged in terms of safety.

Since the main purpose of the industry in the past was to obtain ore-saturated brine for later beneficiation, there was less concern with the environment – solution mining was adopted with a minor effective constructive control (Jeremic, 1994). Consequently, caverns poorly located and with highly irregular shapes were generated. They have often presented integrity problems with catastrophic consequences such as excessive subsidence, sinkholes, damage and failure in regions and structures, among others (Johnson, 2005; Zechner et al., 2011).

A relatively recent case of the damage caused by poorly located caverns is the Bayou Corne sinkhole, in Louisiana (USA, 2012). The Bayou Corne salt cavern was abandoned and roof-overlying layers have undergone successive failures until a large sinkhole was formed. Besides that, the rock failure also caused in situ gas release into the surface. It is believed that the major factor for this environmental disaster was the location of the cavern, which was less than 100 meters away from the salt dome edge. This geological boundary often has dominance of altered materials that may have slipped into the cavern, provoking progressive failure along the edge. This event has triggered a major concern on the long-term integrity of abandoned caverns (Bérest, 2013; Sobolik and Lord, 2014).

Brazil has very recent damage cases most likely associated with past solution mining in addition to geological peculiarities. As previously mentioned, Alagoas (city of Maceió) and Recôncavo (Matarandiba Island) salt basins have been brine exploration regions since the 1970's. In Maceió, 35 brine wells located in the Mundaú Lagoon coast of the city have become large salt caverns. Over time, and possibly combined with specificities of the structural geology of the region, a significant subsidence has been verified and has begun to damage the constructions of the neighborhoods in the region (Pinheiro, Mutange and Bebedouro). Vassileva et al. (2021) have carried out an assessment on this geological incident. Their work shows that the subsidence has been monitored from 2004 to 2020, and the maximum subsidence in this period was of about two meters. Subsidence rates have varied from 4 cm/year to 27 cm/year, but have

reduced to 20 cm/year in the beginning of 2020. In the period of the high subsidence rate (by 27 cm/year), 2018, the damage caused in the constructions and roads have become notorious. The city was hit by heavy rains and posteriorly an earthquake of magnitude of 2.4 mR happened – the three events (infrastructure damage, heavy rain and earthquake) happened within three months. Some inhabitants of the region had to be relocated. Those authors have suggested that the extensive subsidence can be primarily associated to the solution-mined caverns. Shallow seismicity has also been observed by 2019. More so, Euillades et al. (2020) have also analyzed this case by means of SAR interferometry and suggested that the meaningful subsidence observed in the surface occurred as consequence of the displacement of normal faults that cross the area. This fault system has been reactivated likely due to the stress changes provoked by the brine exploration activities that resulted in the caverns in the subsurface. These events in Maceió have also been investigated by the Brazilian Geological Service (CPRM, 2019) and by the company currently responsible for the mines. In the view of the author of the thesis, the upward growth of the caverns observed in field has overloaded the overburden layers that, in turn, might not support. If this is the case, progressive subsidence and sinkholes might be generated – a typical scenario of “chimney caving” (see the work of Augarde et al. (2003) for instance). Moreover, a cause and effect relationship among the salt cavern enlargement due to brine production, subsidence and seismic events may be possible, similar to what has already been mentioned elsewhere in the context of reservoir compaction (see Section 3.3.2). Regarding the Matarandiba Island (municipality of Vera Cruz, Bahia), the Brazilian Geological Service has investigated the emergence of a sinkhole in a region of salt brine exploration. Important information and findings are indicated in a preliminary report (Guimarães et al., 2018). The elliptical-shaped sinkhole was firstly noticed in May 2018, measuring 69.95 and 29.43 meters in the main axes and 45.4 meters in depth. By two months later, these dimensions evolved to 77.9, 33.0 and 44.9 meters respectively. More updated measurements (by June 2020) can be obtained on the website of the company responsible for the wells<sup>40</sup>: 112, 49.5 and 26.9 meters respectively. The first brine producing well was drilled in 1976, and in total 51 wells have been drilled until 2018. Ten of them have been operating until that year. In this region, the salt layer is at about 1,200-1,300 meters-depth and exhibits thicknesses between 20 and 60 meters. The target layer is bedded, stratified (mainly with anhydrite) and presents a high purity level (by

---

<sup>40</sup> Public data.

92% halite). The report findings are in line with the general observations of the other cases involving solution mining. The 51 brine wells have become 51 caverns and some of them are interconnected, enlarging the underground void spaces. There is no further information on the hydrogeology, which could eventually support hypotheses of additional underground dissolution (other than those inherent to solution mining). The conjunction of these factors besides an eventual fault reactivation related to stress changes in the surroundings of the caverns could explain the appearance of the sinkhole. In terms of social impact, the village near the sinkhole has not been affected to date. As these incidents occurred in Brazil are still recent, it is expected that more academic research will provide more in-depth answers in the near future.

More so, another example of a mine accident that, at first, combines anthropogenic mining actions with geological particularities of the field was the collapse of the 3rd Berezniki potash mine (Russia) in 1986, until then one of the largest potash mines in world (Andrejchuk, 2002).

Fortunately, nowadays there is engineering and environmental awareness in this kind of application. Johnson (2008) points out that most of the collapses are related to solution mining caverns opened about 50-100 years ago and the modern project criteria have practically eliminated these problems in recent mines.

#### **3.2.4. Introduction to solution mining**

Solution mining is a chemical/transport process and consists of in situ leaching or dissolution in which mineral extraction from subsurface is carried out by a solvent (Bays, 1962; Treybal, 1980). There are two processes to saturate the water injected with dissolved salt producing saturated brine: diffusion and circulation. The diffusion is a process through which sodium and chloride ions migrate from salt to water at the well wall (interface between salt and water). Since this is an ionic process and does not involve mass transfer, water saturation by diffusion is an extremely slow process. On the other hand, the circulation (convection) involves mass transfer. In the contact between salt and water over the well wall, temperature changes, gravity segregation and pressure gradients lead to a faster saturation process (Bays, 1962). According to Durie and Jessen (1964a), the natural convection is of utmost importance for the controlled dissolution of salt. The water density at the contact with the salt shall increase as the salt is dissolved and moves down by natural convection.

In an engineering view, considering evaporitic ores (generally salt and potash), solution mining consists on drilling a well until a certain depth of the ore and complete it (with casing and cement sheath) a few meters above the top of the target formation. Pipes are ran in the interior of the casing and unsaturated water is injected through them. As the salt (or the target ore) is dissolved in the solvent and the saturated solution is withdrawn, cavities are formed.

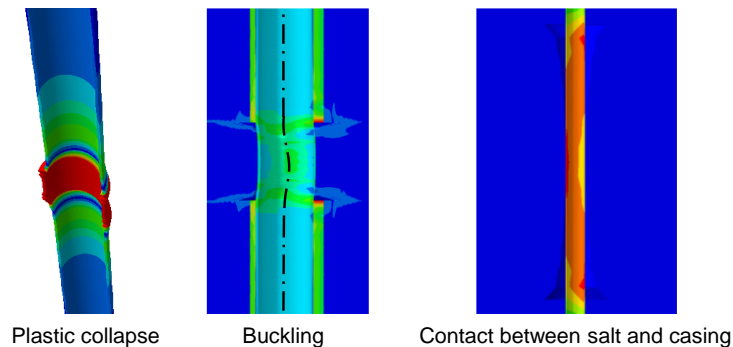


Figure 20. Potential scenarios for casing damage in washout intervals.

Besides the applications of mining and storage, modelling salt dissolution is also of interest to well engineering in the context of Pre-salt since any kind of engineering work that promotes significant contact between salt and unsaturated water may generate cavities. Using synthetic drilling muds such as oil-based muds (OBMs) prevents from salt dissolution around the well; however, these fluids are dangerous for the environment in case of leakage and more expensive (Calcada et al., 2015). The alternative is to use WBMs, which are safer for the environment and cheaper. Besides reducing costs and limitations, using seawater as drilling fluid increases considerably the rate of penetration (Willson et al., 2004), leading to a faster and consequently shorter drilling job. Nonetheless, due to the same principle of the solution mining, this kind of fluid is expected to dissolve the well wall, generating intervals with significantly enlarged sections or cavities (washout intervals). This may cause not only the instability in the rock formation around the cavities but also a bad cementing job. It results in an inefficient hydraulic isolation of the well and eventually in casing damage due to plastic collapse, buckling over the laterally unsupported intervals and nonuniform loads provoked by an irregular contact with the creeping salt (Firme et al., 2015a), Figure 20. Additionally, intercalations of halite and with less soluble evaporites such as anhydrite exposed to WBMs are expected to remain as undissolved intervals so-called “anhydrite mechanical stops”<sup>41</sup> (Falcão, 2009). The Brazilian oil and gas industry has been

<sup>41</sup> Expression from the work of Falcão (2009), page 389, freely translated from “batentes de anidrita” in Portuguese.

carrying out studies in this area, including the development of computational tools to simulate salt dissolution (Folsta et al., 2011; Lomba et al., 2013a, 2013b; Meneses et al., 2017; Plucenio et al., 2013; Silva et al., 2017). An example of unintentional salt dissolution is the case of the geological accident of Wink Sink #1 (Johnson, 1989). It occurred in West Texas, in early 1980's. An oil well was drilled in 1928, produced between 1928 and 1951 and remained plugged between 1951 and 1964. When the well was drilled, a WBM may has been adopted (creating washouts) and the cementing job was not efficient. During the period when the well was plugged, progressive dissolution of the Salado formation (halite and anhydrite) occurred due to fresh water percolation from the above aquifers. Casing underwent partially corrosion due to the contact with salt water from the formation. Apart from that, the well left openhole intervals between Tecovas (siltstone and sandstone) and Dewey Lake (shale and siltstone) formations when it was plugged. When the dissolved region became sufficiently big, the overlying layers could not support and successive failures occurred until the surface was reached, generating a sinkhole of average diameter of 110 meters and about 34 meters depth.

It should be noted that not only salt and potash are prone to dissolution by solution mining or analogous processes. There is the dissolution by hydrogeological mechanisms (sometimes unrelated to engineering works) forming sinkholes and karstic cavities. Surface and subsurface karstic landscapes correspond to about 20% of the Earth exposures disregarding ice zones (Ford and Williams, 2007) and account for underground flow networks that are often unknown since they may be submerged, filled with material (Luu et al., 2019) or buried by sediments. An introduction to the karst research in Brazil have been presented by Auler and Farrant (1996), who estimated that epigenic karst is seen on 5% to 7% of Brazilian outcrops. Other karstic features such as paleokarst and hypogenic karst have not been accounted for in this percentage, besides offshore karstified carbonates. The geology of the Northeast Brazilian onshore karstified carbonates has been a widely developed research line in the recent years. Furthermore, evaporitic rocks composed by calcium sulphate (anhydrite and gypsum) are also susceptible to alterations and dissolution in contact with water, although to a lesser extent. As an example, almost all regions in Italy have gypsum cavities, in addition to natural and anthropogenic sinkholes (Waele et al., 2017). For comparison, gypsum/anhydrite solubility is about 2.4 g/L while halite solubility is about 360 g/L (Johnson, 2008). Cavities generated by anhydrite/gypsum dissolution are also an important hazard. This phenomenon is prone to happen in water tunnels and

especially in water injection wells. Calcium sulphate is generally deposited forming gypsum. It completely loses water in subsurface, turning into anhydrite and undergoing volume reduction. With water injection in the formation (by a well for instance), the inverse process may happen, with volume expansion (Mohriak and Szatmari, 2009; Szatmari et al., 2009). Johnson (2008) also mentions the anhydrite tendency to turn into gypsum when it is in contact with water. Case studies (quantitative) involving anhydrite/gypsum dissolution in engineering works are quite rare in open literature. One of the studies that mentions the anhydrite dissolution around water tunnels in hydroelectric plants has been presented by Gysel (2002). In a somewhat similar context, the author of the thesis has been involved in the recent past in a project with industry to develop a workflow for numerical analyses of integrity of injection wells under local anhydrite dissolution intervals. The dissolution was attributed to the water ascending flow from the reservoir and reaching the evaporitic stratum. The interested reader in more details and results of this work is referred to the work of Pereira et al. (2018).

Finally, another important aspect to consider is the differences in mineralogy and geological structure among the evaporitic deposits worldwide. This variability has significant influence on the mechanical behavior and solubility performance of the formation. Much of the scientific literature available is in the context of Europe (Asse mine and Gorleben salts) and North-America (WIPP and Gulf of Mexico salts). In general, these salt formations exhibit high purity and homogeneity levels (Fredrich et al., 2007; Hunsche, 1993; Willson et al., 2003). On the other hand, Brazilian salt formations frequently exhibit stratifications. Halite is often intercalated with highly soluble and mobile salts such as carnallite and tachyhydrite, or with less soluble and mobile rocks such as anhydrite. Considering the structure, Brazilian evaporitic formations often consist of thick bedded layers or massive domes (Costa et al., 2019a; Ribeiro da Silva and Pereira, 2017). The latter casts a positive scenario for vertical-developing caverns. Chinese salt formations, in turn, generally develop in relatively thin bedded layers, are stratified and of low purity level, motivating the generation of horizontal-developing caverns (Li et al., 2014; Liang et al., 2016; Ma et al., 2013; T. Wang et al., 2015; Xing et al., 2015). Naturally, excessively soluble or insoluble rocks affect the solution mining effectiveness especially when these intervals are unforeseen. As consequence, the final shape of the cavern and even its integrity can be harmed (Keime et al., 2012; Li et al., 2017, 2016).

### 3.2.5. Cavern construction (opening) by solution mining

The construction process of a solution mined cavern starts with a well, which is drilled until close to the planned cavern floor. A casing is run and cemented a few meters above the planned roof and pipes are run inside this casing. Water is injected through these pipes to dissolve the salt. The resultant brine (the targeted solute) is withdrawn, resulting in the underground cavern. The annular space between the injection and extraction pipes is filled with an inert fluid (blanket). Since the blanket does not react with the salt and the injected fluid, it creates an isolated layer along the annulus space and around the cavern roof, preventing them from excessive dissolution. Figure 21 sketches the main steps of solution mining.

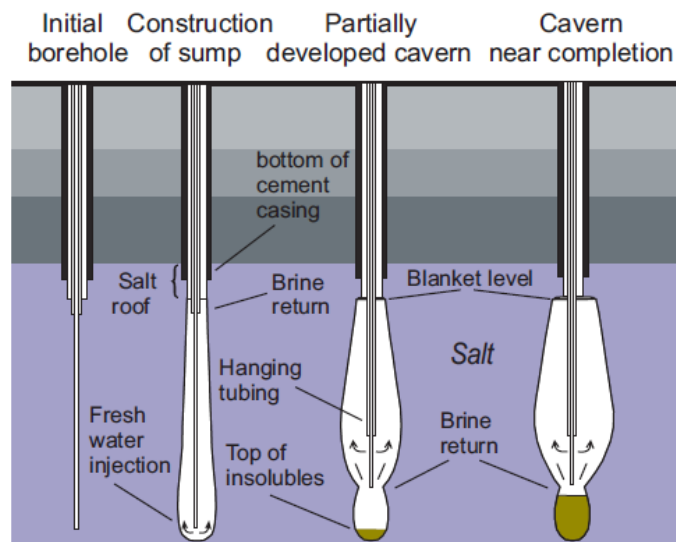


Figure from Evans et al. (2008)

Figure 21. Sketch of salt cavern opening by solution mining (Evans et al., 2008).

Based on the works of Durie and Jessen (1964b, 1964a), there are two alternatives for the water injection in the formation: direct circulation and reverse circulation. Figure 22 illustrates these circulation methods. When the circulation is direct, water is injected by the internal pipe and brine is withdrawn by the annular space. Once initially the injection pipe is placed close to the planned cavern floor, the cavity is likely more spread in the floor than in the roof. In general, a conical geometry is expected, with the widest section at the cavity floor. More so, the injection pipe can be displaced to adjust the cavity geometry. When the circulation is reverse, water is injected through the annulus space and the brine is withdrawn by the internal section of the pipe. The disadvantage of this method is that the focus of water injection is fixed since it is sited in the annular space and not in the pipe. The expected geometry is also conical, but with the widest section at the

cavity roof. These circulation methods can be combined for a better shape adjustment. Moreover, Simoes (2010) points out that the distance between injection and production pipes should be as large as possible in order to brine reaches the ideal concentration. The dissolved layer must be thick enough to comply with this practice. It is also possible to use more than one well so that water injection and brine withdrawal occur in distinct wells. This separation of functions between the wells also allows the use of higher temperatures in the injection water, what likely accelerates the dissolution. Besides that, depending on the distribution of the wells, the cavern shape adjustment may be favored. Lastly, directional and horizontal wells for solution mining can be constructed when the cavern host rock cannot be accessed by a vertical well or is significantly thin.

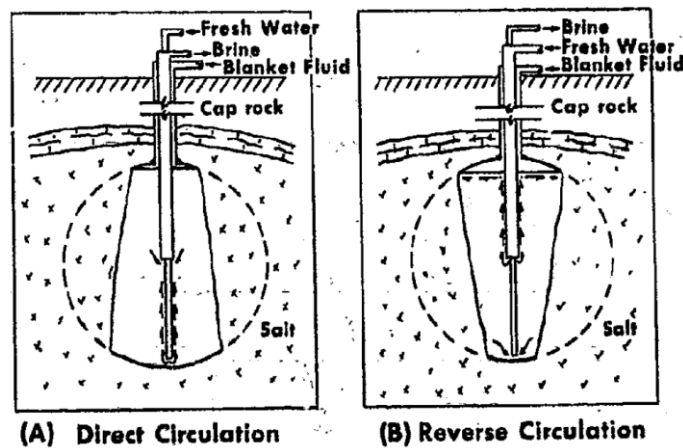


Figure from Kazemi and Jessen (1964)

Figure 22. Sketch of solution mining technique: direct (a) and reverse (b) circulation (Kazemi and Jessen, 1964).

### 3.2.6. Cavern destination and operation

The destination and the type of operation of the cavern mainly impacts its internal pressure, temperature and eventually percolation through the vicinity. Besides creep deformation, changes in the cavern geometry may happen in case of dissolution. As a consequence, mechanical integrity and tightness problems may arise in the short- and/or in the long-term. The purpose of the cavern and the type of stored material are also determinant to forecast possible engineering and environmental complications. Simplistically, this section has addressed four types of destination and operation: mining, hydrocarbon storage, new energy applications and waste disposal.

In mining applications, the controlled dismantling of the rock formation is necessary for the ore extraction. The face advance of the mine modifies the geometry increasing the void spaces; however, it is expected to happen under controlled excavation levels keeping the stability of the openings (cavities, room, galleries, among others) in such a way that underground catastrophic collapses and/or sinkholes at surface are avoided. Considering a solution-mined cavern for brine production, analogous safe practices regarding the brine extraction rates and the monitoring of the cavern geometry using sonar are needed. Provided that the mine is with an adequate hydraulic isolation and far from potentially problematic geological regions, the main concern is the evolution of the underground spaces regarding the support capacity of the pillars and the overburden rock layers.

In hydrocarbon storage, the cavern geometry tends not to change significantly over time except by shrinkage due to salt creep. On the other hand, the internal pressure and the temperature are expected to change periodically. Considering underground gas storage, there is often a contingency operation scheme. Costa et al. (2012) presents an example of that. During a year, in one month the maximum gas storage is achieved, and during this period, the internal pressure is raised to the maximum. In other month, the internal pressure is reduced to the minimum value and the cavern remain so until the next cycle. Other examples of cyclic internal pressures during the cavern operation can be found in the works of Xing et al. (2015), Khaledi et al. (2016), Mahmoudi et al. (2017), Wang et al. (2018), among others. This periodic reduction in the gas pressure raises questions on the cavern integrity. According to Cosenza et al. (2002), during the cavern operation, the changes in the internal pressure may trigger dilation. With the opening of cracks and fissures, percolation paths for fluids and gases are opened (see Section 2.1.2) and dissolution may happen over these paths. Chemical reactions may influence the mechanical strength. Regarding (only) the temperature effect, Sicsic and Bérest (2014) have mentioned two scenarios in which thermal fractures have been observed in wells and gas caverns. According to these authors, an intense heating may cause spalling in caverns and an intense cooling may generate fractures perpendicular to the cavern wall (see Section 2.2).

More so, a rapid gas depressurization implies cavern cooling, and therefore one has the mechanical, the thermal and the coupled effects of pressure reduction together. Sriapai et al. (2012) have carried out experiments in pure halite samples subjected to temperatures similar to underground storage caverns for gas or compressed air. They have observed that the temperature effect is larger under

higher mean stresses and that salt short-term strength decreased as the temperature increased. The effect of temperature in the rock strength may be intensified in a salt cavern operation considering a number of loading/unloading cycles over the lifespan. For reference purposes, usually one observes a stress reduction of 1 MPa per °C. Since salt tensile strength is lower than 2 MPa, a sudden salt cooling may trigger tensile cracks and enhance permeability (Cosenza and Ghoreychi, 1996).

In the new energy applications such as CAES, there are similarities with the behavior of gas caverns. Many observations made for the thermomechanical behavior of salt come from this context – see Section 2.2 and references therein.

Lastly, in the waste disposal, some of the materials may be high heat-generating. This is the case of high-level waste (HLW) for instance, that may reach temperatures of order of 230°C (Hansen, 2012; Hansen and Leigh, 2011). In these circumstances, the mechanical, hydraulic and chemical response of the salt cavern still needs to be more investigated. On the other hand, still according these authors, the previous experience with (isothermal) transuranic waste has demonstrated the adequate performance of salt as storage medium.

### **3.2.7. Cavern abandonment**

Once the cavern has reached its operational lifespan or has presented an incident that prevents it from continuing to work, it has to be abandoned. The cavern abandonment tends to be a little more complex than well abandonment because the cavern internal pressure increases over time as consequence of the multiphysical processes inherent to the interaction between the brine and the cavern walls. Briefly, according to Bérest et al. (1996, 2001), the cavern abandonment consists of plugging the access well with cement isolating a large bubble of saturated brine (or waste plus brine) inside the cavern. This “abandonment” brine inside the cavern is initially at a pressure called in the caverns literature “halmostatic” – the brine column height. These abandonment procedure has not changed significantly with time – by 2015, Thoraval et al. (2015) has presented a similar approach as the most accepted technique. In the “end” of the abandonment process, the brine pressure inside the cavern likely reaches an equilibrium pressure, between the halmostatic pressure and the geostatic mean stress – this equilibrium pressure often tends more to the halmostatic pressure. The exceptions are the very deep caverns, caverns with large volumes or heights,

salt rocks with very low permeability and with high creep rates. In these cases, the equilibrium pressure tends more to the geostatic mean stress.

This abandonment procedure carries with it the risk of the formation undergoing fracture since there is a pressure increase inside the plugged (closed) cavern. Tensile stresses are expected at the cavern roof. The brine pressure is expected to exceed the geostatic stresses, raising the risk of fracturing upwards. The authors above point out that the dynamics of the pressure increase in closed caverns is related to: i) the elastic compressibility of the brine-filled cavern; ii) the brine heating over time and the corresponding thermal expansion; iii) the brine saturation evolution resulting from the cavern wall dissolution (enlarging the cavern); iv) the creep of the host formation (confining the brine); and v) the brine percolation throughout the salt formation – salt permeability is very low (from about  $1.0E-21$  to  $1.0E-17$  m<sup>2</sup>) and a little percolation of brine is expected since a hydraulic gradient is maintained by salt creep and brine thermal expansion in a closed cavern.

Regarding the brine heating with time, it happens due to the thermal gradient between cold water adopted in the solution mining (and in the abandonment brine) and the warmer rock formation. There is a practical rule that states that a temperature variation of 1°C provokes an internal pressure variation of 1 MPa in the brine inside the closed cavern. If the abandoned cavern is fractured due to a very high internal pressure, excessive brine flow may pollute the overlying aquifers. There is also the risk of brine leaks through the well plug since cement degrades over time. At the same time, brine percolation has the positive effect of relieving the pressure inside the abandoned cavern. Still regarding brine leakage, Thoraval et al. (2015) point out that shallow caverns with low permeabilities and creep rates exhibit very low leakage rates (several L/year). On the other hand, deep caverns with not low permeability and high creep rates exhibit high leakage rates (several hundred m<sup>3</sup>/year). It also depends on the durability of the cement plug and on the occurrence of a mechanical failure in the cavern. With respect to salt dissolution, Durup et al. (2007) mention that, in general, the abandonment brine is not fully saturated when the cavern is closed. Thus, dissolution occurs until brine reaches about 100% saturation. It triggers an increase in the cavern volume and reduction of internal pressure. If freshwater is injected in the cavern to be abandoned, the cavern volume is expected to increase by 15% beyond the water injected volume until it becomes saturated. More so, the salt dissolution is endothermic – the rock formation absorbs heat, reducing the brine temperature.

Still according to Thoraval et al. (2015), if the cavern is sealed right after to be filled with brine, the increasing brine pressure due to thermal expansion may fracture the salt cavern – this is a key difficult in cavern abandonment. Shallow and small caverns reach or come close to the thermal equilibrium temperature faster than deep and large caverns. In the latter case, it may need several decades to reach the thermal equilibrium. There are some practices recommended to minimize these effects that lead to internal pressure increase. Bérest et al. (1996) suggest to retard the well plugging to let the salt host formation heats the brine. Thus, the subsequent thermal expansion happens while the well is still opened, in such a way that the brine has enough space to dilate and eventually flow out of the well. A reference brine withdrawal rate is between 1 and 10 m<sup>3</sup>/day at the beginning of the warming process. This value tends to reduce as the thermal equilibrium is being reached (Thoraval et al., 2015). This minimizes the pressure increase due to confined fluid; however, the problem of this technique is the time required for the thermal equilibrium. It may raise legal problems due to the schedule of the operator responsible for abandoning the cavern. A second practice is to reduce brine pressure inside the cavity (using a pump), letting the cavern shrinks by creep and the abandoned space becoming smaller. However, even being efficient for deep caverns, a severe pressure reduction may lead to rock integrity problems. The third practice is to inject gas in the cavern before plugging to increase its compressibility. A fourth practice is mentioned by Durup et al. (2007), and consists of the heating the abandonment brine before injecting to anticipate the thermal expansion before the confined fluid condition (when the cavern is closed). The main obstacle for this practice is the cost.

Naturally, these abandonment practices must adapt to each field and engineering reality, considering the variability in the geomechanical conditions and the infrastructure available in each cavern site. Three cases of cavern abandonment are presented in the literature (Bérest et al., 2001; Durup et al., 2007; van Heekeren et al., 2009). These cases have shown that reaching the brine equilibrium pressure – a value between the halmostatic pressure and the geostatic mean stress – is of utmost importance; however, it is challenging to monitor the changes in this pressure over time since the cavern shrinks by creep and brine percolates throughout the host formation.

Computational simulations play a very important role in cavern abandonment predictions. According to Durup et al. (2007), the cavern abandonment dynamics casts two coupling relations. The changes in the brine temperature trigger pressure

variation, but the opposite does not happen (one-way coupling). This may not be the case of natural gas filling the cavern rather than brine. More so, the cavern shrinkage by salt creep increases the brine pressure (due to confined fluid effect), and the opposite also happens, i.e., the high internal pressure deaccelerates creep deformation (analogous effect to the drilling muds in wells crossing salt layers). Therefore, it casts a two-way coupling. Similarly, Thoraval et al. (2015) suggest coupled analyses in the contexts of creep and percolation (HM), and brine thermal expansion, creep and percolation (THM). The well leakage likely reduces the risk of hydrofracturing the cavern wall. Considering the risk of long-term pollution of groundwaters, it depends on the cavern geometry and the durability of the cement plug. That said, two scenarios should be considered: one assuming brine percolation through the rock mass and along the well and other considering also a serious damage in the plugs.

### **3.3. Salt caprock of Pre-salt reservoirs**

#### **3.3.1. Overview on reservoir compaction and subsidence<sup>42</sup>**

Hydrocarbon production from deep-buried reservoirs casts geomechanical threats that result from reservoir compaction such as surface subsidence, faulting, and casing collapse (Dusseault et al., 2001b; Zoback, 2010). These consequences are expected since hydrocarbon production causes reservoir depletion and compaction that, in turn, triggers significant stress changes in the surroundings. Doornhof et al. (2006) have presented an assessment on the physics involved in reservoir compaction and surface subsidence. Although not always, in most cases subsidence results from anthropogenic exploration activities in subsurface that impacts the surface (ground). In general lines, the surface subsidence is noticed as a bowl which is wider than the reservoir depleted radius that undergoes compaction, and tends to be symmetric even if the compacted region is not. While reservoir compaction depends substantially on its properties, the subsidence response tends to exhibit an average mechanical response of the overburden rock formations since the bowl results from the superposition of the mechanical response of each subsurface component (above the reservoir).

---

<sup>42</sup> Parts of this section were updated for presentation from the article “Mechanical behavior of carbonate reservoirs with single karst cavities” written by the author and the first advisor of the thesis (Firme et al., 2021) and published in *Geomechanics for Energy and the Environment*.

Initial and straightforward compaction and subsidence estimations for particular scenarios such as homogeneous lithology, linear poroelasticity and regular reservoir shapes can be obtained using classic analytical solutions available in the literature (Geertsma, 1973; Tempone et al., 2010; van Opstal, 1974). Recent analytical works have enhanced these classical solutions by supporting discretized non-regular 3D geometries with elementary pressure variations (Muñoz and Roehl, 2017; Quevedo et al., 2015) and plane strain overpressured reservoir models (Wangen et al., 2018). In the latter, the model is composed by reservoir and overburden, and overpressure is represented by a Fourier series. On the other hand, numerical simulations have led to more realistic modeling by allowing significant flexibility in terms of heterogeneities, irregular geometries, more sophisticated constitutive models and boundary conditions, multiphysical coupling, among others (Chin et al., 2000; Firme et al., 2014a; Yin et al., 2010). These simulations have reduced the level of uncertainty inherent to reservoir geomechanics (Pereira et al., 2016) while required more in-depth knowledge and computational resources.

It is common knowledge that 60% of world's oil and 40% of world's natural gas are stored in carbonate reservoirs (Montaron, 2008). It is also generally accepted that approximately 85% of the carbonate reservoirs are naturally fractured (Lamarche et al., 2012) and therefore exhibit complex hydromechanical behavior. In addition, carbonate reservoirs have likely experienced karstification at different scales, resulting in a heterogeneous porous structure composed by pores, fissures, conduits, vugs and caverns (Klimchouk, 2006). Li et al. (2018) point out that "carbonate strata are rich in oil and natural gas resources, and are one of the riskiest bedrocks for construction of highways, railways, tunnels, and other infrastructure"<sup>43</sup>. From the O&G perspective, the intricate pore structure of carbonates plays antagonist roles. Considering the adverse effects, unpredicted karstic features such as void spaces and conduits may be catastrophic for the integrity of the drilling equipment and the formation surroundings. Many drilling bit drops along karstic cavities have been reported (Loucks, 1999). Those features, eventually associated to fracture corridors, may also cast a severe or total lost circulation zone and promote the communication between injection and production wells. In the more critical scenario, hydrocarbon recovery is unfeasible (Akbar et al., 2001; Bagni et al., 2020; Lamarche et al., 2012; Loucks, 1999; Rabelo et al., 2015). On the other hand, karstification has positive effects. According to Cazarin

---

<sup>43</sup> Excerpt from page 153 of the work of Li et al. (2018).

et al. (2019), karstification is an essential process to generate secondary porosity and permeability in carbonate reservoirs and aquifers. Despite the difficulty in estimating porosity and permeability over an intricate porous structure, vuggy zones often exhibit high permeability (Akbar et al., 2001; Camacho-Velázquez et al., 2005). Fractures may also enhance oil recovery (Lamarche et al., 2012), and karstic features may act as hydrocarbon storage environments (Loucks, 1999). In line with the above, Balsamo et al. (2020) characterize fractured and karstified carbonates as “often major aquifers and hydrocarbon reservoirs”<sup>44</sup>.

In spite of the study of carbonate rocks is an extensive line of research and this thesis is dedicated to salt rocks, a brief introduction to carbonate rocks is welcome in the sense of expressing their importance in the O&G engineering projects. Carbonate rocks, which constitute reservoirs with large hydrocarbon reserves, are generally sealed by salt rocks. That said, these two rock groups are of particular relevance in reservoir geomechanics since they are fundamental for the Pre-salt O&G system. The basics of the mechanical behavior of carbonate rocks in this context has been previously discussed in a dedicated paper (Firme et al., 2021) and references therein. Fokker et al. (2018) have presented an assessment on subsidence in the Dutch Wadden sea, whose observations can be generally extended for similar contexts. These authors have divided the processes that originate subsidence into natural and anthropogenic. Among the natural causes, their work mention sediment compaction, isostasy and tectonics. By anthropogenic causes, they mention hydrocarbon production, solution mining, coal mining, gas storage, geothermal activities. This section is dedicated to the theoretical basis of salt rocks as caprocks of Pre-salt reservoirs; therefore, the focus is on the subsidence due to hydrocarbon exploration.

### **3.3.2. A brief historic review of subsidence due to hydrocarbon exploration**

One of the first records of surface subsidence resulting from exploration activities was in the Gosse Creek field (Texas, USA), 1918. An article presented by Pratt and Johnson (1926) has reported this case. The producing area of Gosse Creek field consists of unconsolidated clays and sands. Excluding other causes such as erosion or a sinkhole generation due to subsurface dissolution – although it is a salt dome area, the dome is deeper than the producing region –, the excessive fluid (oil and water), gas and sand withdrawal from the producing region

---

<sup>44</sup> Excerpt from page 1 of the work of Balsamo et al. (2020).

has triggered the surface subsidence. The sunken area coincides with the production region, where the wells are sited (see Figure 7 of their work). Furthermore, the periods of surface sinking and of production coincide. Still according to these authors, before 1917 – year when the production started –, no sinking (subsidence) was noticed in the region. Another important field in North America that has undergone significant surface subsidence is the Wilmington field (California, USA). According to Nagel (2001), this field was discovered in 1932 and the production started in 1936. The subsidence has been monitored since 1940. In 1958, the subsidence rate was about 38 cm/year and water injection (to recover the reservoir pressure) started. In 1966, the subsidence rate was almost null. The total subsidence has reached a value of about nine meters in 1968.

The North Sea chalk reservoirs are critical scenarios of compaction and subsidence. According to Risnes (2001), the North Sea chalk is characterized as a granular material with high porosity (sometimes higher than 40%). The basic failure mode of high porosity chinks is the shear failure between grains. This mode can occur by compression at low confinement stresses, pore collapse at high confinement stresses and tensile failure. The pore collapse mechanism may happen even if a purely hydrostatic loading applies. Additionally, the chalk strength is influenced by porosity, silica content and by the type of fluid in the pores. In this context, two widely studied fields have to be commented: Valhall and Ekofisk. Njå (2012) has studied the decommissioning of Valhall field due to well integrity problems. In this field, the water depth is by 70 meters. The reservoir is composed by unconsolidated high porous (weak) chalk (by 2,450 meters deep) and the caprock consists of a 1,000 meters-thick soft and weak claystone. It exhibits microfractures due to the high pressure of the chalk reservoir below (pressure of 44.81 MPa and temperature of 93°C). Oil and gas migration has created a gas cloud at 1,350 meters deep. The production in this field has started in 1982, and it has reached more than 500 MMbbls. The reservoir underwent severe depletion, exhibiting a compaction of more than 10 meters. The seafloor subsidence was of about 6.3 meters. For a long time, subsidence rate was of 25 cm/year. These high compaction and subsidence displacements have collapsed many wells. After a repressurization of Valhall reservoir, the subsidence rate reduced to 12 cm/year. Furthermore, Larsen (2007) has analyzed a number of aspects of Ekofisk field with focus on gas in overburden. The reservoir is also chalk. As a reference, the initial pressure and temperature were of 49.2 MPa and 131°C considering an elevation of 3,170 meters. Still according to this author, the field was discovered in 1969 and

production has started in 1971. Gas injection to attenuate reservoir depletion started in 1975. In 1984, a significant level of subsidence was observed, and a more focused subsidence bowl monitoring has started since then (Rentsch and Mes, 1988). Water injection to recover reservoir pressure started in 1986/7; however, it failed in the objective of controlling compaction and subsidence. A water weakening effect occurred in chalk reservoir, allowing compaction and subsidence to continue despite reservoir pressure recovery (Sylte et al., 1999). The maximum seafloor subsidence was about 8.5 meters, and subsidence rate was about 10-15 cm/year by 2007 (Larsen, 2007). Close to this field, the West Ekofisk has similarities in terms of materials and field conditions. It underwent a reservoir depletion of 41 MPa between 1977 and 1998, and a subsidence over 3.5 meters was noticed (Nagel, 2001). Still in the context of the chalk reservoirs of North Sea, Eiksund et al. (1995) have studied the impact of reservoir creep (during compaction) on subsidence of Ekofisk. Chalk creep has been analyzed considering a strain-hardening model originally developed for soft soils. It has been observed that the material depends strongly on the initial porosity – what is generally the case of chalks and carbonates. The authors have concluded that, although chalk creep had a contribution to the reservoir compaction, this contribution alone was not sufficiently high to justify the amount of subsidence experienced in the field by 1984/5. Subsidence can be reduced by recovering reservoir pressure; however, there will still be a contribution from reservoir creep.

The subsidence values of these North Sea fields, despite being large, have only affected exploration structures. The implications of that on the structure integrity and serviceability could be mitigated despite the costs involved. However, depending on the context, significantly lower subsidence levels can have serious engineering and safety consequences. This is the case of the Netherlands for instance, where subsidence values of order of centimeters can structurally affect the dikes in the regions below the sea level, constituting a serious threat to the surrounding inhabited regions (Nagel, 2001). In this context, one mentions the Groningen onshore field, which largest gas field in Europe and one of the largest in the world. According to van Thienen-Visser et al. (2015), the production has started in 1963 and has been projected to continue (at first) by 2080. The reservoir is the Rotliegend sandstone. It is at burial depths of 2,600 and 3,200 meters, and exhibit thicknesses between 100 and 300 meters and porosities from 0.12 to 0.22. The pressure in the reservoir was reduced from 35 MPa to 10 MPa due to production between 1963 and 2012. The Rotliegend sandstone is overlain by a salt

caprock with variable thickness (Zechstein formation), representing a highly non-homogenous overburden. The center subsidence was of 35 cm in 2015 (Waal et al., 2015) and the predicted value in 2080 is by 60 cm (van Thienen-Visser et al., 2015b). Although these subsidence values are much lower than those of North Sea fields such as Valhall and Ekofisk, there is a major concern in terms of the structural damage in constructions which are close to the sea level. In addition to that, seismic events (earthquakes) have been noticed since when subsidence accelerates. As Verdoes and Boin (2021) point out,

“in the northern part of the Netherlands, earthquakes never occurred – until recently. In December 1986, an earthquake struck the Drenthe province, near a gas extraction site. (...) the number of earthquakes really accelerated in the Groningen province, where (...) gas has been extracted since 2000. At the time of writing, in late 2020, over 1700 small earthquakes have been registered in the northern provinces of the Netherlands.”<sup>45</sup>

Among these events, Waal et al. (2015) mention the case of Huizinge village, where an earthquake with a magnitude of 3.6 occurred in 2012, damaging constructions and making the inhabitants insecure to continue living there. van Wees et al. (2018) have analyzed relation between the reservoir creep (compaction) and the induced seismic events in Groningen field. The time-dependent hydrocarbon reservoir compaction is a well-known phenomenon. Its contribution to compaction can be of same magnitude of the elastic contribution, both in clastic and shale reservoirs. The reservoir creep is expected to be by 10% of the time-dependent compaction after the production ends, in addition to the contribution of the overburden and the sideburden. It is expected to reduce the seismic events in a more gradual way after the production ends. The challenge still in open is to adequately identify the creep mechanisms that govern Groningen reservoir. Given the impact of earthquakes, a significant reduction in production (80%) was applied to the central area of the field in January 2014. It was observed that when the production has reduced, there was a massive reduction in the seismic events. Even so, a lower earthquake (magnitude of 3.4) occurred in Zeerijp city (also in the Groningen region) in 2018 and, in the light of the previous events and the possible future ones, the gas production has been suspended in the region (Verdoes and Boin, 2021). Another Dutch field to be analyzed is the Ameland gas field. This is the first gas sited in the Wadden Sea area, North Netherlands. The gas production has started in 1986 and lasted by 25 years (van Thienen-Visser et

---

<sup>45</sup> Excerpt from page 150 of the work of Verdoes and Boin (2021).

al., 2015a). According to these authors, the subsidence reached 35 cm in 2011 and a prediction for 2050 would be of 42 cm. The reservoir is the Rotliegend sandstone, overlain by Zechstein salt. Marketos et al. (2015b) have presented an assessment on the long-term subsidence of this field. These authors point out that a large number of natural gas fields in the Netherlands are overlain by thick salt layers (such as Groningen field). The production has stopped almost completely by 2000, but subsidence has still evolved. As a differential in relation to standard approaches, salt caprock creep has been investigated as a possible reason for the continued subsidence. Among other findings (to be addressed in the next section), they have observed that the caprock creep can enhance the subsidence calculated using elastic approaches by over 50%.

From the above cases (as well as in the case of salt caverns), it is observed that studying subsidence as a consequence of depleted hydrocarbon fields is of strategic importance in related engineering projects. The reservoir and/or caprock creep is discreetly considered as an influencing factor in compaction and subsidence. Although the damage to constructions and populations may vary from case to case, rock damage resulting from a not stood subsidence may generate sinkholes or create significant discontinuities (eventually allowing polluting fluid leakage), which may be catastrophic. Once the reader is introduced to the general subsidence problem, the next section addresses the contribution of salt creep to the mechanical response of the overburden and therefore to the subsidence.

### **3.3.3.**

#### **The influence of salt caprock creep on subsidence**

To analyze the role that salt creep plays on subsidence, an important concept in subsidence resulting from reservoir depletion is introduced: the “subsidence-depletion delay” effect (hereinafter “subsidence delay”) (Hettema et al., 2002). It consists of the time interval between the beginning of reservoir depletion and the beginning of relevant subsidence in the surface. Graphically, the subsidence delay is measured by means of a linear extrapolation of the subsidence curve interval when a near-linear behavior is observed (Figure 23).

The subsidence delay has been observed a number of depleted fields, such as Lacq gas field (carbonate reservoir, France), Groningen and Ameland gas fields (sandstone reservoirs, Netherlands), Bachaquero and Tia Juana heavy oil fields (uncemented sandstone reservoirs, Venezuela), Valhall and Ekofisk oil fields (chalk reservoirs, Norway), and Troll East gas field (poorly cemented sandstone

reservoir, Norway). As a reference, the time delays are of the order 0.70 and 10 MPa in depletion or 1.6 to 13 years.

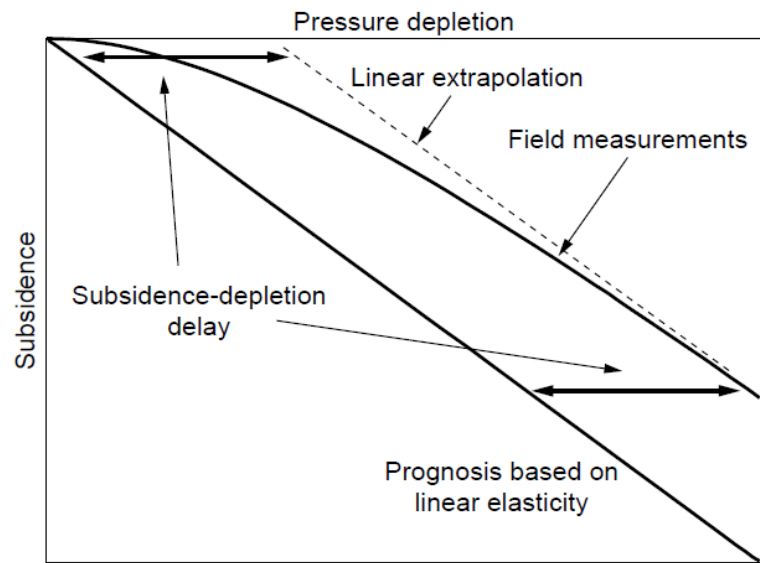


Figure from Hettema et al. (2002)

Figure 23. Schematic illustration of the subsidence delay (Hettema et al., 2002).

According to these authors, the subsidence delay can be caused by pressure diffusion, overburden inertia, reservoir compaction mechanisms and surroundings deformation. The pressure diffusion has found to be of little relevance although it always present. The same has been observed for the overburden inertia in most reservoirs a few minutes after depletion starts. On the other hand, the reservoir compaction mechanisms have a greater impact on the subsidence delay. The four mechanisms analyzed by the authors are the natural overcompaction, reservoir creep, loading rate effect and elastic-plastic transition. The natural overcompaction is more relevant in causing subsidence delay in shallow reservoirs. The reservoir creep is a possible mechanism to cause the subsidence delay, although creep (of the reservoir analogue material) seems to have a greater influence on the deformability of the samples in laboratory tests than what is expected in the reservoir. The loading rate effect refers to the ratio between the geological and the reservoir depletion loading rates. Since the depletion rates are significantly higher than the geological rates, the subsidence delay can be a consequence. The elastic-plastic transition can occur if reservoir undergoes plastic deformation during the depletion period. In this case, compaction and subsidence rates increase and it is reflected as a subsidence delay. Lastly, the surroundings deformation is influenced by the reservoir geometry and depletion, eventually in a nonlinear way. This source of subsidence delay demands a comprehensive geomechanical analysis, since it can be affected by compaction-induced deformations, stress

paths, nonuniformities in depletion, creep, among others. Otherwise, these effects cannot be adequately considered. In summary, based on the above study, rock creep – either in reservoir or in overburden layers – is indicated as possible mechanism responsible for subsidence delay.

In a past work, Firme et al. (2014a) have presented a comparative numerical study of constitutive models to simulate reservoir compaction and surface subsidence, where all the rock layers (reservoir, overburden, sideburden and underburden) have been simulated using linear-elastic, Mohr-Coulomb and Modified Cam-Clay constitutive models. A conceptual geomechanical model representative of a North Sea-like field has been considered. When the Modified Cam-Clay model was adopted, a shear-enhanced compaction mechanism triggered plastic deformations in the reservoir during depletion. It reflected on the compaction and subsidence results by a meaningful increase in the displacement rates, as shown in Figure 24 (a). This is an illustrative example of a subsidence delay caused by the elastic-plastic transition mentioned above.

Considering the giant gas fields in the world, about 62% of the caprocks are shales and 38% are evaporites (Grunau, 1981). In oil fields, these numbers are expected not to vary much. Both of these caprocks exhibit creep behavior; however, to the author's best knowledge, just a few works analyzing the salt caprock creep in the context of reservoir geomechanics are available in the literature – apart from well, cavern or dome simulations.

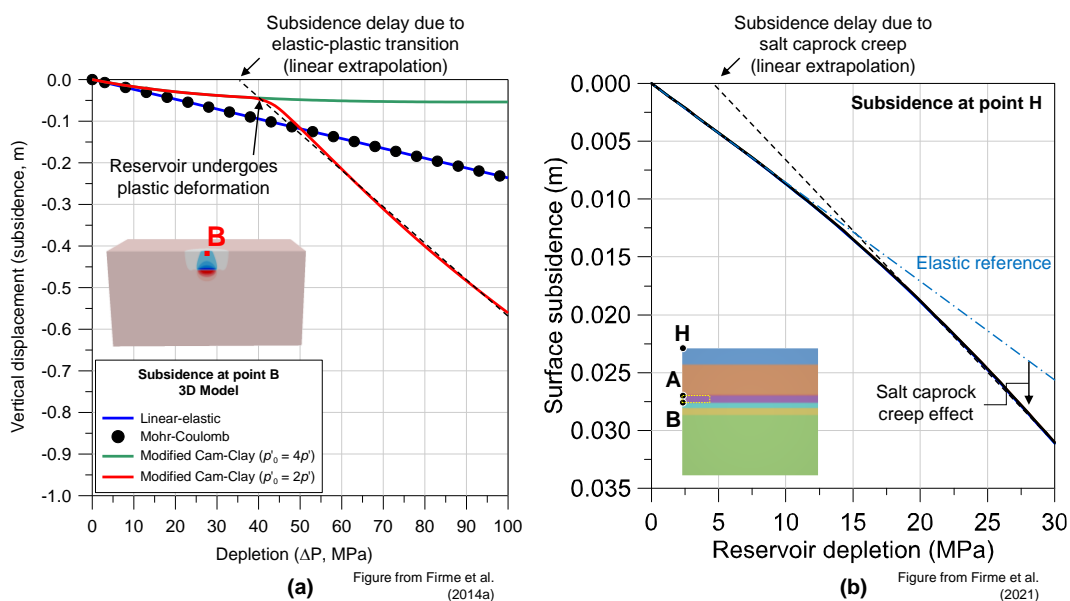


Figure 24. Subsidence in the center of the depleted radius in function of reservoir depletion. Representation of the subsidence delay due to elastic-plastic transition (a) and salt caprock creep (b). Adapted from Firme et al. (2014a) and Firme et al. (2021).

In the context of the gas fields in the Netherlands, Marketos et al. (2016a, 2016b, 2015a, 2015c, 2015b) have presented a series of studies about the combined effect of reservoir depletion and salt caprock creep on subsidence. Salt creep has been simulated using a viscoelastic model (Maxwell material) and using a power law/Arrhenius creep model analogous to the DM model (see Section 2.1.1.2). Their main conclusions are: i) the salt caprock creep can enhance the subsidence calculated using elastic approaches by over 50%; ii) the time-dependent subsidence can be divided into two mechanisms. The first is called “shear stress-driven flow” and consists of a rapid and significant subsidence contribution (increase) beyond the elastic response, and the second is called “pressure-driven flow”, which is a slow decrease in subsidence over time – therefore, the subsidence bowl is initially deep and narrow and with time becomes shallower and wider; iii) the time-dependent subsidence is not proportional to the content withdrawn from the reservoir; and iv) the salt steady-state creep governs the caprock response – the transient creep has little effect on subsidence results; however, there is still the challenge of choosing the adequate creep constitutive model and parameters.

In Brazil, Amaral et al. (2017) have analyzed the impact of injecting cold water (at 29°C) for hydrocarbon recovery in a carbonate reservoir during 16 years. In this scenario, caprocks are mainly evaporites (salt). Considering the Pre-salt scenario, salt is the caprock. Salt creep has been simulated using the Mohr-Coulomb model with a low cohesion value and a null friction angle. These authors have observed that the reservoir underwent compaction despite being subjected to water injection. The horizontal stresses have decreased significantly in the carbonate reservoir while no significant changes have been observed in the salt formation. Since the salt caprock integrity has been kept, it seems that thermal stresses have been alleviated by creep. Recently, Firme et al. (2021) have shown an study on the mechanical behavior of carbonate reservoirs with a centered karstic cavity. A conceptual Brazilian Pre-salt lithology has been considered. Although the focus of the study is the mechanical response of the carbonate in terms of compaction, subsidence and stress paths, salt caprock creep has been considered using the DM model, that simulates the steady-state creep rate. The results have shown that salt creep adds a subtle nonlinearity in the subsidence, and the values are slightly higher than those considering only elasticity. For the conditions considered in the work, the creep contribution for subsidence was of

small magnitude. This context illustrates a subsidence delay due to surroundings deformation – salt caprock creep in particular, Figure 24 (b).

Lastly, an up-to-date topic in worldwide hydrocarbon plays is CCS. In this particular context, one mentions the strategic injection of CO<sub>2</sub> in depleted reservoirs to reduce (and ideally to eliminate) carbon emissions. To this end, ensuring the caprock integrity is essential to reduce risks of fluid migration to overlying formations (Li and Laloui, 2017). Reinjecting CO<sub>2</sub> at high flow rates promotes reservoir overpressurization and, therefore, reduction in the effective stresses. The stress state perturbation can induce seismic effects and fault reactivation (just like hydrocarbon production and solution mining, both previously discussed). The reservoir deformation and the surface or seafloor uplift triggered by the CO<sub>2</sub> injection are mechanical responses that should be assessed (Li et al., 2015). More so, since CO<sub>2</sub> is handled on the surface and injected in a supercritical state, significant cooling occurs around the injection well in reaction to the new conditions of temperature and pressure in the reservoir depth (Joule-Thompson effect). This effect can generate cooling of over 20°C in the rock formation around the injection well (Oldenburg, 2007), inducing tensile thermal stresses. A stratified overburden can be beneficial to hydraulic isolation by casting several flow barriers between reservoir and surface (Rutqvist, 2012). In these circumstances, comprehensive analyses to check the caprock integrity in order to predict and avoid CO<sub>2</sub> leakage are of utmost importance. Regarding the salt caprock, special attention has to be paid to the creep behavior due to cooling since the latter may be more relevant than the poroelastic/poroelastoplastic effect (Amaral et al., 2017) and thermal (tensile) fractures have already been noticed in salt caverns subjected to severe temperature drops due to rapid depressurization (Bérest et al., 2016, 2014; Sicsic and Bérest, 2014).

### **3.4. Relevance of the strategic engineering projects in the Brazilian context**

The previous sections have presented a survey of the state of the art in three important groups of strategic engineering projects involving salt rocks: geological barriers, caverns and caprocks. Here, the reasons why the author believes that these projects are of particular relevance to the Brazilian context are presented.

Considering that Brazil has a large number of wells to be abandoned in the near future and the abundance of salt rock formations in the Pre-salt fields, there

is a context that naturally encourages the use of geological barriers formed by salt creep. As mentioned before, the NORSOK D-010 and IBP's guide (IBP, 2017) mention the use a creeping formation (such as shale or salt) to seal the annulus space between the formation and the casing as long as it exhibits creep behavior to close the annulus space forming (at least) 30 meter-length natural plugs and meets the integrity and tightness conditions expected from a WBE. P&A procedures for Brazilian offshore wells are more aligned with the characteristics of North Sea wells, although Brazilian Pre-salt water depths are often greater (about 2,000 meters deep). The properties such as creep deformation and essentially null permeability generally observed in the salt layers that overlain the Pre-salt reservoirs are useful to form geological barriers and isolate hydraulically wells in the terms mentioned by NORSOK in its immediate context in relation to shales. This is considered an innovative alternative for P&A by the Brazilian industry as long as the same requirements as a cement WBE are also met by the salt rock barrier<sup>46</sup>. The past experience in integrity and stability analyses of Pre-salt wells supports the expectation that Brazilian salt would be able to meet these requirements, in addition to possibly being able to close completely the well section (not only the annulus space). This latter alternative depends on removing the casing, what adds technical challenges although it would ensure a rock-to-rock sealing, not affected by material heterogeneities.

Furthermore, salt caverns are strategic applications for Brazil for environmental and economic reasons. Nowadays, there is the trend towards zero emissions of carbon and greenhouse gases in the near future (Evans et al., 2021) and therefore investing on CCS is a need for the industry. The production of the Brazilian Pre-salt reservoirs often deals with high gas-oil ratio (GOR) hydrocarbons. Taking Libra field reservoirs as an example, the initial GOR is about 440 Sm<sup>3</sup>/Sm<sup>3</sup>, and 44% of the associated gas is carbon dioxide (CO<sub>2</sub>) (Anjos et al., 2019). For environmental reasons, the CO<sub>2</sub> should be stored rather than released into the atmosphere. To this end, using CO<sub>2</sub> reinjection methods in depleted carbonate reservoirs would be an alternative that extends field production and promotes CO<sub>2</sub> safe storage. Nevertheless, the Pre-salt carbonates are often naturally fractured and often exhibit vugs and karsts (see Section 3.3.1). The carbonate reactivity to CO<sub>2</sub> and its complex pore structure make it a challenging medium for CO<sub>2</sub> storage. On the other hand, the Pre-salt reservoirs are overlain by thick salt formations whose properties have proven to be adequate to create tight

---

<sup>46</sup> See the context of notes 27 and 28.

media for strategic storage. Salt caverns for decarbonization purposes are already cited in the international literature as a means of contributing to this goal (Evans et al., 2021). The Brazilian industry should be encouraged in this sense considering the abundance of salt formations in the country (onshore and offshore).

In parallel, a current issue is Brazil's need for fertilizers. The potash, one of the main raw materials for fertilizers in agriculture, is obtained from sylvinites, which is a salt rock composed of halite (NaCl) and sylvite (KCl) minerals. Brazil has never been self-sufficient in the potash production and all of its domestic production comes from the Taquari-Vassouras mine, in the state of Sergipe. According to Farias et al. (2021), Brazil is the fourth largest fertilizer consumer in the world is currently the largest potash importer. In 2019, 80% of the potash consumed in the country was imported. The main suppliers are Canada, Russia and Belarus. The recent events related to the Russo-Ukrainian War (since February 2022) have showed a little more Brazil's fragility in relation to potash by the risk of the fertilizer supply from abroad being interrupted or reduced. Considering not only the existing Taquari-Vassouras mine but also the projects to be implemented in the future (Carnallite and Autazes projects), advances in salt computational geomechanics applied to the mining area are a strategic need. As a legacy, the salt mining caverns could be reused for strategic hydrocarbon storage, energy or decarbonization purposes after being decommissioned for mining.

Finally, there is still a gap in the subsidence analyses with regards to the salt caprock creep contribution in the reservoir geomechanics applied to the Brazilian Pre-salt fields. The effect of that in the subsidence delay may be being overlooked and structural problems arising from unforeseen subsidence values may occur. Just like the need for well P&A, Brazil has a number of fields to be abandoned and the Pre-salt fields will have to be abandoned in the future. Thus, adequate predictions of the seafloor subsidence evolution in offshore fields are of utmost importance for environmentally safe decommissioning. Also for an environmental reason, analyzing the salt caprock behavior is a strategic application for Brazil having in mind the trend for decarbonization in the near future (Evans et al., 2021), that demands research efforts on CCS. Although there is some criticism regarding the CO<sub>2</sub> injection in depleted Pre-salt reservoirs due to the complex pore/fracture network of carbonate reservoirs, this is still an alternative to the salt caverns, and has the advantage of the reservoirs would be already available while the caverns would have yet to be solution-mined. Rutqvist (2012) has indicated as beneficial a stratified overburden in casting flow barriers that would oppose to eventual CO<sub>2</sub>

leakage. This is generally the case in Brazilian fields. Santos basin for instance is typically overlain by more than 2,000 meters of stratified evaporites (Mohriak and Leroy, 2012), besides the layers above them. Among other challenges, understanding how the salt caprock responds mechanically and thermomechanically to the reservoir pressure variations and more specifically to the cooling caused by the Joule-Thompson effect due to the CO<sub>2</sub> injection is essential to verify the safety ensured by the caprock to the CO<sub>2</sub> stored below it.

In the light of the above, this thesis adds value to the research and industry communities by making use of computational geomechanics by means of an in-house and flexible framework for numerical simulations to analyze part of these Brazilian up-to-date salt-related strategic engineering projects.

## 4 Validation and reference examples

This chapter revisits a number of validation and reference examples available in the literature which have been tested by the author in the verification of salt creep implementations and analyses since his introduction to the salt geomechanics research (Firme, 2013) and subsequent work. The examples in this section include numerical simulations of triaxial creep tests, a hydrostatic compaction test, mining convergence measurements and Pre-salt well closure scenarios. The main purpose is to verify the results obtained using GeMA having experimental data and/or past simulations using other finite element codes as referential.

### 4.1. Triaxial creep tests

#### 4.1.1. Brazilian halite

The first group of simulations is the triaxial creep tests to analyze the time-dependent mechanical behavior of the Brazilian halite. These tests have been part of an extensive experimental program in the context of the exploration of the Brazilian Pre-salt fields. Halite samples formerly from Taquari-Vassouras potash mine and posteriorly from Muribeca formation have been tested (Costa et al., 2005; Poiate Jr., 2012; Poiate Jr. et al., 2006). For the sake of simplicity, this thesis refers to these materials as “Brazilian” halite. Information and results of four single-stage experimental tests carried out in Brazilian halite samples have been compiled from the works above. Table 14 summarizes the test specifications.

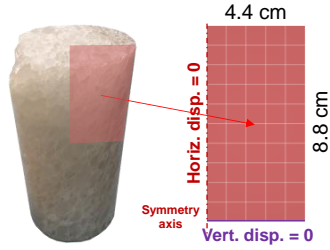
Table 14. Specifications of the triaxial creep tests carried out in Brazilian halite (Costa et al., 2005; Poiate Jr., 2012; Poiate Jr. et al., 2006). Identifications (A-D) attributed by the author of the thesis.

Test	Deviatoric stress ( $\sigma_d$ , MPa)	Duration (h)
A	10	1,600
B	14	1,000
C	16-18	2,200
D	20	620

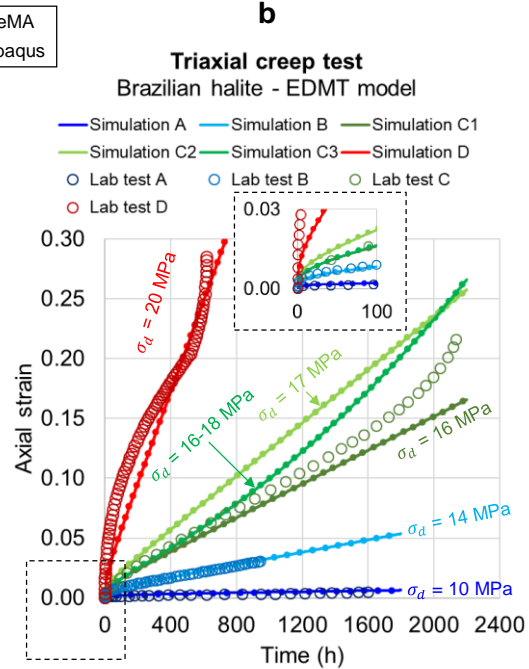
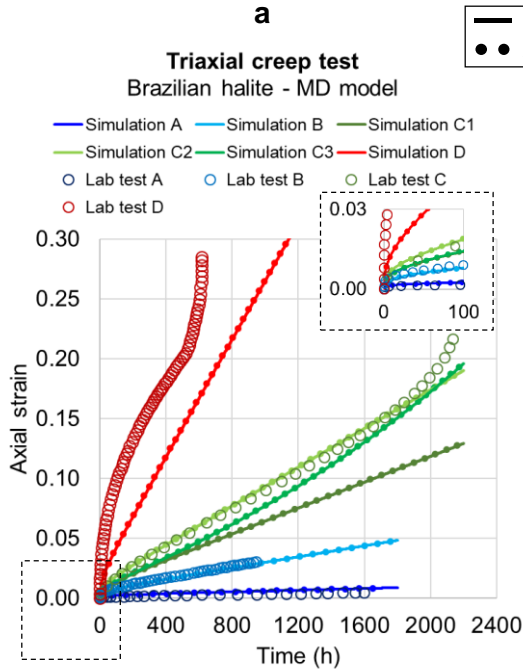
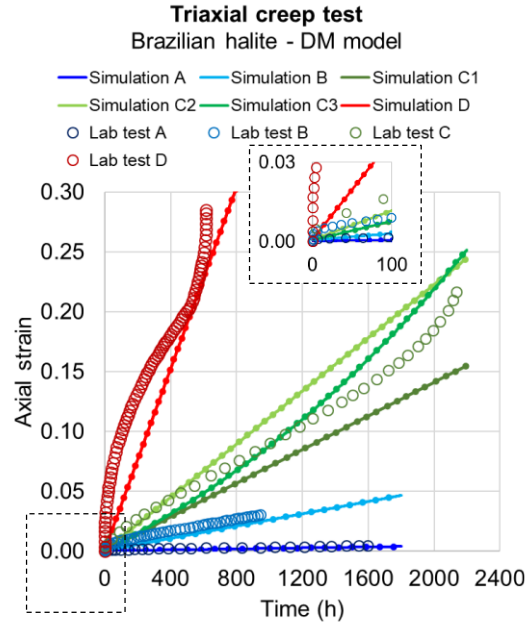
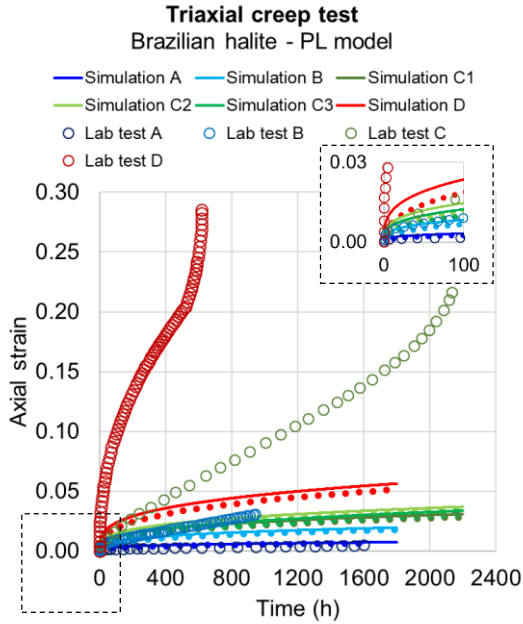
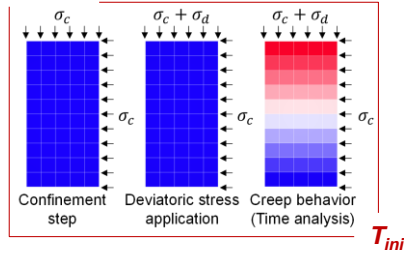
Numerical simulations have been carried out to reproduce the tests as much as possible. The simulations are mechanical and the salt creep behavior is predicted adopting the methodology described in the Section 2.1.1.5. The information about the numerical model given by that section also applies. This procedure is adopted for the four creep constitutive models introduced in Section 2.1.1 (PL, DM, MD, and EDMT) since all of them have been calibrated for the Brazilian halite or have compatible data available. The Brazilian halite properties are summarized in Section 2.5.3. The simulations A, B and D directly correspond to the deviatoric stresses adopted in the laboratory. In test C, the deviatoric stress varied linearly from 16 to 18 MPa over 2,200 hours. The simulations consider this effect in three ways: simulation C1 assumes the initial deviatoric value of 16 MPa applies throughout the test duration; simulation C2 assumes that an average deviatoric stress of 17 MPa applies throughout the test duration; and simulation C3 applies the linear variation in the deviatoric stresses over time. Moreover, all the tests have been carried out at a temperature of 86°C and at a confinement stress of 10 MPa. In the end, the axial strain curves produced by the numerical simulations are compared with the corresponding experimental curves.

With the exception of the recently included test D, these simulations have already been carried out in previous creep model validation efforts by the author using the commercial finite element code Abaqus<sup>TM</sup> and the in-house THM finite element simulator GeoFlux3D (Quevedo et al., 2019; Quevedo, 2012). These past simulations are presented elsewhere (Firme et al., 2018a, 2017, 2016b, 2014b). In this thesis, GeMA has been adopted to perform the simulations. Figure 25 presents the experimental and the numerical results (empty circles and solid lines respectively). The corresponding results using Abaqus<sup>TM</sup> are also plotted as reference (solid dots). Each graph corresponds to one creep constitutive model.

Observing the results using the PL model, Figure 25 (a), the curves have fitted relatively well in most of the experimental results up to 100 hours, but deviated after that time, becoming nearly horizontal. This is expected since the power law often produces fairly good results for transient creep but creep rates tend to become null with time, not predicting adequately the steady-steady creep. The subtle differences between GeMA and Abaqus<sup>TM</sup> results are due to the peculiarities of each time integration algorithm – in the case of the power law, small differences in the time variation may take large proportions because they are raised to a power of 3.



Single stage



— GeMA  
●● Abaqus

Experimental data from  
Costa et al. (2005),  
Poiate Jr. (2012) and  
Poiate Jr. et al. (2006)

Figure 25. Results of triaxial creep tests carried out in Brazilian halite. Simulations considering PL (a), DM (b), MD (c) and EDMT (d) creep constitutive models.

From the results adopting the DM model, Figure 25 (b), good calculations of steady-state creep rate (the curve inclination) are noticed in the simulations of tests A and B. The curves of simulations C1 ( $\sigma_d = 16$  MPa) and C2 ( $\sigma_d = 17$  MPa) have deviated slightly from the experimental curve of the test C. The average creep rate observed in laboratory is between these curves. The curve of simulation C3 ( $16 \leq \sigma_d \leq 18$  MPa) has roughly fitted part of the experimental data. Regarding the simulation of test D, the DM model has calculated a creep rate that approximates the average curve rate up to 500 hours, from when accelerative creep starts. Observing the results obtained with DM model in general, the curves do not match the experimental ones since the formers do not consider the transient creep (there is no curvature in the initial times); however, they do approximate the inclination of the experimental curves.

Analyzing the results adopting the MD model, Figure 25 (c), the transient and the steady-state creep are modelled as shown in the curvature in the initial period followed by a linear trend as time evolves. Very good approximations are observed for test A and B. Regarding test C, the simulation C2 has also shown a very good agreement with experimental data up to about 1,800 hours. The simulation C3 has represented the curvature and provided lower results than the experimental ones. The simulation C1 has underestimated the steady-state creep rate observed in the laboratory. The same has been observed in simulation D. The generally good results obtained with the MD model are expected since the material sensitive parameters have been calibrated for the Brazilian halite using experimental results that, for the most part, corresponded to this stress interval (Firme et al., 2016b).

Lastly, observing the results using the EDMT model, Figure 25 (d), the transient and the steady-state creep have also been modelled. The numerical curves of tests A and B have presented an excellent adjustment to the experimental curves. With respect to test C, simulation C1 has slightly underestimated the experimental curve and simulation C2 has overestimated it. The simulation C3 has represented the curvature and provided results close to the experimental ones up to about 600 hours. Finally, the simulation of test D has shown a good approximation of the corresponding laboratory test.

As general observations, one mentions: i) even the results using DM, MD and EDMT models that have deviated from the experimental results remained within the same order of magnitude; ii) the differences among the results of simulations C1, C2 and C3 using the three constitutive models above are subtle

and reflect the specificities of each model regarding the parameters and the creep phases supported; iii) the stress interval comprised by these simulations (C1-C3) cast an equivalent behavior of the salt in test C; and iv) it seems that the deviatoric stress varying with time (and eventually other experimental circumstances) has influenced the mechanical behavior of the salt sample in a way which is not being considered in the numerical simulations.

In the light of the results, the MD and the EDMT creep constitutive models have stood out for their accuracy in simulating the transient and the steady-state creep phases. As pointed out in Section 2.1.1.4, using the EDMT model for the Brazilian halite – the material which is the object of study of the thesis –, is preferable since the calibrated data for the DM model (which is adopted in the steady-state creep phase of the EDMT model) have proven to be fairly reliable and the addition of the transient function for the calculation of the transient creep has proven to be effective.

#### **4.1.2. Gulf of Mexico halite**

The next group of simulations is the triaxial creep tests to analyze the time-dependent mechanical behavior of the salt from onshore formations of Gulf of Mexico. These tests have been part of an extensive experimental program in the context of the SPR (see Section 3.2.2) (Munson, 1999). Halites from Gulf of Mexico often present high purity levels (Fredrich et al., 2007) and lower mobility than typical Brazilian halites. Among the published experimental data, tests carried out in the West Hackberry and Big Hill salts have been selected by the author due to their similarity with the Brazilian halite in terms of creep behavior (see Figure 5.28 from Poiate Jr. (2012)). More so, these tests allow to analyze the salt creep behavior at room and high temperatures, moderate deviatoric stresses and the effect of changes in temperature and deviatoric stress during the test.

In a previous work, these results have been adopted as validation references for the implementation of the MD model in a subroutine to be run in Abaqus™ (Firme et al., 2016b). In this thesis, the MD model has been implemented in GeMA and these triaxial creep test examples are revisited to validate the code. The numerical models are similar to that presented Section 2.1.1.5; however, the samples are 20 cm high by 10 cm in diameter (Wawersik et al., 1980). Considering the axisymmetry and the symmetry at the half of the sample, the numerical models have 10 cm high by 5 cm in radius. The axisymmetric finite element model has 253

nodes and 72 8-node quadratic elements with reduced integration. The properties adopted for West Hackberry and Big Hill salts are given by Munson (1999) – they are not listed here for the sake of brevity. The test specifications, numerical results and discussions of each salt are presented in the sections below.

#### 4.1.2.1. West Hackberry

Four laboratory tests carried out in West Hackberry salt have been selected as reference for the numerical simulations. In these tests, the deviatoric stresses were all around 20 MPa. Table 15 summarizes the test specifications. Therefore, this variable has been fixed and only the effect of the temperature in the creep behavior has been analysed. Hence, two numerical simulations are performed: simulation WH01-03 considers a room temperature (22°C) and simulation W02-04 considers a relatively high temperature (80°C). The numerical simulations are mechanical and the workflow is the same of that introduced in Section 2.1.1.5.

Table 15. Specifications of triaxial creep tests carried out in West Hackberry salt (Munson, 1999).

Test	Deviatoric stress ( $\sigma_d$ , MPa)	Temperature (°C)	Duration (h)
WH01	20.4	22	475
WH02	20.0	80	263
WH03	20.0	22	262
WH04	19.9	80	72

Figure 26 presents the experimental and the numerical results (empty circles and solid lines respectively). The corresponding results obtained using Abaqus™ (solid dots) from the author and the fitting curves (dashed lines) calculated by Munson (1999) are also plotted as reference. An excellent agreement between the experimental and the numerical results using the MD model has been observed. It not only validates the implementation of MD model in GeMA, but also highlights a good adjustment of this constitutive model to a room and to a relatively high temperature. Furthermore, from the results, the transient creep has proven to be relevant and the temperature has played an important role in the mechanical response. By 320 hours of test, the axial strain of the sample at 80°C is by five times the value of the sample at 22°.

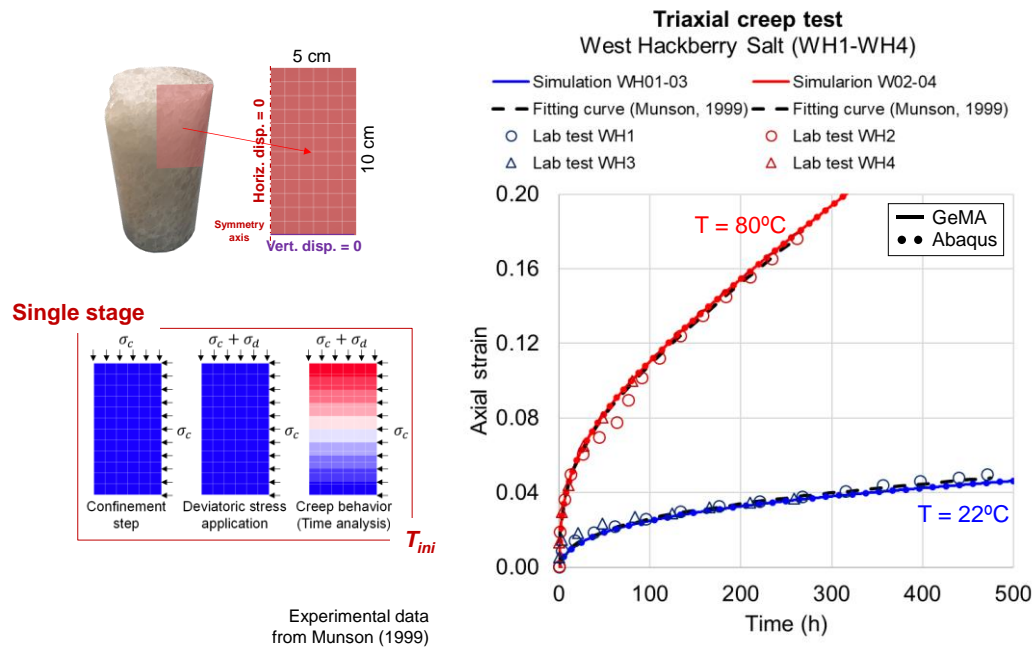


Figure 26. Results of triaxial creep tests carried out in West Hackberry salt.

#### 4.1.2.2. Big Hill

A multistage test carried out in Big Hill salt has also been considered. In this test, there are four stages during which the deviatoric stress and the temperature vary. The variation in the deviatoric stresses is very subtle in the first three stages (from 14.9 to 15.1 MPa) and more significant in the last (from 15.1 to 17.9 MPa). With respect to temperature, the initial value is 60°C. Then, temperature increases of 20°C in the end of the first stage and decreases of 20°C in the end of the second stage. From the third stage on, the temperature remains constant. Table 16 summarizes the test specifications.

Table 16. Specifications of the multi-stage triaxial creep test carried out in Big Hill salt (BH01).

Stage	Deviatoric stress ( $\sigma_d$ , MPa)	Temperature (°C)	Duration (h)
1	14.9	60	370
2	15.0	80	70
3	15.1	60	934
4	17.9	60	243

The numerical simulation is mechanical and the thermal expansion or contraction is considered when there is a temperature variation in the model. Note that this simulation does not represent a full thermomechanical coupling since temperature variation is homogenous, applied to all the nodes of the mesh (there

is no thermal conduction). Moreover, the temperature changes are also accounted for in the equations of the MD model (see Section 2.1.1.3). Each test stage follows the workflow presented in Section 2.1.1.5).

Figure 27 (a) shows the evolution of the deviatoric stress, temperature (as indicated in Table 16) and thermal strain caused by warming and cooling the sample over time. In addition, Figure 27 (b) shows the experimental and numerical results (empty circles and solid lines respectively). Just like the previous example, the corresponding results obtained using Abaqus™ (solid dots) from the author and the fitting curves (dashed lines) calculated by Munson (1999) are also plotted as reference. A very good agreement between the experimental and the numerical curves using the MD model have been observed almost up to the end of the third stage. After that, both the numerical curves and the curve fitted by Munson (1999) subtly underestimate the axial strains.

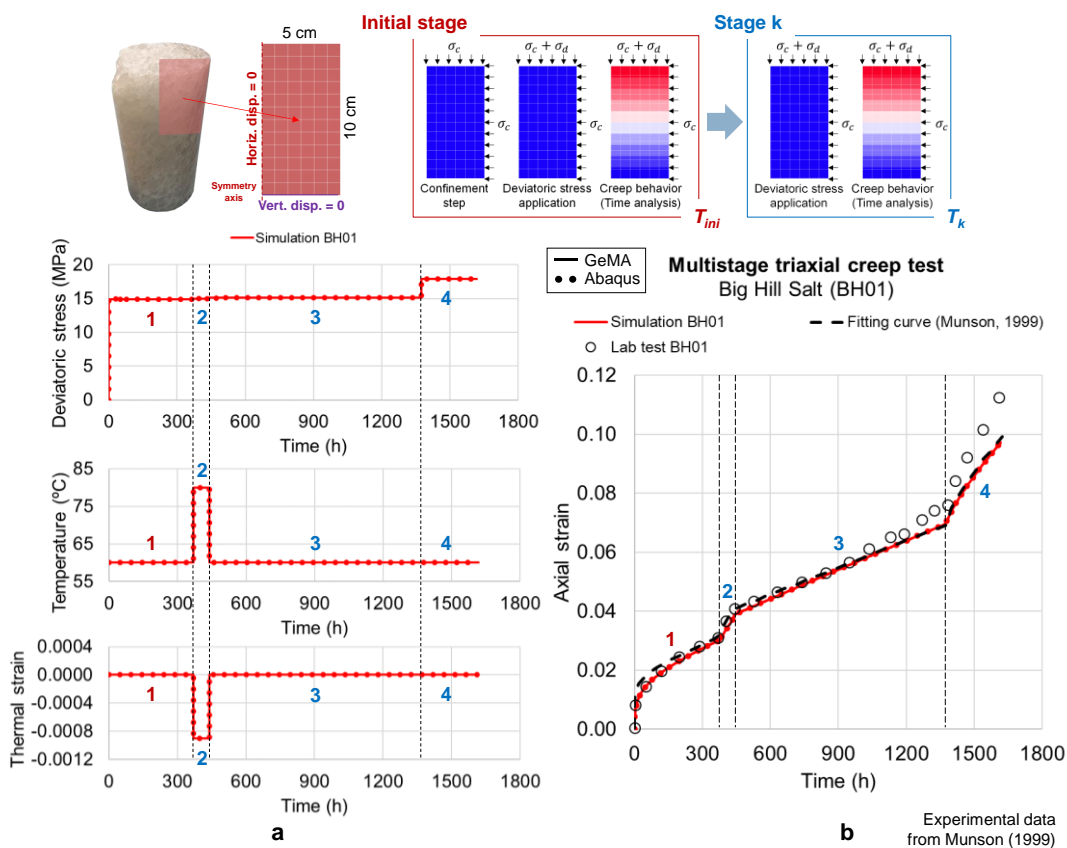


Figure 27. Results of a multistage triaxial creep test carried out in Big Hill salt.

To better analyze the effect of the temperature changes in the mechanical response of the sample, an additional analysis considering only the effect of the temperature change in the creep model and neglecting the instantaneous thermal expansion/contraction of the sample has been performed – this simulation is

indicated by “No TS”. The comparison between the results is shown in Figure 28. It can be observed that the instantaneous thermal strains are of small magnitude and are fully recovered when the initial temperature of the sample is restored (see the thermal strains before 370 hours and after 440 hours) – this is conceptually expected considering the thermoelasticity. The sample expansion and contraction due to warming and cooling are also indicated. When analyzing the complete creep curve, the results including or not the thermal strains are almost the same (provided that the temperature changes are considered in the creep constitutive model).

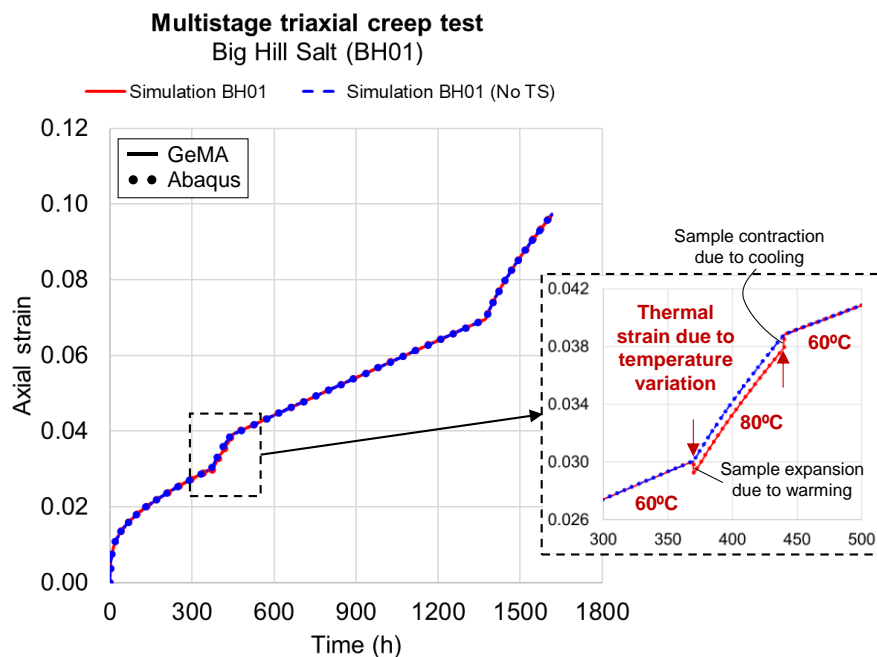


Figure 28. Results of a multistage triaxial creep test carried out in Big Hill salt – thermal strain contribution.

#### 4.2. Hydrostatic compaction test

A hydrostatic compaction test from the literature carried out in a Rothbach sandstone sample (from Eastern France) has been simulated to check the implementation of the hydromechanical correlations from Section 2.3 in the finite element workflow adopted in GeMA. Although this application does not involve salt, the correlations to be checked are adopted in the thesis to analyze the repercussion of the mechanical/thermomechanical response on the hydraulic behavior of salt (the TM+H approach, see Section 2.5.1).

To this end, a numerical model similar to that presented Section 2.1.1.5 is adopted. In this case, the samples are 38.1 mm high by 18.4 mm in diameter (David et al., 2001). Taking advantage of the axisymmetry and the symmetry at the

half of the sample, the numerical models have 19.05 mm high by 9.2 mm in radius. The axisymmetric finite element model has 253 nodes and 72 8-node quadratic elements with reduced integration. Typical sandstone elastic properties are adopted (see Section 2.5.3). Those authors present experimental results which are adopted as validation reference for the numerical solutions obtained with GeMA. As an additional check, the changes in permeability caused by the changes in mean effective stress and porosity are directly calculated (apart from the code) considering mean stresses and volumetric strains known in advance.

Regarding the simulation workflow, a hydrostatic compression is applied to the numerical model in order to simulate the mean effective stress changes in the interval where the hydromechanical correlations are defined. For each time increment, the porosity is calculated based on the volumetric strain increment using equation (29) and the porosity-dependent permeability is calculated using equation (28). In parallel, the mean stress-dependent permeability is calculated based on the mean effective stress increment using equation (30). This sandstone exhibits a porosity by 23%, being considered as a high porosity rock. According to David et al. (2001), the empirical power  $\chi$  in the porosity-permeability correlation ranges from 1 to 25, in which the higher values correspond to the high porosity rocks. More so, the empirical parameter  $\omega$  in the mean stress-permeability correlation ranges from 0.001 to 0.020 MPa<sup>-1</sup> for high porosity and granular rocks.

Figure 29 (a) presents the results of the porosity-permeability correlation using GeMA (solid lines) and the directly calculated values (solid dots). A good agreement with experimental data (empty dots) is noticed when adopting  $\chi$  equals to 25 – the value indicated for high porosity rocks. The dashed lines limit the interval where the hydromechanical correlations have been calibrated. If the minimum value of  $\chi$  (indicated for low porosity rocks) were adopted, the changes in the permeability would be smaller, as conceptually expected. Next, Figure 29 (b) presents the corresponding results of the mean stress-permeability correlation. A very good agreement with experimental data is also observed when adopting  $\omega$  equals to 0.020 MPa<sup>-1</sup> – the maximum value indicated for high porosity rocks. If the minimum value for high porosity rocks were adopted (0.001 MPa<sup>-1</sup>), the changes in the permeability would also be smaller. The results have indicated a significant sensitivity to the empirical parameters adopted in the correlations. Thus, an adequate association between the type of rock and the empirical parameters that best represent it qualitatively is essential.

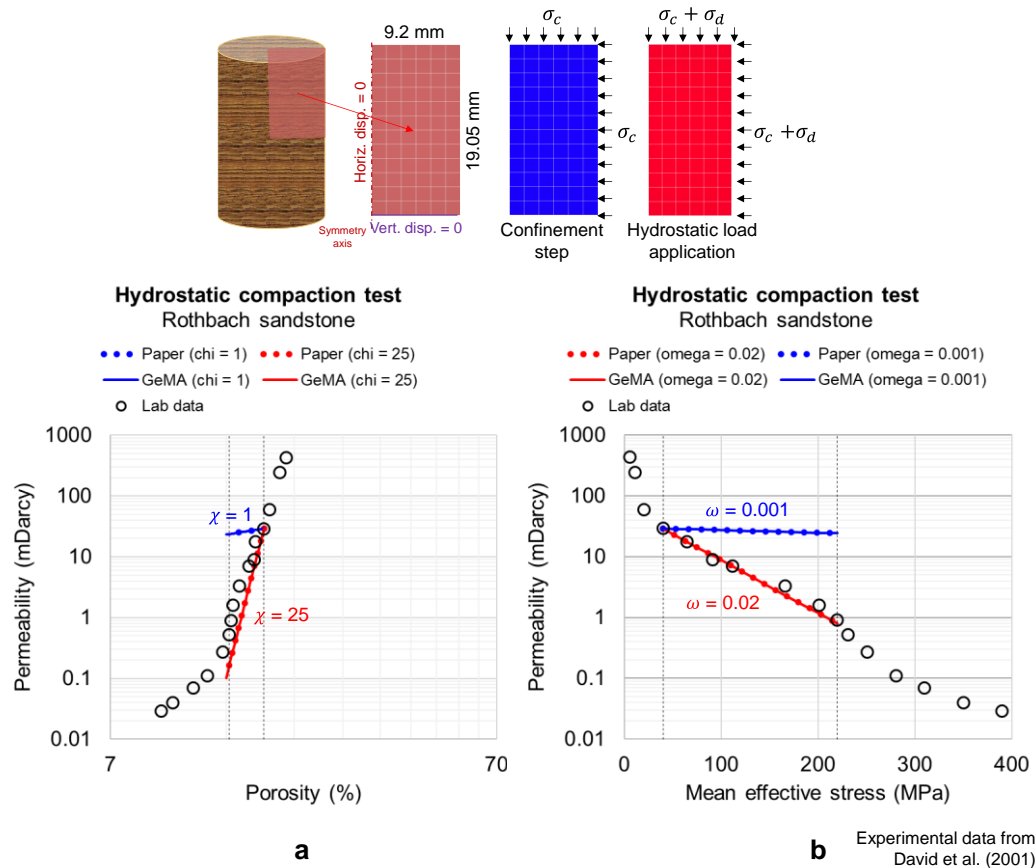


Figure 29. Results of a hydrostatic compaction test carried out in Rothbach sandstone – porosity-dependent permeability (a) and mean stress-dependent permeability (b).

Based on the results of the simulation of this hydrostatic compaction test and the comparison with experimental data, it is considered that the hydromechanical correlations implemented in GeMA are working properly and therefore can be used in the TM+H approach for salt rocks.

#### 4.3. Brazilian mine gallery

The Taquari-Vassouras potash mine is a panel-gallery mine located in the state of Sergipe (Brazil). The lithology of the mine is challenging and the ore extraction activities need to deal with a highly mobile salt layer, tachyhydrite, that underlays the mine floor in a very large extension. The mining challenges in this site have encouraged a large-scale rock mechanics program whose contribution to the Brazilian salt geomechanics extends to the present day (Costa, 1984). In this context, an isolated gallery of the mine where the host formation is halite-dominant is analyzed. Measurements of vertical convergence<sup>47</sup> of this gallery over

<sup>47</sup> In this context, the vertical convergence corresponds to the difference between the vertical displacements of the gallery floor and roof. Likewise, the horizontal convergence refers to the difference between the horizontal displacements at half-height of cavern right and left walls.

about 6 years are presented in the work of D'Élia (1991). These measurements were collected in five sections of the gallery – four of them present similar trends, representing a reliable validation reference.

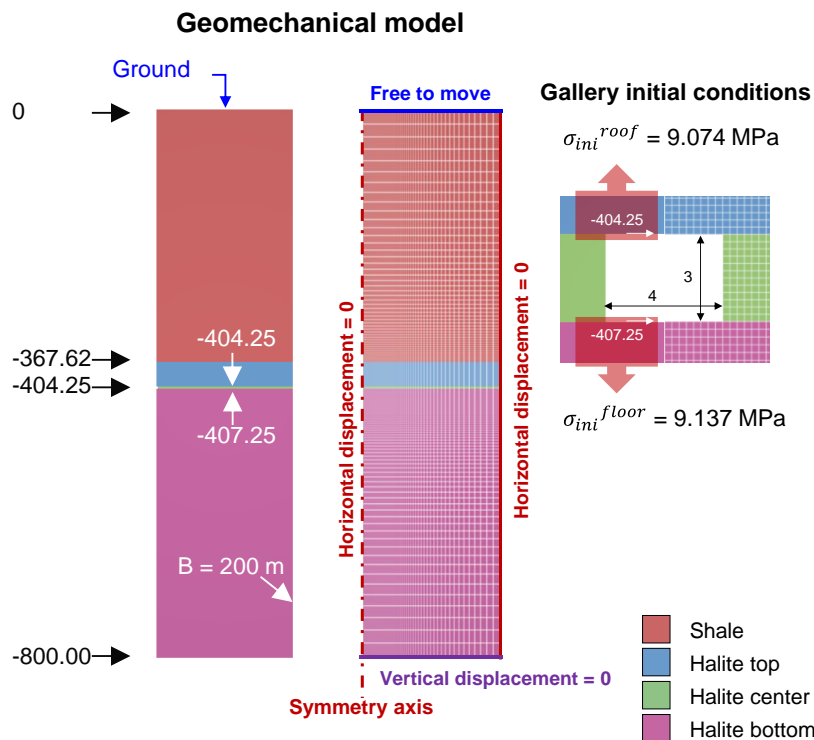


Figure 30. 2D plane strain finite element model of the Brazilian mining gallery. Elevations and dimensions in meters.

The objective of this example is to simulate the vertical convergence of the mine using the four creep constitutive models introduced in Section 2.1.1 (PL, DM, MD, and EDMT). The lithology adopted in the gallery model is a simplified version of the original one presented by Costa (1984). It comprises a sedimentary package from the ground level (0) to the elevation -367.62 m and a thick halite-dominant formation from this elevation on. This formation is assumed to be homogenous for the purpose of the application. The gallery section is 4.0 m wide by 3.0 m high (D'Élia, 1991) and its roof elevation is -404.25 m. The geomechanical model considers a 2D longitudinal plane strain state and takes advantage of the symmetry. The finite element mesh is composed by 8-node quadratic elements with reduced integration (elements type "Q8"). The lateral and bottom limits are far enough from the gallery to avoid spurious boundary effects. Figure 30 shows the geomechanical model, the finite element mesh and the main attributes.

The simulation of this mining gallery has already been carried by the author out in previous validation efforts of creep models using Abaqus™ (Firme, 2013; Firme et al., 2016b, 2018a). In this thesis, the GeMA framework has been adopted.

The salt creep behavior is predicted by adopting a simplified form of the methodology described in Section 2.5.1. The analyses are mechanical and the temperature field is assumed constant over the simulation time. Therefore, only the time-dependent (creep) mechanical problem needs to be solved. Besides that, considering the purpose of validating displacement-based results, the repercussion of the mechanical behavior on the hydraulic behavior of salt is not calculated. The sedimentary rocks above the salt formation follow an elastoplastic behavior according to the Mohr-Coulomb criterion with non-associative flow rule. Typical shale properties are adopted. The rock properties adopted in each constitutive model are summarized in Section 2.5.3.

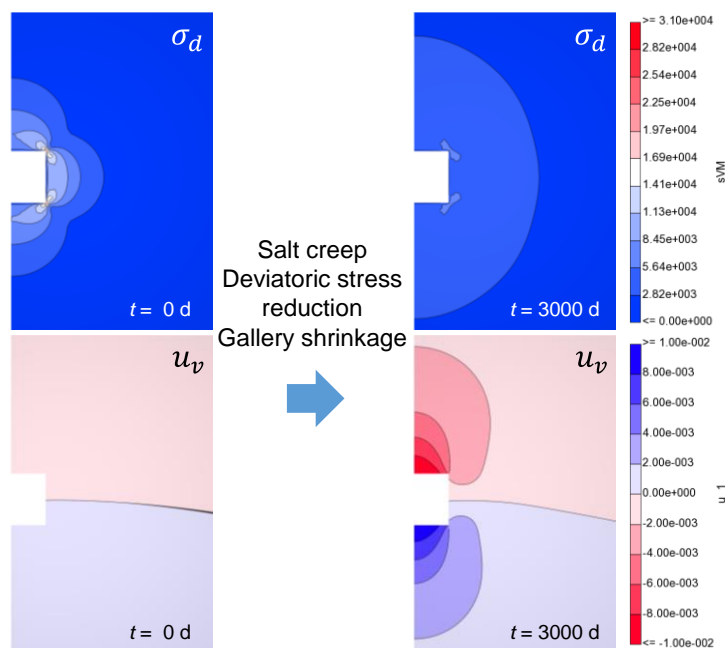


Figure 31. Contours maps of deviatoric stress ( $\sigma_d$ ) and vertical displacements ( $u_v$ ) in the Brazilian mining gallery surroundings.

The initial (geostatic) stresses are assumed isotropic and are assigned by the superposition of the gravitational loads. Figure 30 also indicates the vertical stress values at cavern roof and floor. The temperature is assumed constant of 43°C, which is the average temperature in the mine. In a similar way to the simulation of the triaxial creep tests, the simulation of the mine convergence is composed of three steps. In the first step, the initial stresses are assigned ensuring that the model initializes with null deformations. In the second step, the gallery corresponding elements are removed simulating the excavation process. It generates deviatoric stresses in the surroundings, provoking an instantaneous elastic response. In the third step, the model follows relieving deviatoric stresses by creep during the simulation time. As a consequence, the gallery shrinks over

time due to creep deformation, Figure 31. The displacement field is monitored over time in order to calculate the vertical convergence of the gallery.

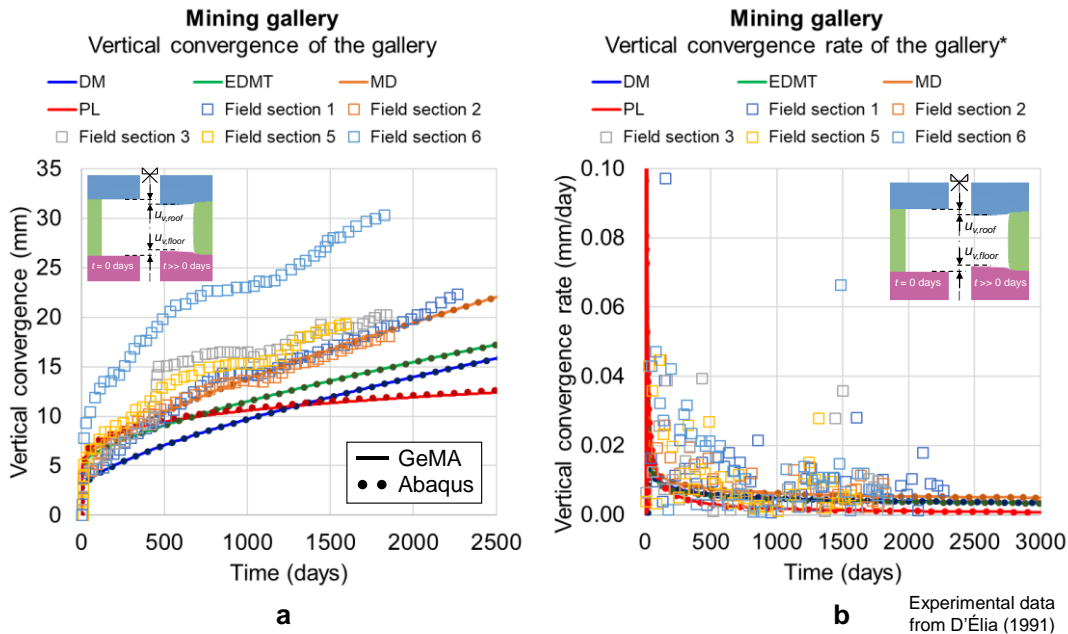


Figure 32. Vertical convergence (a) and vertical convergence rate (b) of the Brazilian mining gallery. Convergence measurements from D'Élia (1991).

Figure 32 shows the field and the numerical vertical convergence of the gallery (empty squares and solid lines respectively). The corresponding results obtained using Abaqus<sup>TM</sup> (solid dots) are also presented as reference. The convergence absolute values are presented in Figure 32 (a) and the convergence rates are shown in Figure 32 (b). Just like the triaxial creep test in Section 2.1.1.5, the author of the thesis has calculated the convergence rates ( $\dot{u}_v$ ) based on the convergence measurements ( $u_v$ ). The scattered rate points in the graph may be related to the discrete time differentiation ( $\dot{u}_v = \partial u_v / \partial t \approx \Delta u_v / \Delta t$ ). The displacements right after the excavation are not known since the instruments for measurement of convergence have been installed after the excavation. In numerical models, these displacements result from the instantaneous elastic deformation after removing the elements in the excavated region. Consequently, a more significant deviation between the numerical and experimental results is expected in the initial part of the curves. Hence, the main criterion for checking the results is the rate values. Analyzing the results of the two constitutive models that consider transient and steady-state creep (MD and EDTM), the solution using the MD model (orange curves) has fitted the field measurements very well, while the results using the EDTM model (green curves) have deviated from field data after about 400 days. This difference can be explained by the fact that, although the

EDMT model follows a well-established database for the steady-state creep phase, data have been calibrated considering triaxial tests carried out at 86°C, and the average temperature of the gallery is 43°C. The adjustment of the parameters to the temperature of the engineering problem by means of a thermal activation factor (see equation (8)) has influenced the results, leading to steady-state creep rates slightly lower than those observed in the field. The results using the DM model (blue curves) have remained below the field measurements. This shows that the contribution of the transient creep, which is not considered by this model, is relevant in the context of the mining gallery convergence. Over time, the convergence rate obtained with this model has become the same as that using the EDMT model since both have the same formulation for the steady-state creep rate. Lastly, the results obtained using the PL model (red curves) also have remained below the field measurements. Different from the DM model, transient creep has been adequately simulated (until 400 days). However, the convergence has horizontalized with time, not simulating adequately the steady-state creep rate.

Considering the results in addition to the partial conclusions indicated in Section 4.1.1, the EDMT model using the current parameter set (see Table 6) presents a good performance in simulating the creep behavior of the Brazilian halite. Since many engineering applications in Pre-salt wells exhibit temperatures in the order of 70°C – closer to temperature of the laboratory tests (86°C) –, the differences observed in the vertical convergence of the gallery at 43°C do not undermine the good representativeness of this model.

#### **4.4. Pre-salt well closure**

##### **4.4.1. Isothermal Pre-salt well**

A realistic application of an offshore Pre-salt well is revisited to validate the creep constitutive models and the workflow in GeMA for well closure simulations. Historically, the well represented in this simulation was successfully drilled in 1997. It combined a modern drilling technology with sophisticated computational modelling to predict the creep behavior in the salt interval (Falcão, 2009). The salt interval of this well, hereinafter “Brazilian Pre-salt well”, has been studied by Medeiros (1999). Besides the numerical simulations, this author has presented caliper logs run after drilling and 10 hours later. The well closure between these two instants is taken as a field validation reference.

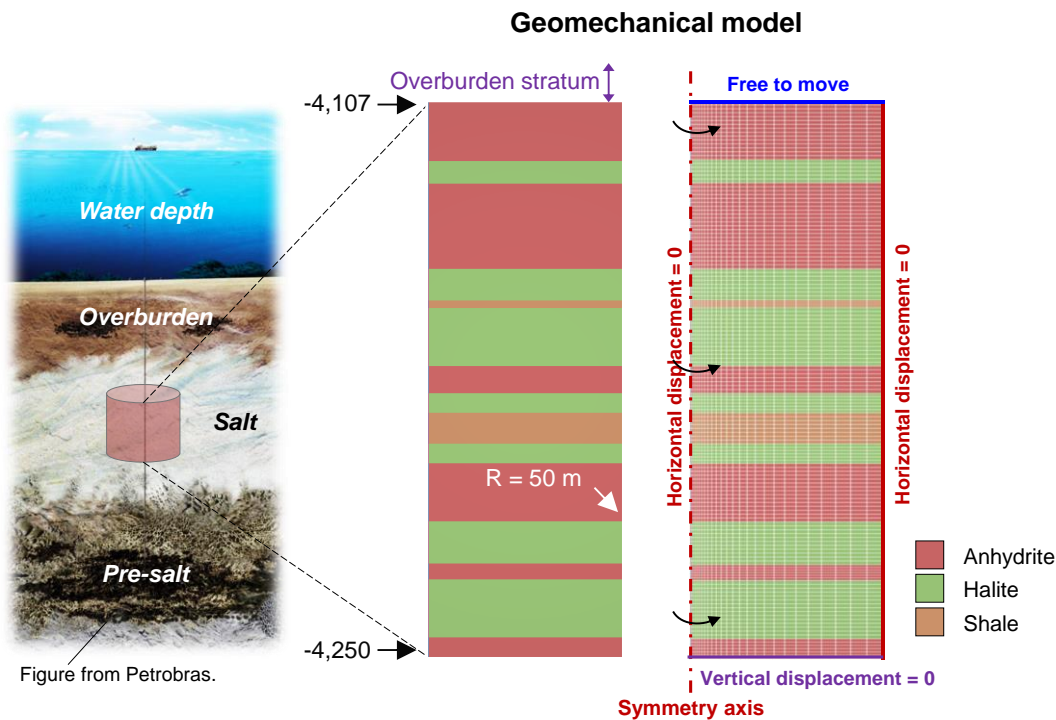


Figure 33. Axisymmetric finite element model of the Brazilian Pre-salt well. Elevations and dimensions in meters.

The Brazilian Pre-salt well develops between the elevations -4,107 m and -4,250 m (from the sea level) and crosses an interval made up by intercalations of halite and anhydrite or shale. A water depth of 345 m and a sedimentary stratum that develops from the seafloor to the salt top are assumed. In this interval, the well nominal diameter is of 12.25 inches (0.31115 m) and is drilled using a mud weight of 14.3 ppg (16.8025 kN/m<sup>3</sup>). The geomechanical model is axisymmetric. The finite element mesh is composed by 8-node quadratic elements with full integration (type “Q8”). The lateral and bottom limits are far enough from the well to avoid spurious boundary effects. Figure 33 presents the geomechanical model, the finite element mesh and the main attributes.

The simulation of this Pre-salt well has already been carried out by the author in previous validation efforts of creep models using Abaqus™ (Firme, 2013; Firme et al., 2018a, 2016b, 2014b). Here, the GeMA framework has been adopted. Just like the mining gallery examples, the salt creep behavior is predicted adopting a simplified form of the methodology described in Section 2.5.1. The analyses are mechanical and the temperature field is known. Although in this case the temperature varies with depth, the values are constant over the simulation time so that only the time-dependent mechanical problem needs to be solved. Considering the purpose of validating the displacement-based results, the repercussion of the

mechanical response on the hydraulic behavior of salt has not been calculated. The non-salt rocks (anhydrite and shale) follow an elastoplastic behavior according to the Mohr-Coulomb criterion with non-associative flow rule. The properties adopted in each constitutive model are summarized in Section 2.5.3.

The initial (geostatic) stresses are assumed isotropic and are assigned by the superposition of the gravitational loads. The temperature estimation follows assuming the temperature of 4°C in the seafloor and adopting the geothermal gradients of 30°C/km in the sedimentary stratum (between the seafloor and the model top) and 12°C/km in the salt interval (Costa et al., 2015, 2012). For the sake of reference, the calculated temperature in the model bottom (elevation -4,250 m) by using these geothermal gradients is of 118.576°C, and according to Medeiros (1999) the temperature provided by well logging at the elevation -4,307 m is of 390K ( $\approx 117$  °C). Analogously to the mining gallery examples, the well closure simulation is composed of three steps. In the first step, the initial stresses and temperatures are assigned ensuring that the model initializes with null deformations. In the second step, the well (borehole) corresponding elements are removed simulating the drilling process. The mud pressure calculated from the drilling mud weight is applied upon the well wall. This unbalances the well surroundings, provoking an instantaneous elastic response. In the third step, the model follows relieving deviatoric stresses by creep during the simulation time. As a consequence, the well closes over time due to creep deformation. A simulation time of 720 hours (30 days) is considered.

Firstly, the results using GeMA (solid lines) after 10 hours are compared with caliper data (gray thin solid line), as shown in Figure 34. The corresponding results obtained using Abaqus™ (solid dots) are also presented as reference. In this part of the study, the four constitutive models introduced in Section 2.1.1 (PL, DM, MD, and EDMT) are considered. In order to isolate the creep contribution, it has been assumed that creep is the unique relevant mechanism for well closure during the caliper logs run after drilling and 10 hours later (available in the work of Medeiros (1999)). Therefore, the differences between these two measurements have to be considered rather than the absolute values. To this end, the author of the thesis has post-processed the field data to reflect the well closure by creep alone in Figure 34. Similarly, the numerical results consider only the creep-related displacements, i.e., the instantaneous elastic response after well drilling has been subtracted. The results using the PL model are a bit overestimated, while those using the DM model are underestimated. The latter case is explained by the fact that DM model does

not simulate adequately the transient phase of creep, and the short period considered (10 hours) falls into this phase. On the other hand, the PL model using the parameter set for the Brazilian halite has oversized the transient creep displacements. Comparing the numerical results of MD and EDTM models with the caliper log, a good agreement at most halite layers is observed. As previously noticed, the EDTM model using the consolidated parameter set (see Section 2.5.3) present a good numerical prediction of the Brazilian halite creep. As general observations, the caliper logs in the anhydrite and shale layers have exhibited more deviation in relation to the numerical results – the transitions with salt (representing the great difference in mobility) may be less severe in field –, and the order of magnitude of the well closure is fairly kept regardless the creep model adopted

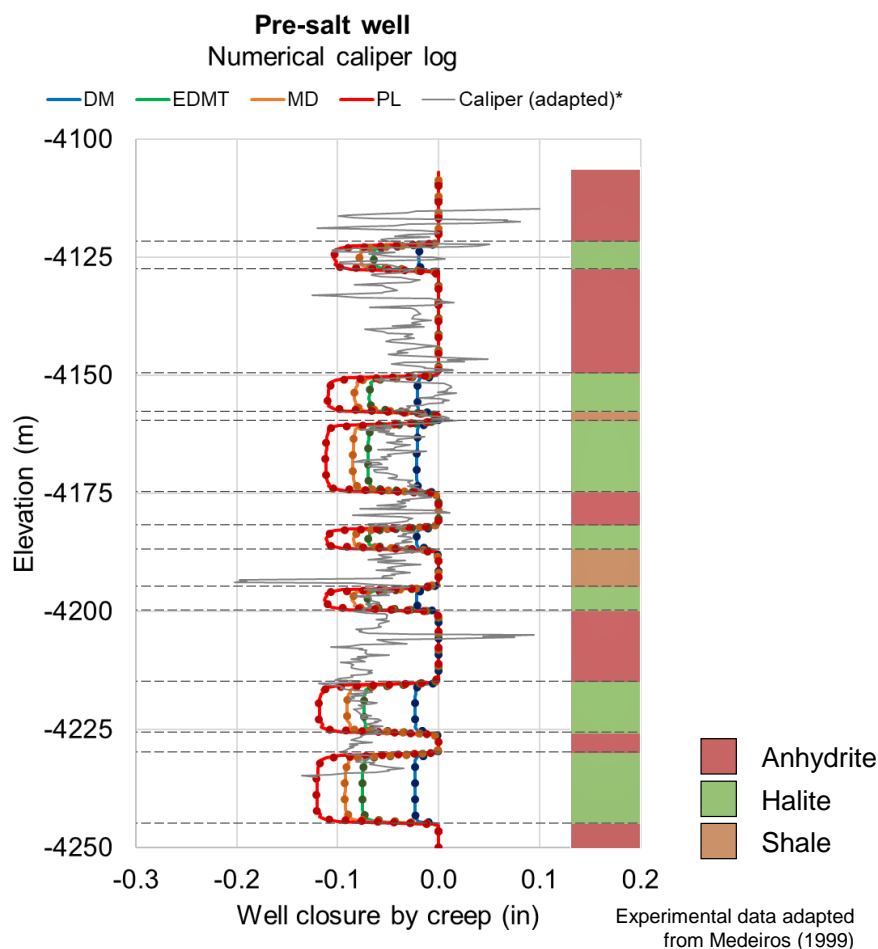


Figure 34. Validation of the numerical simulations carried out in the Brazilian Pre-salt well. The caliper logs presented by Medeiros (1999) have been post-processed by the author of the thesis to reflect the well closure by creep between 0 and 10 hours after well drilling.

Next, Figure 35 presents the contour maps of horizontal displacements and strength indicator (ratio) after 10 hours considering the EDTM creep model. The partial closure of the well by creep is visible in Figure 35 (a), although there is an exaggeration factor in the contour map. While this behavior can be problematic

during drilling and can lead to stuck pipe events, it can also be advantageous to close an abandoned well by forming a geological barrier. It would avoid long-term problems in the rock-cement interaction in the case of using conventional cement plugs (see Section 3.1.3.2). Figure 35 (b) shows the strength indicator after 10 hours of well closure by creep. This parameter is given by the ratio between the deviatoric stress of the problem and the critical deviatoric stress for dilation considering DeVries' dilatancy boundary in the case of salt (see Section 2.1.2.4) or the critical deviatoric stress for shear failure considering the Mohr-Coulomb criterion in non-salt rocks (see Section 2.5.2). Ratio values between zero and one are admissible – zero represents null deviatoric stresses and one means the material reached the dilation or plasticity envelope, with the qualitative meaning that the material undergoes plastic deformation or damage.

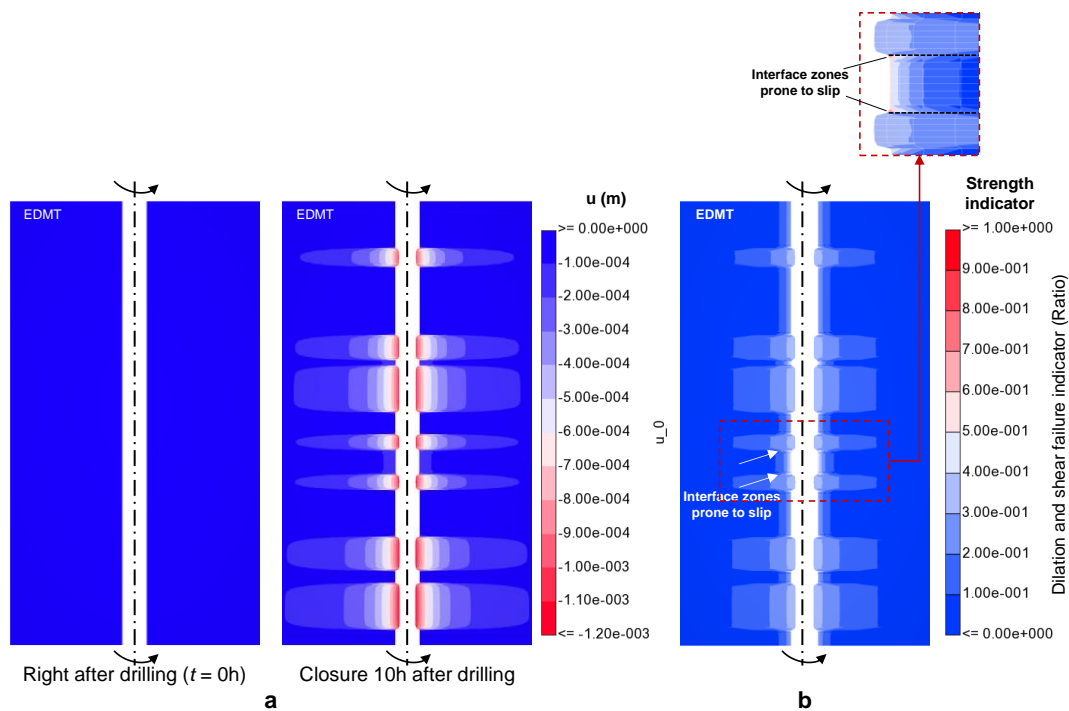


Figure 35. Contour maps of horizontal displacements and the strength indicator (ratio) after 10 hours of simulation in the Brazilian Pre-salt well.

From Figure 35, it can also be seen that the interfaces between salt and non-salt rocks are subjected to shear provoked by the opposition of the non-salt rocks (elastoplastic) to the creep deformation of the neighboring salt rocks. In the limit of shear strength, interlayer slippage may occur due to shear-induced failure causing in turn fluid leakage.

Continuing the numerical simulation up to 30 days, Figure 36 (a) shows the well diameter evolution after drilling ( $t = 0$ ), after 10 hours and after 30 days. As a practical application of casing project, two nominal outer diameters are considered:

9 7/8 inches and 9 5/8 inches. In this context, a minimum cement sheath of 1.5 inches in diameter is required. Therefore, considering the well diameter of 12.25 inches, the minimum admissible well diameter to run the casing of 9 7/8 inches is 11.375 inches, or 11.125 inches to run the casing of 9 5/8 inches. Analyzing the displacement results, it can be seen that even after 30 days in openhole, the well diameter is still adequate to run both casings ensuring an adequate cement sheath thickness.

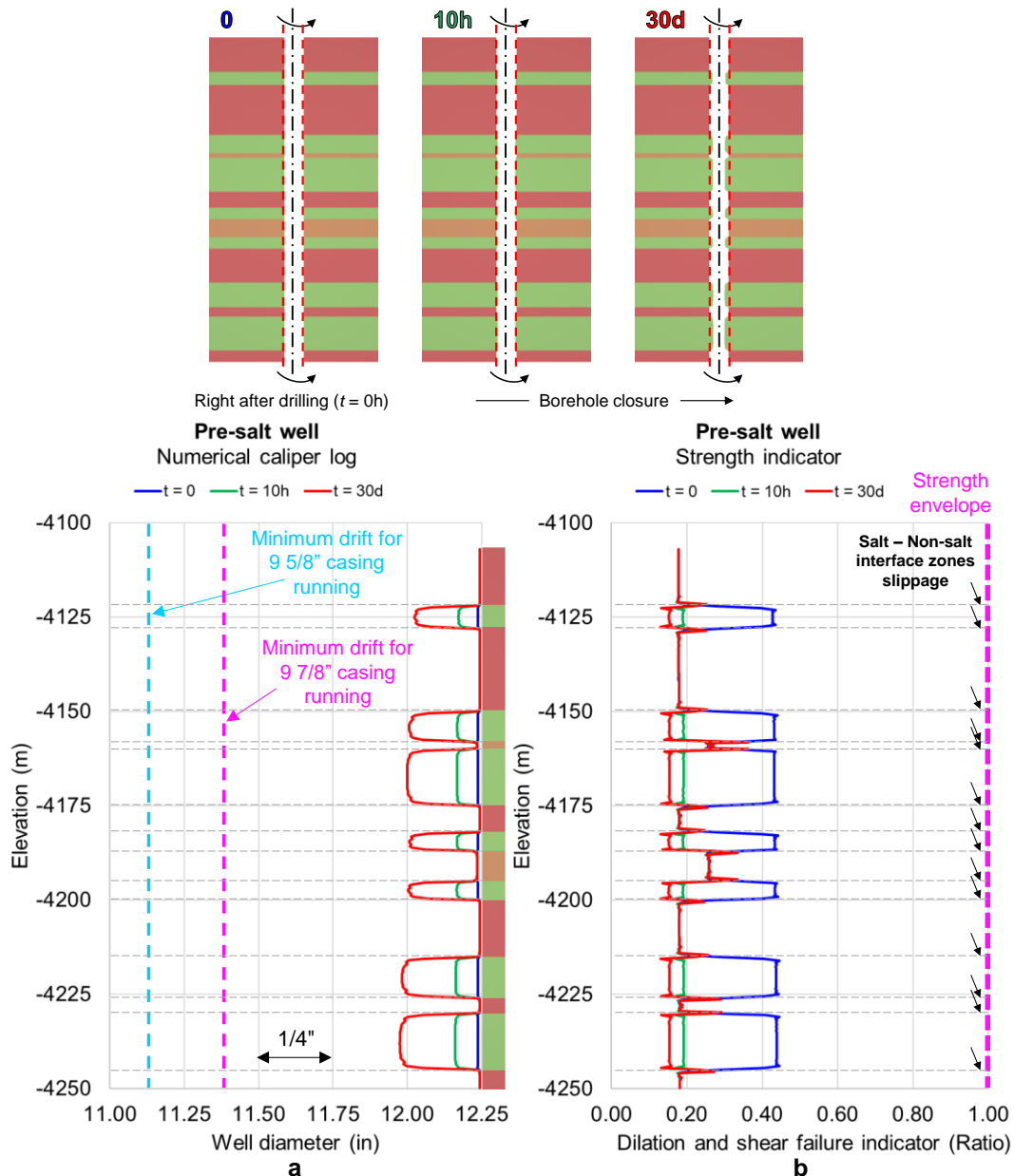


Figure 36. Well diameter (a) and the strength indicator (b) evolution over 30 days of simulation in the Brazilian Pre-salt well.

Regarding rock integrity, Figure 36 (b) calls attention to the salt and to the interfaces. While the dilation indicator in the salt tends to reduce over time due to

the creep deformation, the opposite occurs in the interfaces with non-salt rocks – as salt creeps, shear stresses increase in the interfaces. Hence, a good cementing job of these intervals ensuring the appropriate hydraulic isolation of the well is essential.

#### **4.4.2. Thermomechanical Pre-salt well**

Conceptual models of Pre-salt wells subjected to changes in the temperature (cooling) are considered to check the workflow for coupled thermomechanical creep analyses in GeMA. These models have been originally presented by Gonçalves (2011) and Lira et al. (2015). They have analyzed the effect of using a drilling fluid cooler than the formation on well closure by creep. The simulations have been carried out in axisymmetric models and using an in-house solver. Halite and tachyhydrite<sup>48</sup> homogenous intervals and a halite-tachyhydrite-halite intercalation are considered.

In addition to the axisymmetric model such as the original references of this study, this thesis also analyzes the corresponding 2D plane strain and 3D models. The models are divided into three groups, namely A1 (homogeneous halite), B3 (homogeneous tachyhydrite) and C3 (halite-tachyhydrite-halite intercalation)<sup>49</sup>. The details related to the geomechanical models are given in each corresponding section. In all cases, the salt creep behavior is predicted using the DM model (see Section 2.1.1.2) and adopting the methodology described in Section 2.5.1, except the repercussion on the hydraulic behavior which is not analyzed. The salt properties are provided in the references cited above. Although these values are very similar to those from Section 2.5.3, the formers are adopted here so that the results of this application are compatible with those of the original references.

The initial (geostatic) stresses are assumed isotropic and are calculated by the superposition of the gravitational loads. The temperature estimation is based on geothermal gradients – the same values of the previous example apply (see Section 4.4.1), except in the salt interval, for which a value of 10°C/km is adopted. The simulation workflow is composed of three steps. In the first step, the initial stresses and temperatures are assigned ensuring that the model initializes with null deformations. In the second step, the well corresponding elements are

---

<sup>48</sup> Tachyhydrite exhibits much higher creep rates than halite.

<sup>49</sup> To ease the comparison of results, the nomenclatures of the models presented by the authors of the original study have been kept.

removed simulating the drilling process. The mud pressure calculated from the drilling mud weight and the temperature resulting from the cooling effect are applied upon the well wall and in the wall nodes respectively. This unbalances the well surroundings, provoking an instantaneous thermoelastic response. In the original references of the study, several temperature variations have been analyzed. Considering the purpose of this application here, only the maximum and the intermediate well cooling are adopted (-29°C and -14°C respectively). An isothermal scenario (null cooling) is also considered, in which the thermomechanical problem turns into a mechanical problem. In the third step, the model follows relieving deviatoric stresses by creep during the simulation time and the temperature changes evolve throughout the formation by thermal conduction. The well closes over time due to creep deformation. A simulation time of 720 hours (30 days) is considered in this thesis, although the comparison with the references is made until 480 hours (20 days). Both times are generally representative of the period during which the well stays uncased after drilling.

Lastly, all the results using GeMA, are compared to those of axisymmetric models from the original references of the study (Gonçalves, 2011; Lira et al., 2015) – these results are hereinafter called “reference solution”. The 2D models correspond to the elevation where the results are collected in the axisymmetric and 3D models (at point P, in the half-height of the interval). In parallel, the axisymmetric, 2D plane strain and 3D analyzes have also been carried out in Abaqus™ in order to have one more reference to verify the solution of the coupled thermomechanical problem in GeMA.

#### **4.4.2.1.**

##### **Well models considering homogenous halite (A1)**

The first group of models is the A1, which is a 100 meter-length halite interval between the elevations -1,750 m and -1,850 m (from the sea level). In this synthetic site, the water depth is of 750 m. The tops of the formation and salt interval coincide. The well nominal diameter is 12.25 inches (0.31115 m) and the drilling mud weight is 10 ppg (11.75 kN/m<sup>3</sup>). An axisymmetric model and a 2D transversal plane strain model crossing the well at elevation -1,800 m are considered. The meshes are composed by axisymmetric and 2D 8-node quadratic elements with reduced integration (type “Q8”) respectively. The elements have displacement and temperature as degrees of freedom – quadratic and linear functions interpolate the former and the latter fields respectively. The lateral and bottom limits are far

enough from the well to avoid spurious boundary effects. Figure 37 shows the geomechanical models, the finite element meshes and the main attributes.

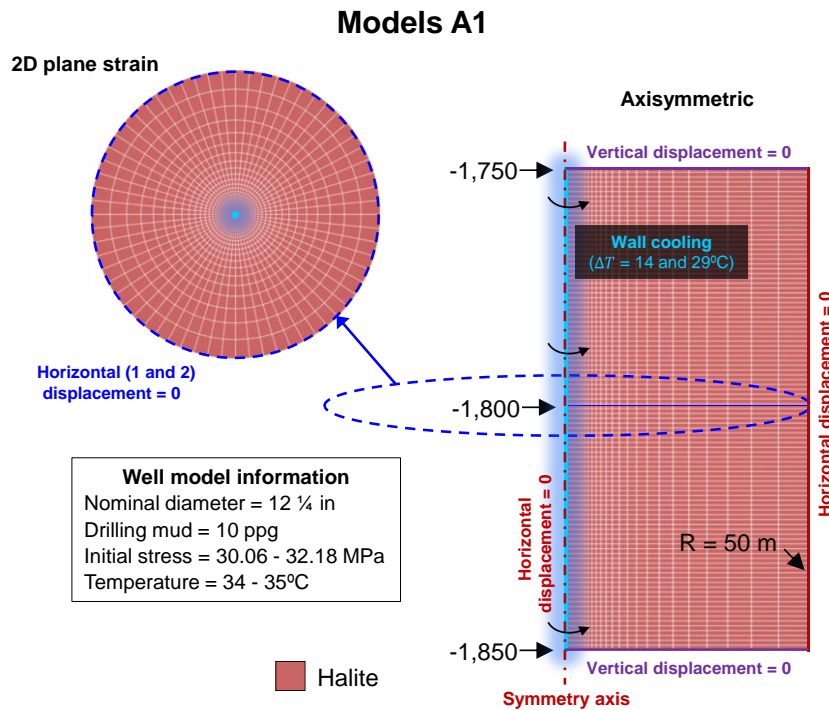


Figure 37. Axisymmetric and 2D plane strain models A1. Elevations and dimensions in meters.

Figure 38 presents the results of models A1 using GeMA (solid lines) compared to the reference solutions (dashed lines). The corresponding results using Abaqus™ (solid dots) are also plotted as reference. Both the axisymmetric (Figure 38 (a)) and 2D plane strain (Figure 38 (b)) simulations have presented a very good agreement with the reference solutions for the three temperature cases. Small differences in displacements would be more noticeable in the results of halite (lower displacement scale) than those of tachyhydrite for example – this indicates that the accuracy of the solutions obtained in halite is high. Analyzing the behavior of the well after the instantaneous thermoelastic response to drilling, the creep deformation effect is notorious and tends to close the well when it is not cooled ( $\Delta T = 0$ , isothermal condition). When the intermediate cooling ( $\Delta T = (-) 14^\circ\text{C}$ ) is applied, the creep behavior is attenuated quite significantly, although the displacements still tend to close the well. Finally, when a noticeable cooling ( $\Delta T = (-) 29^\circ\text{C}$ ) is applied, the creep deformation is also notorious but the trend is inverted, tending to open the well over time. In the light of these observations, the cooling plays a significant role in attenuating salt creep. Besides the cooling effect, the inversion trend (from well closure to opening) is also a consequence of dealing with a relatively shallow

well. If the well were deeper, the cooling would attenuate creep but the trend would be to close the well in all cases (see Figure 5.5 from Gonçalves (2011)).

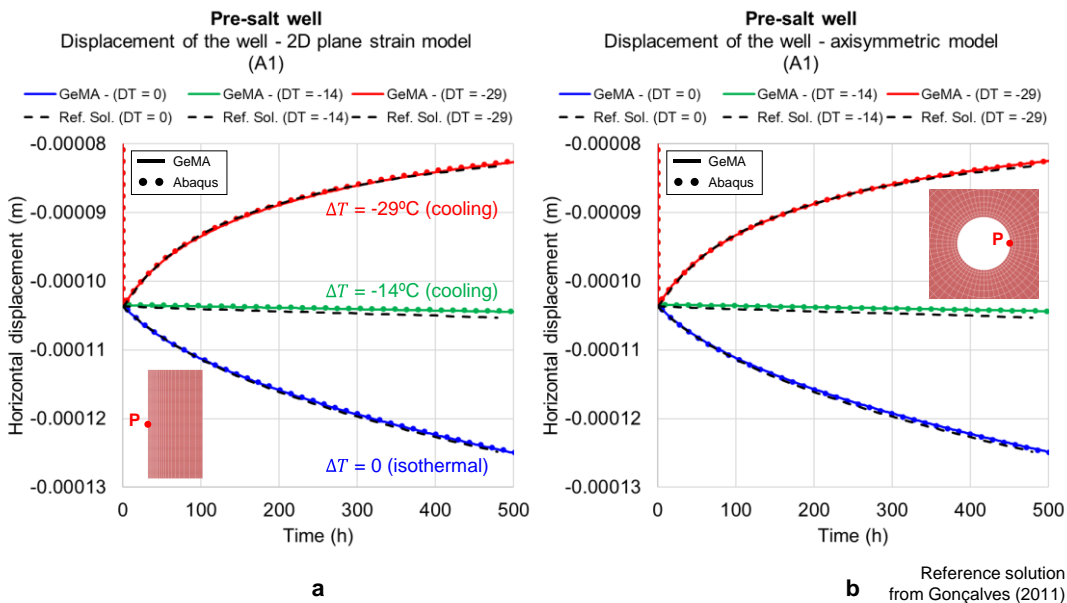


Figure 38. Horizontal displacement (radial closure) of point P in models A1: axisymmetric (a) and 2D plane strain (b).

#### 4.4.2.2. Well models considering homogenous tachyhydrite (B3)

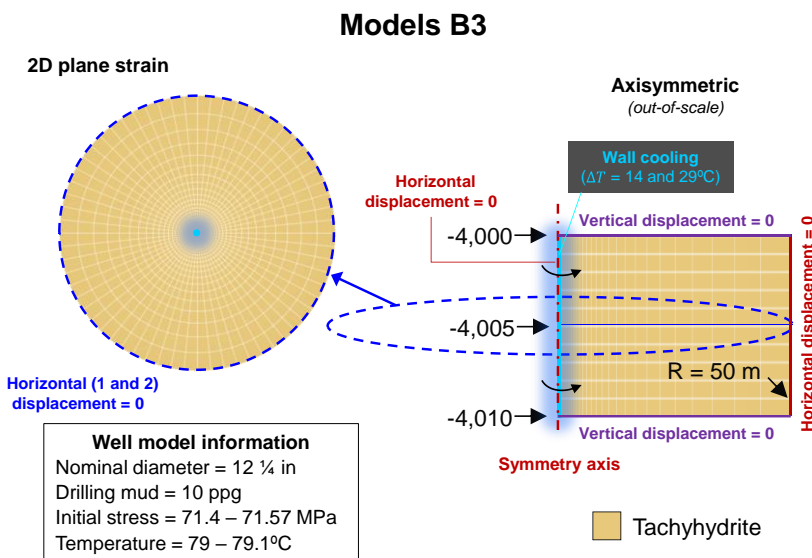


Figure 39. Axisymmetric and 2D plane strain models B3. Elevations and dimensions in meters.

The second group of models is the B3, which is a 10 meter-length tachyhydrite interval between the elevations -4,000 m and -4,010 m (from the sea level). In this synthetic site, the water depth is 1,500 m. The tops of the formation and salt interval coincide. The well diameter, the drilling mud weight and the

specifications of the axisymmetric and 2D plane strain models are the same as models A1 (see Section 4.4.2.1), with the exception of the elevation of the 2D model, which in model B3 is -4,005 m. Figure 39 presents the geomechanical models, the finite element meshes and the main attributes.

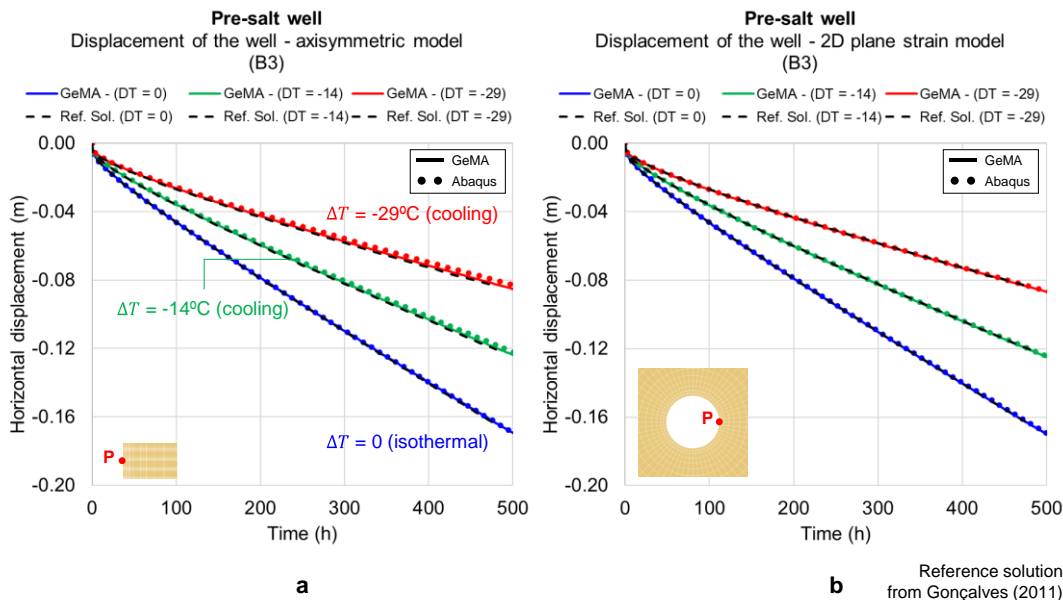


Figure 40. Horizontal displacement (radial closure) of point P in models B3: axisymmetric (a) and 2D plane strain (b).

Figure 40 shows the results of models B3 using GeMA (solid lines) compared to the reference solutions (dashed lines). The corresponding results using Abaqus<sup>TM</sup> (solid dots) are also plotted as reference. Once more, both the axisymmetric (Figure 40 (a)) and 2D plane strain (Figure 40 (b)) simulations have presented a very good agreement with the reference solutions for the three temperature cases. Tachyhydrite is much more mobile than halite and the models B3 are significantly deeper than models A1; therefore, the displacement scale in these simulations is notably higher than the previous ones with halite. After the instantaneous thermoelastic response to the well drilling, the creep deformation effect is notorious and tends to close the well in all cases. From these simulations, one observes that the lower the well temperature, the lower the creep deformation.

#### 4.4.2.3.

#### Models with halite-tachyhydrite-halite intercalation (C3)

The third group of models is the C3, which is a 100 meter-length halite-tachyhydrite-halite intercalation (40, 20 and 40 meter-length respectively) between the elevations -4,000 m and -4,100 m (from the sea level). In this synthetic site, water depth is of 1,500 m. The tops of the formation and the interval coincide. The

well nominal diameter is 14.75 inches (0.37465 m) and the drilling mud weight is 12 ppg (14.1 kN/m<sup>3</sup>). An axisymmetric model and a 3D model are considered. Since the tachyhydrite layer within the intercalation is relatively thin, a 2D plane strain model is not representative. The finite element meshes are composed by axisymmetric 8-node and 3D 20-node quadratic elements with reduced integration (types “Q8” and “Brick20” respectively). The 3D elements also have quadratic interpolation functions for displacements and linear interpolation functions for temperatures. The lateral and bottom limits are far enough from the well to avoid spurious boundary effects. Figure 41 (a) shows the geomechanical models, the finite element meshes and the main attributes of the models.

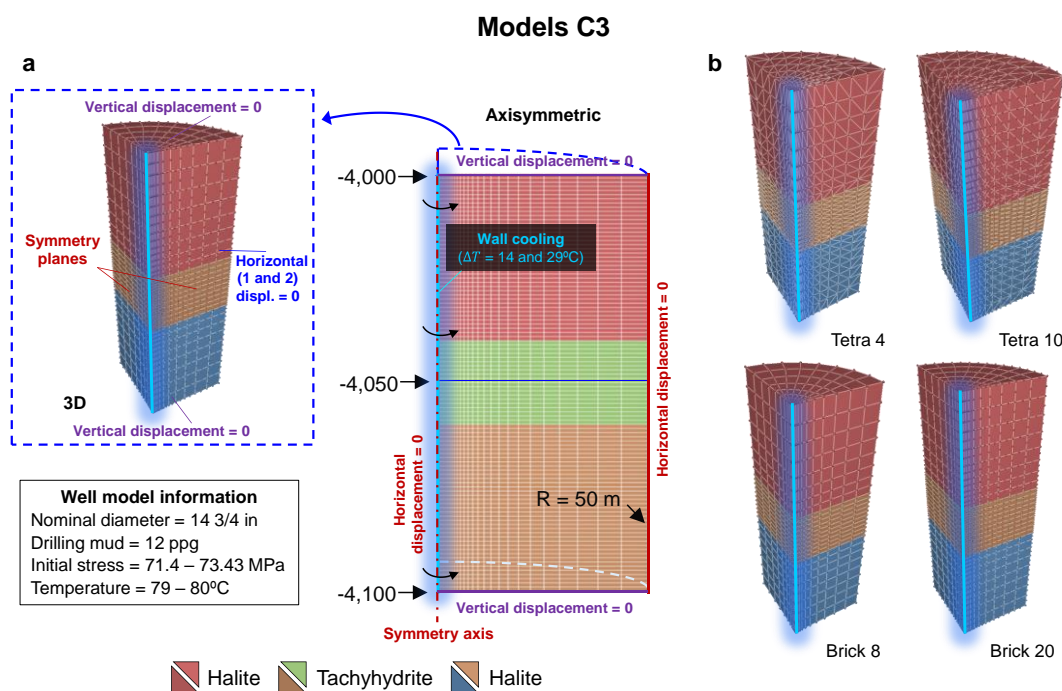


Figure 41. Axisymmetric and 3D models C3. Elevations and dimensions in meters.

Figure 42 shows the results of models C3 using GeMA (solid lines) compared to the reference solutions (dashed lines). The corresponding results using Abaqus<sup>TM</sup> (solid dots) are also plotted as reference. Observing the axisymmetric results (Figure 42 (a)), those obtained using GeMA (and Abaqus<sup>TM</sup>) are subtly higher than the reference solutions. This difference is particularly attributed to the mesh discretization, since a closer adjustment is noticed in the 3D results, in which the mesh is coarsen than the axisymmetric one. As a whole, although models C3 are a little deeper than B3, the displacements of the former are lower since the halite layers above and below the tachyhydrite partially restrict its high mobility. Furthermore, just like in the models B3, the creep deformation effect is notorious,

tends to close the well in all cases and the lower the well temperature, the lower the creep deformation.

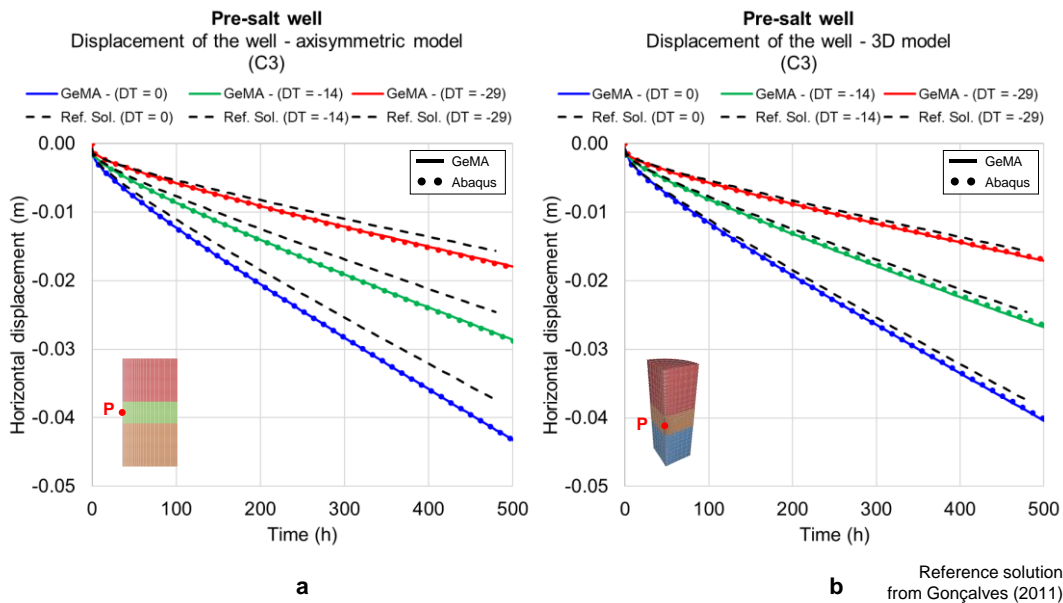


Figure 42. Horizontal displacement (radial closure) of point P in models C3: axisymmetric (a) and 3D (b).

In a second moment of this study, simulations to compare the results using four types of 3D elements in GeMA have been carried out. As Figure 41 (b) shows, besides the 20-node bricks previously adopted, 8-node bricks (linear), 10-node tetrahedrons (quadratic) and 4-node tetrahedrons (linear) have been tested. The scenario with the greatest temperature variation ( $\Delta T = (-) 29^{\circ}\text{C}$ ) has been adopted for this test. The mesh discretization parameters are the same in all models. Figure 43 (a) presents the displacements obtained with each of the element types. In this context, using linear elements (4-node tetrahedrons and 8-node bricks) underestimates the displacements, specially in the model using the 4-node tetrahedrons. In the models in which quadratic elements are adopted (10-node tetrahedrons and 20-node bricks), the results are closer to the reference solution (based on quadratic axisymmetric elements). Finally, Figure 43 (b) shows the temperature at 720 hours along the horizontal coordinate of the models (segment A-A'). All the models have exhibited the same results. It is expected, since the interpolation functions for temperature are linear (regardless of whether the interpolation of the displacements is linear or quadratic) and all the models have the same corner node coordinates in the segment A-A'. For reference purposes, the cooled radius of the model is about 10 meters after 720 hours of simulation, which is approximately 53 times the well radius.

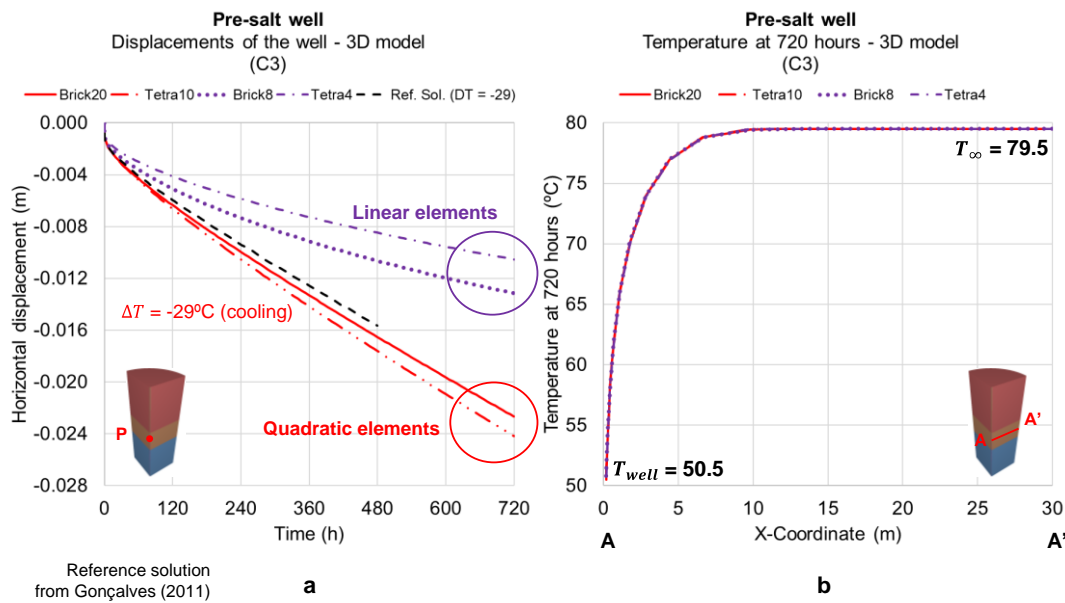


Figure 43. Horizontal displacement (radial closure) of point P (a) and temperature at 720 hours (b) of models C3: comparison of results using different 3D elements (8-node and 20-node bricks, and 4-node and 10-node tetrahedrons).

#### 4.5.

#### Closing remarks related to the validation and reference examples

The examples presented in this chapter have analyzed the salt creep behavior in different loading and temperature conditions by means of mechanical and thermomechanical simulations using axisymmetric, 2D plane strain and 3D models. The implementation of the hydromechanical correlations has also been checked. Through these applications, analogous structures of those of strategic projects involving salt rocks discussed in Chapter 3 have been analyzed in a preliminary way. GeMA framework has succeeded in solving these problems and produced results in very good accordance with experimental data and numerical solutions available in the literature. At this point, the author understands that this computational tool is validated for the case studies to be presented in the next chapters, which make use of mechanical and/or thermomechanical simulations and hydromechanical correlations.

## 5

# Case study of well abandonment using salt as geological barrier

### 5.1.

#### Objective

This chapter presents a conceptual case study of a Pre-salt well abandonment using salt as a geological barrier. The objective of this application is to get the big picture of this innovative procedure for well abandonment and to look towards its applicability to realistic cases. To this end, numerical simulations using GeMA framework are carried out considering the thermomechanical response of the well with special regards to salt creep and its impact on well closure, integrity and tightness. Methods to stimulate salt creep such as reducing the well pressure and heating the well are tested adopting feasible ranges. As output, the analyses aim at answering: i) if the well closes completely by salt creep and how long it takes to close; ii) if the well wall and vicinity stand sound during well closure; and iii) how the hydraulic properties evolve as the well closes.

### 5.2.

#### Lithology and geomechanical model

A conceptual model representative of an offshore Brazilian Pre-salt well has been conceived. The well is sited in a region where the water depth is of 2,000 meters and crosses a 2,000 meter-length standard sedimentary formation from the seafloor to the top of evaporitic formation. The well crosses the salt formation and the interval between elevations of -4,930 and -5,070 meters is considered. The idealized lithology consists of a 100 meter-length halite layer overlaid and underlaid by 20 meter-length anhydrite layers. The nominal diameter of the well is 12.25 inches (0.31115 m) and the drilling mud weight is 12 ppg (14.1 kN/m<sup>3</sup>).

In its current version, this study focuses on a 2D transversal plane strain model of the well at an elevation of -5,000 meters. Only one quarter of the well and surroundings are modelled by taking advantage of the double symmetry of the model. The finite element mesh is composed by 2D 8-node quadratic elements with reduced integration (type "Q8"). As in the models in Section 4.4.2, these

elements have quadratic interpolation functions for displacements and linear interpolation functions for temperatures. The lateral and bottom limits are far enough from the well to avoid spurious boundary effects. Figure 44 presents the geomechanical models, the finite element mesh and the main attributes.

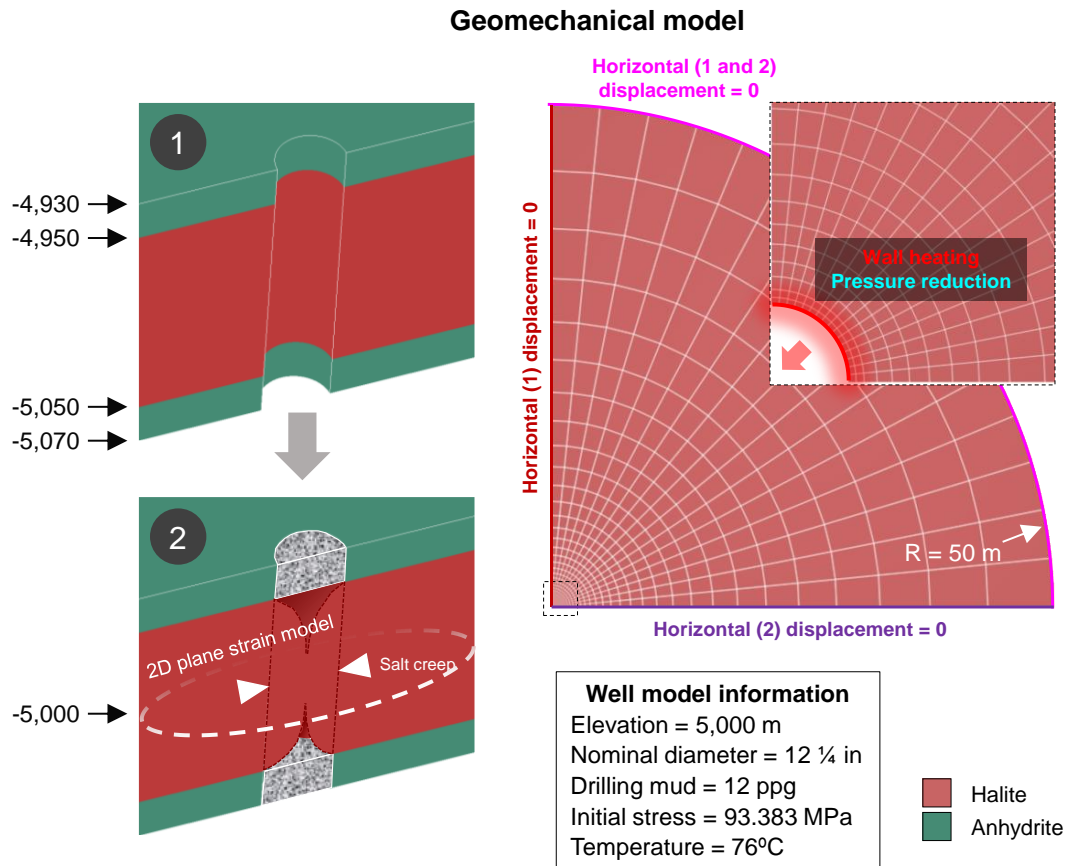


Figure 44. 2D plane strain model of the Pre-salt well. Elevations and dimensions in meters (unless otherwise stated).

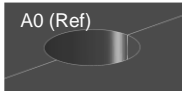
### 5.3. Initial and boundary conditions

As with the previous applications to wells in the thesis, the initial (geostatic) stresses are assumed isotropic and are assigned by the superposition of the gravitational loads. The density values are given in Section 2.5.3. The contribution of the sedimentary stratum above the evaporitic formation for the geostatic stresses is considered adopting a typical shale density. The temperature estimation is based on geothermal gradients – the values are the same adopted in Section 4.4.1. Figure 44 indicates the calculated values of the in-situ stresses (compression) and temperatures of the model (93.383 MPa and 76°C respectively).

With respect to the boundary conditions, the left and the bottom borders (symmetry axes) of the model have displacements restricted in the respective perpendicular directions and the circumferential border has displacements restricted in both directions (see Figure 44).

To analyze the salt creep behavior as the mechanism to form the geological barrier, four representative scenarios of boundary conditions are proposed. Initially, there is a reference model (A0) that assumes that the abandonment fluid weight and the temperature of the formation remain constant in the well. Creep acts solely due to the stress changes in the well caused by the section milling or equivalent procedure for casing removal. In order to accelerate the well closure in the predictions, creep stimulation methods such as reducing the well pressure and heating the well are adopted. To this end, choosing realistic values for these variations is essential for an adequate feasibility check in terms of well engineering. Model A1 consists of reducing the abandonment fluid weight from 12.0 to 10.21 ppg (from 14.1 kN/m<sup>3</sup> to 12.0 kN/m<sup>3</sup>) to represent the replacement of mud with brine over an approximate 30-day period after section milling. Besides that, considering that the salt formation is at relatively high temperatures in the evaporitic intervals (76°C) and also the values typically adopted in the literature, the author of the thesis believes that a realistic fluid warming to trigger well heating is of no more than a few tens of Celsius degrees. In this way, model A2 consists of heating the well wall in 20°C during the abandonment period. Lastly, model A3 considers the combined effect of models A1 and A2. Table 17 summarizes the scenarios considered in this study.

Table 17. Summary of the scenarios of boundary conditions.

Model ID		Scenario
A0 (Reference)		Constant abandonment fluid pressure and well temperature.
A1		Reduction in the abandonment fluid pressure and constant well temperature.
A2		Constant abandonment fluid pressure and well heating.
A3		Reduction in the abandonment fluid pressure and well heating.

## 5.4. Hypotheses, methodology and alignment with international literature

This study is carried out in the light of the following hypotheses: i) the geological barrier is formed by the creeping wall of the well, that tends to close the openhole left after casing removal; ii) mechanical and thermomechanical analyses are considered for creep stimulation depending on the scenario; iii) in all cases, the temperature effect is considered in the salt creep constitutive model; iv) the changes in the hydraulic behavior are credited only to the mechanical or thermomechanical response; and v) the behavior of the well and barrier after closure is not analyzed in the current version.

Having in mind the context of the well abandonment using the salt host formation as a geological barrier, the casing needs to be removed from the well (to restore the openhole condition) so that the interval that crosses the salt layer becomes free to creep. The numerical modelling has to be incremental to take into account the main steps of the well construction, operation and abandonment (see Firme et al. (2017) for instance). In a recent earlier work using Abaqus™, the author has divided the well chronology into seven steps, as shown in Figure 45.

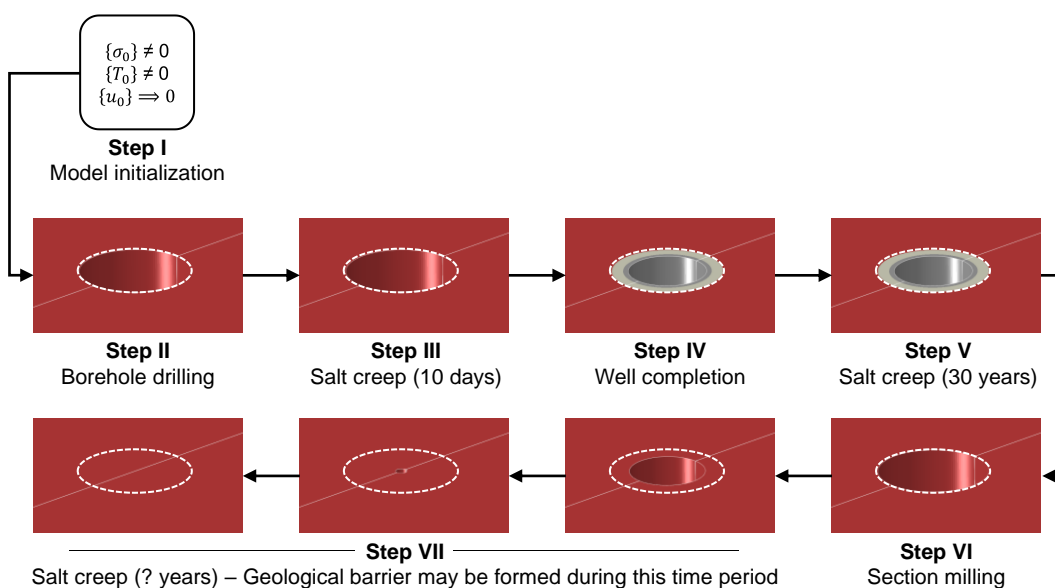


Figure 45. Workflow for the well abandonment simulations considering salt as barrier.

Step I corresponds to the initial step when the in-situ stress state (geostatic loading) and temperature are assigned with the guarantee that the model remains undeformed. Step II consists of the well drilling, in which the corresponding elements are removed and the drilling mud pressure is simultaneously applied upon the well wall. Step III consists of letting the openhole creep over 10 days. In

step IV, the casing is run and the annulus is fully cemented. In step V, the salt continues to creep around the well over 30 years, which is the well lifespan. After that time, step VI corresponds to end of the well lifespan and the beginning of the abandonment period – section milling (or analogous) is represented by removing the casing and cement elements. An abandonment fluid pressure is simultaneously applied upon the openhole wall. Finally, in step VII, the salt continues to creep around the openhole wall and the complete closure is expected to happen. In this step, a pragmatic 30-year period is considered – this is justified only in the scope of the numerical analyses since one does not know at first how long the openhole will take to close completely. Depending on the scenario, if the openhole does not close within this period, the analysis simply ends and the scenario is discarded.

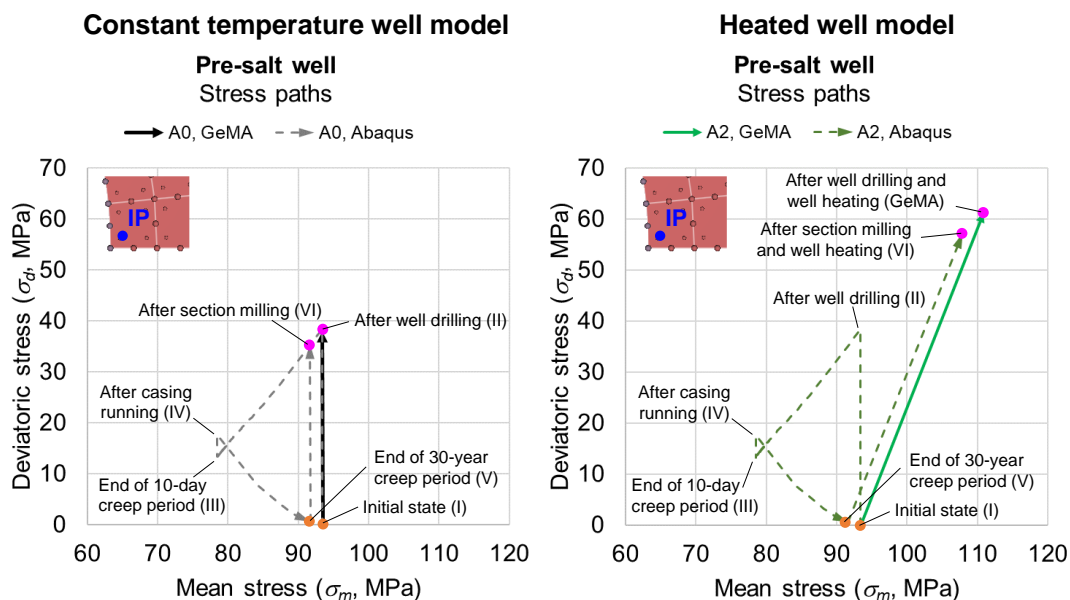


Figure 46. Comparison between the stress paths obtained using Abaqus™ and GeMA.

Subsequently, having the use of GeMA framework and the development of salt geomechanics functionalities into it as part of the contribution of this thesis (see Section 2.5.4), this case study has been revisited using that simulation tool. However, GeMA still<sup>50</sup> does not support the inclusion of new mesh regions in the model after the analysis has started (the opposite is already supported i.e., mesh excavation). This temporary limitation has casted a challenge in the representation of the stress state before the section milling. Aiming at circumventing this limitation, the stress paths of the well wall have been analyzed both considering the events before the section milling (using Abaqus™, dashed lines) and neglecting them (using GeMA, solid lines), as shown in Figure 46. The reference model (A0),

<sup>50</sup> By March 2022.

isothermal, and Model A2, in which the well is heated well after section milling, are considered. In both models, the points in the stress path plots corresponding to the initial step (I) and the step before section milling (step V) are close – compare the orange dots. It means that, when salt creep is opposed by casing over a long time (30 years in this case), the stress state in the wall returns to very close its initial state before well drilling. This happens because the casing is much stiffer than the salt; therefore, the former absorbs the creep-induced loading of the latter and restricts its displacement. If the same mud weight is adopted for both drilling and milling, the stress state produced by well drilling is very close to that produced by section milling, as indicated by the lilac dots. These results (orange dots) are just not equal because the material has not fully recovered the confinement it had before drilling. These findings indicate that a well drilling simulation using GeMA such as those of Sections 4.4.1 and 4.4.2 can be adopted to roughly represent the section milling simulation.

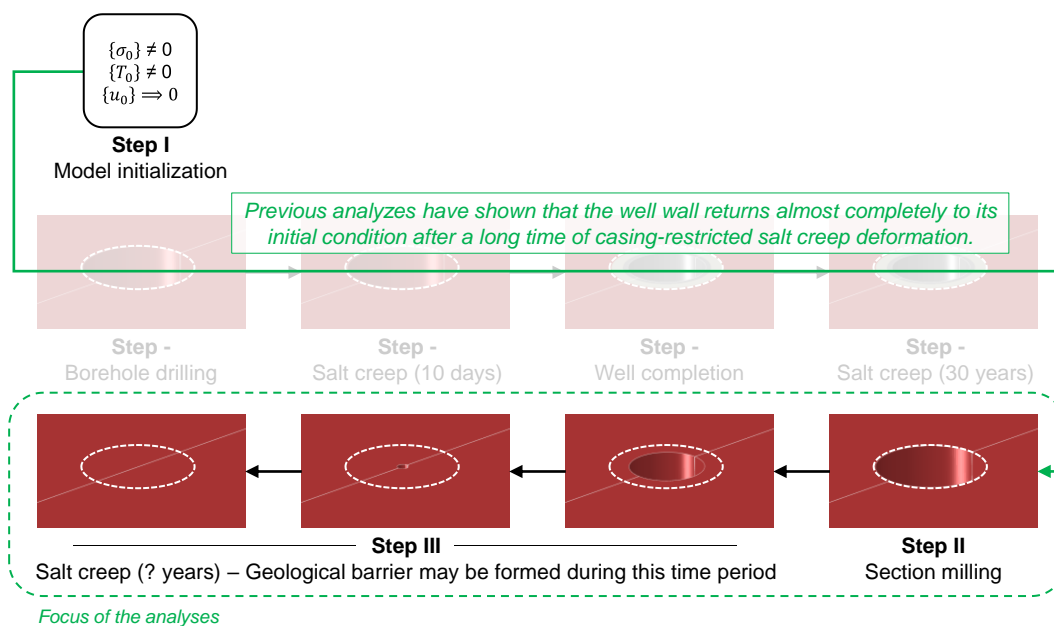


Figure 47. Simplified workflow for the well abandonment simulations considering salt as barrier.

Based on the findings above, the workflow for well abandonment simulation using GeMA has been simplified to what is presented in Figure 47, analogous to that adopted in thermomechanical reference examples (see Section 4.4.2). In the step I, the in-situ stress state and temperature are assigned with the guarantee that the model remains undeformed. In the step II, the well drilling represents the section milling (or analogous) and the abandonment fluid pressure is simultaneously applied upon the openhole wall. When applicable, the well is also heated in this step. Lastly, in the step III, salt creep acts over time and the openhole

closure is expected to happen. As in the earlier analyses, a 30-year period after section milling is considered and the geological barrier is expected to form during this period.

In this study, salt creep is simulated using the EDMT model. The salt properties summarized in Section 2.5.3 apply. Furthermore, after the section milling, the well surroundings are assumed to behave as a DRZ (see Section 2.3) and the thermomechanical behavior impacts the hydraulic behavior of salt in the creeping surroundings (that becomes the barrier). Hence, the TM+H approach described in Section 2.5.1 is adopted. To analyze the changes in the hydraulic behavior of salt, an initial porosity of 0.01 and an initial permeability of  $9.0\text{E-}16\text{ m}^2$  ( $\sim 0.91\text{ mD}$ ) are considered<sup>51</sup> (Stormont et al., 1991).

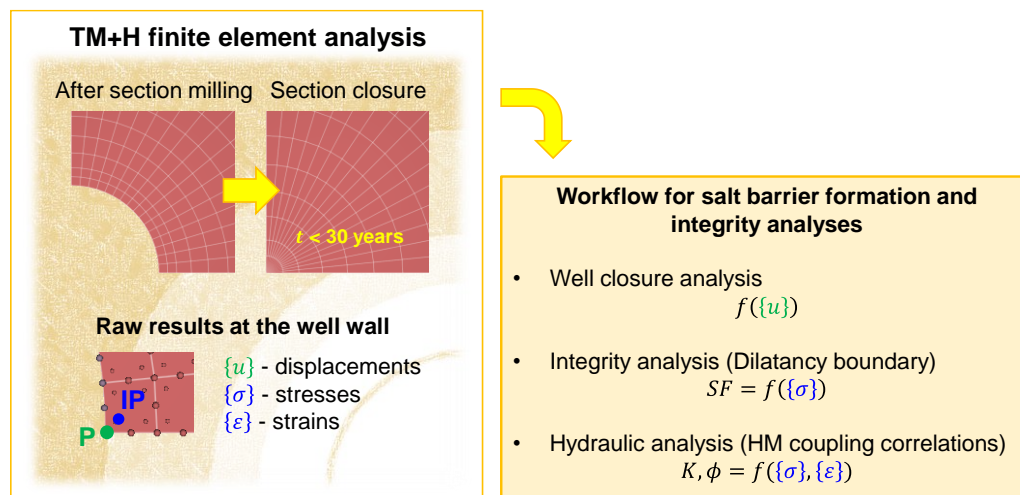


Figure 48. Workflow of the TM+H approach applied to the well abandonment.

Figure 48 illustrates the use of this methodology in the particular context of well abandonment. The well closure is measured in point P on the openhole wall while stress- and strain-related variables are measured at the Gauss point (IP) closest to point P. Since the hydraulic parameters are correlated to strains and stresses, these parameters are also calculated at the indicated Gauss point.

This type of application is in line with other studies dedicated to salt as an abandonment material and salt creep as a process that forms geological barriers (see Section 3.1.3.2). In order to hasten the well closure by creep and make this abandonment concept more feasible to the industry, creep stimulation methods such as reducing well internal pressure or heating the well and/or backfilling the

<sup>51</sup> Representative values of a borehole subjected to a gas injection test after excavation, from Stormont et al. (1991). In view of the most critical permeability scenario, a gas permeability value was selected.

well with crushed salt have been suggested. The long-term tightness (i.e., the evolution of porosity and permeability) of the barrier is also mentioned as an important issue to be investigated (Orlic et al., 2019; Orlic and Buijze, 2014). Moreover, Hou et al. (2012) have presented a case study of well abandonment in which a heavy WBM adopted as milling fluid was posteriorly replaced with a lighter fluid to relief the openhole walls and enhance salt creep to close the well. Furthermore, in the context of salt caverns, pre-heating the (abandonment) brine before injecting it inside the cavern has been mentioned as an option to reduce the internal pressure increase after the cavern is plugged despite the high cost with energy (Thoraval et al., 2015). As contributions to the existing applications in this area, this thesis analyzes the integrity and tightness of the geological barrier which is being formed. Moreover, the temperature effect caused by heating the well is considered by means of coupled thermomechanical simulations in such a way that the temperature stimulates the salt creep behavior as long as it migrates into the formation by conduction.

## **5.5. Results and discussions**

For a better exposition, the results of this case study are divided into three groups: i) displacements and temperatures; ii) stresses and strains; and iii) permeability and porosity. Each of these groups of results is presented and discussed in the sections below.

### **5.5.1. Displacements and temperatures**

Figure 49 (a) presents the evolution of the well diameter in the models from section milling on. In these and the following graphs, the curves end when the well is completely closed – this is indicated with an “x”. From the results of model A0 (reference model, black line), the openhole does not close completely after a 30-year period. By extrapolation, the well closure would occur in approximately 50 years. When the well abandonment pressure is reduced to an equivalent brine pressure (model A1, blue line), the openhole closes completely in 9.99 years. Conversely, when the openhole wall is heated (model A2, green line), the effect is a little greater: the openhole closes in 7.68 years. When both methods are combined (model A3, red line), the openhole complete closure occurs in 2.55 years. Considering the waiting times until the well closes completely and the salt geological barrier is formed, models A0, A1 and A2 are operationally unfeasible

despite the abandonment concept has been verified. Model A3 exhibits a significant reduction in the waiting time by combining the creep stimulation methods, although taking 2.55 years to close the well is still a long time for the industry. Furthermore, the temperature evolution throughout the surroundings has been monitored in the heated models (A2 and A3), Figure 49 (b). As expected, the heated radius increases with time since there is a transient thermal conduction.

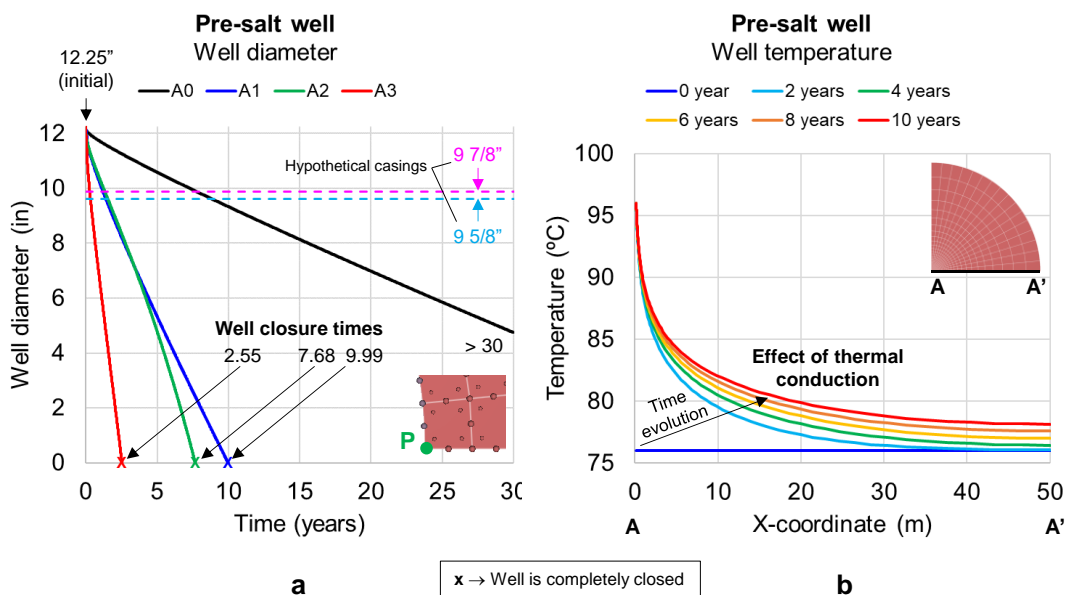


Figure 49. Well diameter evolution (a) and temperature evolution (b) over time.

More so, if the casing were neither milled nor removed from the well as indicated in Figure 49 (a), the time for closing the annulus space would be significantly shorter than that to close the entire section. Considering a hypothetical casing of 9 5/8 inches in nominal diameter, it would be totally embraced by the salt in 0.33 years (about 120 days) considering Model A3. If a casing of 9 7/8 inches were adopted, this time would be of 0.28 years (about 102 days) in the same scenario. Table 18 summarizes the times for well closure in these circumstances.

Table 18. Summary of the times for well closure.

Model ID	Time for well closure (years)		
	Full well closure	Around a 9 5/8" casing	Around a 9 7/8" casing
A0 (Reference)	> 30	8.81	7.80
A1	9.99	1.41	1.22
A2	7.68	1.53	1.34
A3	2.55	0.33	0.28

For the integrity and tightness analyses, the goal for complete well closure by salt creep is considered in order to focus on the most critical condition for the well and for the geological barrier which is being formed.

### 5.5.2. Stresses and strains

While the well diameter evolution provides the big picture of the gradual formation of the geological barrier, stresses and strains are useful to analyze the integrity of the barrier which is being formed. Figure 50 (a) shows the evolution of the mean stresses (solid lines), deviatoric stresses (dashed lines) and Lode angle (dotted lines), and Figure 50 (b) presents the dilation indicator. This ratio has been calculated based on DeVries' dilatancy boundary (see Section 2.1.2.4 and the context of Figure 35). The section milling provokes a lateral unconfinement of the well interval since, in practice, the cased well turns into an openhole. From the results of model A0 (reference model, black lines), the mean stresses (that confine the well) reduce over time. The deviatoric stresses show an abrupt increase due to the section milling; however, the deformation energy is dissipated by salt creep and the deviatoric stresses reduce as time went by. Despite some oscillations after milling, the Lode angle converges to zero and remains so until the end of the analysis. In fact, the case of a 2D plane strain model and incompressible flow leads to an isochoric shear condition indicated by a Lode angle equals to zero (Rauter et al., 2020). This demonstrates that the isochoric shear is the dominant mechanism during the geological barrier formation provided that one analyzes far from the top and bottom of the barrier. The dilation indicator presents the same pattern of the deviatoric stresses resulting in higher values in first years after milling and reduces as salt creeps. It converges to 0.30, which means that the deviatoric stress at the well wall is about 30% of the critical value for dilation. This brings the physical meaning that the barrier in formation is sound. In model A1 (blue lines), where creep is stimulated by the reduction in the well pressure, the same conceptual behavior of the reference model is noticed. However, the reduction in the mean stresses and the instantaneous increase in the deviatoric stresses after milling are more significant since the well pressure is lower than that of the reference model. Therefore, higher values of the dilation indicator are noticed (by 0.40). Observing model A2 (green lines), in which creep is stimulated by well heating, the results initially follow the same conceptual pattern as the other models after milling although with different values. However, there is an inflection in the mean and deviatoric stresses by one year after the section milling. From this

moment on, both the mean and deviatoric stresses increase. This change in the behavior is attributed to a transient heating effect in the well vicinity. The heated radius around the well increases with time as heat is transferred into the well by conduction (see Figure 49 (b)) and therefore thermal stresses and creep deformation are enhanced. After this inflection, the dilation indicator has increased and was about 0.35 when the well closed completely. Moreover, model A3 (red lines), which combines the creep stimulation methods of models A1 and A2, presents similar conceptual results. Although the inflection in the mean and deviatoric stresses also happens since the well is heated, the combination of pressure reduction and well heating has accelerated the well closure before this change in the behavior was more visible. The dilation indicator has converged to approximately 0.42. Lastly, the initial values of the dilation indicator have reached one in some models, although they evolved to much lower values right after. This effect is addressed in the verification of the stress paths.

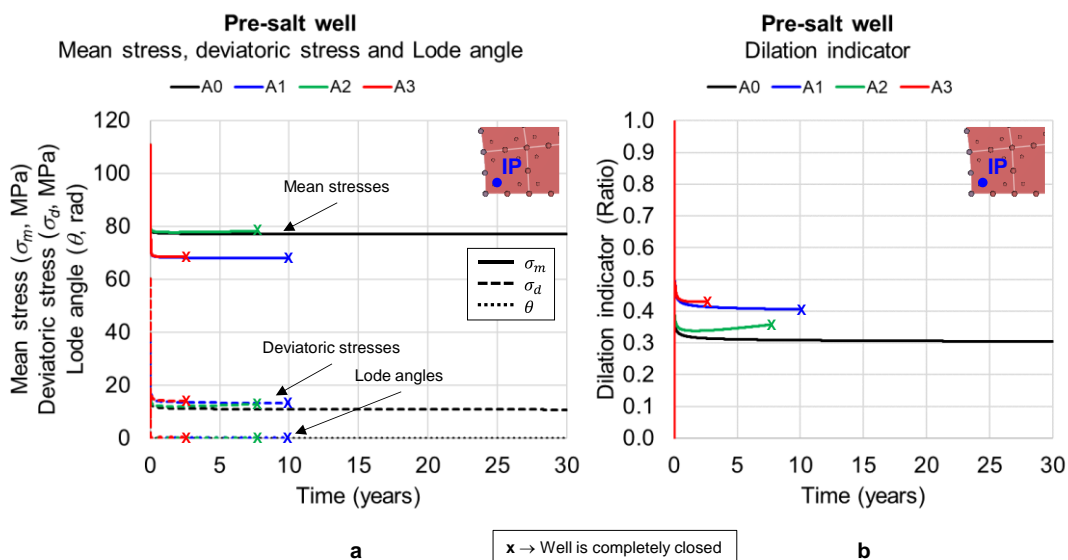


Figure 50. Mean stresses (solid lines), deviatoric stresses (dashed lines) and Lode angle (dotted lines) (a) and dilation indicator (b) over time.

Next, the stress paths (p-q diagrams) of the well wall have been analyzed. To ease viewing the results, Figure 51 shows separately the stress paths of each model compared to the reference model. The dilatancy boundaries for compression, extension and isochoric shear calculated using equation (24) are also plotted to indicate the admissible stress domains. In all graphs, the initial stress state (before section milling) is indicated with “1”, the stress state right after milling (represented by the well drilling procedure) and heating (if applicable) is indicated with “2” and the final stress state when the well is completely closed is indicated with “3”.

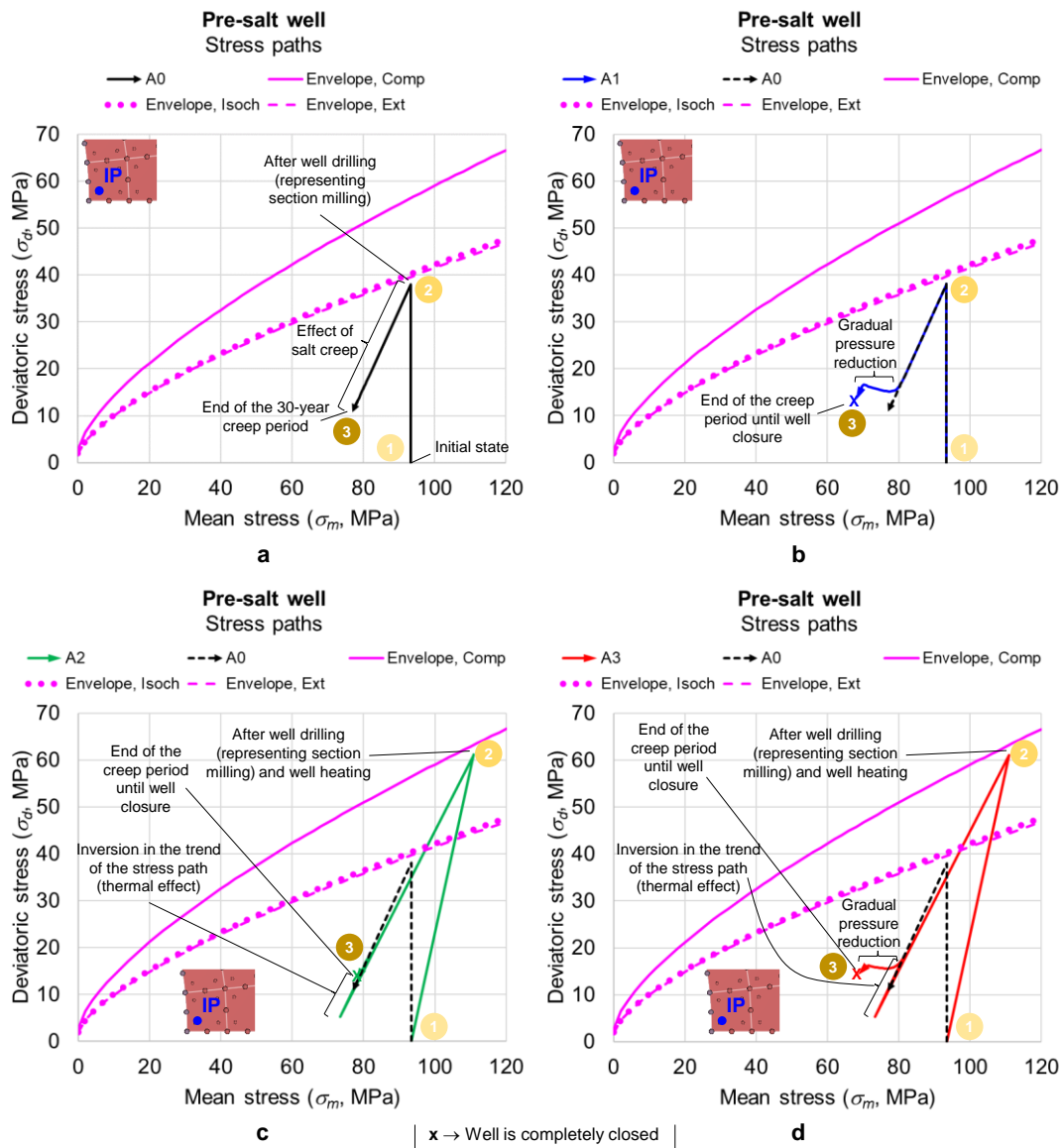


Figure 51. Stress paths (p-q diagram) from section milling to well complete closure – model A0 (a), model A1 (b), model A2 (c) and model A3 (d).

Observing model A0 (reference model, black line), Figure 51 (a), the stress path exhibits a vertical upward trend due to the section milling. Then, there is a downward trend to the left compatible with the creep behavior under constant well pressure and temperature after milling. In model A1 (blue line), Figure 51 (b), the stress path exhibits a vertical upward trend due to the section milling just like model A0. It is followed by an initial downward trend to the left after section milling; however, a trend inversion in the deviatoric stresses is noticed during the 1-month period when the well pressure is gradually reduced to an equivalent brine pressure (deviatoric stresses increase in turn). Once this pressure value is reached and kept until the end of the analysis, the model creeps with constant well pressure and the stress path points again downwards left just like model A0. In model A2 (green

line), Figure 51 (c), the stress path shows a remarkable upward trend to the right after section milling using a warmed fluid. It reflects the combined effect of milling and heating. Then, there is a downward trend to the left followed by a trend inversion (upward right). This inversion is credited to a transient heating effect in the well vicinity (as commented in the context of Figure 50). After that, the path points again downwards left until well closure as the previous models. In model A3 (red line), Figure 51 (d), the combined effect of the stress path peculiarities from models A1 and A2 are observed until well closure. Still regarding models A2 and A3, the instantaneous effect of the section milling using a warmed fluid has caused the stress path to exceed the dilatancy boundaries of extension and isochoric. This is understood to be a side effect of the instantaneous well heating. Since the stress paths in all the models have evolved downwards left right after milling and the dilation indicators have decreased rapidly to less than 0.45 (see Figure 50 (b)), this condition is not taken as prohibitive. Any eventual initial damage is likely reverted over time due to self-healing. Lastly, the fact that all the models exhibit final stress states significantly below the dilatancy boundaries is evidence that a sound and potentially tight geological barrier is formed by salt creep.

### 5.5.3. Porosity and permeability

The next step is to verify the repercussion of the thermomechanical response on the hydraulic behavior of the salt. From right after section milling on, geomechanics (including thermal effects) impacts porosity and permeability due to volumetric deformation and mean stress (confinement) variation. All the procedures related to section milling are likely responsible for the creation of a DRZ around the well in the field; for this reason, the consequences in the hydraulic behavior of salt should be considered from the end of this procedure on. Figure 52 (a) presents the evolution of the volumetric strains (solid lines) over time. In all models, there is an instantaneous volumetric strain due to section milling plus the temperature effect in the heated models and then it varies very little with salt creep after milling. This is coherent with the hypothesis that creep is isochoric (see Section 2.1), not producing relevant volumetric strains. Comparing models A0 (black line) and A1 (blue line), one notices the effect of the well pressure reduction in increasing the volumetric strain of model A1. The same is noticed comparing models A2 (green line) and A3 (red line). Besides that, by comparing models A0 and A2 and models A1 and A3, the well heating has increased the volumetric strains of models A2 and A3 in relation to their corresponding isothermal models.

This effect is expected since the thermal changes generate instantaneous thermal volumetric strains (see Equation (26)). More so, model A2 and A3 has presented a subtle inversion trend in the volumetric strains – this has been observed with the stresses (see section 5.5.2). The porosity (dashed lines) has been calculated based on the volumetric strains using equation (29) and follow the same trends of those of volumetric strains. This is physically coherent since the pores tend to enlarge and the microcracks tend to open as the volumetric strains increase and salt becomes prone to dilation. Finally, having the porosity values, the next step is to calculate the porosity-dependent permeability using equation (28), Figure 52 (b). In this correlation, the empirical power adopted for salt is one (value for a very low porosity rock). As a consequence, the porosity-dependent permeability (solid lines) follows the same trend of the porosity (dashed lines) in each model. As a whole, the permeability enhancement triggered by the porosity is of very low magnitude. In fact, the well closure by salt creep occurs in an isochoric manner (see Figure 50 (a) and context) and the use of equations relating permeability to porosity likely underestimates the permeability evolution.

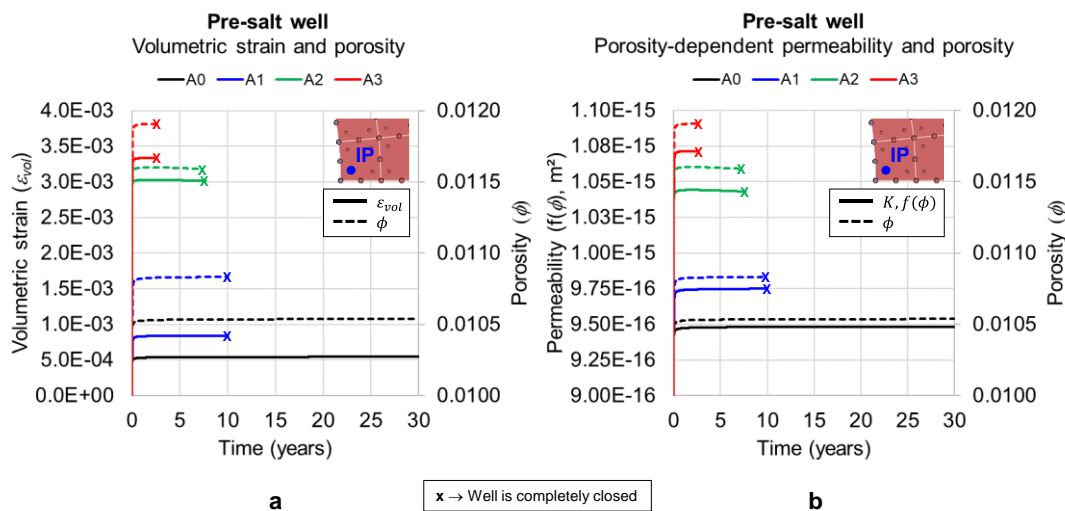


Figure 52. Volumetric strain (a) and porosity-dependent permeability (b) over time.

As an alternative to this approach to permeability, there is the mean stress-dependent permeability. Kuhlman and Matteo (2018) have pointed out that the expression relating permeability to mean stresses (such as Equation (30)) is likely more representative of the well vicinity, which becomes a DRZ after section milling. Thus, Figure 53 (a) presents the evolution of the mean stress-dependent permeability (solid lines) over time. The evolution of the mean stress (dashed lines) is also plotted as reference. The results show a similar conceptual behavior than

that of porosity-dependent permeability; however, higher values occur when the permeability is calculated based on the mean stresses.

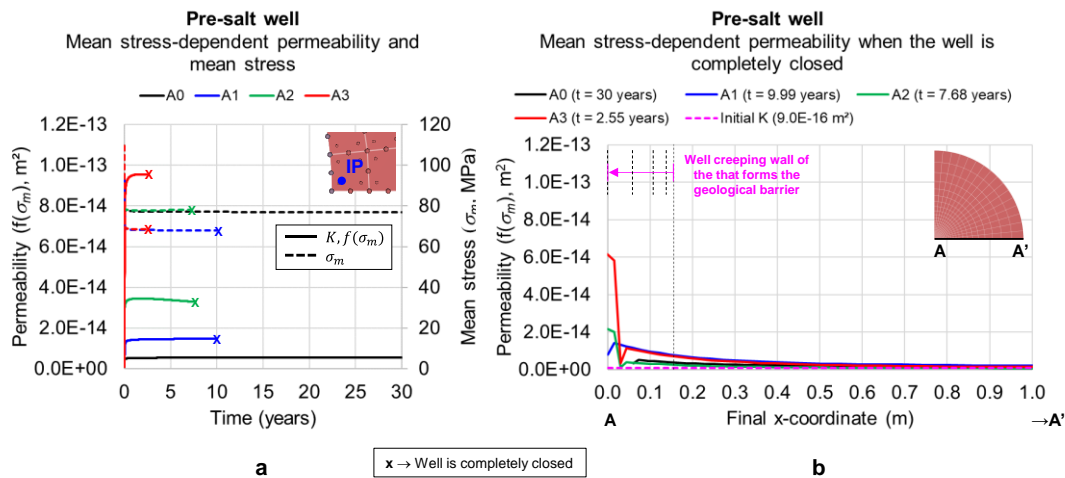


Figure 53. Mean stress-dependent permeability results over time (a) and along the segment A-A' when the well is completely closed (b).

Naturally, the empirical parameters adopted in the correlations have influenced the results. Analyzing model A3 since it is the most critical, the maximum values of porosity-dependent and mean-stress dependent permeability are  $1.07E-15 m^2$  and  $9.53E-14 m^2$  respectively ( $\approx 1.2$  and 106 times the initial permeability value respectively). Considering the latter, if the parameter  $\omega$  were taken  $0.023 MPa^{-1}$  rather than  $0.11 MPa^{-1}$  (also acceptable for low porosity and crystalline rocks, see the context of Equation (30)), the maximum permeability would be  $2.39E-15 m^2$  ( $\approx 2.65$  times the initial permeability value), still higher than the porosity-dependent value. All these values are still in the permeability range of disturbed salt (between  $1.0E-11$  to  $1.0E-21 m^2$ ) (Cosenza and Ghoreychi, 1996), although the initial value considered in the simulations,  $9.0E-16 m^2$ , is already a relatively high value for a disturbed salt in the vicinity of the milled section (as a DRZ) (Stormont et al., 1991). Nevertheless, it seems more appropriate to keep the maximum value acceptable for the parameter  $\omega$  in order to maximize the mean stress-dependent permeability enhancement.

More so, Figure 53 (b) shows the stress-dependent permeability evolution throughout the well surroundings (along the segment A-A') when the well is completely closed<sup>52</sup>. Considering the emphasis to the geological barrier in formation, the final x-coordinates of the nodes of segment A-A' are considered

<sup>52</sup> The differences between the results at the final time in Figure 53 (a) and at coordinate  $x = 0$  in Figure 53 (b) are due to the extrapolation of the permeability result from neighboring Gauss points to this node, which is in the border an excavated region in the finite element mesh. In the history plots, this quantity is collected from the Gauss point; therefore, this numerical issue does not happen.

rather than the initial ones. As seen before, with the exception of model A0, the well has closed completely in all other models. By comparing the results of models A2 and A3 with those of A0 and A1, the well heating has triggered a more significant permeability enhancement close to the creeping wall, while its effect seems to be lower when moving away from the wall. In addition, by comparing the results of models A1 and A3 with those of A0 and A2 a little away from the wall, the pressure reduction in the well seems to be more relevant for the permeability enhancement than well heating is. As a reference, Stormont et al. (1991) have carried out brine and gas injection tests in boreholes to analyze the changes in salt permeability due to excavation. The most hydraulically affected region in the DRZ was of about 1.5 times the well radius. Although the specifications of their field application and the current study are different, one gets the x-coordinate of approximately 0.23 meters (1.5 times the radius of 6.25 inches) by applying this proportion as a rough estimate in this case study. From Figure 53 (b), the most affected radius in terms of permeability enhancement is up to about 0.50 meters in final coordinates (or about 0.60 in original coordinates), so there is a proximity in terms of order of magnitude.

Lastly, the mean stress-dependent permeability is plotted versus the mean stress in Figure 54 in order to emphasize the permeability-dependence on the confinement stress. For the sake of clarity, the author makes use of the term “permeability path” analogously to “stress path” for the purpose of expressing the evolution of the permeability in function of the mean stress. Similar to the stress paths plots, in all graphs, the initial permeability condition (before section milling) is indicated with “1”, the condition right after milling and heating (if applicable) is indicated with “2” and the final condition when the well is completely closed is indicated with “3”. The changes in the porosity and permeability are accounted for from right after section milling on, when salt creep is effectively acting to close the well and to form the geological barrier. For this reason, the initial permeability condition (1) and that right after milling (2) are the same in the isothermal models (A0 and A1). In the heated models (A2 and A3), there is an instantaneous increase in the mean stress from condition (1) to (2) due to thermal stresses. However, the permeability changes only occur after condition (2).

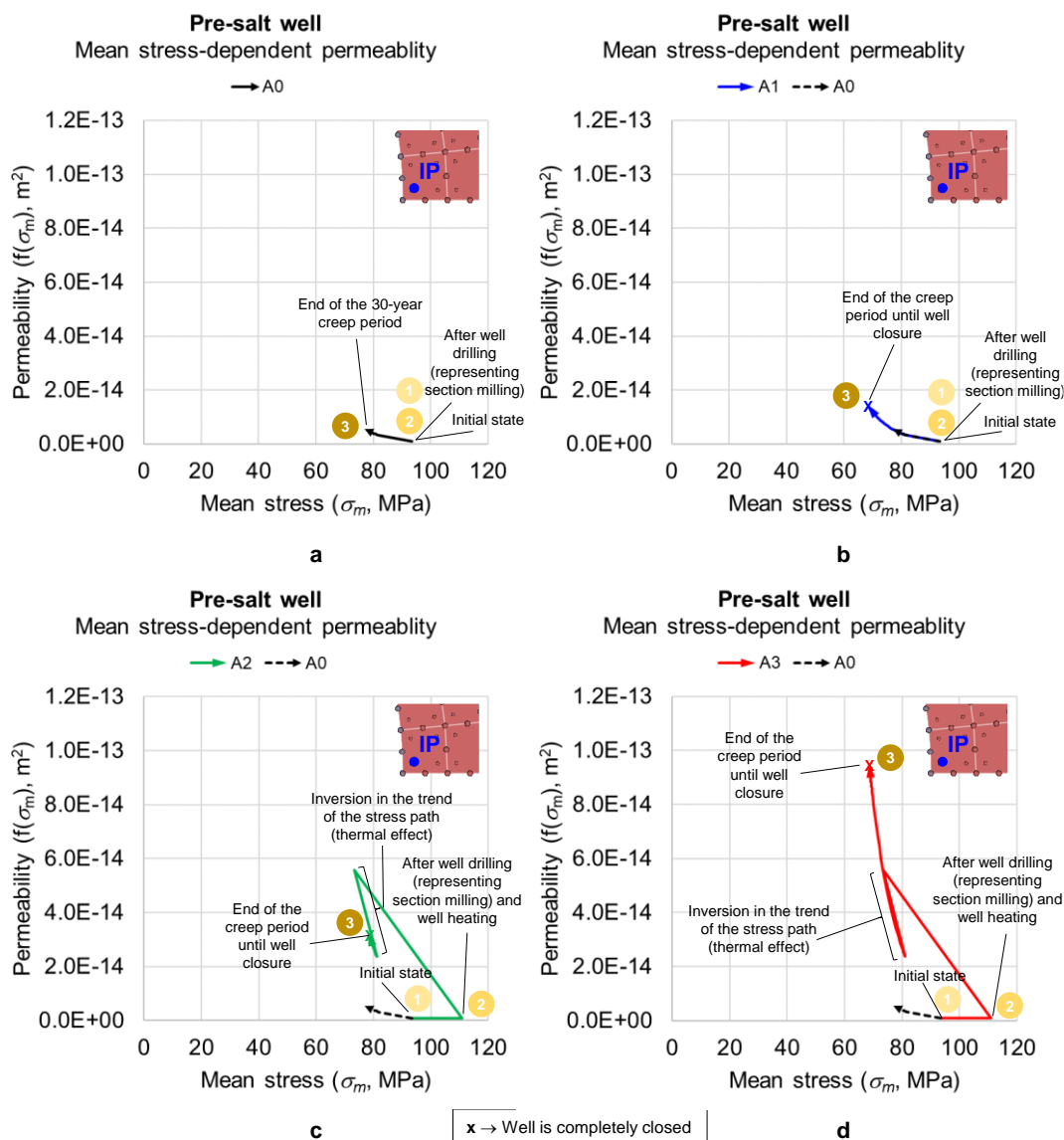


Figure 54. Mean stress-dependent permeability in function of the mean stress (“Permeability” paths) of models A0 (a), A1 (b), A2 (c) and A3 (d).

Observing model A0 (reference model, black line), Figure 54 (a), the permeability of the well undergoes a subtle nonlinear increase as the mean stress reduces after milling – the permeability path follows a subtle upward trend to the left. In general, this is conceptually expected since the reduction in the salt confinement makes microcracks open and pores enlarge, enhancing the permeability of the medium. The nonlinear path is also expected since the permeability depends on the mean stress increment to the 0.11 power (see Equation (30) and context). Therefore, although the well has not closed completely during 30 years of simulation, the reference model presents a hydraulic response physically and mathematically coherent until the end. In model A1 (blue line), Figure 54 (b), the permeability path follows the same trend of model A0, but with a

higher extent and evolving to a more noticeable nonlinearity. The mean stress reduction and the consequent permeability enhancement are greater than they are in model A0. This response is coherent with the fact that there is a pressure reduction to stimulate the creep behavior until the well is completely closed. Next, in model A2 (green line), Figure 54 (c), the permeability path exhibits a strong upward trend to the left followed by a sharp downward trend to the right – this is likely due to the inversion trend observed in the stress paths (see Figure 51 (c) and context), which has been credited to a transient heating effect in the well vicinity. After that, the permeability path follows a sharp upward trend to the left until the well closes. The permeability enhances as the mean stress reduces in a higher rate than those of models A0 and A1. It happens because salt creep develops higher rates in heated models (A2 and A3) than in isothermal models (A0 and A1). Finally, in model A3, Figure 54 (d), the permeability path develops a trend similar to that of model A2. The difference is that in model A3 the permeability enhancement with the mean stress reduction occurs in an even higher rate than that of model A2, since salt creep is stimulated not only by well heating but also by pressure reduction. As a general observation, the confinement reduction causes discontinuities and pores to open and, consequently, permeability is enhanced. Having in mind the condition of the salt rock as a DRZ in the well vicinity and the permeability results, the concept of mean stress-dependent permeability seems to be more adequate, as suggested by Kuhlman and Matteo (2018).

## **5.6. Partial conclusions**

This case study has presented a first approach to investigate the formation of a salt geological barrier in a conceptual model of a Pre-salt well. The main objectives were: i) to verify if the well closes completely by salt creep and how long it takes to close; ii) to verify if the well wall and vicinity stands sound during well closure; and iii) to analyze how the hydraulic properties evolve as the closes.

The results have shown that: i) the well can close completely by creep. Both pressure reduction (model A1) and well heating (model A2) accelerate significantly the openhole closure. The combination of these two methods accelerates creep even more (model A3); ii) the well integrity is maintained during closure. The closure has developed in an isochoric manner evidenced by volumetric strains tending to a constant value and null Lode angles over time; and iii) the reduction in the mean stresses in the surroundings as the well creeps reduce the rock

confinement resulting in the increase in porosity and permeability. The confinement has proven to be more decisive in influencing the permeability of the well vicinity (DRZ) than the porosity since the well deforms an isochoric way. The final permeability was of more than 100 times the initial permeability value in the most critical scenario; however, it has yet to be analyzed whether this enhancement is enough to trigger relevant flow/reactive transport in the geological barrier formed.

These findings have a proof-of-concept purpose to guide more in-depth studies. Some hypotheses regarding the best way to consider the creep stimulation methods and to calculate the hydraulic variables can be reviewed in future versions. Although the concept for the geological barrier formation has been verified, the author of the thesis believes that a more significant time saving is still needed to make this abandonment method competitive with traditional methods regarding time (and consequently cost). The study has also addressed the alternative of using salt as barrier to close only the annulus space outside the casing, such as what is considered for shale as barrier. In this case, the times required for salt to form the barrier are significantly reduced.

Overall, the results have agreed with the theoretical expectations regarding salt creep and the repercussion of the thermomechanical behavior on the hydraulic behavior of the well vicinity as the geological barrier forms.

## 6 Case study of salt cavern<sup>53</sup>

### 6.1. Objective

This chapter revisits a case study of a synthetic offshore salt cavern for natural gas storage. This cavern was originally presented by Costa et al. (2012). The author and the advisors of the thesis have recently studied this salt cavern using a commercial finite element code (Firme et al., 2018b, 2019). In those works, only the mechanical approach to the problem has been performed. In this thesis, an updated and extended version of this study is carried out using GeMA framework to analyze the cavern integrity and the repercussion of the mechanical response in the hydraulic behavior during construction and operation. As output, the analysis aims at answering: i) if the cavern stands sound due to the simultaneous action of the internal pressure variations and salt creep during construction and operation; and ii) how the hydraulic properties of the cavern evolve with time.

### 6.2. Lithology and geomechanical model

A representative scenario of a Brazilian Pre-salt environment in Santos basin is considered. The rock stratum is composed of argillite, shale, sandstone and a salt (halite) layer that hosts the cavern. In this region, the water depth is of 2,149 meters. A basement layer below the elevation -4,980 meters is assumed. The cavern develops within the interval from -2,901 to -3,201 meters inside the halite layer. A protection slab of 200 meters of halite above the cavern is ensured. The final geometry of the cavern ideally approximates a capsule shape with 100 meters in diameter and 300 meters in maximum height. These dimensions make up a nominal volume of  $2.09\text{E}+06 \text{ m}^3$ . However, the storage volume is smaller than that

---

<sup>53</sup> Parts of this chapter were revised and extended for presentation from the article "Salt caverns history and geomechanics towards future natural gas strategic storage in Brazil" written by the author and the advisors of the thesis (Firme et al., 2019) and published in Journal of Natural Gas Science and Engineering. In this thesis, the numerical simulations have been carried out in GeMA. The repercussion of the mechanical response on the hydraulic behavior of the cavern is a contribution of the thesis – it is not available in the original publication.

since there is insoluble material deposited on the cavern floor and blanket material around the cavern roof.

The geomechanical model is axisymmetric and the finite element mesh is composed by 8-node quadratic elements with reduced integration (type “Q8”). The lateral and bottom limits are far enough from the cavern to avoid spurious boundary effects. Figure 55 shows the geomechanical model, the finite element mesh and the main attributes.

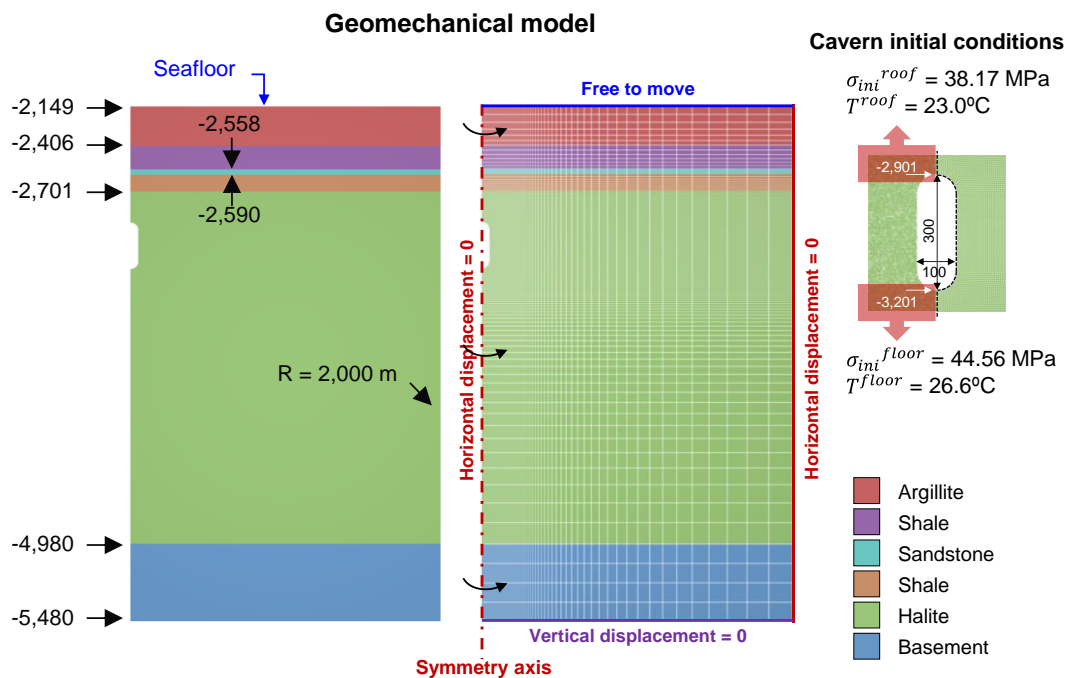


Figure 55. Axisymmetric finite element model of the salt cavern. Elevations and dimensions in meters.

### 6.3. Initial and boundary conditions

The initial (geostatic) stresses are assumed isotropic and are assigned by the superposition of the gravitational loads<sup>54</sup> ensuring that the model initializes with null deformations. Similarly, the temperature estimation is based on geothermal gradients. The density values and the geothermal gradients are given in sections 2.5.3 and 4.4.1 respectively. Figure 55 indicates the calculated in-situ stresses (compression) and temperatures at the cavern roof and floor (38.17-44.56 MPa and 23.0-26.6°C respectively).

<sup>54</sup> In the current version of this study, the pore pressure effects are not considered in the model. The standard sedimentary rocks are considered as limiting layers of the salt formation.

Regarding the boundary conditions, the left (symmetry axis) and right borders have displacements restricted in the x-direction and those of the bottom border are restricted in the y-direction. The top border is free to move since it represents the seafloor (see Figure 55). Furthermore, to analyze the cavern response during the construction, solution mining is represented by a transient pressure acting in the cavern. The procedure for that is seen in more detail in Section 6.4.1. During the cavern operation, the range of operating pressures inside the cavern is limited by the roof stress ( $\sigma_{ini}^{roof}$ ). The minimum stress acting on the cavern is taken in order to avoid hydraulic fracturing. Since the salt formation is under an isotropic initial stress state, the reference stress for this purpose is 38.17 MPa. Considering a natural gas storage application, the minimum pressure value ranges from 30% to 50% the reference stress (Costa et al., 2015). In this application, the minimum gas pressure ( $p_g^{min}$ ) has been taken as 50% of  $\sigma_{ini}^{roof}$  to avoid dilation. The maximum gas pressure ( $p_g^{max}$ ) value ranges from 70% to 90% of  $\sigma_{ini}^{roof}$ . The upper percentage, 90% (Minkley et al., 2015) is adopted in order to maximize gas pressure range.

#### **6.4. Hypotheses, methodology and alignment with international literature**

This study is carried out in the light of the following hypotheses: i) the final shape of the cavern is known and it is affected only by salt creep; ii) the analysis is mechanical and the temperature effect is considered as a parameter of the constitutive model of creep; iii) the changes in the hydraulic behavior are credited only to the mechanical response; iv) thermal fractures, spalling and other sorts of material damage that result in geometry change are not considered; v) the well for cavern construction remains sound and does not influence globally the mechanical behavior of the cavern so that the numerical model represents only the cavern inside the rock formation; vi) the cavern is centered in the lithology model; and vii) there is a significant horizontal continuity throughout the cavern immediate surroundings.

The temperature field is known in advance. Although the temperature varies with depth, the values are constant in each coordinate and do not vary with time so that only the time-dependent mechanical problem needs to be solved. Therefore, a simplified form of the TM+H approach (see Section 2.5.1) is adopted in which the thermomechanical problem turns into a mechanical problem. More so, the cavern surroundings may be hydraulically disturbed from the beginning of

construction on since the mechanical response impacts the hydraulic behavior of salt. Analyzing the hydraulic changes occurred in the cavern is one of the main contributions of this study in relation to the previous ones carried out by the author and those available in the literature. Just like in the previous case (see Section 5.4), an initial porosity of 0.01 and an initial permeability of  $9.0E-16 \text{ m}^2$  ( $\sim 0.91 \text{ mD}$ ) are considered (Stormont et al., 1991). Salt creep is simulated using the EDMT model and the non-salt sedimentary rock layers (argillite, shale and sandstone) follow an elastoplastic behavior according to the Mohr-Coulomb criterion with non-associative flow rule. The rock properties are summarized in Section 2.5.3. Shale properties are also adopted for argillite and the basement layer is modelled using basalt properties.

The cavern integrity is monitored over an operation period of 50 years (plus the construction period). Two engineering criteria related to strains and stresses apply (Costa et al., 2015). The first criterion refers to the accumulated strains. Over the cavern lifespan, the accumulated strains cannot exceed 10% and strain rates cannot exceed  $5.0E-07 \text{ h}^{-1}$ . The second criterion refers to damage and is monitored using the dilation indicator. This ratio is calculated based on DeVries' dilatancy boundary in the case of salt and based on the Mohr-Coulomb criterion in the case of non-salt rocks (see Section 2.1.2.4 and the context of Figure 35). Considering a safety margin against damage, the dilation indicator should not exceed 0.6 over the cavern lifespan. If salt exceeds this value, this does not mean that it is damaged (since dilation is identified by a unity value of this ratio), but it would cast an undesirable integrity condition.

The mechanical analysis of the cavern comprises the periods of construction and operation. Each of these periods presents specific responses. Therefore, they are treated separately in sections 6.4.1 and 6.4.2 respectively.

#### **6.4.1. Cavern construction**

The simulation of the cavern construction opening by solution mining follows a mechanical approach using a transient pressure acting upon the cavern wall. This approach does not describe the geometry evolution over the dissolution process – the final geometry must be known in advance. This methodology, however, seeks a better definition of the stress changes caused to get a particular geometry by reproducing the gradual lateral unloading around the cavern during

dissolution and subsequent steps. Figure 56 schematizes the steps of the cavern construction.

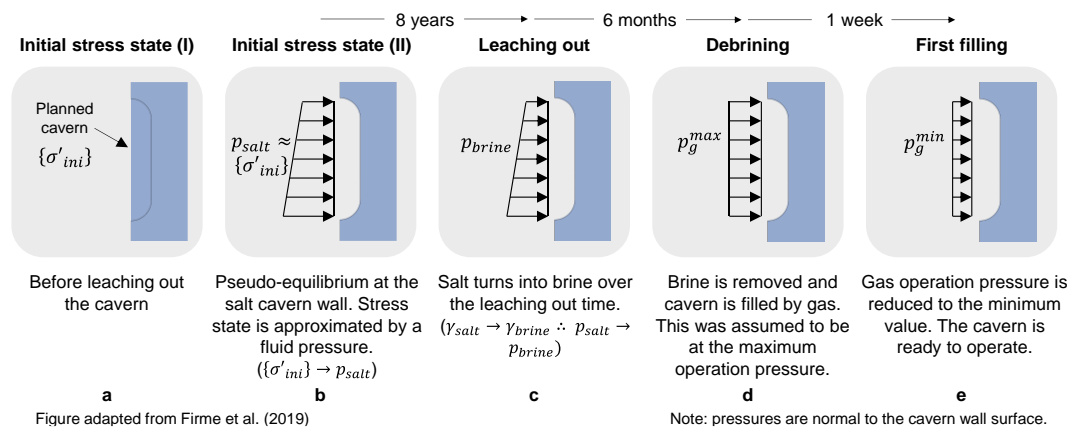


Figure 56. Cavern construction steps. Adapted from Firme et al. (2019).

Initially, the rock formation is under the geostatic equilibrium (Figure 56 (a)). Then, the cavern construction period starts. This period is didactically divided into four steps: cavern pseudo-equilibrium, leaching out, debrining and first filling. Firstly, the elements corresponding to the cavern are removed and a salt-equivalent fluid pressure,  $p_{salt}$ , is applied simultaneously upon the cavern wall, so that  $p_{salt} \approx \{\sigma'_{ini}\}$ . This pressure virtually replaces the pre-existent stress state  $\{\sigma'_{ini}\}$  over the cavern wall and ensures the removal of elements produces essentially null deviatoric stresses. Thus, there is a pseudo-equilibrium of the cavern wall (Figure 56 (b)). Secondly, the leaching out step simulates in a mechanical sense the salt turning into brine over time. The unit weight adopted in the salt-equivalent fluid pressure ( $p_{salt}$ ) is reduced from 21.29 kN/m<sup>3</sup> (salt) to 12 kN/m<sup>3</sup> (brine) over time considering a realistic dissolution rate. Therefore, salt-equivalent pressure gradually turns into brine-equivalent pressure ( $p_{salt} \rightarrow p_{brine}$ ). Considering an average dissolution rate of 30 m<sup>3</sup>/h (Lux and Düsterloh, 2015) and the nominal volume of the cavern, this procedure results in a leaching out period of nearly 8 years (Figure 56 (c)). Literature presents similar mechanical approaches for the solution mining process. DeVries et al. (2005) for instance remove the cavern corresponding elements, apply a boundary pressure equivalent to the brine pressure and let the cavern wall deform by creep by 1.5 years, which is the estimated leaching out period in their work. Khaledi et al. (2016) divide their cavern into smaller regions and remove each region at a 160 day-interval. Wang et al. (2018) use a methodology such as the adopted here, reducing the internal pressure from the salt-equivalent value to the brine-equivalent value over the leaching out period observed in the field. Thirdly, the debrining phase consists of

withdrawing the brine and filling the cavern with gas (Khaledi et al., 2016). The hydrostatic brine-equivalent pressure now turns into the uniform gas operation pressure. This is a less time-consuming process (in the order of months). In this study, it is assumed to take 6 months and the gas pressure is taken as the maximum operational value ( $p_{brine} \rightarrow p_g^{max}$ ), Figure 56 (d). Finally, there is the first filling phase (Khaledi et al., 2016), which is a quick process. In this phase, the gas pressure is rapidly reduced to the minimum operational pressure ( $p_g^{max} \rightarrow p_g^{min}$ ). This step is assumed here to take a one-week period (Figure 56 (e)). After these four steps, the cavern is ready to operate.

#### 6.4.2. Cavern operation

As the cavern is ready to operate, the use of the storage space over time is represented by the internal pressure scheme. For that, it is assumed an annual operation cycle for gas pressure presented by Costa et al. (2015), which is related to the contingent use of the cavern. Other examples of cavern operation pressure schemes are found in the works of Xing et al. (2015), Khaledi et al. (2016), Mahmoudi et al. (2017), Wang et al. (2018), among others. Figure 57 depicts the operation scheme. The cavern stays at minimum internal pressure over 305 days of a year (Figure 57 (a), (b)). Next, the pressure is raised to the maximum value during 30 days (Figure 57 (c)) and it decreases to the minimum value during 30 days (Figure 57 (d)), ending a one-year cycle. This scheme applies annually until the end of the cavern lifespan. Furthermore, Figure 58 presents the evolution of the internal pressure over the operation period applied to this study. The main pressure stages (when the minimum and maximum values apply) are indicated with “1”, “2” and “3”.

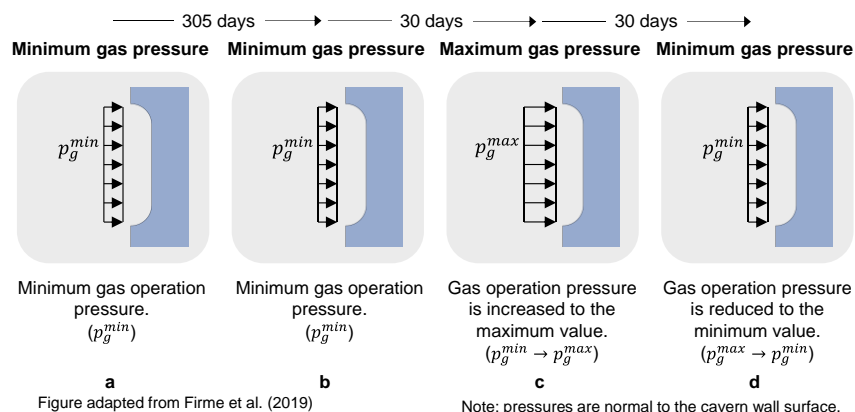


Figure 57. Cavern operation scheme workflow. Adapted from Firme et al. (2019).

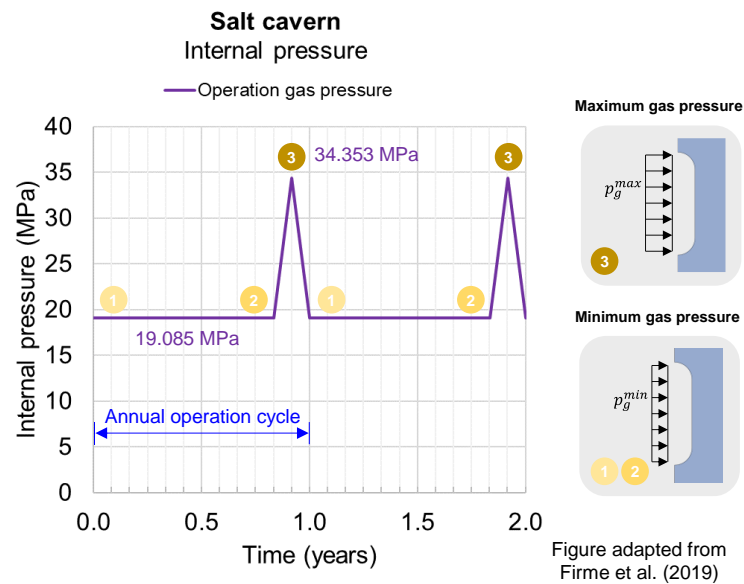


Figure 58. Cavern operation scheme applied to this study. Adapted from Firme et al. (2019).

## 6.5. Results and discussions

For a better exposition, the results of this case study are divided into the two periods of the cavern: construction and operation. Each of these groups of results is presented and discussed in the sections below.

### 6.5.1. Construction period

During the cavern construction period, the main variables to be controlled are the stresses, strains and by-variables in order to make sure that the mechanical simulation of the cavern construction does not produce severe stress changes and hydraulic perturbation in the model.

Figure 59 shows the evolution of the internal pressure and of the deviatoric stresses at control points of the cavern (roof, half-height and floor) during the construction period. Similarly, Figure 60, Figure 61 and Figure 62 present respectively the corresponding Lode angle, dilation indicator and volumetric strain over the same period. In the leaching out step (Figure 59 (a)), the deviatoric stress does not increase much (a little over 5 MPa) with the reduction in the internal pressure acting upon the cavern wall, which represents the salt turning into brine over time. Deviatoric stresses of low magnitude after 8 years are a reasonable output considering the stress changes of small magnitude caused by the dissolution around the cavern wall. In this sense, the methodology has behaved

coherently. The Lode angles (Figure 60 (a)) of the cavern roof and floor converge to that of extension ( $-30^\circ$ ), while the half-height converges to a little below zero (isochoric shear), similar to the Pre-salt well study (see Figure 50 (a) and context). These results reflect on relatively low values of dilation indicator (Figure 61 (a)) and volumetric strain (Figure 62 (a)).

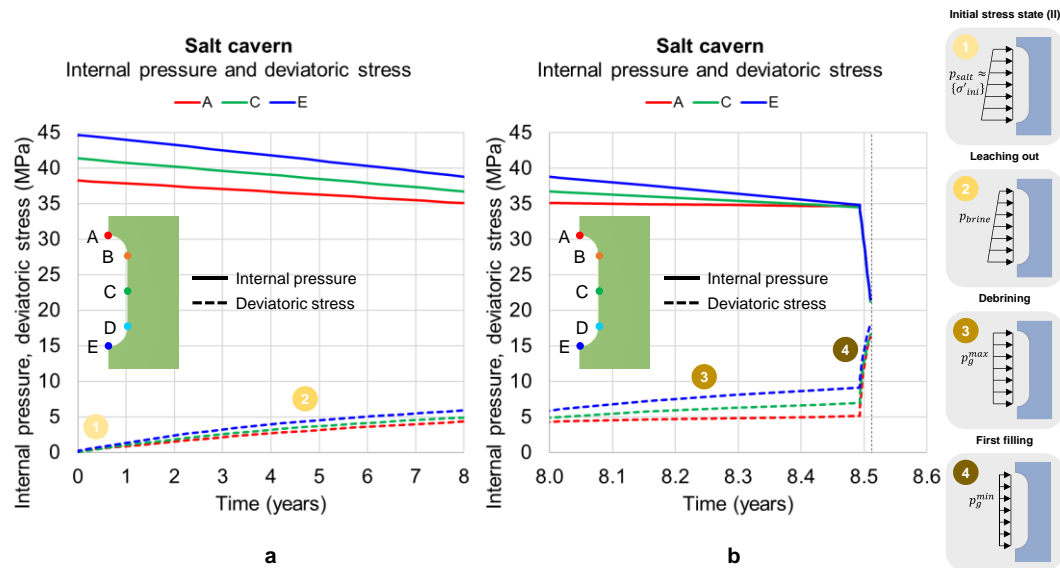


Figure 59. Internal pressure and deviatoric stress over the construction period: interval between pseudo-equilibrium and leaching out (a); and interval between leaching out and first filling (b).

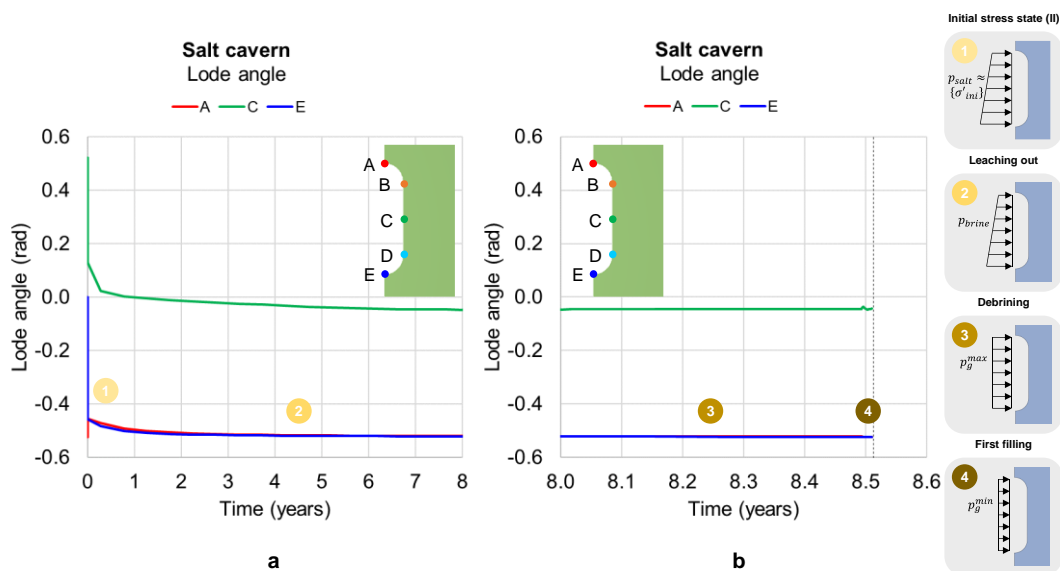


Figure 60. Lode angle over the construction period: interval between pseudo-equilibrium and leaching out (a); and interval between leaching out and first filling (b).

In the debrining and first filling steps (Figure 59 (b)), it can be noticed that the internal pressures on the cavern roof, half-height and floor converge to the same value 6 months after the leaching out step. This is expected since the brine hydrostatic pressure turns into a gas uniform pressure. As a consequence, the

deviatoric stresses increase due to the internal pressure reduction. Considering that the same pressure is applied to different elevations (roof, half-height and floor), deeper elevations undergo higher stress deviations. The same behavior is observed in the dilation indicator (Figure 61 (b)) and generally in the volumetric strain (Figure 62 (b)). The exception is the volumetric strain of the roof, which does not vary significantly – it is likely due to the operation pressures, which are limited to the stress at the cavern roof; therefore, this region is subjected to lower stress deviations than the half-height and the floor. The Lode angles (Figure 60 (b)) also do not exhibit significant changes.

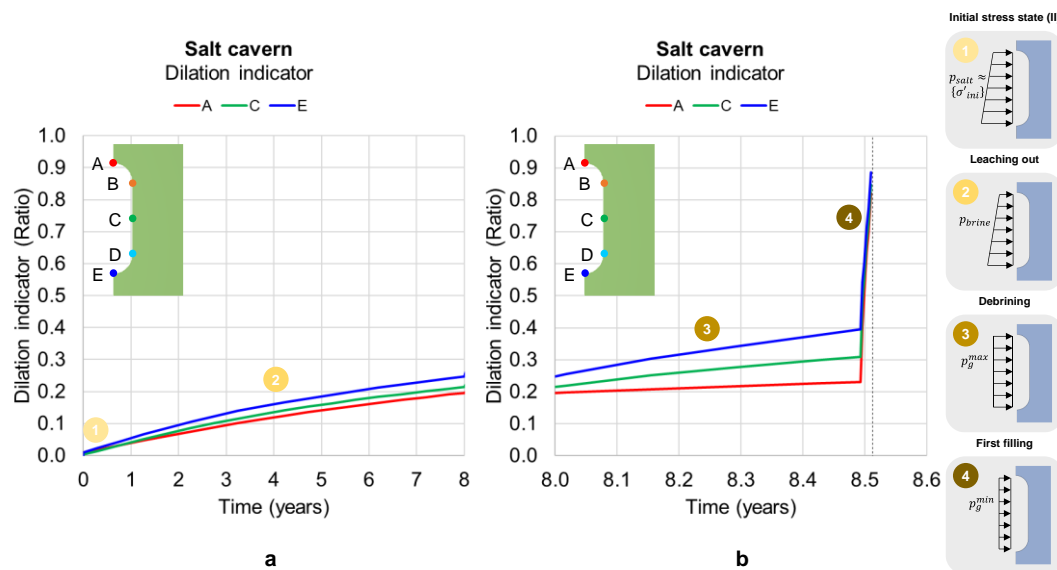


Figure 61. Dilation indicator over the construction period: interval between pseudo-equilibrium and leaching out (a); and interval between leaching out and first filling (b).

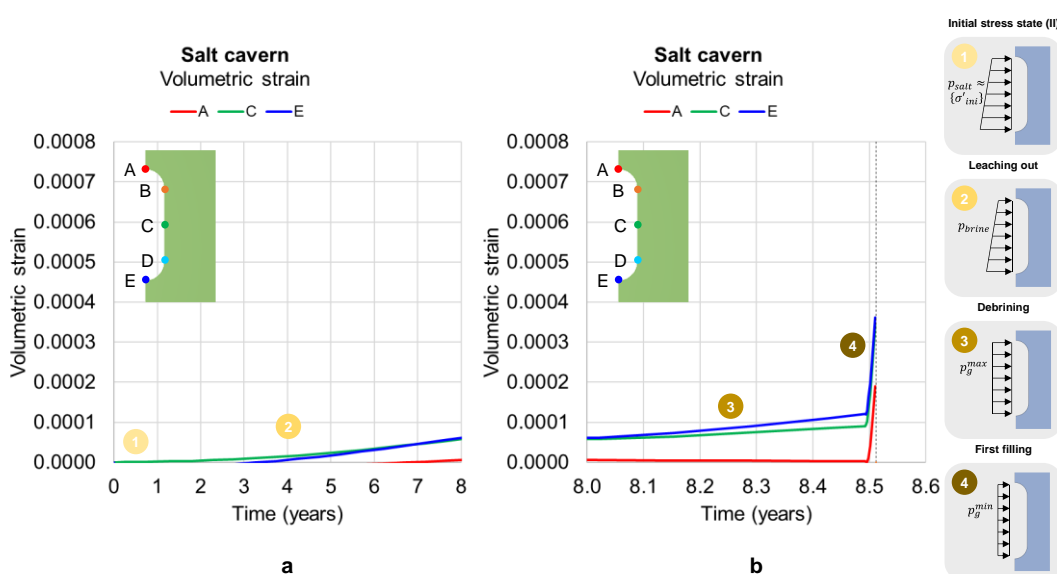


Figure 62. Volumetric strain over the construction period: interval between pseudo-equilibrium and leaching out (a); and interval between leaching out and first filling (b).

Next, a severe internal pressure reduction from the maximum to the minimum operational pressure – the first filling step – triggers a strong increase in the deviatoric stresses in the cavern wall (Figure 59 (b)). The Lode angles do not exhibit significant changes despite subtle ripples during first filling step (Figure 60 (b)). By observing the values of the dilation indicator in this step (Figure 61 (b)), the project limit for this parameter (0.6) is exceeded although none of the control points undergoes dilation. Thus, this is not faced as a prohibitive condition at first. The evolution of the ratio is monitored over the lifespan to provide the big picture of the cavern integrity. Figure 62 (b) shows an increase in the volumetric strains; however, values are still low, indicating no meaningful dilation.

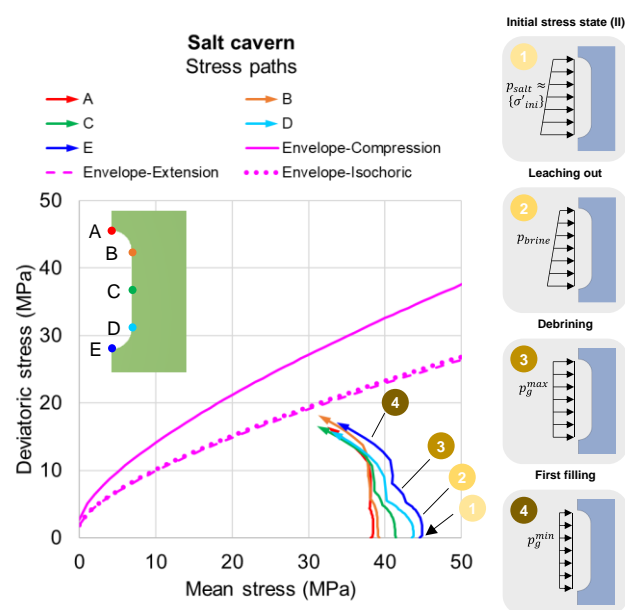


Figure 63. Stress paths of the cavern wall over the construction period.

Additionally, Figure 63 presents the stress paths at five control points of the cavern wall (the three previously mentioned plus two intermediate points). Unloading stress path trends are developed in accordance with the stress changes caused by the construction. These paths remain inside the admissible domain – below the extension envelope in special, since the cavern roof and floor deform exhibiting Lode angles that indicate lateral extension. Nevertheless, although the dilatancy boundaries are not exceeded, the final locations of the paths in the end of the construction period are close to the extension and the isochoric envelopes. This justifies the high values of dilation indicator observed in Figure 61 (b).

Once the mechanical problem is solved, the next step is to verify the repercussion of this response on the hydraulic behavior of the cavern (see sections 2.5.1 and 5.5.3). The solution mining and the subsequent construction steps create

a mechanically disturbed region around the cavern. Since tightness is essential for storage caverns, the changes in the hydraulic behavior of the salt cavern should be analyzed from the beginning of construction on.

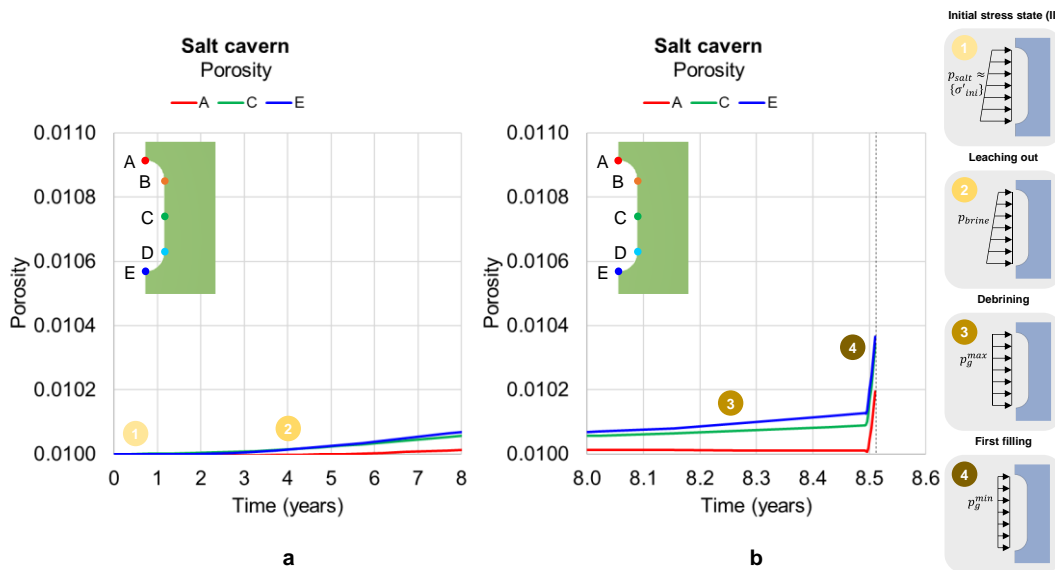


Figure 64. Porosity over the construction period: interval between pseudo-equilibrium and leaching out (a); and interval between leaching out and first filling (b).

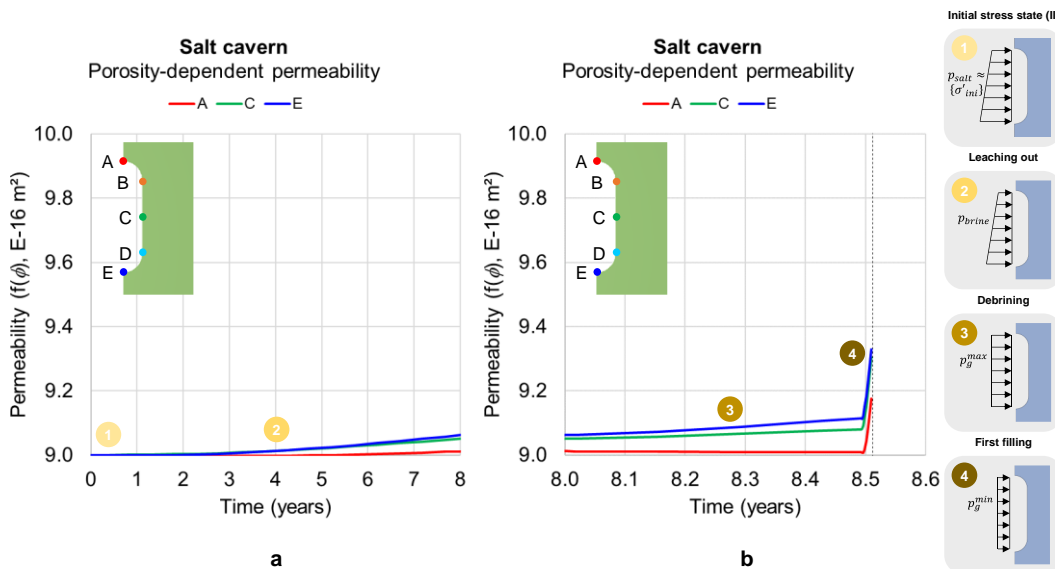


Figure 65. Porosity-dependent permeability over the construction period: interval between pseudo-equilibrium and leaching out (a); and interval between leaching out and first filling (b).

Having the volumetric strains (Figure 62) and using equation (29), Figure 64 shows the porosity at the previously indicated control points of the cavern. Next, the porosity-dependent permeability is calculated using equation (28) and the mean stress-dependent permeability is calculated adopting equation (30), Figure 65 and Figure 66 respectively. In the leaching out step, the results of porosity

(Figure 64 (a)) and of porosity-dependent permeability (Figure 65 (a)) have followed the same trend of the volumetric strains, i.e., a very subtle increase in the cavern floor and half-height and with almost no changes in the roof. This is in line with the observations in the previous study (see Section 5.5.3). The increase in porosity is physically coherent since the volumetric strains trigger pore enlargement and microcrack opening as the salt region becomes prone to dilation. Observing the mean stress-dependent permeability (Figure 66 (a)), similar concepts are noticed; however, the magnitude of the changes is larger than in the porosity-dependent permeability. In the debrining step, the porosity (Figure 64 (b)), porosity-dependent permeability (Figure 65 (b)) and mean stress-dependent permeability (Figure 66 (b)) continue increasing subtly. In the first filling step, these three variables increase sharply following the same trends of the volumetric strains. From start to finish of construction, the maximum change in permeability is from  $9.0\text{E-}16$  to  $30.7\text{E-}06$   $\text{m}^2$  in the cavern floor (3.4 times the initial value) considering the dependence on the mean stress. In the same period, the porosity varies from 0.01 to 0.01036 (1.036 times the initial value). The change in the porosity-dependent permeability follows the same rate of the porosity since the correlation (equation (28)) is linear when using a unity power.

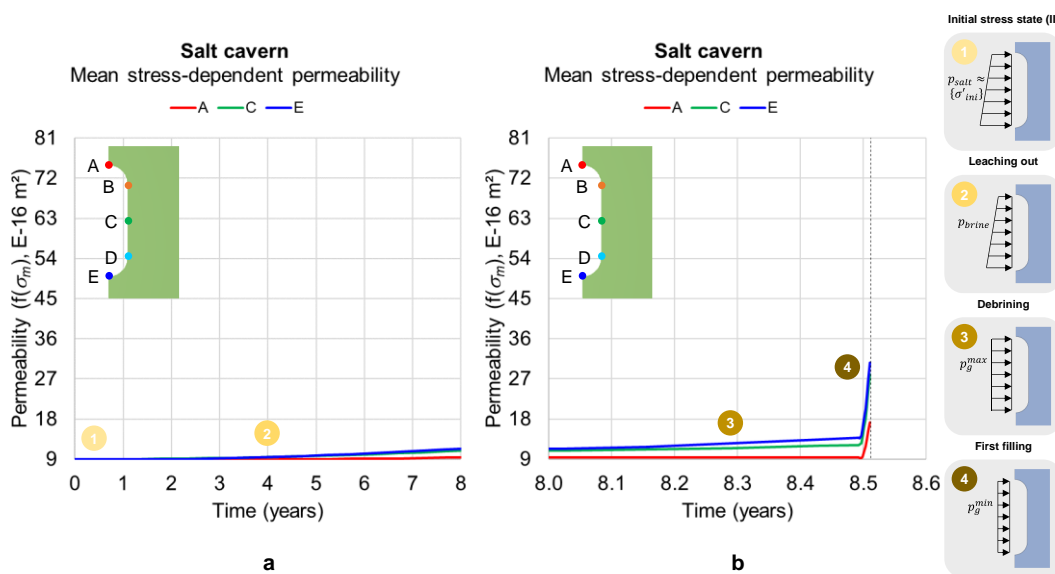


Figure 66. Mean stress-dependent permeability over the construction period: interval between pseudo-equilibrium and leaching out (a); and interval between leaching out and first filling (b).

### 6.5.2. Operation period

In order to emphasize the mechanical behavior and the hydraulic changes of the cavern over the operation period, the results corresponding to the construction

period are hidden from now on. In the following plots, the starting times (0 years) refer to the beginning of the operation.

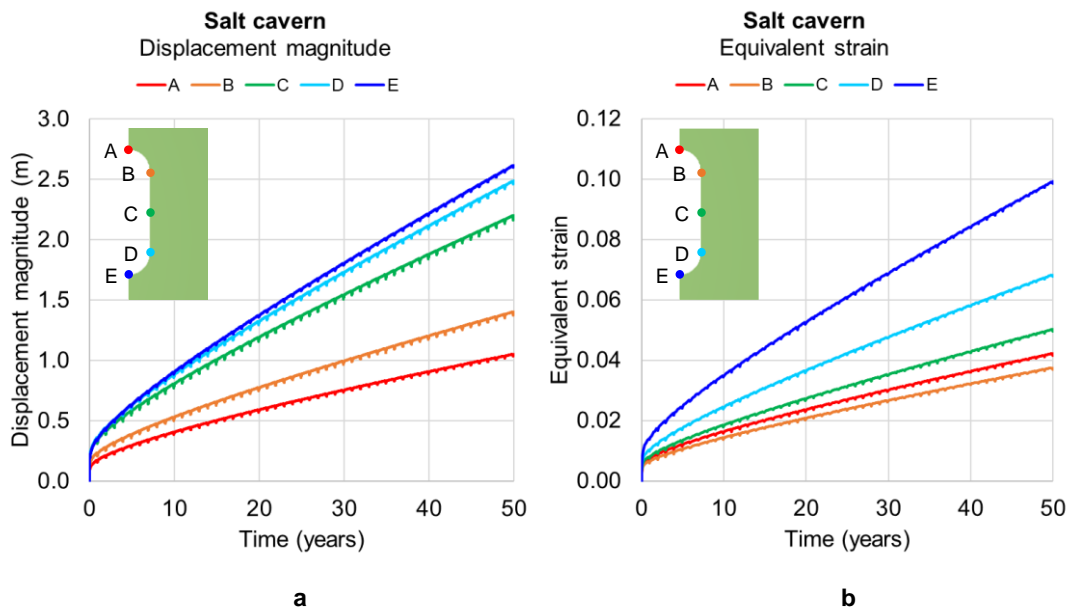


Figure 67. Displacement magnitude (a) and equivalent von Mises strain (b) of the cavern wall over the cavern lifespan.

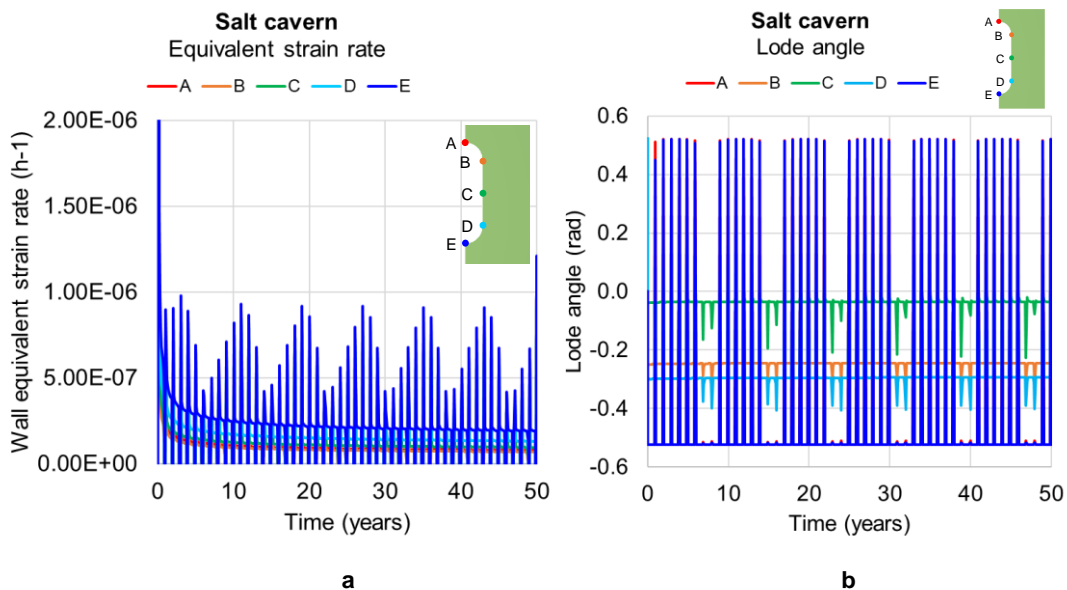


Figure 68. Equivalent von Mises strain rate (a) and Lode angle (b) of the cavern wall over the lifespan.

Figure 67 (a) shows the displacement magnitude of the cavern wall over the lifespan. The peaks along the curves are related to the 60-day loading/unloading periods of the gas pressure in the cavern (see Figure 58). The displacement magnitudes at lower-elevation points (D and E) are more than double the roof subsidence (point A). This is somehow expected since the stratification of standard sedimentary rocks above the salt cavern contributes to support the cavern roof,

and shallower elevations (points A and B) develop lower deviatoric stresses in comparison to deeper elevations. For the sake of reference, considering this cavern and having in mind the differences in the model and methodology, Costa et al. (2012) have obtained roof, half-height and floor displacements of about 0.75, 1.8 and 1.8 meters respectively in 30 years of simulation operating at 50% of mean stress of the cavern roof (see Figure 11 of their work). In this thesis, the displacement magnitude values at roof and floor are very close. The displacement magnitude at the half-height is slightly lower than that of the reference. More so, the cavern floor displacement magnitude after the first loading cycle has been compared to the theoretical elastic value<sup>55</sup> ( $u_{el} = (1 + \nu)\Delta p/E$ ) considering the same pressure variation ( $\Delta p = 15.268$  MPa, see Figure 58). The numerical model has undergone a downward displacement of  $1.77E-02$  meters while the corresponding theoretical displacement was  $8.18E-04$  meters. This indicates that salt creep plays a significant role during the internal pressure variation so that wall strains are not solely elastic. Next, Figure 67 (b) presents the equivalent von Mises<sup>56</sup> strains of the cavern wall over its lifespan. The accumulated strain on the cavern floor (point E) almost reaches the engineering limit of 10% in the end of operation. Nevertheless, this strain criterion is satisfied until 50 years. Still analyzing the engineering criteria, Figure 68 (a) shows the equivalent strain rates of the cavern wall over the lifespan. Notable peaks caused by the discretization of the partial derivative that provides the creep rate and the loading/unloading periods have impaired curve visualization. However, a convergence in the values is noticed in the periods of constant pressure. The creep rates exceed the project limit of  $5.0E-07$  h<sup>-1</sup> in the first years. Nevertheless, the rates evolve to lower values over the cavern lifespan despite the periodic peaks due to loading/unloading. After about two years of operation, all the constant parts of the curves are lower than the project limit, and they reach nearly 50% (or less) of the limit at the end of the cavern lifespan. More so, Figure 68 (b) presents the evolution of the Lode angles with time. Significant peaks are observed during the loading/unloading periods, when stress changes are more significant, but the values return to their original magnitude during the construction period (see Figure 60 and context).

---

<sup>55</sup> This comparison was suggested by an anonymous reviewer during the peer review process of the article "Salt caverns history and geomechanics towards future natural gas strategic storage in Brazil" (Firme et al., 2019) in the Journal of Natural Gas Science and Engineering. This contribution is sincerely acknowledged.

<sup>56</sup> "von Mises" refers to the flow rule adopted in the generalization for the multi-axial space.

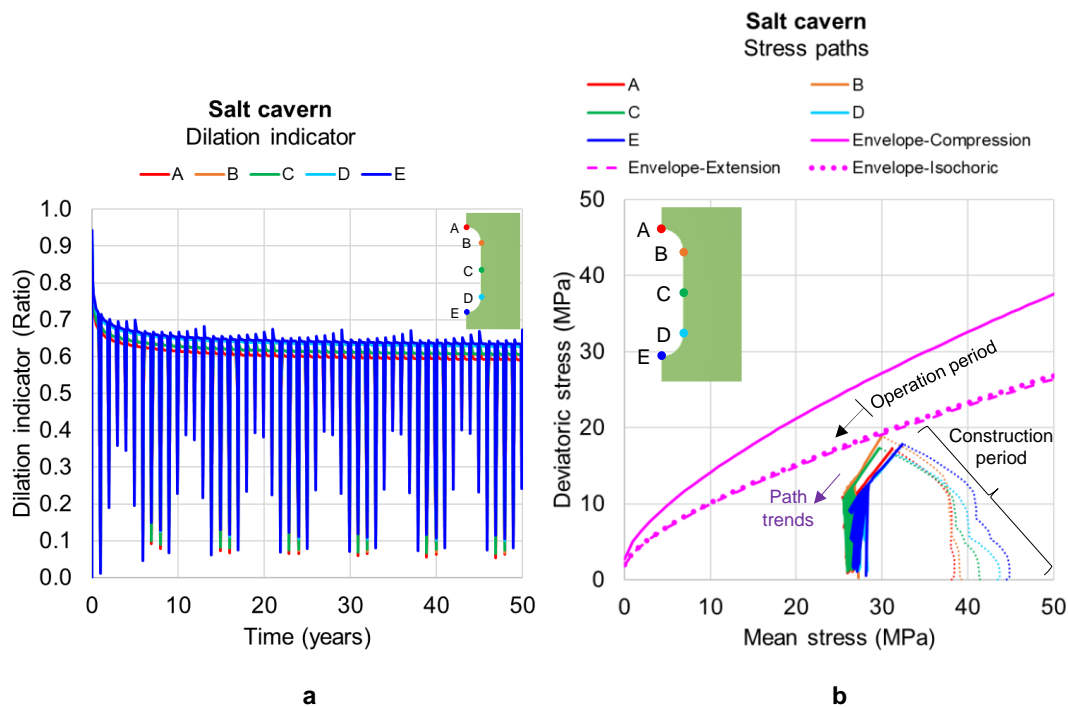


Figure 69. Dilation indicator of the cavern wall over the lifespan (a) and stress paths over the operation period (b).

In order to analyze the cavern integrity, Figure 69 (a) shows the dilation indicator of the cavern wall over the lifespan. As with the strain rates, notable peaks are observed. Higher values are present in the beginning of the operation due to the first filling step in the construction (see Figure 61 and context), but these values evolve to an almost horizontal trend with time. This effect is expected since the cavern wall alleviates stresses by creep leading to ever lower deviatoric stresses (and consequently lower ratios) until a new loading/unloading cycle occurs. The highest long-term ratio is about 0.673. In addition to that, Figure 69 (b) shows the stress paths at the five control points of the cavern wall. The paths over the construction time (from Figure 63) are dashed and are still exhibited to provide the whole picture of the stress evolution. Considering the operation period (solid lines), noisy curves are noticed as a consequence of the annual loading/unloading cycles. Nonetheless, the control points are always inside the admissible region and definitely move away from the extension and isochoric envelopes. Despite lying on an admissible domain over its entire lifespan, the ratio values presented in Figure 69 (a) are higher than 0.6. This fact raises an alert regarding the margin of safety of the cavern, although it is not considered prohibitive for the following reasons: the limit of 0.60 is an engineering criterion, seeking to implicitly account for a number of uncertainties that salt cavern projects deal with; and the dilatancy boundary adopted in this thesis, DeVries' boundary, is more restrictive than the

criterion adopted in the original publications of this study (Section 2.1.2.5). To provide the whole picture of the cavern integrity, Figure 70 shows the contour maps of the dilation and shear failure indicator in the model in noticeable periods.

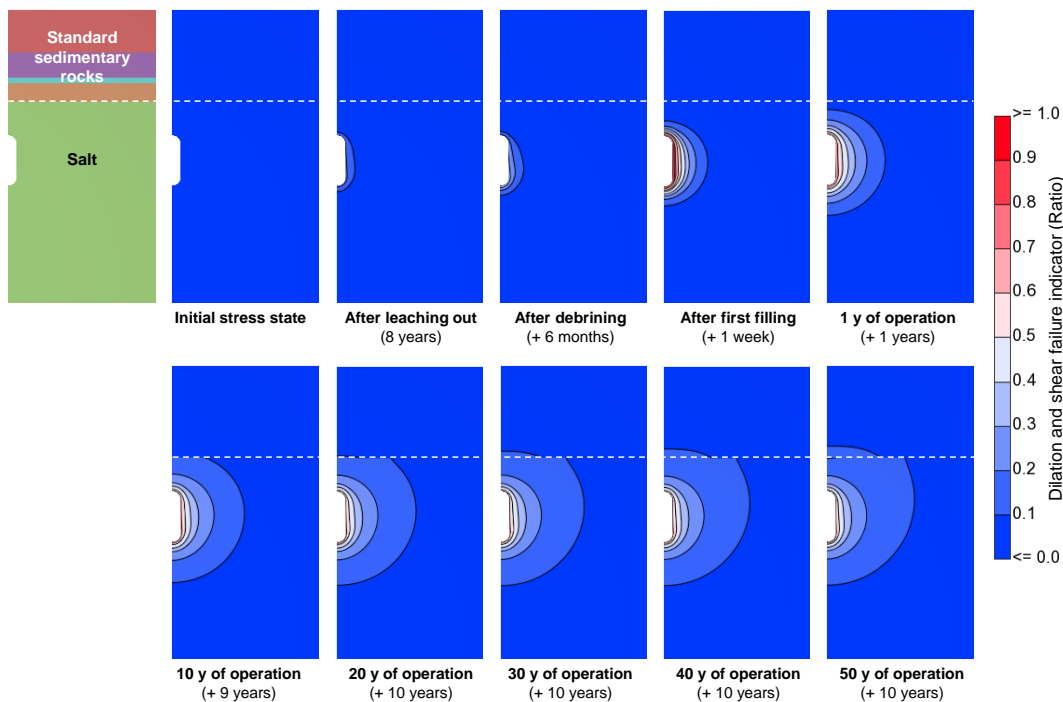


Figure 70. Contour maps of the dilation and shear failure indicators of the cavern over the lifespan.

The previous graphs have shown history results, demonstrating how variables evolve with time. In the following graphs, the dilation and shear failure indicators are exhibited along three key segments throughout the cavern: segment A-F-A', from the cavern roof to the seafloor (model top); segment C-C', from the cavern half-height wall to a distant horizontal coordinate; and segment E-E', from the cavern floor to a deeper elevation. To this end, five noticeable cavern-related times are considered: the one in the beginning of leaching out (I), the one right after leaching out (II), the one right after debrining (III), the one right after the first filling (IV) and the one in the end of cavern operation (V). As previously mentioned, the dilation indicator is calculated considering DeVries' dilatancy boundary in the case of salt and the shear failure indicator is calculated according to the Mohr-Coulomb criterion in non-salt sedimentary rocks (see Figure 35 and context).

Figure 71 (a) presents the dilation and shear failure indicators of the segment A-F-A', where point A corresponds to the cavern roof (elevation -2,901 m); point F is the salt formation top (elevation -2,701 m) and the transition with the standard sedimentary rocks; and point A' is the seafloor and the model top (elevation -2,149 m). Considering the sub-segment A-F, one notices null ratios at the beginning of

the leaching out step (I), as expected from the geostatic pseudo-equilibrium (see Section 6.5.1), and an increase in the ratios close to the cavern roof right after the leaching out step (II). A very subtle increase is observed right after the debrinining step (III). The higher value of dilation indicator (by 0.85) occurs on the cavern roof (point A) right after the first filling step (IV). This is expected since the cavern experiences lower internal pressures and undergoes higher deviatoric stress during this construction step. The curve of the end of the operation (V) shows a decrease in the ratio values close to the roof with time. This is coherent with the fact that the cavern immediate surroundings release stresses by creep. Thus, deviatoric stresses tend to decrease, and so do ratios. In the sub-segment F-A', there is a discontinuity at point F, which is the interface between the salt and the standard sedimentary rocks (non-salt rocks, see also Figure 70). From this elevation upwards, the indicator refers to shear failure and is calculated based on the Mohr-Coulomb model. These layers seem to be relatively insensitive to the cavern construction period since the ratio is negligible during the construction time steps (I, II and III). They accumulate non-negligible ratios only during the cavern lifespan (50 years), although the values are very far from the Mohr-Coulomb shear strength envelope.

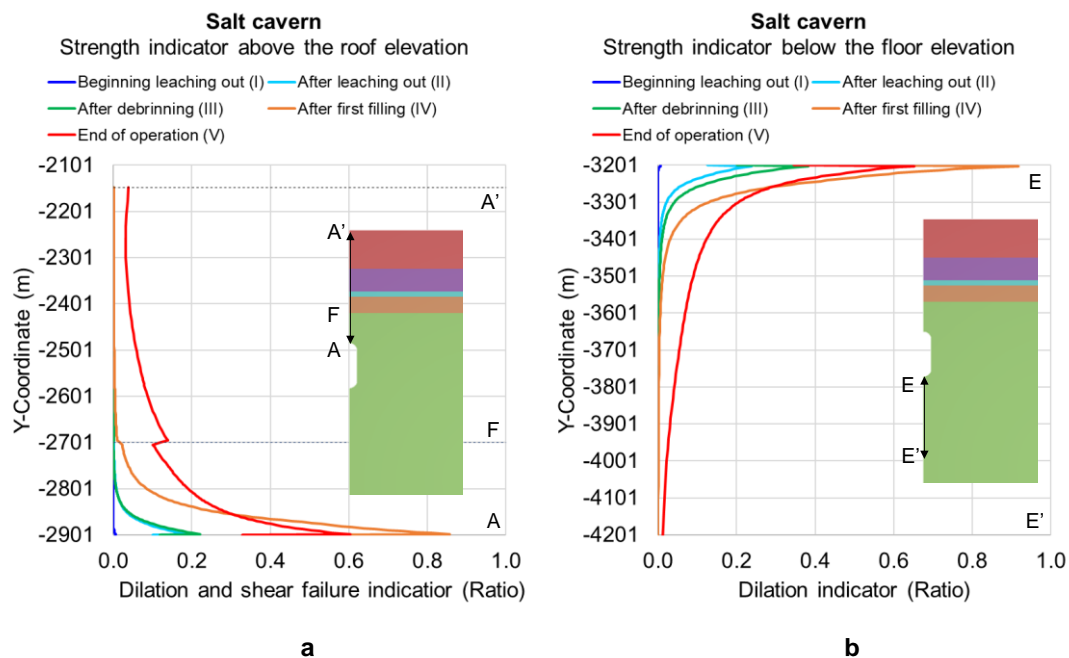


Figure 71. Dilation and shear failure indicators along the vertical segments A-F-A' (a) and E-E' (b) in the cavern model.

Next, Figure 71 (b) shows the dilation indicator of the segment E-E', where point E corresponds to the cavern floor (elevation -3,201) and point E' is 1,000 meters deeper (elevation -4,201 m). The same conceptual observations previously



from the volumetric strains, Figure 73 (b). One observes that the values have not changed substantially after the first years of operation. This is coherent with the fact that volumetric strains tend to constant values over time. Analyzing in the cavern floor, the porosity in the end of the operation is 0.01056. Considering the initial value of 0.01, this porosity change is not relevant for engineering purposes.

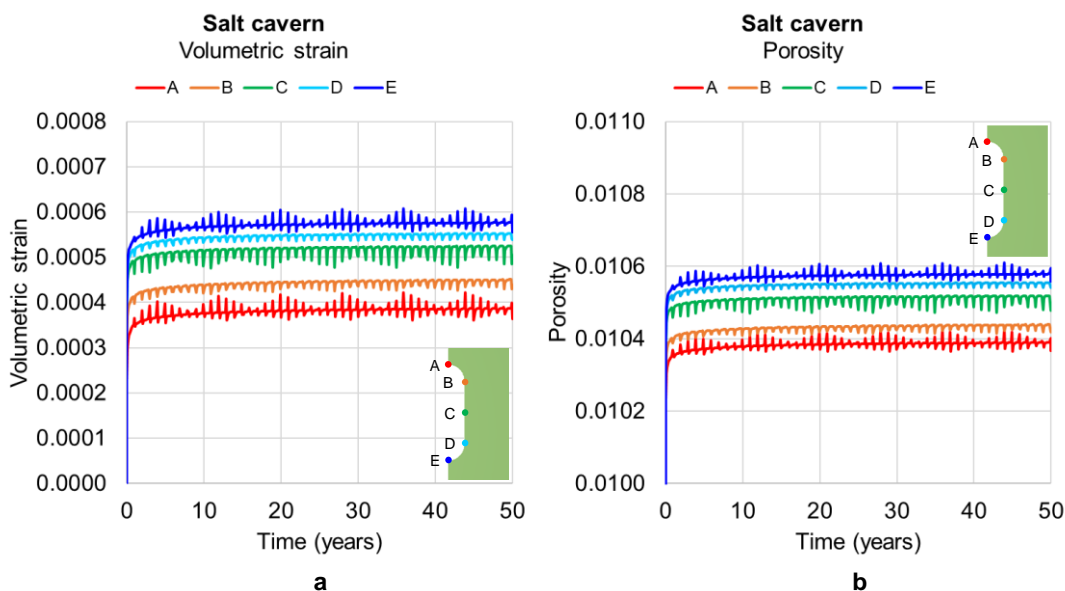


Figure 73. Volumetric strain (a) and porosity (b) of the cavern wall over the lifespan.

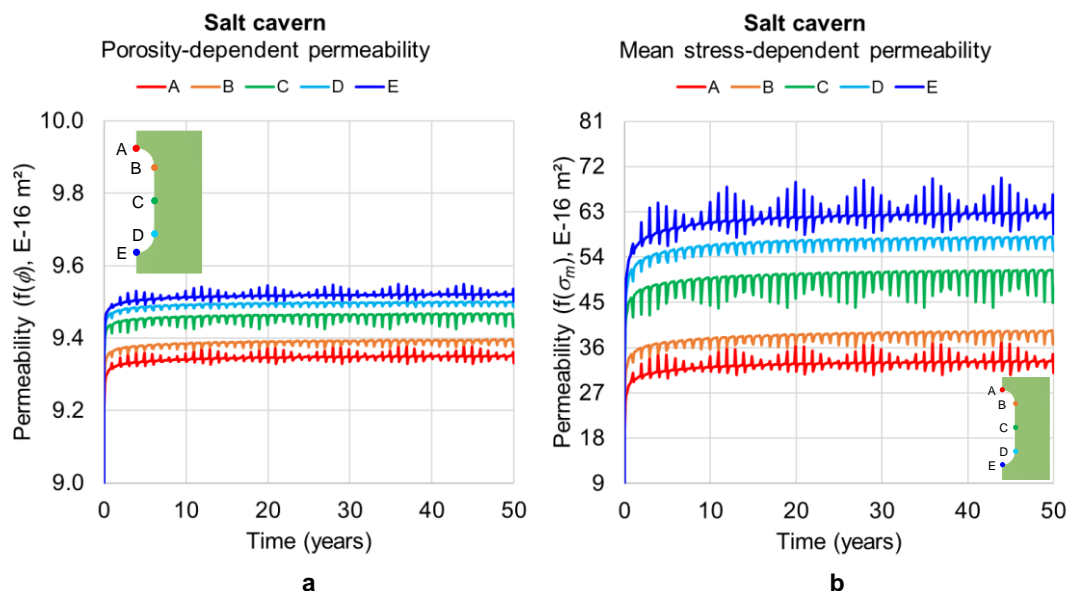


Figure 74. Porosity-dependent (a) and mean stress-dependent (b) permeability of the cavern wall over the lifespan.

The permeability is calculated based on the porosity, Figure 74 (a). Analyzing the cavern floor, the value at the end of the operation is  $9.5022 \times 10^{-16} \text{ m}^2$ . Compared to the initial value, this represents an increase of  $0.5022 \times 10^{-16} \text{ m}^2$  in the porosity-

dependent permeability. Considering all the pressure cycles and the long creep time that the cavern has been subjected to, this change is considered as not harmful for the tightness. Then, the mean stress-dependent permeability is calculated, Figure 74 (b). Also analyzing at cavern floor, the mean stress-dependent permeability at the end of the analysis is  $58.5855E-16$  m<sup>2</sup>, which is about 6.51 times higher than the initial value. This permeability change is more relevant and indicates again that the concept of mean stress-dependent permeability is more adequate in the context of salt openings as mentioned by Kuhlman and Matteo (2018) regarding DRZs.

Since the mean stress-dependent permeability is the hydraulic variable that has suffered the greatest impact from the combined effect of several pressure cycles and salt creep, this is plotted along the three key segments throughout the cavern (A-F-A', E-E' and C-C') previously adopted to show the dilation and shear failure indicator (see Figure 71 and Figure 72). Hence, Figure 75 (a) presents the mean stress-dependent permeability over the segment A-F-A'. By observing the sub-segment A-F (in the salt) during the construction period, the permeability affected region is limited to about 25 meters above the cavern roof and a more noticeable increase occurs after the first filling step. After that, during the operation period, the permeability enhancement evolves significantly and extends up to the salt top (200 meters above the cavern roof), in the transition with the sedimentary stratum. In sub-segment F-A' (non-salt sedimentary rocks), the permeability enhancement is negligible. For the sake of simplicity, the initial permeability of these rocks is considered the same of the salt. Since these non-salt layers are relatively far from the cavern, the changes in stresses and strains do not affect them significantly; therefore, both permeability correlations do not produce meaningful changes. Furthermore, Figure 75 (b) shows the mean stress-dependent permeability over segment E-E'. The results follow the same concepts observed in sub-segment A-F. However, the permeability enhancement is of greater magnitude since the stresses in the lower region of the cavern are higher than those of the upper region, and it reflects on the calculation of the mean stress-dependent permeability. Lastly, Figure 76 presents the mean stress-dependent permeability over segment C-C'. The same concepts observed in segment E-E' apply; the permeability enhancement is lower than it is in segment C-C' since the stress level in the cavern half-height elevation is lower than that of the floor. Although the maximum permeability changes occur in the cavern wall, as indicated in the history plots (see Figure 74 and context), these path plots have succeeded

in show the span of the hydraulically disturbed region around the cavern, in order to guide more in-depth hydraulic/transport-related studies.

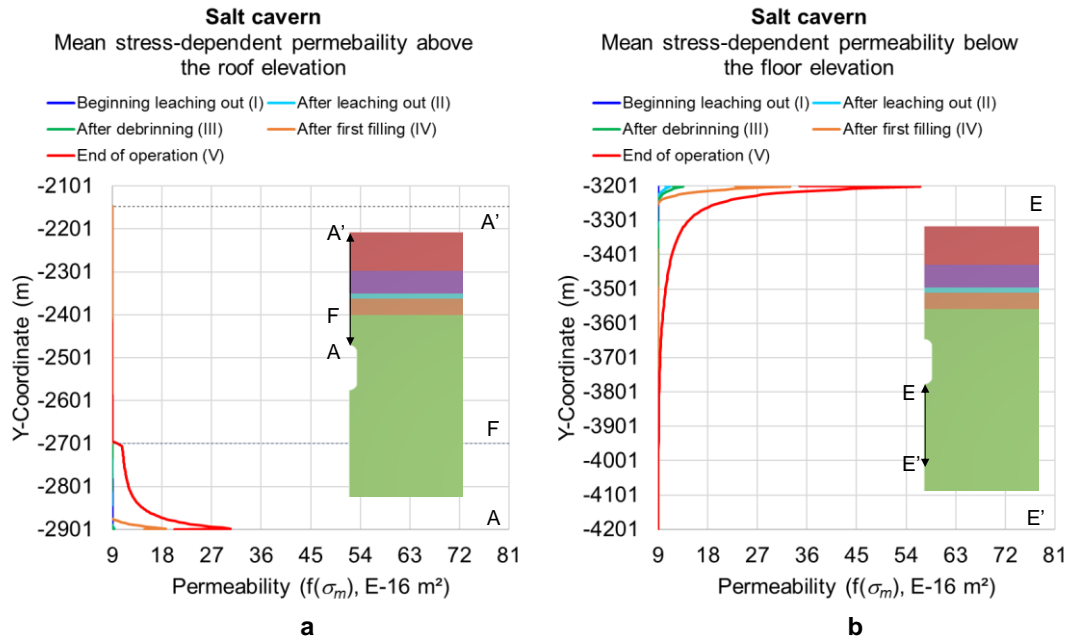


Figure 75. Mean stress-dependent permeability along the vertical segments A-F-A' (a) and E-E' (b) in the cavern model.

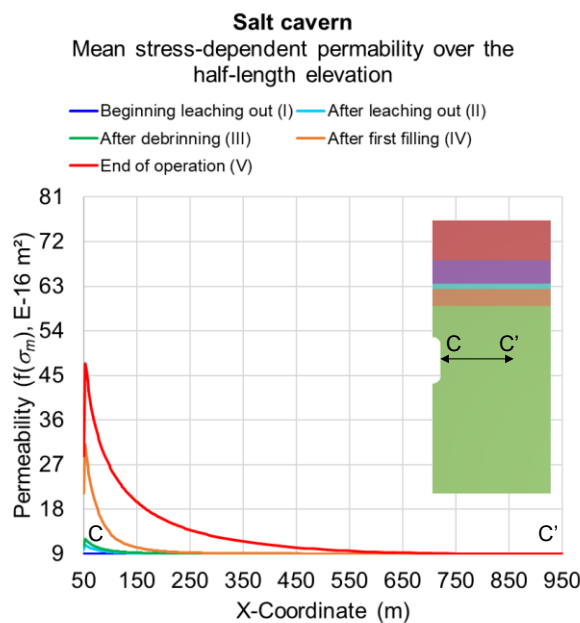


Figure 76. Mean stress-dependent permeability along the horizontal segment C-C' in the cavern model.

### 6.6. Partial conclusions

This case study has demonstrated a compiled methodology to analyze the mechanical response of salt caverns with repercussion on the hydraulic behavior.

The solely mechanical approach has been presented in the past (Firme et al., 2018b, 2019), while the hydraulic post-analysis is a contribution of the thesis. The main objectives were: i) to verify if the cavern stands sound due to the simultaneous action of the internal pressure variation and salt creep during construction and operation; and ii) to analyze how the hydraulic properties of the cavern evolve with time.

The results have shown that: i) the approach to simulate the solution mining and the subsequent cavern construction steps by using a transient pressure has led to physically coherent results in terms of producing low stress and strain perturbations – solution mining is a gradual dissolution process, less mechanically severe than an excavation. The first filling step in the cavern construction period has been the most critical since the cavern experiences the lowest internal pressure very quickly. Moreover, DeVries' dilatancy boundary of salt has not been exceeded at any moment on the cavern wall – the mechanical integrity is maintained; and ii) the porosity and the porosity-dependent permeability enhancements have been subtle during construction and operation – this is coherent with the low volumetric strain variation observed. Furthermore, the mean stress-dependent permeability has shown a significant enhancement with time. As a reference, the final value at the cavern floor was by 6.51 times the initial value. The enhancement span – by a few hundred meters from the cavern walls – is also significant especially by the end of operation.

The mechanical approach for salt caverns suits adequately global stability analyses. This application is expected to serve as a basis for future simulations of cavern abandonment and use for CCS. More specific improvements particularly in representing salt damage and thermal fractures would also be welcome. Regarding the hydraulic response, the permeability dependence on the mean stress has been significant. The maximum permeability value at the end of the analysis is still in the range qualified as disturbed salt (Cosenza and Ghoreychi, 1996). It is yet to be verified whether the increase in permeability and its span around the cavern are sufficient to have a considerable impact on flow/transport through the cavern walls.

## 7

### Case study of salt as caprock of Pre-salt reservoir

#### 7.1.

##### Objective

This chapter presents a case study of a synthetic Pre-salt reservoir overlain by a thick salt layer. The study that originates this application has been developed in the context of carbonate reservoirs with karstic cavities (Firme et al., 2021). In this thesis, the focus is to analyze combined effect of the reservoir compaction/expansion and the salt caprock creep behavior during hydrocarbon production and CO<sub>2</sub> injection. As output, the analyses intend to answer: i) what is the effect of reservoir compaction on salt caprock creep; ii) what is the effect of both compaction and creep on subsidence; iii) how this mechanical response is modified in the case of an injection in the reservoir so that the initial pore pressure is recovered; and iv) what is the effect on the hydraulic behavior of the caprock.

#### 7.2.

##### Lithology and geomechanical model<sup>57</sup>

The lithology has been conceived from seismic logs, geologic horizons, and interpreted facies from Lapa Field, Santos Basin (Brazil), presented by Ribeiro da Silva and Pereira (2017). The geologists' work has been incorporated with simplifications in order to generate a conceptual model that honors the horizons around a real well as much as possible (see Figure 7 of their work). A brief description of the lithology follows. The upper layer is the overburden (elevations from -2,800 to -3,400 meters). This is a sedimentary package composed by siliciclastic rocks. Below the overburden, there is a thick evaporitic rock interval (named Ariri formation). A 1,115 meter-length halite layer and a basal 20 meter-length anhydrite layer above the carbonates are considered (from -3,400 to -4,535 meters). This salt layer acts as the reservoir caprock. Next, geologists have divided the Pre-salt formation in three main facies named Barra Velha, Itapema and

---

<sup>57</sup> Parts of section 7.2 and 7.4 were revised and updated for presentation from the article "Mechanical behavior of carbonate reservoirs with single karst cavities" written by the author and the first advisor of the thesis (Firme et al., 2021) and published in *Geomechanics for Energy and the Environment*. In this thesis, the same lithology is adopted but with another focus. Results and findings are different from the original publication.

Piçarras. Barra Velha is a quality reservoir composed by a vuggy carbonate formation (from -4,535 to -4,800 meters). Itapema consists of dark shale and carbonate (calcirudite, from -4,800 to -5,000 meters). The texture of calcirudite shows shell fragments called “coquinas” (Oliveira et al., 2014; Ribeiro da Silva and Pereira, 2017; Silva, 2016). Piçarras is composed by siliciclastic sediments – conglomerates and sandstone (from -5,000 to -5,250 meters) (Domingues, 2011; Ribeiro da Silva and Pereira, 2017). Finally, the last formation is Camboriu, which consists mainly of basalt (from -5,250 to -7,500 meters) (Silva, 2016). A disk-shaped reservoir with 1,000 meters in radius is assumed in the Barra Velha formation. The lithology is illustrated in Figure 77.

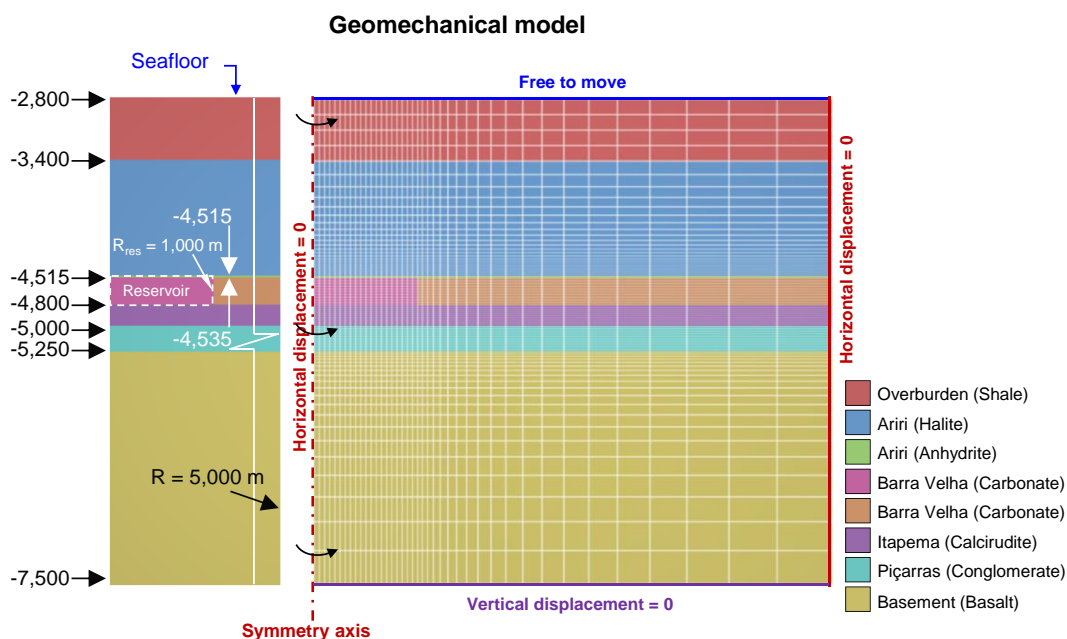


Figure 77. Axisymmetric finite element model of the Pre-salt section. Elevations and dimensions in meters.

The geomechanical model is axisymmetric and the finite element mesh is composed by 8-node quadratic elements with reduced integration. In the reservoir, the elements have quadratic interpolation functions for displacements and linear interpolation functions for pressures following a typical coupled hydromechanical element formulation to simulate reservoir depletion/injection. Outside the reservoir, the elements follow the standard displacement-based formulation. The lateral and bottom limits are far enough from the reservoir to avoid spurious boundary effects in the numerical analyses. Figure 77 presents the geomechanical model, the finite element mesh and the main attributes.

### 7.3. Initial and boundary conditions

To estimate the in-situ stress state, the vertical stresses are calculated by the superposition of the gravitational loads. In the non-salt sedimentary rocks, the effective horizontal stresses consider a horizontal stress coefficient of 0.65, as observed in the carbonates (Silva, 2016). An isotropic stress state is assumed in the evaporites (anhydrite and halite). Initial pore pressures are taken as the hydrostatic column over depth except along the salt interval, where they are null. The specific weight of water of 10 kN/m<sup>3</sup> is adopted. The geostatic stress state is assigned ensuring that the model initializes undeformed. The temperature estimation is based on geothermal gradients. The rock density values and the geothermal gradients are given in sections 2.5.3 and 4.4.1 respectively. Figure 78 (a) shows the initial conditions assigned to the model.

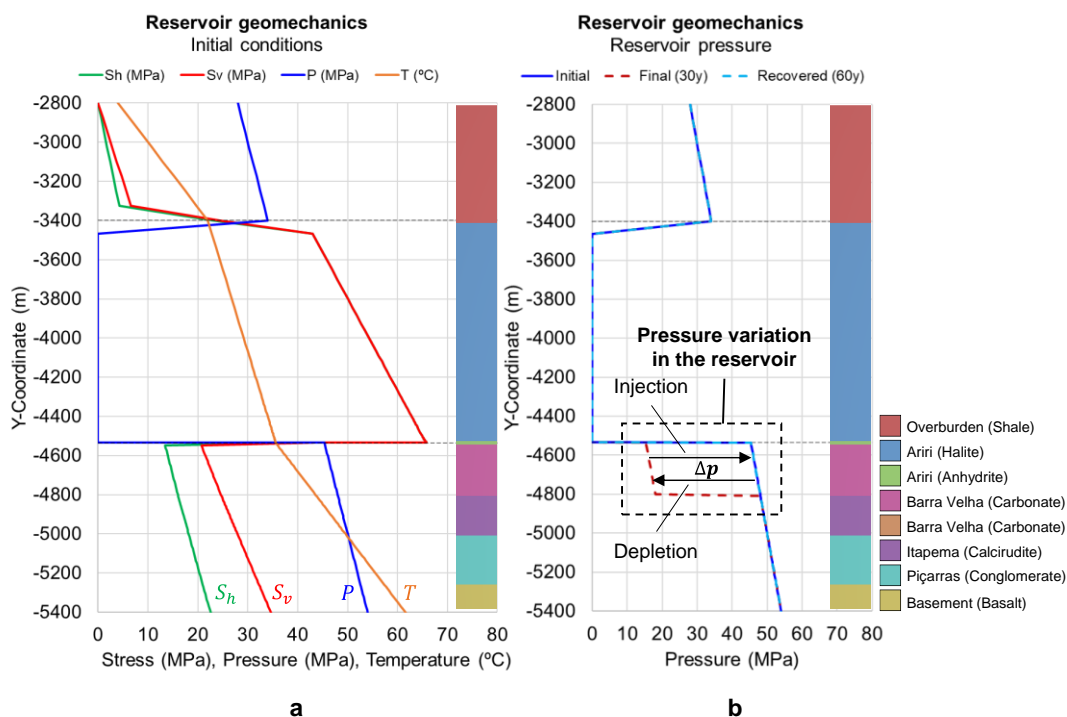


Figure 78. Initial conditions (a) and pore pressure variation (b) assigned to the geomechanical model.

With respect to displacement restrictions, the left (symmetry axis) and right borders are fixed in the x-direction and the bottom border is fixed in the y-direction. The top border is free to move since it represents the seafloor (see Figure 77).

This study is divided into two phases regarding the pore pressure-related boundary conditions, Figure 78 (b). The first phase considers the hydrocarbon production, which is simulated by the reservoir depletion. Two depletion schemes

are assumed, as schematized in Figure 79. The first scheme is linear so that the depletion evolves in such a way that the reservoir undergoes 30 MPa of pore pressure reduction at the end of 30 years (1 MPa/year). The second scheme is a nonlinear synthetic curve which was inspired by a realistic well production curve presented by Mason (2012). The curve shape has been roughly kept while the initial and final values have been set to 0 years and 0 MPa, and 30 years and 30 MPa, respectively. This curve has been adopted to analyze if the reservoir depletion rate influences the salt caprock creep. The second phase of the study considers the subsequent use of the depleted reservoir for CO<sub>2</sub> storage. This is represented by an injection that fully recovers the initial pore pressure of the reservoir. Pressure recovery follows the same schemes and times adopted in depletion. The results considering reservoirs with recovered pressure are compared to scenarios in which the depleted reservoir remains so until the end of the analysis (it is abandoned without recovering pressure). Regardless of the pressure variation scheme, reservoir depletion causes deviatoric stresses in the vicinity. These stresses trigger salt caprock creep deformation and consequently subsidence is influenced both by compaction and by caprock creep. Additionally, some degree of hydraulic perturbation in the reservoir surroundings is expected.

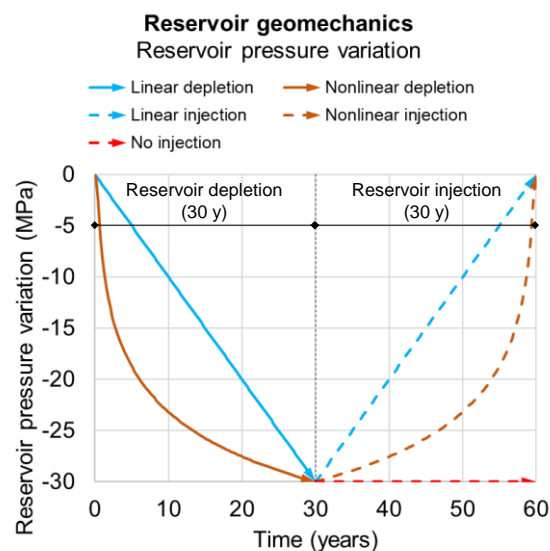


Figure 79. Schemes of reservoir depletion and injection.

#### 7.4. Hypotheses, methodology and alignment with international literature<sup>58</sup>

This study is carried out in the light of the following hypotheses: i) Terzaghi's effective stress principle applies to all the rock layers except salt; ii) the fluid flow

<sup>58</sup> See previous note.

develops in enough time to meet a steady-state condition; iii) the carbonate formation has such a hydraulic transmissivity that it is possible to consider the hydraulic communication inside the reservoir; viii) the pore pressure variation affects the mechanical response of the model, but the opposite is not considered – the scheme is essentially a one-way coupling; v) the reservoir compaction due to depletion closes eventually pre-existing fractures; vi) both the initial pore pressure state and the changes with time are known in advance; vii) the temperature is considered as a parameter of the creep constitutive model – it does not vary with time; viii) the hydraulic changes in the caprock are credited only to the mechanical response to reservoir depletion and injection; and ix) the CO<sub>2</sub> injection impacts the model only in the pore pressure field and in the subsequent mechanical response – thermal and chemical effects are not considered.

Conceptually, the analyses are hydromechanical in the reservoir and mechanical outside it. Due to the effective stress principle, by assuming a unity Biot coefficient and that the total stresses do not change with time, the pressure changes (indicated by the depletion curves) result in the effective stress changes in the reservoir, affecting the surroundings. Therefore, the hydromechanical problem in the reservoir is reduced to a mechanical problem since all degrees of freedom related to pore pressure are pre-defined. As previously mentioned, the temperature field is considered as a parameter of the creep constitutive model. In the end, only the time-dependent mechanical problem has to be solved. In order to analyze the repercussion of reservoir depletion in the hydraulic behavior of salt, an initial porosity of 0.01 and an initial permeability of  $9.0E-16 \text{ m}^2$  (~ 0.91 mD) are considered (Stormont et al., 1991), as in previous applications (see sections 5.4 and 6.4). These values are compatible with a DRZ around the well, which is implicitly considered in the symmetry axis of the axisymmetric model. Far from the well, lower permeability values would be expected (compatible with undisturbed salt); however, the study is focused on the hydraulic changes triggered by the stress changes around the reservoir; therefore, considering the same initial value highlights the hydraulically disturbed regions.

In the first phase of the study, the role played by reservoir compaction on salt creep and the effect on subsidence is analyzed employing all the four creep models discussed in the thesis (PL, DM, MD and EDTM models). An additional model that assumes salt caprock as a solely linear elastic material (without creep behavior) is considered for the sake of comparison. In the second phase, the effect of a CO<sub>2</sub> injection that promotes a full pressure recovery in the reservoir is analyzed. In this

phase, only EDMT creep and linear elastic (no creep) models are considered. The sedimentary rock layers follow an elastoplastic behavior according to the Mohr-Coulomb criterion with non-associative flow rule. Regarding the properties, the overburden is modelled using typical literature shale properties. Both Barra Velha and Itapema formations (carbonate and calcirudite) are modeled with elastic parameters calibrated by Domingues (2011) for a travertine of Itaboraí, Rio de Janeiro state, Brazil<sup>59</sup>. The Mohr-Coulomb model parameters adopted here have been calibrated by Corrêa (2016) for travertine samples from Acquasanta Terme, Italy. Piçarras formation is modelled using literature properties of conglomerate (Costa et al., 2019a) and the basement takes the properties from Nevada Test Site basalt (Goodman, 1989). Lastly, the salt formation (halite and anhydrite) adopts the same properties as the previous applications. These rock properties are summarized in Section 2.5.3.

Recent works in reservoir geomechanics have adopted similar methodologies. Firme et al. (2014a) have investigated the reservoir compaction and surface subsidence of a synthetic 3D model representative of a North Sea field using elastic and elastoplastic constitutive models. A similar methodology to the one presented here was considered, although salt rocks were not present in the study. Angus et al. (2015) have studied the Valhall reservoir by means of finite element flow-geomechanics analyses to predict seafloor subsidence. The geostatic stresses have been assigned by the superposition of the gravitational loads and effective horizontal stresses through a horizontal stress coefficient. Initial pore pressures have been assigned as the hydrostatic column over depth eventually increased by overpressure. The model top corresponds to the seafloor. A two-way flow-geomechanics coupling has been adopted considering a simulation time of 25 years. Zoccarato et al. (2018) have presented an assessment of the uncertainties associated to the geomechanical parameters of deep hydrocarbon reservoirs. The study has adopted one-way flow-geomechanics coupling by which the pore pressure field is calculated using a multiphase flow simulator and the geomechanical model provides the displacement field and by-variables that result from the pore pressure change. Rocca et al. (2019) have carried out a synthetic case study based on the Adriatic basin (Po Plain, Italy) formations using a 3D finite element model to predict subsidence. Rock material behavior follows the elastoplastic model with a Mohr-Coulomb criterion. Initial

---

<sup>59</sup> According to Domingues (2011), the travertine of Itaboraí is considered a Pre-salt carbonate reservoir analog based on the presence of quartz in the mineralogy and its apparent strength.

conditions have also been assigned to the model considering the superposition of the gravitational loads, the horizontal stresses adopting a horizontal stress coefficient and hydrostatic pore pressures.

More specifically on the creep behavior of the caprock (salt) during hydrocarbon production and afterwards, the main references are the works of Marketos and collaborators (Marketos et al., 2016a, 2016b, 2015c, 2015b, 2015a). In these works, axisymmetric, 2D plane strain and 3D models have been analyzed. The reservoir depletion has been mechanically assigned by means of an external compression in the reservoir. The salt caprock has been modelled as a viscoelastic material using a Maxwell model or by superimposing a linear elastic behavior to an empirical constitutive model analogous to the DM model. The non-salt layers have been modelled as elastic materials. Recently, Firme et al. (2021) have presented a study on the mechanical behavior of a carbonate reservoir with a centered karstic cavity. Although the focus of the article was the mechanical response of the carbonate, the salt caprock creep has been considered using the DM model. Apart from salt, the other rock formations have been modelled using the elastoplastic Mohr-Coulomb criterion.

The contributions of this study to the existing applications are: i) although the hydromechanical approach for the reservoir depletion/injection adopted in this thesis has as implication the reservoir compression/expansion such as the approach adopted in Marketos' works, full hydromechanical coupling can be adopted in the future with minor additional attributes of the numerical model since the formulation already supports it; and ii) the effect of injection in the reservoir (such as a CCS operation) that recovers its original pressure, its impact on the salt caprock creep and the hydraulic changes resulting from this process are analyzed.

## **7.5. Results and discussions**

Since the study has been divided into two phases, the results are separated into two groups: hydrocarbon production period and CO<sub>2</sub> injection period. The corresponding results are presented and discussed in the sections below.

### **7.5.1. Hydrocarbon production period**

The first phase of the study simulates the hydrocarbon production by means of a predefined depletion applied to all degrees of freedom of pore pressure of the

reservoir. Firstly, history plots in noticeable points located on the model symmetry axis are analyzed – this axis virtually represents a well. The reservoir compaction at the axis is calculated by the difference between the vertical displacements of the reservoir bottom and top (points B and A, respectively). The subsidence is measured at the seafloor (point H of the model top).

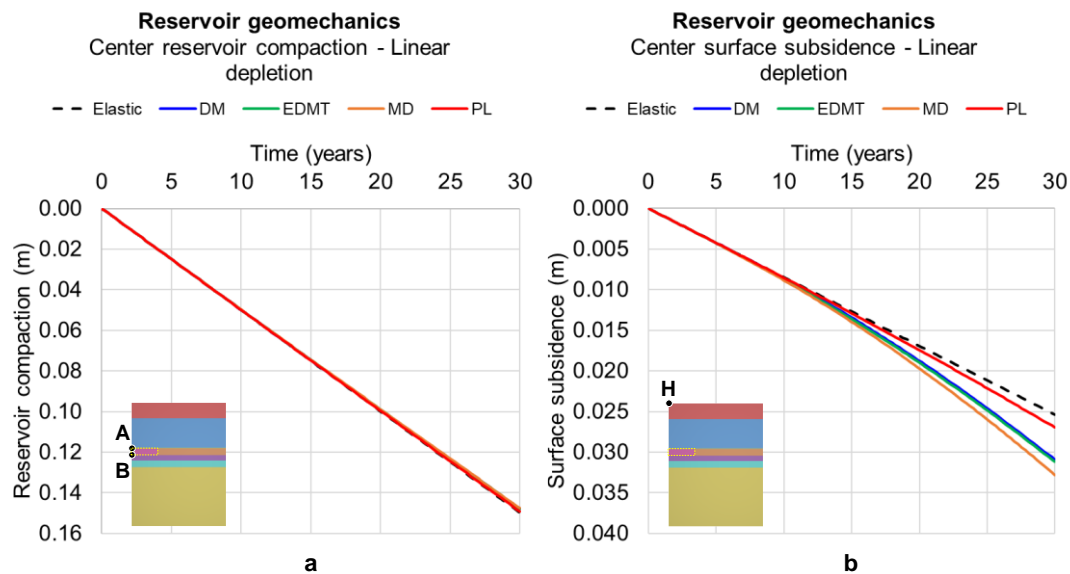


Figure 80. Center reservoir compaction (a) and surface subsidence (b) – linear depletion scheme.

Figure 80 shows the reservoir compaction (a), and the surface subsidence (b) at the symmetry axis considering the linear depletion scheme (see Figure 79 and context). The compaction results (Figure 80 (a)) evolve almost linearly with reservoir depletion that, in turn, evolves linearly with time. As a reference for comparison, the analytical (elastic) solution for uniaxial compaction of this reservoir is 0.169 m. The numerical results are lower than the analytical solution, indicating that the reservoir does not exhibit a fully uniaxial response. Subtle nonlinear effects are observed when comparing the results with those of the model with elastic caprock (black dashed lines). This response is attributed to the salt caprock creep and has a greater influence on the overburden and model top than it has in the reservoir surroundings. For this reason, the nonlinearity is more noticeable in the subsidence results (Figure 80 (b)), with an increase in the downward displacements. The results using the PL model (red lines) to represent salt creep are closer the elastic results than the other creep models, since the results obtained with this model tends to become horizontal with time, not representing adequately the steady-state creep.

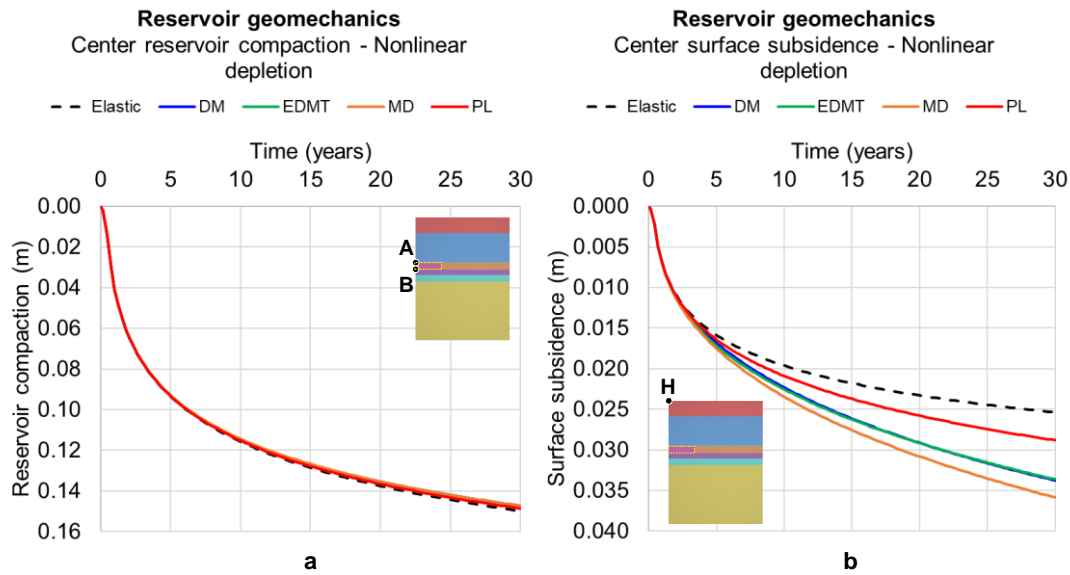


Figure 81. Center reservoir compaction (a) and surface subsidence (b) – nonlinear depletion scheme.

Figure 81 presents the corresponding results obtained with the nonlinear depletion scheme (see Figure 79 and context). The compaction results (Figure 81 (a)) evolve nonlinearly with reservoir depletion, following a similar trend to the depletion curve. Although the curves are all nonlinear, the compaction results are still very similar among the creep constitutive models adopted. In general, most of the observations made in the results considering the linear depletion scheme applies in this case. The accumulated reservoir compaction at the end of 30 years of depletion is approximately the same as in the model linearly depleted. However, by observing Figure 81 (b), the final subsidence values are higher than those of the previous model (compare with Figure 80 (b)) except in the model in which the caprock is assumed elastic. This observation indicates that the nonlinear depletion scheme impacts the caprock creep, therefore impacting the displacement field above the reservoir.

Next, the displacements are evaluated along the horizontal coordinate of the model at the end of the depletion i.e., when it is of 30 MPa, in order to show the maximum compaction and subsidence values. In the path plots, the reservoir compaction is given by the difference between the vertical displacements of the reservoir bottom and top (segments BD and AC, respectively), and the surface subsidence is measured along the model top (segment HI).

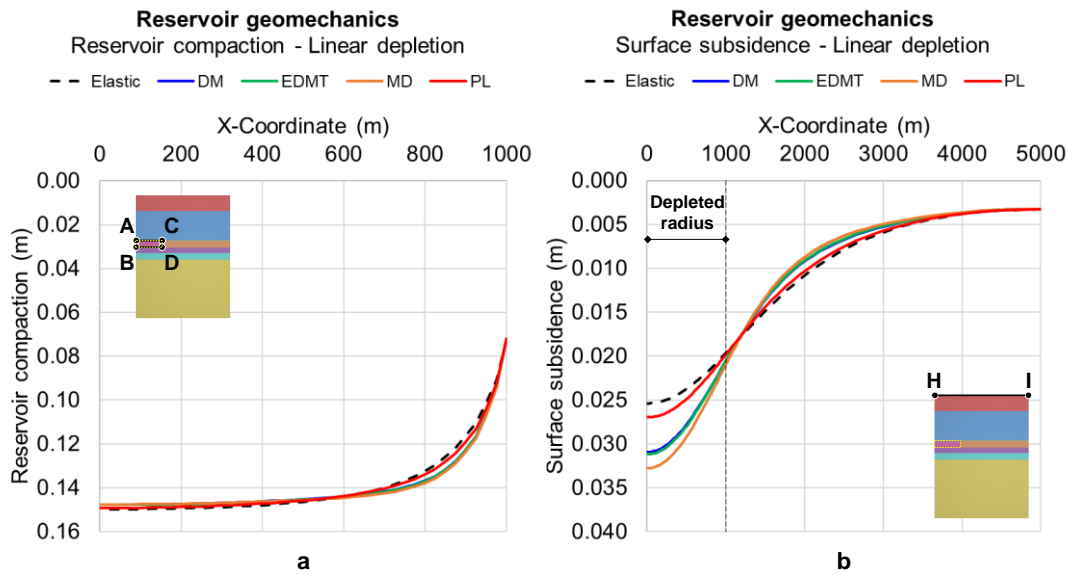


Figure 82. Reservoir compaction (a) and surface subsidence (b) in the end of the linear depletion (30 years).

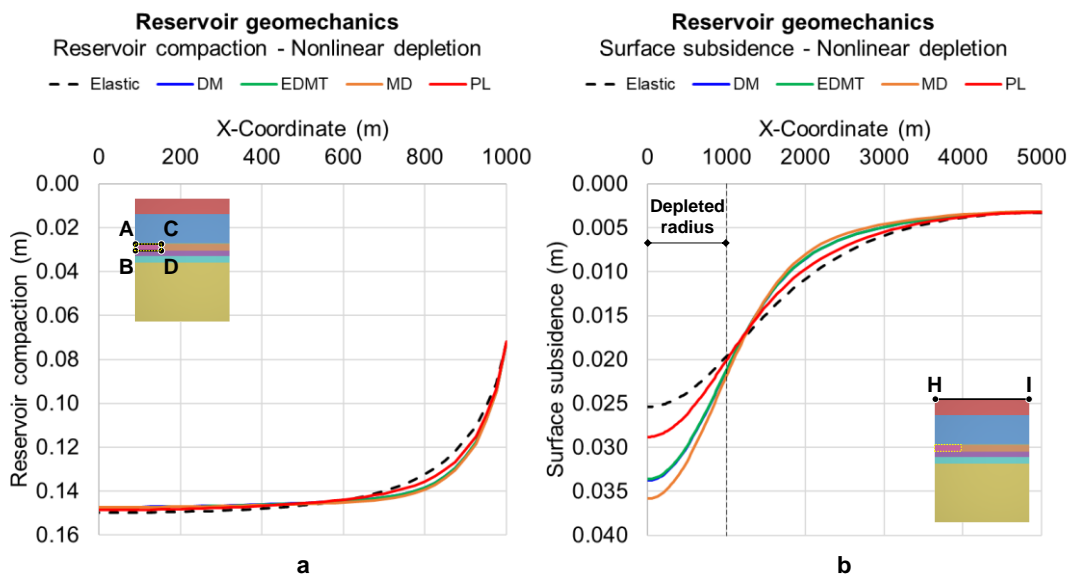


Figure 83. Reservoir compaction (a) and surface subsidence (b) in the end of the nonlinear depletion (30 years).

Figure 82 shows the reservoir compaction along the depleted radius (a) and the surface subsidence (b) considering the linear depletion scheme. By observing the compaction results (Figure 82 (a)) and in accordance with what has already been noticed, reservoir compaction is little sensitive to the caprock creep model. Far from the center, the creep behavior seems to increase compaction slightly, while the opposite occurs close to the center. As previously noticed, the PL model results are closer to the elastic solution than the other creep models due to its limitation to represent adequately the steady-state creep. From the subsidence results (Figure 82 (b)), one notices that caprock creep contribution makes

subsidence higher in the horizontal extension of the reservoir (inside the depleted radius) in comparison to the elastic results, but lower than such results away from the reservoir extension (outside the depleted radius). From this graph, when considering caprock creep in the analysis over the field production period, the subsidence bowl tends to have a higher center value and a smaller lateral extension than the bowl obtained considering an elastic caprock. Despite these conceptual observations, the differences in the displacements of the models are small in terms of engineering.

Lastly, Figure 83 presents the corresponding results considering the nonlinear depletion scheme. The compaction results (Figure 83 (a)) have shown very small differences in relation to the results considering the linear depletion scheme (see Figure 82 (a)). Regarding the subsidence results (Figure 83 (b)), as observed in the center values (see Figure 81), the nonlinear depletion scheme triggers higher subsidence values along the reservoir than those of the linear depletion model, while lower values occur away from the reservoir.

### **7.5.2. CO<sub>2</sub> injection period**

The second phase of the study considers a reservoir injection period that recovers the initial pressure of the reservoir. This ideally represents a type of CCS operation in which CO<sub>2</sub> is injected in a depleted reservoir. In this phase, the salt caprock behavior is modelled as solely elastic (no creep) and as a creeping material using the EDMT model. The results up to 30 years are the same as those in the corresponding figures since the reservoir is depleted before being injected. When CO<sub>2</sub> injection begins, different mechanical responses are noticed as the reservoir pore pressure is being recovered. It is assumed that the mechanical properties of rocks do not change during the injection process in the reservoir.

Figure 84 shows the reservoir compaction (a) and the surface subsidence (b) at the symmetry axis considering the linear depletion/injection scheme. In the compaction results (Figure 84 (a)), one observes that if reservoir pressure is fully recovered, compaction is reverted and the reservoir practically returns to the condition before depletion. The reversion is complete in the case of the elastic caprock while a very subtle reservoir expansion is noticed in the case of the creeping caprock. On the other hand, if reservoir pressure is not recovered (dashed curves), the center reservoir compaction values vary very little in the case of creeping caprock, remaining essentially the same of those at the end of depletion.

In the case of the elastic caprock, no changes in compaction occur. Regarding the subsidence results (Figure 84 (b)), the condition before the reservoir depletion is completely recovered in the case of elastic caprock. However, the recovery is not complete in the case of creeping caprock. The difference between the results adopting the elastic and the EDMT creep model to represent the caprock is related to the steady-state creep contribution, which is not recoverable (see Section 2.1). Still regarding the creeping caprock, the subsidence response also indicates that even if reservoir pressure is not recovered (dashed curves) i.e., the reservoir remains depleted until the end of the analysis, salt creep deformation evolves and therefore subsidence accumulation continues. Next, Figure 85 presents the corresponding results considering the nonlinear depletion/recovery scheme. The same concepts observed in results using the linear pressure variation scheme apply, with the exception of the curve shapes, which follow the nonlinear depletion/injection scheme. As previously observed, the subsidence values (Figure 85 (b)) are higher than those of the previous model (see Figure 84 (b)), indicating that the nonlinear depletion/recovery scheme impacts the displacement field above the reservoir. Therefore, the residual subsidence after reservoir injection is also higher than that in the previous model. Nonetheless, the differences in the displacements are small despite the conceptual observations in each scenario.

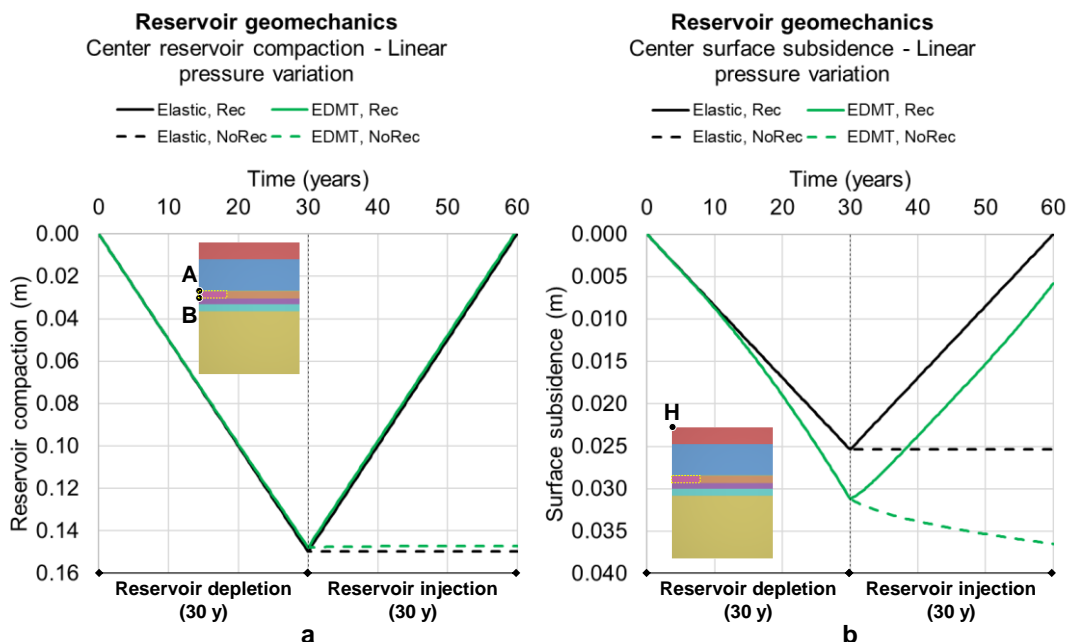


Figure 84. Center reservoir compaction (a) and surface subsidence (b) over time – linear depletion/injection scheme.

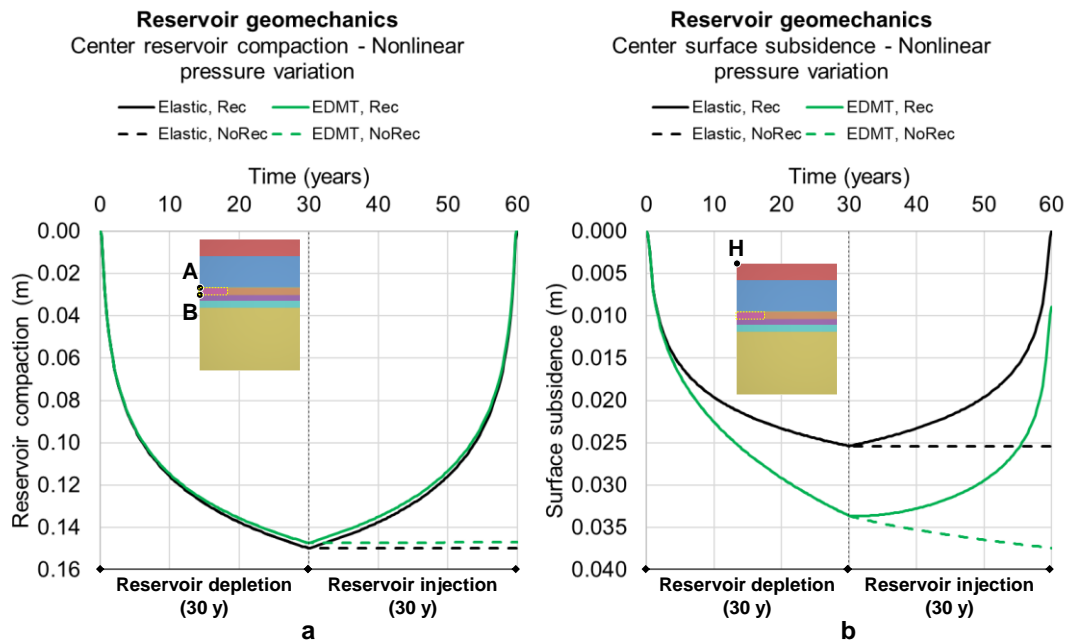


Figure 85. Center reservoir compaction (a) and surface subsidence (b) over time – nonlinear depletion/injection scheme.

Furthermore, Figure 86 shows the reservoir compaction along the depleted/injected radius (a) and the surface subsidence (b) considering the linear pressure variation scheme. By observing the compaction results (Figure 86 (a)) after reservoir depletion, very subtle reservoir expansion occurs until approximately half of depleted radius when pressure is fully recovered (dotted curves). On the other hand, a small creep deformation is still accumulated if pressure is not recovered (dashed curves). As observed in Figure 82 (b), the caprock creep contribution during reservoir depletion implies a deeper subsidence bowl and a smaller lateral extension in comparison to an elastic caprock. When the reservoir pressure is recovered, a discrete surface heave is observed in the horizontal coordinates away from the depleted/injected radius (Figure 86 (b)). Inside this radius, the elastic part of the subsidence is recovered, while the steady-state creep part remains as a residual subsidence. Without recovering the reservoir pressure, the caprock continues deforming by creep and the subsidence is still affected by it. Figure 87 presents the corresponding results considering the nonlinear pressure variation scheme. The conceptual observations are essentially the same of the models subjected to the linear scheme, differing only in the magnitude of the results.

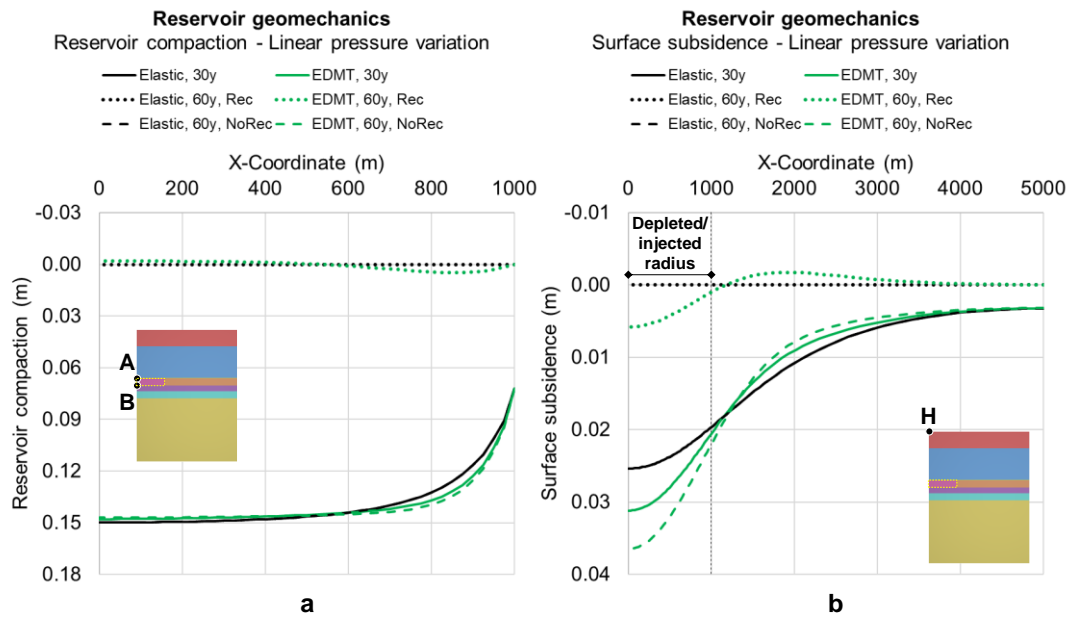


Figure 86. Reservoir compaction (a) and surface subsidence (b) in the end of depletion (30 years) and in the end of injection (60 years) – linear depletion/injection scheme.

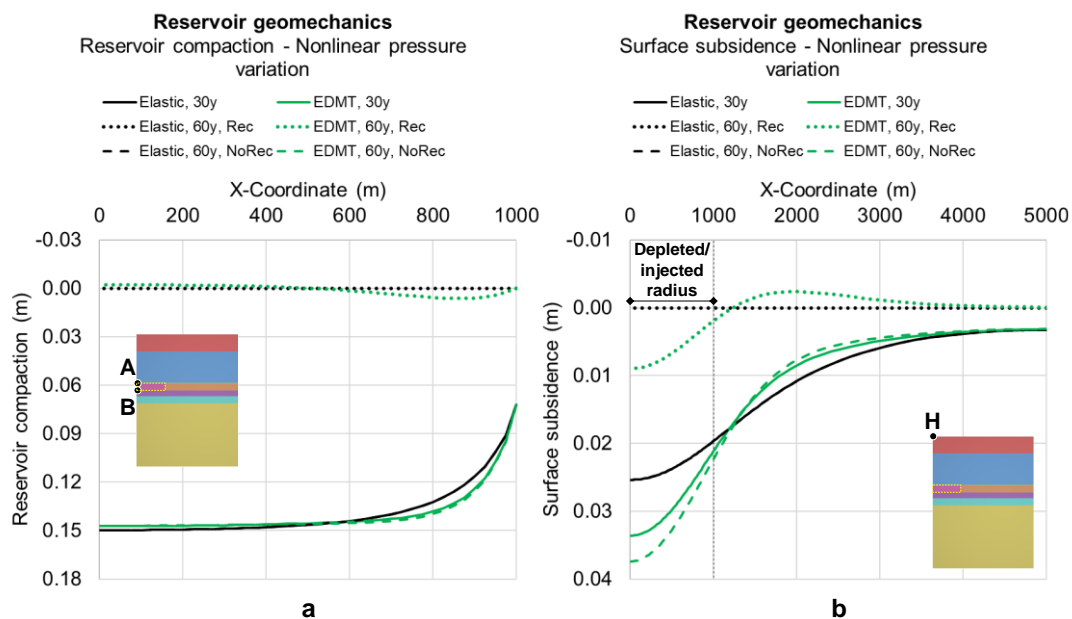


Figure 87. Reservoir compaction (a) and surface subsidence (b) in the end of depletion (30 years) and in the end of injection (60 years) – nonlinear depletion/injection scheme.

In order to get the big picture of the mechanically disturbed zone above the depleted/injected reservoir, Figure 88 shows the vertical displacements along the symmetry axis, over model depth. In these graphs, negative values mean subsidence. The results considering the linear (Figure 88 (a)) and the nonlinear (Figure 88 (b)) depletion/injection schemes are very similar. The main difference is that salt creep deformation generates greater displacements (comparatively) in the model that considers the nonlinear pressure variation. Observing the results

considering the creeping caprock (green lines) and comparing with the elastic results (black lines) at the end of reservoir depletion (30 years), salt creep enhances the downward displacements in the overburden, with subsidence increase at the seafloor, and attenuates the upward displacements of the underburden, retarding the reservoir bottom heave effect. More so, the mechanical changes due to salt creep after 30 years affect not only the overburden but also the underburden – both when injection is considered (dotted lines) and when it is not (dashed lines), but in different ways. If injection is considered, both effects described above are attenuated, and results are relatively close to the elastic ones, except in the reservoir and surroundings, where a considerable difference persists. A complete displacement reversion is not reached. On the other hand, if injection is not considered, there is evolution of the trends observed after reservoir depletion.

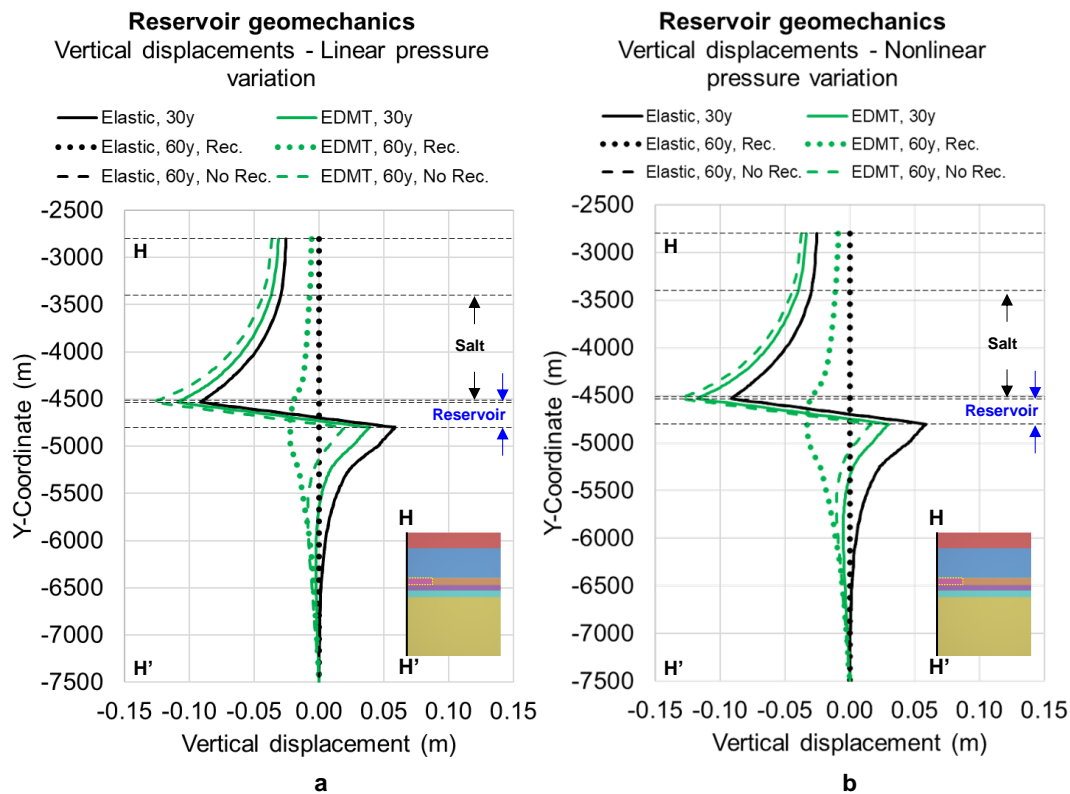


Figure 88. Vertical displacements along the vertical segment H-H' in the end of depletion (30 years) and in the end of injection (60 years) – linear (a) and nonlinear (b) depletion/injection scheme.

To provide an overview of the vertical displacements field, Figure 89 and Figure 90 present the contour maps in the scenarios described above considering the linear and the nonlinear depletion/injection scheme respectively.

Continuing the investigation of the mechanically disturbed zone above the depleted/injected reservoir, the stress paths ( $p$ - $q$  diagrams) of the salt bottom and

top, and seafloor are analyzed. These results are collected at the Gauss points (IP) closest to the corresponding node coordinates of these locations.

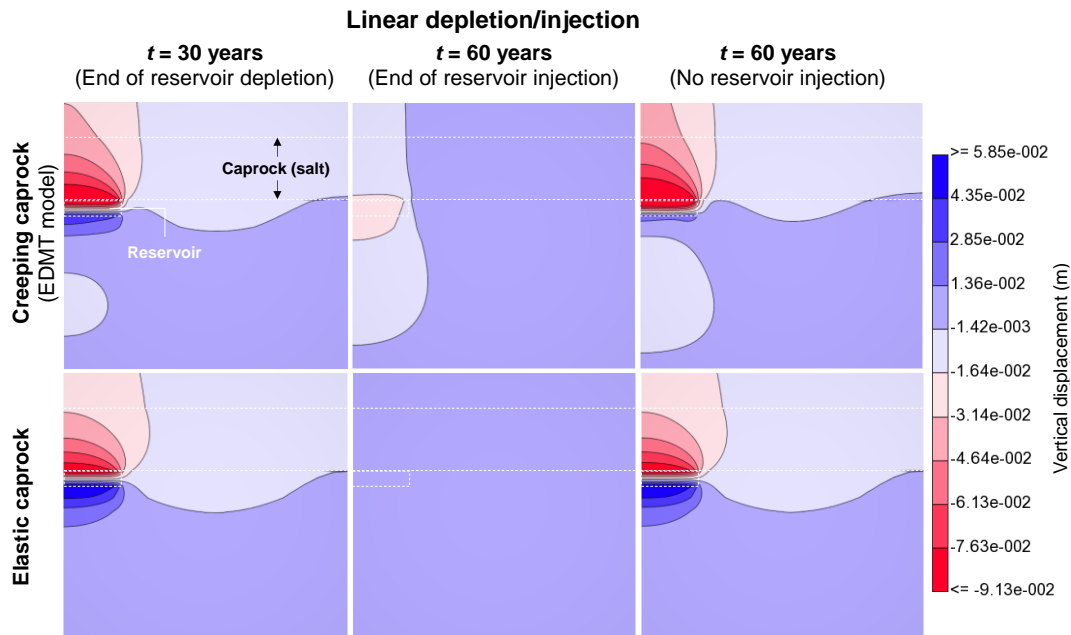


Figure 89. Countour maps of the vertical displacements in the end of depletion (30 years) and in the end of injection (60 years) – linear depletion/injection scheme.

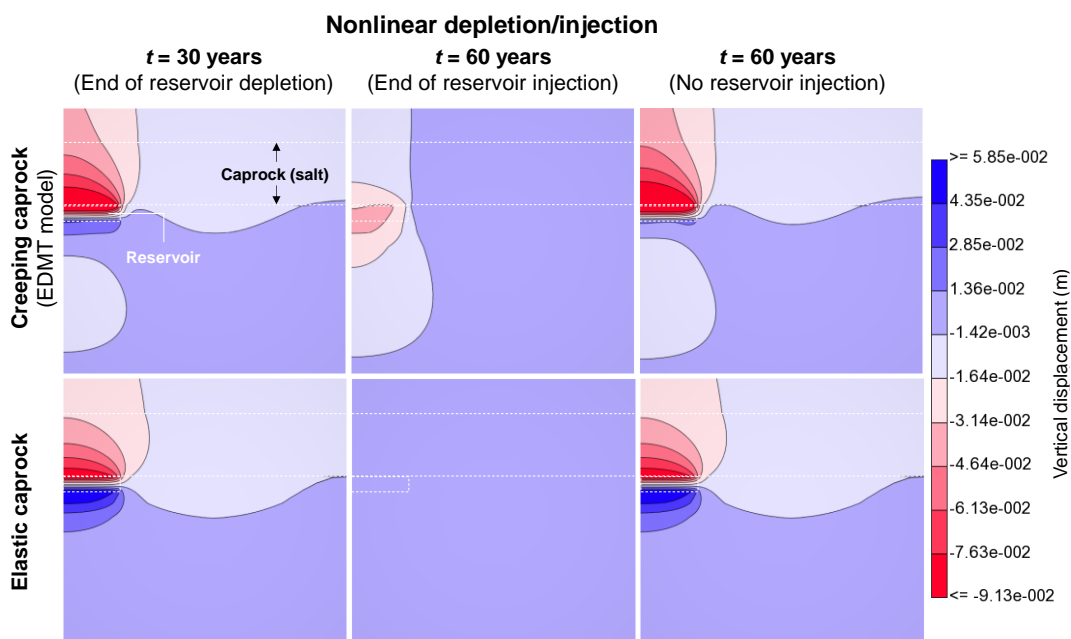


Figure 90. Countour maps of the vertical displacements in the end of depletion (30 years) and in the end of injection (60 years) – nonlinear depletion/injection scheme.

Figure 91 (a) shows the stress paths of salt bottom considering a linear pressure variation scheme. Reservoir depletion causes the path to develop an upward trend to the right in the model, considering the elastic caprock (black line). On the other hand, when considering the creeping caprock (green line), salt creep

makes the path to develop in an upward trend to bend to the left. It indicates that creep reduces progressively both the mean and deviatoric stresses. After depletion, if the reservoir undergoes injection (solid lines), the stress state of the model with elastic caprock returns to the initial state, while the model with a creeping caprock exhibits a sharp downward trend to the left, indicating a significant reduction in the deviatoric stresses, with a simultaneous reduction in the mean stresses. The inversion in the stress path when the mean stress is about 64.6 MPa represents an inversion in the Lode angle from  $-30^\circ$  to  $+30^\circ$ . If reservoir pressure is not recovered after depletion (dashed lines), the stress path of the model with elastic caprock does not evolve and the final stress state is the same of that in the end of depletion. In the model with creeping caprock, the path exhibits a downward trend to the left, indicating that the deviatoric stresses are alleviated by creep.

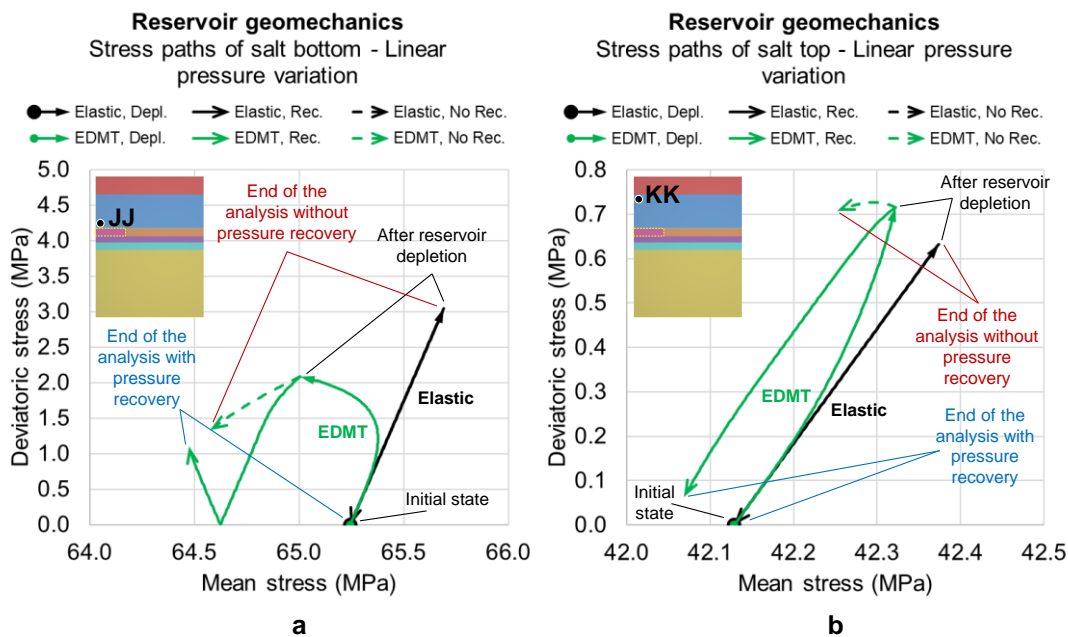


Figure 91. Stress paths (p-q diagram) of salt bottom (a) and top (b) – linear depletion/injection scheme.

At the salt top, Figure 91 (b), the stress paths for a linear pressure variation scheme are similar in terms of trends of each model. However, the entire process (from the initial to final stress state) has led to stress changes lower than 1 MPa, which are likely not relevant for engineering purposes. This indicates that the caprock is predominantly affected in the lower portion, close to the reservoir. Analyzing the corresponding results in the nonlinear depletion/injection scheme, similar responses compared to that of linear depletion/injection are noticed at the

salt bottom (Figure 92 (a)) and top (Figure 92 (b)). The main difference is that the stress paths are subtly more spread in the nonlinear depletion/injection models.

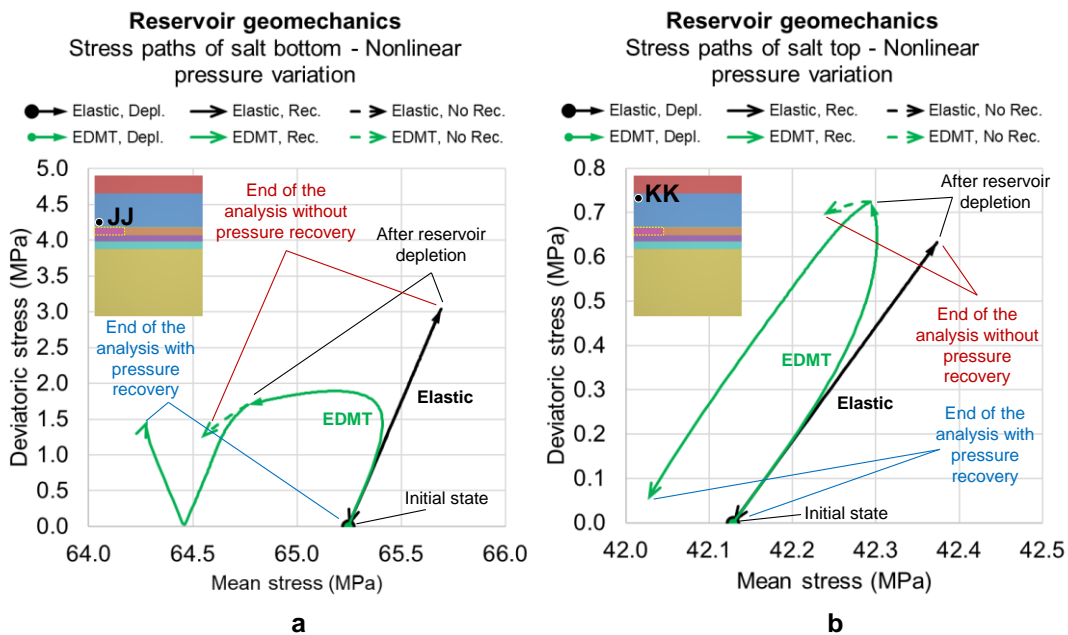


Figure 92. Stress paths (p-q diagram) of salt bottom (a) and top (b) – nonlinear depletion/injection scheme.

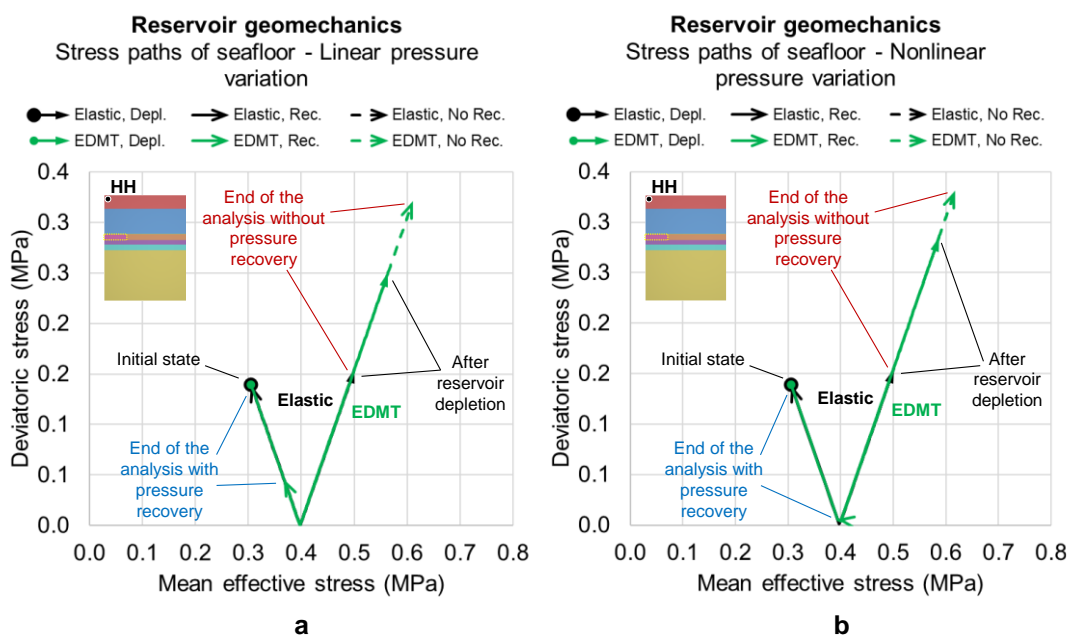


Figure 93. Stress paths (p'-q diagram) of seafloor (model top) – linear (a) and nonlinear (b) depletion/injection scheme.

Figure 93 shows the stress paths of the seafloor. In this case, the integration point is in the overburden (an elastoplastic rock). The purpose here is to analyze the impact of caprock creep in the rock formation above the salt. The mean stresses are much lower than those in previous figures because effective stresses

are adopted in the overburden (while the effective stresses are taken equal to the total stresses in the salt). Both in the linear (Figure 93 (a)) and nonlinear (Figure 93 (b)) depletion/injection schemes and in the elastic and creeping caprocks, the stress paths follow linear and coincident trends. The main difference is the final stress state reached considering caprock as an elastic or a creeping material. The results indicate that even not being in the caprock, the seafloor is still influenced by creep. This is observed by the fact that final stress state is not completely recovered when the reservoir is injected, and the stress path continues evolving in an upward trend to the right when depletion ends and the reservoir is abandoned in the depleted state. However, the entire process (from the initial to the final stress state) has led to stress changes lower than 1 MPa, which are not relevant for engineering purposes in this context.

Finally, the repercussion of the mechanical response to reservoir depletion/injection on the hydraulic behavior of the salt caprock and at the seafloor is analyzed. Considering the previous applications in which porosity and porosity-dependent permeability have shown very subtle changes over time, only the mean stress-dependent permeability has been calculated and discussed. The permeability is collected at the same Gauss points of the stress paths.

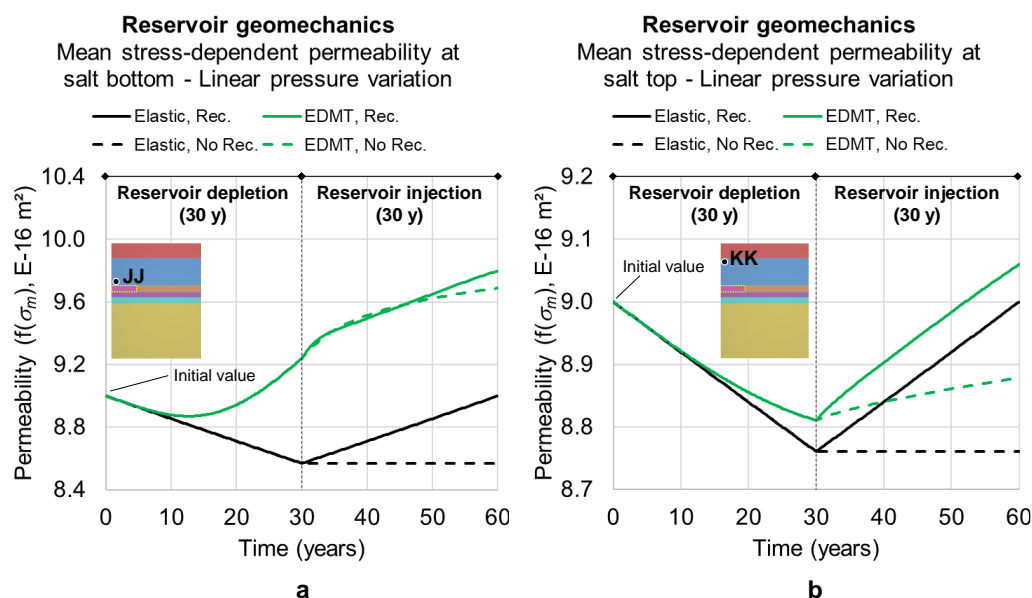


Figure 94. Mean stress-dependent permeability at salt bottom (a) and top (a) over time – linear depletion/injection scheme.

Figure 94 (a) and Figure 94 (b) present the permeability changes over time at the salt bottom and top respectively due to reservoir depletion/injection considering the linear scheme. Analyzing the reservoir depletion period, elasticity and creep have played opposite roles in the permeability evolution. While the

permeability decreases linearly as the reservoir is (linearly) compacted in the model with elastic caprock, the permeability reduces in the beginning, then it increases nonlinearly with time at salt bottom and presents a rate reduction at salt top in the creeping caprock model. This reflects the fact that compaction leads to an increase in salt confinement in the elastic caprock, while salt confinement increases and then decreases in the creeping caprock, and consequently permeability is enhanced (see also Figure 91 (a)). After 30 years, if the reservoir pressure is recovered (solid lines), the creeping caprock still reduces the confinement due to creep and there is permeability enhancement. Observing the elastic caprock, the permeability linearly recovers its initial value. If the reservoir pressure is not recovered and it remains in the depleted state until the end of the analysis (dashed lines), the permeability enhancement rate reduces in the creeping caprock (although it is still enhanced), while the permeability remains constant over time in the elastic caprock. This response in the models with creeping caprock can be explained by the simultaneous action of creep alleviating strain energy and pressure changes in the reservoir, impacting the mechanical behavior through mean stress changes. Since the permeability correlation depends on mean stresses, each stress change impacts permeability.

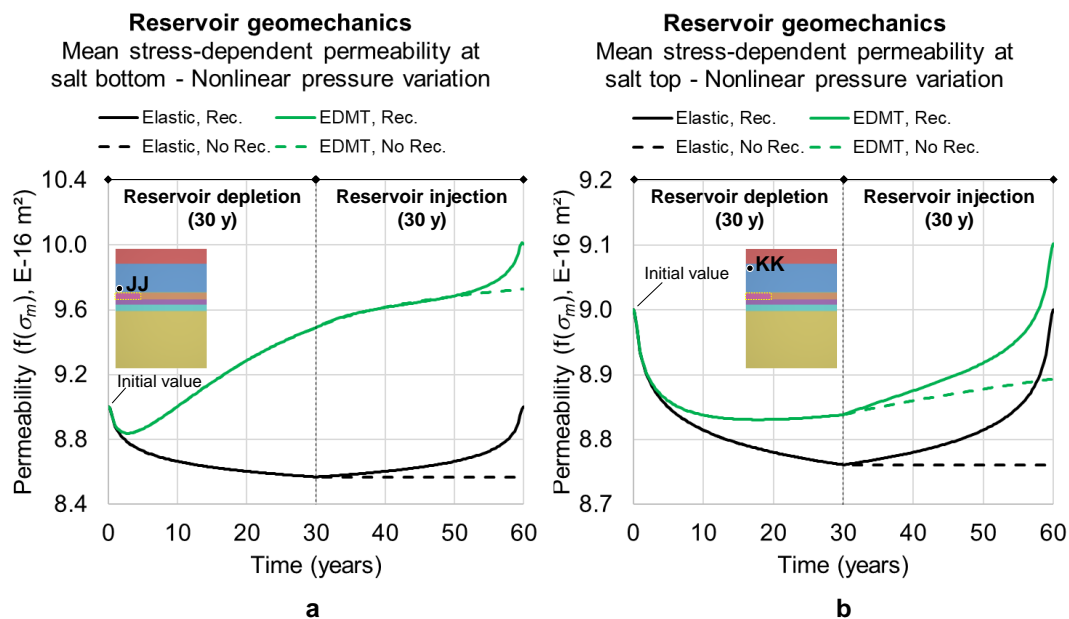


Figure 95. Mean stress-dependent permeability at salt bottom (a) and top (a) over time – nonlinear depletion/injection scheme.

The corresponding results when adopting a nonlinear depletion/injection scheme are respectively presented in Figure 95 (a) and Figure 95 (b). Although the hydraulic changes have followed the same concepts, the nonlinear depletion/injection causes the model with the elastic caprock to follow the same

trend, i.e., permeability changes are nonlinear such as depletion and injection, and permeability remains constant when the reservoir is depleted but not injected. Observing the results of the model with the creeping caprock, the nonlinearity of the permeability changes is reinforced, since nonlinear stress changes are somehow accounted for to the 7.55 power in the EDMT model. Since the permeability is correlated to the stresses, the curve reflects a higher order polynomial that influences the mechanical response.

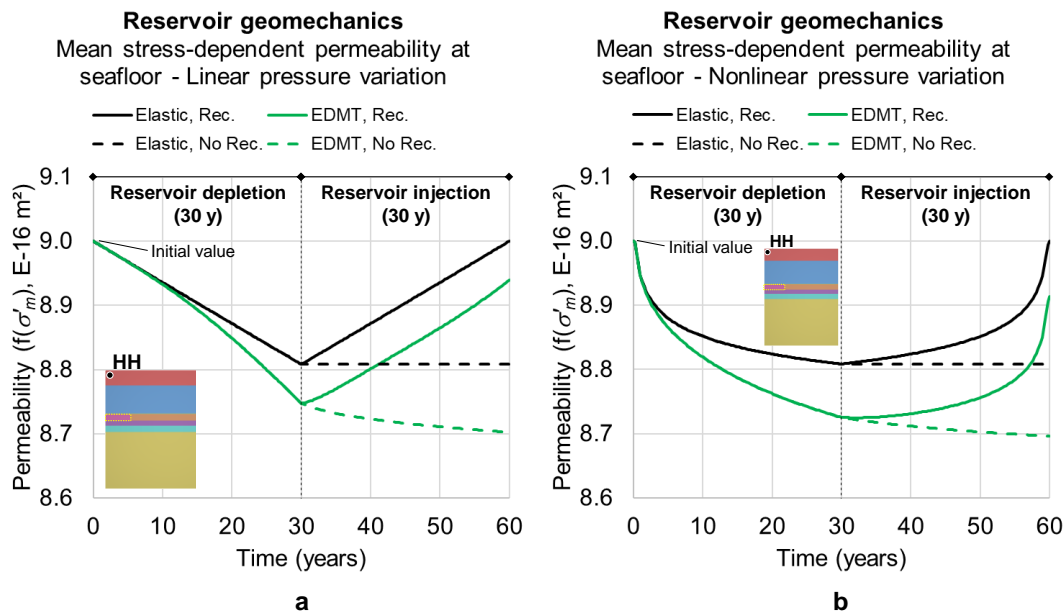


Figure 96. Mean stress-dependent permeability at seafloor (model top) over time – linear (a) and nonlinear (b) depletion/injection scheme.

Lastly, the permeability changes are analyzed at the seafloor. Figure 96 (a) shows the results considering the linear depletion/injection scheme and Figure 96 (b) presents the corresponding results obtained with the nonlinear scheme. The curve shapes are similar to those of surface subsidence (see Figure 84 (b) and Figure 85 (b) respectively). This is expected since the top of the overburden is relatively far from the salt – the caprock creep behavior affects the displacements above the salt but to a lesser extent. The qualitative conclusions are similar to those of subsidence, since this study has assumed that the permeability changes are totally correlated to the mechanical response of the model.

## 7.6. Partial conclusions

This study has analyzed the combined effect of the reservoir compaction/expansion and salt caprock creep behavior during hydrocarbon production and CO<sub>2</sub> injection (a type of CCS operation). Linear and nonlinear

reservoir pressure schemes have been considered. The main objectives were: i) to analyze the effect of reservoir compaction on salt caprock creep; ii) to analyze the combined effect of compaction and creep on subsidence; iii) to evaluate how the mechanical behavior of the model has been altered by reservoir injection; and iv) to analyze what was the effect on the hydraulic behavior of the caprock.

The results have shown that: i) subtle nonlinear effects have been noticed when comparing reservoir compaction over time in models that account for caprock creep with those adopting a solely elastic caprock; ii) the nonlinear effect has been more noticeable in the subsidence results since salt creep has a greater influence on the overburden than it has in the reservoir surroundings. While compaction was practically insensitive to caprock creep, differences in the subsidence results have been slightly higher. Furthermore, the caprock creep leads to subsidence bowls with a higher center value and a smaller lateral extension than those observed in the model adopting an elastic caprock; iii) in the injection period, even when the reservoir pressure is completely recovered, the compaction and subsidence are not fully recovered in the models with the creeping caprock. The differences between the values adopting the elastic and the creeping caprock are credited to the steady-state creep contribution, which is not recoverable. Still regarding the creep behavior of the caprock, the subsidence responses have also shown that salt continues deforming by creep even if reservoir pressure is not recovered. Moreover, the stress paths at the salt bottom and top, and at the seafloor have shown noticeable conceptual differences when the creep behavior is considered in the caprock or not. However, the entire process from the initial to final stress state has led to low stress changes which are not relevant for engineering purposes; and iv) the permeability changes in the caprock have been subtle, although it was possible to observe the effect of the caprock creep and reservoir pressure variation scheme on the results. The correlation between the changes in mean stresses and in permeability has presented the big picture of the impact of the mechanical response on the hydraulic behavior of the caprock.

For the conditions considered in this study, the creep contribution to subsidence, stress paths and changes in permeability were of small magnitude, although conceptually notorious. Meanwhile, this application aims at serving as a reference for more advanced analyses of CCS in depleted Pre-salt reservoirs.

## 8

# Conclusions and suggestions for future work

### 8.1.

#### General conclusions

This thesis has presented a comprehensive investigation on the mechanical behavior of salt with focus on creep constitutive modelling, dilation, thermal effects, and the impact of the mechanical response on the hydraulic behavior. Computational geomechanics has been adopted to simulate strategic engineering projects in energy and decarbonization contexts involving salt rocks such as the abandonment of Pre-salt wells, salt caverns and salt as caprock of carbonate reservoirs. Conceptual and realistic geomechanical models have been analyzed using the finite element method through the in-house framework GeMA.

Using an in-house framework has required the implementation of creep constitutive models (PL, DM, MD, EDMT), specific boundary conditions (transient pressure schemes) and post-calculation output variables (dilation and shear failure indicators, and hydraulic properties), besides the adequacy of the existing simulation workflows to deal with the engineering problems which were object of study of the thesis (see Section 2.5.4). The level of customization allowed by the in-house tool for the attributes implemented and adopted has been beneficial. The doctoral research has also contributed to the improvement of the tool in engineering problems involving salt rocks with those developments.

### 8.2.

#### Specific conclusions from the simulations

The reference examples presented in Chapter 4 have primarily aimed at verifying and validating the implementations developed in the thesis. In the simulation of the multistage triaxial creep test carried out in Big Hill salt (see Section 4.1.2.2), heating the sample from 60°C to 80 °C has caused instantaneous thermal elastic strains of small magnitude. This temperature change is in the range usually applied in well simulations, and its impact on the behavior of salt has been found to occur mainly in the creep constitutive model. In the simulation of an isothermal Pre-salt well (see Section 4.4.1), the interfaces between salt and non-

salt rocks have developed stress states close to the shear strength. If failure occurs, these interfaces would become paths for fluid loss, affecting well serviceability and causing environmental problems.

The case study of well abandonment using salt as geological barrier (see Chapter 5) has demonstrated that a Pre-salt well can close completely by creep after casing removal. Pressure reduction and well heating have accelerated creep deformation significantly, and this is the driving mechanism to form the geological barrier. In the most critical scenario, the final permeability was of more than 100 times the initial permeability value. Some boundary conditions may be conservative, resulting in a low well closure rate compared to the time required by conventional P&A methods. This, however, does not compromise the conceptual observations. Using salt as barrier promotes the “rock to rock” sealing concept desired in more restrictive P&A regulations.

The case study of the salt cavern (see Chapter 6) has shown that a large opening in a salt formation is capable of mechanically supporting cycles of pressure increase and decrease caused by the contingency supply of natural gas. The simulation of the solution mining in a mechanical way by means of a transient pressure has led to reasonable results since dissolution triggers more gradual stress changes than standard excavation. The repercussion of the mechanical response on the hydraulic behavior of salt has been monitored and the permeability of the cavern wall has shown a significant rise during the operation period. In the most restrictive case, the final permeability at the cavern floor is about 6.51 times the initial value. The hydraulically disturbed region – by a few hundred meters from the cavern walls – is also significant especially by the end of operation. This calls attention since the tightness of the cavern walls is of utmost importance for storage.

The case study of salt as caprock (see Chapter 7) has contributed to the understanding of the combined effect of reservoir compaction and salt caprock creep. There are few works considering this combined effect, which is relevant both for hydrocarbon production and CCS purposes in Pre-salt reservoirs. Subtle nonlinear effects have been noticed in the subsidence results since salt creep has a greater influence on the overburden than it has in the reservoir surroundings. Caprock creep has led to subsidence bowls with a higher center value and a smaller lateral extension than those in the model adopting an elastic caprock. In the injection period, even when the reservoir pressure is completely recovered, the

compaction and subsidence are not fully recovered in the models with the creeping caprock due to the steady-state creep contribution, which is not recoverable. More so, salt continues deforming by creep even if the reservoir is abandoned in the depleted condition. The stress paths have shown noticeable differences when the creep behavior is considered in the caprock. However, the entire process from the initial to the final stress state has led to low stress changes, which are not relevant for engineering purposes. Lastly, the permeability changes in the caprock have been subtle, although the effect of the caprock creep and reservoir pressure variation scheme on the results is conceptually notorious.

### **8.3. Final remarks**

Based on the validation examples and case studies, it is understood that the main patterns of the multiphysical behavior of salt in strategic energy projects have been analyzed with major emphasis on how the mechanical behavior affects or is affected by the coupling with other physics. The results of the thesis have evidenced that salt is a material suitable for several strategic engineering projects by demonstrating good mechanical response and tightness. The findings of this doctoral research add value to the consolidated knowledge in the area and shall serve as a guide for further advanced and specific analyses.

### **8.4. Suggestions for future work**

The continuation of this research in salt geomechanics should follow in two ways: improvements in the models studied in the thesis and development of new models with more realistic field lithologies.

Regarding the improvements in the models studied in the thesis, a first recommendation is to consider the slippage behavior of the interfaces between rock layers in the heterogenous-layered models. In the study of well abandonment using salt as barrier, one should revisit the abandonment-related boundary conditions, analyze the long-term behavior of the barrier after the well closure and check whether the permeability enhancement is enough to trigger relevant flow/reactive transport through the geological barrier. More so, backfilling the well with granular salt is another relevant alternative for Pre-salt well abandonment that should be studied. In the study of the salt cavern, improvements should focus on the thermomechanical impact of the cyclic pressure variation, the use of the cavern for CCS purposes and the abandonment period. Furthermore, the combined

behavior of a cavern cluster (instead of a single cavern) is also an important issue. In the study of salt as caprock, considering the temperature changes around the well during hydrocarbon production and CO<sub>2</sub> injection would be an important contribution. Moreover, a full hydromechanical coupling to simulate depletion and injection is important to better represent the pressure variation throughout the reservoir.

With respect to future geomechanical models in the context, more realistic field lithologies should be considered. This includes models directly derived from geological sections, with non-horizontal layers and salt domes. The scenarios studied in the thesis have assumed bedded salt formations, implying on a well-behaved stress condition before the stress perturbations due to drilling, excavation and reservoir compaction. Different responses could be noticed in salt domes especially if close to dome flanks. In such cases, stress anisotropy and salt-related geodynamics could lead to higher creep rates and preferential creep directions. Besides the modelling complexity, an important challenge in models with irregular layers and salt formations is the stress initialization. The stresses internally calculated using rock densities – a geostatic state based on a self-weight assignment – generate initial displacements and deviatoric stresses that trigger creep in salt. Depending on the flexibility allowed by the numerical code adopted, the initial displacements can be reset to zero; however, the creep behavior induced by the geostatic loading has to be considered. A final condition for the stress initialization has to be established before applying the engineering procedures such as well drilling, cavern excavation or solution mining, reservoir depletion, among others.

## 9

## References

- Abshire, L.W., Desai, P., Mueller, D., Paulsen, W.B., Robertson, R.D.B., Solheim, T., 2012. Offshore permanent well abandonment. *Oilf. Rev.* 24, 42–50.
- Akbar, M., Vissapragada, B., Alghamdi, A.H., Allen, D., Herron, M., Carnegie, A., Dutta, D., Olessen, J.-R., Chourasiya, R.D., Logan, D., Stief, D., Netherwood, R., Russell, S.D., Saxena, K., 2001. A snapshot of carbonate reservoir evaluation. *Oilf. Rev.* 12, 20–41.
- Alejano, L.R., Alonso, E., 2005. Considerations of the dilatancy angle in rocks and rock masses. *Int. J. Rock Mech. Min. Sci.* 42, 481–507.
- Alkan, H., 2009. Percolation model for dilatancy-induced permeability of the excavation damaged zone in rock salt. *Int. J. Rock Mech. Min. Sci.* 46, 716–724. <https://doi.org/10.1016/j.ijrmms.2008.08.002>
- Amaral, R.F., Seabra, G.S., Laquini, J.P., 2017. Assessment of cold water injection geomechanical effects on Brazilian Pre-salt reservoirs and on its saline caprocks, in: *Offshore Technology Conference Brasil. Offshore Technology Conference (OTC), Rio de Janeiro.* <https://doi.org/10.4043/28007-ms>
- Andrejchuk, V., 2002. Collapse above the world's largest potash mine (Ural, Russia). *Int. J. Speleol.* 31, 137–158. <https://doi.org/10.5038/1827-806x.31.1.8>
- Angus, D.A., Dutko, M., Kristiansen, T.G., Fisher, Q.J., Kendall, J.M., Baird, A.F., Verdon, J.P., Barkved, O.I., Yu, J., Zhao, S., 2015. Integrated hydro-mechanical and seismic modelling of the Valhall reservoir: A case study of predicting subsidence, AVOA and microseismicity. *Geomech. Energy Environ.* 2, 32–44. <https://doi.org/10.1016/j.gete.2015.05.002>
- Anjos, S.M.C., Passarelli, F.M., Wambersie, O.E., Lewis, K., Rovina, P.S., Coelho, O., Martins, M., Ribeiro, O.J.S., Fernandes, R.A.R., Borges, F.A., 2019. Libra: applied technologies adding value to a giant ultra deep water Pre-salt field - Santos Basin, Brazil, in: *Offshore Technology Conference Brasil. Offshore Technology Conference (OTC), Rio de Janeiro.*

<https://doi.org/10.4043/29685-ms>

- Ashby, M.F., 1972. A first report on deformation-mechanism maps. *Acta Metall.* 20, 887–897. [https://doi.org/10.1016/0001-6160\(72\)90082-X](https://doi.org/10.1016/0001-6160(72)90082-X)
- Augarde, C.E., Lyamin, A. V., Sloan, S.W., 2003. Prediction of undrained sinkhole collapse. *J. Geotech. Geoenvironmental Eng.* 129, 197–205. [https://doi.org/10.1061/\(ASCE\)1090-0241\(2003\)129:3\(197\)](https://doi.org/10.1061/(ASCE)1090-0241(2003)129:3(197))
- Auler, A., Farrant, A.R., 1996. An brief introduction to karst and caves in Brazil, in: *Proceedings of the University of Bristol Speleological Society*. pp. 187–200.
- Bagni, F.L., Bezerra, F.H., Balsamo, F., Maia, R.P., Dall’Aglio, M., 2020. Karst dissolution along fracture corridors in an anticline hinge, Jandaíra Formation, Brazil: Implications for reservoir quality. *Mar. Pet. Geol.* 115. <https://doi.org/10.1016/j.marpetgeo.2020.104249>
- Bailey, R.W., 1935. The utilization of creep test data in engineering design. *Proc. I. Mech.* E131, 209–284.
- Balsamo, F., Bezerra, F.H.R., Klimchouk, A.B., Cazarin, C.L., Auler, A.S., Nogueira, F.C., Pontes, C., 2020. Influence of fracture stratigraphy on hypogene cave development and fluid flow anisotropy in layered carbonates, NE Brazil. *Mar. Pet. Geol.* 114. <https://doi.org/10.1016/j.marpetgeo.2019.104207>
- Barajas, P., Civan, F., 2014. Effective modeling and analysis of salt-cavern natural-gas storage. *SPE Prod. Oper.* 29, 51–60. <https://doi.org/10.2118/164489-PA>
- Bauer, S.J., Broome, S.T., Hansen, F.D., Lampe, B., Mills, M., Stormont, J., 2015. Gas flow measurements of consolidating crushed salt, in: *49th US Rock Mechanics / Geomechanics Symposium*. American Rock Mechanics Association (ARMA), San Francisco.
- Bays, C.A., 1962. Use of salt solution cavities for underground storage, in: *First Salt Symposium*. Cleveland, pp. 564–578.
- Bérest, P., 2013. The mechanical behavior of salt and salt caverns, in: *Kwasniewski, Lydzba (Eds.), Rock Mechanics for Resources, Energy and Environment (ISRM International Symposium - EUROCK 2013)*. Taylor & Francis Group, Wroclaw, pp. 17–29.
- Bérest, P., Bergues, J., Brouard, B., Durup, J.G., Guerber, B., 2001. A salt cavern

- abandonment test. *Int. J. Rock Mech. Min. Sci.* 38, 357–368.  
[https://doi.org/10.1016/S1365-1609\(01\)00004-1](https://doi.org/10.1016/S1365-1609(01)00004-1)
- Bérest, P., Brouard, B., Djakeun-Djizanne, H., Hévin, G., 2014. Thermomechanical effects of a rapid depressurization in a gas cavern. *Acta Geotech.* 9, 181–186.
- Bérest, P., Brouard, B., Dump, G., 1996. Behavior of sealed solution-mined caverns, in: *Fourth Conference on the Mechanical Behavior of Salt*. TTP Trans Tech Publications, pp. 511–524.
- Bérest, P., Ledoux, E., Legait, B., De Marsiry, G., 1979. Effets thermiques dans les cavités en couches salifère, in: *Proceedings of Fourth ISRM Congress*, Vol. I. pp. 31–35.
- Bérest, P., Sicsic, P., Brouard, B., 2016. Thermomechanical effects of depressurization in a CAES, in: *50th US Rock Mechanics / Geomechanics Symposium 2016*. American Rock Mechanics Association (ARMA), Houston.
- Brandão, N.B., 2016. Modelling of the evolution of the mechanical properties of the cement paste in pre salt wells. MSc. Dissertation - Civil Engineering Department, Pontifical Catholic University of Rio de Janeiro (PUC-Rio) [in Portuguese].
- Brandão, N.B., Roehl, D., Andrade Silva, F., Rosas e Silva, R., 2017. The impact of cement slurry aging creep on the construction process of oil wells. *J. Pet. Sci. Eng.* 157, 422–429. <https://doi.org/10.1016/j.petrol.2017.07.051>
- Brassow, C.L., Thoms, R.L., 2000. Use of solution-mined salt caverns for disposal of hazardous and industrial waste products, in: *Eight Salt Symposium*. The Hague, pp. 229–235.
- Brinkman, H.C., 1949. A calculation of the viscous force exerted by a flowing fluid on a dense swarm of particles. *Appl. Sci. Res.* A1. <https://doi.org/10.1007/BF00411979>
- Calcada, L.A., Martins, L.A.A., Scheid, C.M., Magalhães, S.C., Martins, A.L., 2015. Mathematical model of dissolution of particles of NaCl in well drilling: Determination of mass transfer convective coefficient. *J. Pet. Sci. Eng.* 126, 97–104. <https://doi.org/10.1016/j.petrol.2014.12.011>
- Camacho-Velázquez, R., Vásquez-Cruz, M., Castrejón-Aivar, R., Arana-Ortiz, V., 2005. Pressure-transient and decline-curve behavior in naturally fractured vuggy carbonate reservoir. *SPE Reserv. Eval. Eng.* 8, 95–111.

<https://doi.org/10.2118/77689-PA>

- Cazarin, C.L., Bezerra, F.H.R., Borghi, L., Santos, R. V., Favoreto, J., Brod, J.A., Auler, A.S., Srivastava, N.K., 2019. The conduit-seal system of hypogene karst in Neoproterozoic carbonates in northeastern Brazil. *Mar. Pet. Geol.* 101, 90–107. <https://doi.org/10.1016/j.marpetgeo.2018.11.046>
- Chin, L.Y., Raghavan, R., Thomas, L.K., 2000. Fully coupled geomechanics and fluid-flow analysis of wells with stress-dependent permeability. *SPE J.* 5, 32–45. <https://doi.org/10.2118/58968-PA>
- Corrêa, R.S.M., 2016. Modelling the stress-strain behaviour of fault zones in travertines using finite element method. MSc. Dissertation - Pontifical Catholic University of Rio de Janeiro (PUC-Rio) [in Portuguese].
- Cosenza, P., Ghoreychi, M., 1996. Coupling between mechanical behavior and transfer phenomena in salt, in: 3rd Conference on Mechanical Behavior of Salt (Salt Mech III). pp. 285–307.
- Cosenza, P., Ghoreychi, M., Bazargan-Sabet, B., De Marsily, G., 1999. In situ rock salt permeability measurement for long term safety assessment of storage. *Int. J. Rock Mech. Min. Sci.* 36, 509–526. [https://doi.org/10.1016/S0148-9062\(99\)00017-0](https://doi.org/10.1016/S0148-9062(99)00017-0)
- Cosenza, P., Ghoreychi, M., Chanchole, S., 2002. Effects of fluid-rock interaction on mechanical behaviour of rock salt, in: Cristescu, H. (Ed.), *Basic and Applied Salt Mechanics - Fifth Conference on the Mechanical Behaviour of Salt (Salt Mech 5)*. Bucharest, pp. 57–71.
- Costa, A.M., 1984. An application of computational methods and rock mechanics principles to the design and analysis of underground mine excavations. DSc. Thesis - COPPE, Federal University of Rio de Janeiro [in Portuguese].
- Costa, A.M., Amaral, C., Poiate Jr., E., Pereira, A., Martha, L.F.M., Gattass, M., Roehl, D., 2012. Underground storage of natural gas and CO<sub>2</sub> in salt caverns in deep and ultra-deep water offshore Brazil, in: Zhou, Q. (Ed.), *Harmonising Rock Engineering and the Environment (12th ISRM Congress)*. Beijing, pp. 1659–1664. <https://doi.org/10.1201/b11646-314>
- Costa, A.M., Amaral, C.S., Poiate Jr., E., 2015. Hydrocarbon production and storage using offshore underground salt caverns, in: Roberts, Mellegard, Hansen (Eds.), *The Mechanical Behavior of Salt VIII Conference (Salt Mech*

8). Taylor & Francis Group/CRC Press/Balkema, Rapid City, pp. 209–216.  
<https://doi.org/10.1201/b18393-28>

Costa, A.M., Costa, P.V.M., Meneghini, J.R., Nishimoto, K., Sampaio, C.M., Brandão, C., Breda, A., 2019a. Hybrid subsea CCS system-CO<sub>2</sub> storage in offshore ultra deep-water salt caverns. *Curr. Trends Civ. Struct. Eng.* 1, 1–22.  
<https://doi.org/10.33552/CTCSE.2019.01.000513>

Costa, A.M., Costa, P.V.M., Miranda, A.C.O., Goulart, M.B.R., Udebhulu, O.D., Ebecken, N.F.F., Azevedo, R.A., Eston, S.M., Tomi, G., Mendes, A.B., Meneghini, J.R., Nishimoto, K., Sampaio, C.M., Brandão, C., Breda, A., 2019b. Experimental salt cavern in offshore ultra-deep water and well design evaluation for CO<sub>2</sub> abatement. *Int. J. Min. Sci. Technol.* 29, 641–656.  
<https://doi.org/10.1016/j.ijmst.2019.05.002>

Costa, A.M., Medeiros, F.A.S., Fonseca, C.F.H., Amaral, C.S., Gonçalves, C.J.C., 2000. Drilling through long salt intervals in Campos Basin-Brazil, in: Eighth Salt Symposium. The Hague, pp. 247–252.

Costa, A.M., Poiate, E., Amaral, C.S., Gonçalves, C.J.C., Falcão, J.L., Pereira, A., 2010. Geomechanics applied to the well design through salt layers in Brazil: A history of success, in: 44th US Rock Mechanics Symposium and 5th US-Canada Rock Mechanics Symposium. American Rock Mechanics Association (ARMA), Salt Lake City.

Costa, A.M., Poiate Jr., E., Falcão, J.L., Coelho, L.F.M., 2005. Triaxial creep tests in salt applied in drilling through thick salt layers in Campos basin-Brazil, in: IADC/SPE Drilling Conference. Amsterdam. <https://doi.org/10.2118/92629-MS>

Costa, P.M. V., Costa, A.M., Meneghini, J.R., Nishimoto, K., Sampaio, C.M., Assi, G., Malta, E., Goulart, M.B.R., Bergsten, A., Udebhulu, O.D., Azevedo, R.C., Eston, S.M., Tomi, G., Ebecken, N.F.F., Rosa, L.P., Miranda, A.C.O., Brandão, C., Breda, A., 2020. Parametric study and geomechanical design of ultra-deep-water offshore salt caverns for carbon capture and storage in Brazil. *Int. J. Rock Mech. Min. Sci.* 131.  
<https://doi.org/10.1016/j.ijrmmms.2020.104354>

CPRM, 2019. Estudos sobre a instabilidade do terreno nos bairros Pinheiro, Mutange e Bebedouro, Maceió (AL). Brasília.

- D'Élia, P.C., 1991. Analysis and back-analysis of the creep behavior in underground excavations by the finite element method. MSc. Dissertation - COPPE, Federal University of Rio de Janeiro (UFRJ) [in Portuguese].
- David, C., Menendez, B., Zhu, W., Wong, T.F., 2001. Mechanical compaction, microstructures and permeability evolution in sandstones. *Phys. Chem. Earth, Part A Solid Earth Geod.* 26, 45–51. [https://doi.org/10.1016/S1464-1895\(01\)00021-7](https://doi.org/10.1016/S1464-1895(01)00021-7)
- De Simone, M., 2016. Thermo-mechanical stress analyses in wellbore considering analytical and numerical approaches. MSc. Dissertation - Civil Engineering Department, Pontifical Catholic University of Rio de Janeiro (PUC-Rio) [in Portuguese].
- De Simone, M., Pereira, F.L.G., Roehl, D.M., 2017. Analytical methodology for wellbore integrity assessment considering casing-cement-formation interaction. *Int. J. Rock Mech. Min. Sci.* 94, 112–122. <https://doi.org/10.1016/j.ijrmmms.2016.12.002>
- Delabroy, L., Rodrigues, D., Norum, E., Straume, M., Halvorsen, K.H., 2017. Perforate, wash and cement PWC - Verification process and an industry standard for barrier acceptance criteria, in: SPE Bergen One Day Seminar. Society of Petroleum Engineers (SPE), Bergen. <https://doi.org/10.2118/185938-ms>
- DeVries, K.L., Callahan, G.D., Mellegard, K.D., 2005a. Numerical simulations of natural gas storage caverns in bedded salt, in: Alaska Rocks 2005, The 40th U.S. Symposium on Rock Mechanics (USRMS): Rock Mechanics for Energy, Mineral and Infrastructure (ARMA Symposium). Anchorage.
- DeVries, K.L., Mellegard, K.D., Callahan, G.D., Goodman, W.M., 2005b. Cavern roof stability for natural gas storage in bedded salt. Rapid City. <https://doi.org/10.2172/850074>
- Domingues, D.P., 2011. Geological and geomechanical characterization of travertines. MSc. Dissertation - Department of Civil and Environmental Engineering, Pontifical Catholic University of Rio de Janeiro (PUC-Rio) [in Portuguese].
- Doornhof, D., Kristiansen, T.G., Nagel, N.B., Pattillo, P.D., Sayers, C., 2006. Compaction and subsidence. *Oilf. Rev.* Autumn, 50–68.

[https://doi.org/10.1007/978-3-642-29104-3\\_15](https://doi.org/10.1007/978-3-642-29104-3_15)

- Dorn, J.E., 1955. Some fundamental experiments on high temperature creep. *J. Mech. Phys. Solids* 3, 85–116.
- Durie, R.W., Jessen, F.W., 1964a. Mechanism of the dissolution of salt in the formation of underground salt cavities. *Soc. Pet. Eng. J.* 4, 183–190. <https://doi.org/10.2118/678-pa>
- Durie, R.W., Jessen, F.W., 1964b. The influence of surface features in the salt dissolution process. *Soc. Pet. Eng. J.* 4, 275–281. <https://doi.org/10.2118/1005-pa>
- Durup, J.G., Vidal, F., Rolin, C., 2007. Pilot abandonment test of a very deep gas storage salt cavern. *Oil Gas Sci. Technol.* 62, 287–296.
- Dusseault, M.B., 1989. Saltrock behavior as an analogue to the behavior of rock at great depth, in: Maury, V., Fourmaintraux, D. (Eds.), *Rock at Great Depth (ISRM International Symposium)*. Balkema, Pau, pp. 11–17.
- Dusseault, M.B., Bachu, S., Davidson, B.C., 2001a. Carbon dioxide sequestration potential in salt solution caverns in Alberta, Canada, in: *Fall 2001 Technical Meeting*. Solution Mining Research Institute (SMRI), Albuquerque.
- Dusseault, M.B., Bachu, S., Rothenburg, L., 2004. Sequestration of CO<sub>2</sub> in salt caverns. *J. Can. Pet. Technol.* 43, 49–55. <https://doi.org/10.2118/04-11-04>
- Dusseault, M.B., Bruno, M.S., Barrera, J., 2001b. Casing shear: causes, cases, cures. *SPE Drill. Complet.* 16, 98–107.
- Dusseault, M.B., Rothenburg, L., Mraz, D.Z., 1987. The design of openings in saltrock using a multiple mechanism viscoplastic law, in: *28th US Symposium on Rock Mechanics*. Tucson, pp. 633–642.
- Eiksund, G., Svano, G., Nagel, N.B., 1995. Creep related subsidence caused by oil and gas extraction, in: *Fifth International Symposium on Land Subsidence*. International Association of Hydrological Sciences (IAHS), The Hague, pp. 277–285. [https://doi.org/10.1016/s0148-9062\(97\)87588-2](https://doi.org/10.1016/s0148-9062(97)87588-2)
- Escobar, R.G., Mejia Sanchez, E.C., Roehl, D., Romanel, C., 2019. Xfem modeling of stress shadowing in multiple hydraulic fractures in multi-layered formations. *J. Nat. Gas Sci. Eng.* 70, 1–15. <https://doi.org/10.1016/j.jngse.2019.102950>
- Euillades, P.A., Euillades, L.E., Rosell, P., Roa, Y., 2020. Subsidence in Maceio,

Brazil, characterized by dinstar and inverse modeling, in: IEEE Latin American GRSS & ISPRS Remote Sensing Conference. <https://doi.org/10.1109/LAGIRS48042.2020.9165567>

Evans, D., Highley, D., Gale, I., Rayner, D., Hill, A., 2008. Underground storage, Mineral Planning Factsheet. <https://doi.org/10.1111/j.1745-6592.1987.tb00961.x>

Evans, D., Parkes, D., Dooner, M., Williamson, P., Williams, J., Busby, J., He, W., Wang, J., Garvey, S., 2021. Salt cavern exergy storage capacity potential of UK massively bedded halites, using compressed air energy storage (CAES). *Appl. Sci.* 11. <https://doi.org/10.3390/app11114728>

Falcão, J.L., 2009. Perfuração de formações salíferas, in: *Sal - Geologia e Tectônica - Exemplos Nas Bacias Brasileiras*. Editora Beca, São Paulo, pp. 386–405.

Farias, P.I. V., Freire, E., Cunha, A.L.C., Antunes, A.M.S., 2021. The strategic diagnosis of the potassium fertilizer industry in Brazil. *J. Geol. Surv. Brazil* 4, 107–121. <https://doi.org/10.29396/jgsb.2021.v4.n2.2>

Finley, R.E., Zeuch, D.H., Stormont, J.C., Daemen, J.J.K., 1994. Sealing of boreholes using natural, compatible materials: Granular salt, in: *SPE/ISRM Rock Mechanics in Petroleum*. Society of Petroleum Engineers (SPE), Delft, pp. 753–760. <https://doi.org/10.2523/28124-ms>

Firme, P.A.L.P., 2013. Constitutive modeling and probabilistic analysis applied to wells in salt zones. MSc. Dissertation - Civil Engineering Department, Pontifical Catholic University of Rio de Janeiro (PUC-Rio) [in Portuguese].

Firme, P.A.L.P., Brandao, N.B., Roehl, D., Romanel, C., 2018a. Enhanced double-mechanism creep laws for salt rocks. *Acta Geotech.* 13, 1329–1340. <https://doi.org/10.1007/s11440-018-0689-7>

Firme, P.A.L.P., Costa, A.M., Poiate Jr., E., Carrion, M.A., Roehl, D., 2015a. Casing integrity of a typical pre-salt wellbore under local salt dissolution conditions, in: *Proceedings, 13th International Congress on Rock Mechanics (ISRM Congress)*. Montréal.

Firme, P.A.L.P., Pereira, F.L.G., Roehl, D., Romanel, C., 2016a. A probabilistic assessment of the casing integrity in a Pre-salt wellbore, in: *50th US Rock Mechanics / Geomechanics Symposium*. American Rock Mechanics

Association (ARMA), Houston.

- Firme, P.A.L.P., Quevedo, R.J., Roehl, D., 2017. Modeling of key lifespan stages of a Pre-salt wellbore, in: 51st US Rock Mechanics/Geomechanics Symposium (ARMA Symposium). American Rock Mechanics Association (ARMA), San Francisco.
- Firme, P.A.L.P., Quevedo, R.J., Roehl, D., Pereira, L.C., Cazarin, C.L., 2021. Mechanical behavior of carbonate reservoirs with single karst cavities. *Geomech. Energy Environ.* 25. <https://doi.org/10.1016/j.gete.2020.100209>
- Firme, P.A.L.P., Quispe, R.Q., Roehl, D., Oliveira, M.F., Parotidis, M., Glassborow, B., 2014a. A comparative study of constitutive models for reservoir compaction and surface subsidence, in: *Rock Mechanics for Natural Resources and Infrastructure - SBMR 2014 – ISRM Specialized Conference*. CBMR/ABMS and ISRM, Goiania.
- Firme, P.A.L.P., Roehl, D., Romanel, C., 2019. Salt caverns history and geomechanics towards future natural gas strategic storage in Brazil. *J. Nat. Gas Sci. Eng.* 72. <https://doi.org/https://doi.org/10.1016/j.jngse.2019.103006>
- Firme, P.A.L.P., Roehl, D., Romanel, C., 2018b. A glance into the mechanical behavior of salt caverns towards future natural gas strategic storage in Brazil, in: Fahland, Hammer, Hansen, Heusermann, Lux, Minkley (Eds.), 9th Conference on the Mechanical Behavior of Salt (Salt Mech IX). Hannover, pp. 843–854.
- Firme, P.A.L.P., Roehl, D., Romanel, C., 2016b. An assessment of the creep behaviour of Brazilian salt rocks using the multi-mechanism deformation model. *Acta Geotech.* 11, 1445–1463. <https://doi.org/10.1007/s11440-016-0451-y>
- Firme, P.A.L.P., Roehl, D., Romanel, C., Poiate Jr., E., Costa, A.M., 2015b. Multi-mechanism deformation creep model applied to Brazilian salt rocks, in: Roberts, Mellegard, Hansen (Eds.), *The Mechanical Behavior of Salt VIII Conference (Salt Mech 8)*. Taylor & Francis Group/CRC Press/Balkema, Rapid City, pp. 339–346. <https://doi.org/10.1201/b18393-41>
- Firme, P.A.L.P., Roehl, D., Romanel, C., Poiate Jr, E., Costa, A.M., 2014b. Creep constitutive modeling applied to the stability of pre-salt wellbores through salt layers, in: 48th US Rock Mechanics/Geomechanics Symposium (ARMA

Symposium). Minneapolis.

- Fjær, E., Folstad, J.S., Li, L., 2016. How creeping shale may form a sealing barrier around a well, in: 50th US Rock Mechanics / Geomechanics Symposium 2016 (ARMA Symposium). American Rock Mechanics Association (ARMA), Houston.
- Florêncio, C.P., 2009. A mineração de evaporitos, in: Mohriak, W., Szatmari, P., Couto Anjos, S.M. (Eds.), *Sal - Geologia e Tectônica - Exemplos Nas Bacias Brasileiras* [in Portuguese]. Editora Beca, São Paulo, pp. 407–414.
- Fokker, P.A., van Leijen, F.J., Orlic, B., van der Marel, H., Hanssen, R.F., 2018. Subsidence in the Dutch Wadden Sea. *Netherlands J. Geosci.* 97, 129–181. <https://doi.org/10.1017/njg.2018.9>
- Folsta, M.G., Martins, A.L., Lomba, R.F.T., Cardoso Jr., W.F., Simão, C.A., Sidi, I.A., Dannenhauer, C.E., 2011. Predicting salt leaching during drilling and cementing operations, in: SPE/IADC Drilling Conference and Exhibition. Amsterdam. <https://doi.org/10.2118/140242-ms>
- Ford, D., Williams, P.D., 2007. *Karst hydrogeology and geomorphology*. Chichester, UK.
- Fossum, A.F., Fredrich, J.T., 2007. Probabilistic analysis of borehole closure for through-salt well design. *Acta Geotech.* 2, 41–51.
- Fossum, A.F., Fredrich, J.T., 2002. Salt mechanics primer for near-salt and sub-salt deepwater Gulf of Mexico field developments, Sandia Report. Albuquerque. <https://doi.org/10.2172/801384>
- França, M.R., 2020. Brazilian P&A Overview, in: Presentation at Webinar in Decommissioning and P&A Section – Brazil Norway. YouTube. [https://www.youtube.com/watch?v=d\\_tneUVyJ-w&feature=youtu.be](https://www.youtube.com/watch?v=d_tneUVyJ-w&feature=youtu.be).
- Fredrich, J.T., Fossum, A.F., Hickman, R.J., 2007. Mineralogy of deepwater Gulf of Mexico salt formations and implications for constitutive behavior. *J. Pet. Sci. Eng.* 57, 354–374. <https://doi.org/10.1016/j.petrol.2006.11.006>
- Furtado, R., Barnabé, P.A., Loureiro, A.B.A., 2018. Descomissionamento offshore no Brasil. *TN Pet.* 122, 42–49.
- Gateway, 2007. Gateway - Environmental Impact Assessment Consent Decision.
- Gateway, n.d. Gateway Gas Storage Facility [WWW Document]. URL

<https://www.hydrocarbons-technology.com/projects/gateway-gas-storage/>  
(accessed 2.26.22).

- Geertsma, J., 1973. A basic theory of subsidence due to reservoir compaction: the homogeneous case. *Verh. K. Ned. Geol. en Mijnbouwk. Genoot.* 28, 43–62.
- Gloyna, E.F., Reynolds, T.D., 1961. Permeability measurements of rock salt. *J. Geophys. Res.* 66, 3913–3921. <https://doi.org/10.1029/jz066i011p03913>
- Gonçalves, G.G., 2011. Estudo paramétrico da influência da temperatura na análise termomecânica durante a escavação em rochas salinas. MSc. Dissertation - Unidade Acadêmica Centro de Tecnologia (CTEC), Universidade Federal de Alagoas (UFAL) [in Portuguese].
- Goodman, R.E., 1989. *Introduction to rock mechanics*, 2nd. ed. John Wiley & Sons, Ltd, New York.
- Goulart, M.B.R., Costa, P.V.M., Costa, A.M., Miranda, A.C.O., Mendes, A.B., Ebecken, N.F.F., Meneghini, J.R., Nishimoto, K., Assi, G.R.S., 2020. Technology readiness assessment of ultra-deep salt caverns for carbon capture and storage in Brazil. *Int. J. Greenh. Gas Control* 99. <https://doi.org/10.1016/j.ijggc.2020.103083>
- Grabner, M., Wächter, E., Nicolussi, K., Bolka, M., Sormaz, T., Steier, P., Wild, E.M., Barth, F.E., Kern, A., Rudorfer, J., Kowarik, K., Stöllner, T., Reschreiter, H., 2021. Prehistoric salt mining in Hallstatt, Austria. New chronologies out of small wooden fragments. *Dendrochronologia* 66. <https://doi.org/10.1016/j.dendro.2021.125814>
- Grunau, H.R., 1981. Worldwide review of seals for major accumulations of natural gas (Abstract), in: *AAPG Bulletin*. American Association of Petroleum Geologists (AAPG).
- Guenot, A., Santarelli, F.J., 1989. Influence of Mud temperature on deep borehole behaviour, in: *Rock at Great Depth (ISRM International Symposium)*. pp. 809–817. [https://doi.org/10.1016/0148-9062\(90\)91486-q](https://doi.org/10.1016/0148-9062(90)91486-q)
- Guimarães, J.T., Grissolia, E.M., Ferreira, J.C.S., Souza, J.L.M., Villar, P.M., Santiago, R., Sobrinho, V.S., 2018. Relatório preliminar: Ilha de Matarandiba/Bahia. Salvador.
- Gysel, M., 2002. Anhydrite dissolution phenomena: three case histories of anhydrite karst caused by water tunnel operation. *Rock Mech. Rock Eng.* 35,

1–21. <https://doi.org/10.1007/s006030200006>

- Hallak, T.V.P., 2017. Plug & abandonment techniques for offshore wells. Undergraduate Project - Federal University of Rio de Janeiro (UFRJ).
- Halvorsen, C., 2016. Plug and abandonment technology evaluation and field case study. MSc. Thesis - Faculty of Science and Technology, University of Stavanger.
- Hambley, D.E., Dusseault, M.B., Mraz, D.Z., 1998. Characterization of saltrock creep behavior. 29th U.S. Symp. Rock Mech. USRMS 1988 179–189. [https://doi.org/10.1016/0148-9062\(89\)90612-8](https://doi.org/10.1016/0148-9062(89)90612-8)
- Hansen, F.D., 2014. Micromechanics of isochoric salt deformation, in: 48th US Rock Mechanics/Geomechanics Symposium (ARMA Symposium). Minneapolis.
- Hansen, F.D., 2012. Underground salt research laboratory at the Waste Isolation Pilot Plant. Sandia National Laboratories. Albuquerque.
- Hansen, F.D., 2011. Salt repository geomechanics research agenda, in: 45th US Rock Mechanics/Geomechanics Symposium (ARMA Symposium). San Francisco.
- Hansen, F.D., Leigh, C.D., 2011. Salt disposal of heat-generating nuclear waste. Sandia National Laboratories (SAND2011-0161). Albuquerque.
- Hettema, M., Papamichos, E., Schutjens, P., 2002. Subsidence delay: field observations and analysis. Oil Gas Sci. Technol. 57, 443–458. <https://doi.org/10.2516/ogst:2002029>
- Heusermann, S., Rolfs, O., Schmidt, U., 2003. Nonlinear finite-element analysis of solution mined storage caverns in rock salt using the LUBBY2 constitutive model. Comput. Struct. 81, 629–638. [https://doi.org/10.1016/S0045-7949\(02\)00415-7](https://doi.org/10.1016/S0045-7949(02)00415-7)
- Hirth, J., Lothe, J., 1982. Theory of dislocations. Interscience, New York.
- Holt, R.M., Larsen, I., Fjær, E., Stenebråten, J.F., 2020. Comparing mechanical and ultrasonic behaviour of a brittle and a ductile shale: Relevance to prediction of borehole stability and verification of shale barriers. J. Pet. Sci. Eng. 187, 106746. <https://doi.org/10.1016/j.petrol.2019.106746>
- Hou, Z., Wundram, L., Meyer, R., Schmidt, M., Schmitz, S., Were, P., 2012.

Development of a long-term wellbore sealing concept based on numerical simulations and in situ-testing in the Altmark natural gas field. *Environ. Earth Sci.* 67, 395–409. <https://doi.org/10.1007/s12665-012-1670-7>

Hunsche, U., 1993. Failure Behaviour of Rock Salt Around Underground Cavities, in: *Seventh Salt Symposium*. Kyoto, pp. 59–65.

Hunsche, U., Hampel, A., 1999. Rock salt - the mechanical properties of the host rock material for a radioactive waste repository. *Eng. Geol.* 52, 271–291. [https://doi.org/10.1016/S0013-7952\(99\)00011-3](https://doi.org/10.1016/S0013-7952(99)00011-3)

IBP, 2017. Diretrizes para abandono de poços. Brazilian Petroleum and Gas Institute (IBP).

Jeremic, M.L., 1994. *Rock mechanics in salt mining*, 1st ed. A. A. Balkema Publishers, Rotterdam.

Johnson, K.S., 2008. Evaporite-karst problems and studies in the USA. *Environ. Geol.* 53, 937–943. <https://doi.org/10.1007/s00254-007-0716-8>

Johnson, K.S., 2005. Subsidence hazards due to evaporite dissolution in the United States. *Environ. Geol.* 48, 395–409. <https://doi.org/10.1007/s00254-005-1283-5>

Johnson, K.S., 1989. Development of the Wink Sink in west Texas, U.S.A., due to salt dissolution and collapse. *Environ. Geol.* 14, 81–92. <https://doi.org/10.1007/BF01728499>

Kaiser, M.J., 2017. Rigless well abandonment remediation in the shallow water U.S. Gulf of Mexico. *J. Pet. Sci. Eng.* 151, 94–115.

Kazemi, H., Jessen, F.W., 1964. Mechanism of flow and controlled dissolution of salt in solution mining. *Soc. Pet. Eng. J.* 4, 317–328. <https://doi.org/10.2118/1007-pa>

Keime, M., Charnavel, Y., Lampe, G., Theylich, H., 2012. Obstruction in a salt cavern: Solution is dissolution, in: *World Gas Conference*. Kuala Lumpur.

Khaledi, K., Mahmoudi, E., Datcheva, M., Schanz, T., 2016. Stability and serviceability of underground energy storage caverns in rock salt subjected to mechanical cyclic loading. *Int. J. Rock Mech. Min. Sci.* 86, 115–131. <https://doi.org/10.1016/j.ijrmms.2016.04.010>

Khalifeh, M., Hodne, H., Saasen, A., Vrålstad, T., 2013. *Techniques and materials*

- for North Sea plug and abandonment operations, in: Offshore Technology Conference. Offshore Technology Conference (OTC), Houston. <https://doi.org/10.4043/23915-ms>
- Khalifeh, M., Saasen, A., 2020. Introduction to permanent plug and abandonment of wells. Springer Cham. <https://doi.org/https://doi.org/10.1007/978-3-030-39970-2>
- Klimchouk, A., 2006. Unconfined versus confined speleogenetic settings: variations of solution porosity. *Int. J. Speleol.* 35, 19–24. <https://doi.org/10.5038/1827-806x.35.1.3>
- Kostick, D.S., 2006. Salt, in: *Metals and Minerals: U. S. Geological Survey Minerals Yearbook 2006*. U. S. Geological Survey, pp. 63.1-63.17.
- Kristiansen, T.G., Dyngeland, T., Kinn, S., Flatebø, R., Aarseth, N.A., 2018. Activating shale to form well barriers: theory and field examples. *Proc. - SPE Annu. Tech. Conf. Exhib. 2018-Septe*, 24–26. <https://doi.org/10.2118/191607-ms>
- Kuhlman, K.L., Matteo, E.N., 2018. Porosity and permeability: literature review and summary, in: Fahland, Hammer, Hansen, Heusermann, Lux, Minkley (Eds.), *9th Conference on the Mechanical Behavior of Salt (Salt Mech IX)*. Hannover, pp. 15–27.
- Kunstman, A.S., Urbanczyk, K.M., 2000. Computer models of the salt cavern leaching process - evolution over the last 35 years, in: *Eighth Salt Symposium*. The Haghe, pp. 279–284.
- Labaune, P., Rouabhi, A., Tijani, M., Blanco-Martín, L., You, T., 2018. Dilatancy criteria for salt cavern design: a comparison between stress- and strain-based approaches. *Rock Mech. Rock Eng.* 51, 599–611. <https://doi.org/10.1007/s00603-017-1338-4>
- Lamarche, J., Lavenu, A.P.C., Gauthier, B.D.M., Guglielmi, Y., Jayet, O., 2012. Relationships between fracture patterns, geodynamics and mechanical stratigraphy in Carbonates (South-East Basin, France). *Tectonophysics* 581, 231–245. <https://doi.org/10.1016/j.tecto.2012.06.042>
- Larsen, A., 2007. Gas in overburden on Ekofisk. MSc. Thesis - Department of Petroleum technology - Institute of Technology and Science, University of Stavanger.

- Lee, A., 2021. Subsea caverns to store hydrogen from gigawatt-scale wind farms in “world first” plan by Engie unit [WWW Document]. Recharg. - Glob. news Intel. Energy Transit. URL <https://www.rechargenews.com/energy-transition/subsea-caverns-to-store-hydrogen-from-gigawatt-scale-wind-farms-in-world-first-plan-by-engie-unit/2-1-1132898> (accessed 2.26.22).
- Li, C., Barès, P., Laloui, L., 2015. A hydromechanical approach to assess CO<sub>2</sub> injection-induced surface uplift and caprock deflection. *Geomech. Energy Environ.* 4, 51–60. <https://doi.org/10.1016/j.gete.2015.06.002>
- Li, C., Laloui, L., 2017. Impact of material properties on caprock stability in CO<sub>2</sub> geological storage. *Geomech. Energy Environ.* 11, 28–41. <https://doi.org/10.1016/j.gete.2017.06.003>
- Li, J., Shi, X., Wang, T., Yang, C., Li, Y., Ma, H., Ma, X., Shi, H., 2016. A prediction model of the accumulation shape of insoluble sediments during the leaching of salt cavern for gas storage. *J. Nat. Gas Sci. Eng.* 33, 792–802. <https://doi.org/10.1016/j.jngse.2016.06.023>
- Li, J., Shi, X., Yang, C., Li, Y., Wang, T., Ma, H., Shi, H., Li, J., Liu, J., 2017. Repair of irregularly shaped salt cavern gas storage by re-leaching under gas blanket. *J. Nat. Gas Sci. Eng.* 45, 848–859. <https://doi.org/10.1016/j.jngse.2017.07.004>
- Li, W., An, X., Li, H., 2018. Limestone mechanical deformation behavior and failure mechanisms: a review. *Acta Geochim.* 37, 153–170. <https://doi.org/10.1007/s11631-017-0259-y>
- Li, Y., Liu, W., Yang, C., Daemen, J.J.K., 2014. Experimental investigation of mechanical behavior of bedded rock salt containing inclined interlayer. *Int. J. Rock Mech. Min. Sci.* 69, 39–49. <https://doi.org/10.1016/j.ijrmms.2014.03.006>
- Liang, G. -c., Huang, X., Peng, X. -y., Tian, Y., Yu, Y. -h., 2016. Investigation on the cavity evolution of underground salt cavern gas storages. *J. Nat. Gas Sci. Eng.* 33, 118–134. <https://doi.org/10.1016/j.jngse.2016.05.018>
- Lira, W.W.M., Gonçalves, G.G., Araujo, C.N., Ramos, A.S., Frery, A.C., 2015. Thermomechanical effect of vertical well drilling in salt rocks in selected cases. *Eng. Comput.* 32, 1307–1322. <https://doi.org/10.1108/EC-04-2014-0092>
- Lobanov, I.S., Popov, I.Y., Popov, A.I., Gerya, T. V., 2014. Numerical approach to

the Stokes problem with high contrasts in viscosity. *Appl. Math. Comput.* 235, 17–25.

Lomba, R.F.T., Folsta, M.G., Resende, E.L., Plucenio, D.M., Dannenhauer, C.E., 2013a. Use of salt dissolution software to evaluate drilling strategies of massive salt layers, in: *Offshore Technology Conference Brasil (OTC)*. Rio de Janeiro. <https://doi.org/10.4043/24345-ms>

Lomba, R.F.T., Teixeira, G.T., Pessanha, R.R., Lomba, B.S., Folsta, M.G., Cardoso Jr., W.F., Goncalves, J.T., 2013b. Lessons learned in drilling pre-salt wells with water based muds, in: *Offshore Technology Conference Brasil (OTC)*. Rio de Janeiro. <https://doi.org/10.4043/24355-ms>

Lomenick, T.F., Bradshaw, R.L., 1969. Deformation of rock salt in openings mined for the disposal of radioactive wastes. *Rock Mech.* 1, 5–29. <https://doi.org/10.1007/BF01247355>

Loucks, R.G., 1999. Paleocave carbonate reservoirs: origins, burial-depth modifications, spatial complexity, and reservoir implications. *Am. Assoc. Pet. Geol. Bull.* 83, 1795–1834. <https://doi.org/10.1306/E4FD426F-1732-11D7-8645000102C1865D>

Luu, L.H., Noury, G., Benseghier, Z., Philippe, P., 2019. Hydro-mechanical modeling of sinkhole occurrence processes in covered karst terrains during a flood. *Eng. Geol.* 260. <https://doi.org/10.1016/j.enggeo.2019.105249>

Lux, K.-H., Düsterloh, U., 2015. From birth to long-term life - main aspects regarding THM-coupled simulation of salt cavern behavior as well as regarding improved salt cavern design with special consideration of salt damage, in: Roberts, Mellegard, Hansen (Eds.), *The Mechanical Behavior of Salt VIII Conference (Salt Mech 8)*. Taylor & Francis Group/CRC Press/Balkema, London, pp. 273–289.

Ma, L.J., Liu, X.Y., Fang, Q., Xu, H.F., Xia, H.M., Li, E.B., Yang, S.G., Li, W.P., 2013. A new elasto-viscoplastic damage model combined with the generalized hoek-brown failure criterion for bedded rock salt and its application. *Rock Mech. Rock Eng.* 46, 53–66. <https://doi.org/10.1007/s00603-012-0256-8>

Mahmoudi, E., Khaledi, K., Miro, S., König, D., Schanz, T., 2017. Probabilistic analysis of a rock salt cavern with application to energy storage systems.

Rock Mech. Rock Eng. 50, 139–157. <https://doi.org/10.1007/s00603-016-1105-y>

Marketos, G., Govers, R., Spiers, C.J., 2016a. Rocksalt creep, uncertainties, and their implications for surface subsidence above a producing rocksalt-capped reservoir, in: 50th US Rock Mechanics / Geomechanics Symposium. American Rock Mechanics Association (ARMA), Houston.

Marketos, G., Govers, R., Spiers, C.J., 2015a. Ground motions induced by a producing hydrocarbon reservoir that is overlain by a viscoelastic rocksalt layer: A numerical model. Geophys. J. Int. 203, 228–242. <https://doi.org/10.1093/gji/ggv294>

Marketos, G., Govers, R.M.A., Spiers, C.J., 2015b. Surface subsidence induced by hydrocarbons extraction, and the potential for time-dependent ground deformations, in: 49th US Rock Mechanics / Geomechanics Symposium. American Rock Mechanics Association (ARMA), San Francisco.

Marketos, G., Spiers, C.J., Govers, R., 2016b. Impact of rock salt creep law choice on subsidence calculations for hydrocarbon reservoirs overlain by evaporite caprocks. J. Geophys. Res. Solid Earth 121, 4249–4267. <https://doi.org/10.1002/2016JB012892>

Marketos, G., Spiers, C.J., Govers, R., 2015c. Long-term subsidence study of the Ameland gas field: time-dependence induced, Final Report. Earth Sciences Department - Utrecht University.

Mason, J., 2012. Bakken's maximum potential oil production rate explored. Oil Gas J.

Matos, M., 2021. Abandono de poços – técnicas e oportunidades, in: Presentation at SPE Brazil Tech Tuesday. YouTube. <https://www.youtube.com/watch?v=B-2PIHvk8Ag&t=1666s>.

Medeiros, F.A.S., 1999. Análise do comportamento de colunas de revestimento frente à movimentação do sal em poços de petróleo. MSc. Dissertation - Civil Engineering Department, Pontifical Catholic University of Rio de Janeiro (PUC-Rio) [in Portuguese].

Mejia Sanchez, E.C., Quevedo, R., Roehl, D., 2019. Hydro-mechanical modelling of naturally fractured reservoirs, in: 53rd U.S. Rock Mechanics/Geomechanics Symposium. American Rock Mechanics

Association, New York.

Melo, P.R.C., Carvalho, R.S., Pinto, D.C., 2008. Halita, in: Luz, A.B., Lins, F.A.F. (Eds.), Rochas & Minerais Industriais No Brasil: Usos e Especificações. CETEM/MCT, Rio de Janeiro, pp. 551–584.

Mendes, C.A.T., 2016. GeMA, a new framework for prototyping, development and integration of multiphysics and multiscale simulations in multidisciplinary groups. DSc. Thesis - Department of Informatics, Pontifical Catholic University of Rio de Janeiro (PUC-Rio) [in Portuguese].

Mendes, C.A.T., Gattass, M., Roehl, D., 2016. The GeMA framework - An innovative framework for the development of multiphysics and multiscale simulations, in: M. Papadrakakis, Papadopoulos, V., Stefanou, G., Plevris, V. (Eds.), Proceedings of the 7th European Congress on Computational Methods in Applied Sciences and Engineering. ECCOMAS, Crete Island, pp. 7886–7894.

Meneses, J.P.C.H., Calcada, L.A., Scheid, C.M., Magalhães, S.C., 2017. Determination of the convective mass transfer coefficient in the dissolution of NaCl particles in non-Newtonian fluids. *J. Nat. Gas Sci. Eng.* 45, 118–126. <https://doi.org/10.1016/j.jngse.2017.03.014>

Mills, M.M., Stormont, J.C., Bauer, S.J., 2018. Micromechanical processes in consolidated granular salt. *Eng. Geol.* 239, 206–213. <https://doi.org/https://doi.org/10.1016/j.enggeo.2018.03.024>

Minkley, W., Knauth, M., Fabig, N., Farag, N., 2015. Stability and integrity of salt caverns under consideration of hydro-mechanical loading, in: Roberts, Mellegard, Hansen (Eds.), The Mechanical Behavior of Salt VIII Conference (Salt Mech 8). Taylor & Francis Group/CRC Press/Balkema, London, pp. 217–227.

Mohriak, W., Szatmari, P., 2009. Introdução às propriedades químicas e físicas dos evaporitos, in: Mohriak, W., Szatmari, P., Couto Anjos, S.M. (Eds.), Sal - Geologia e Tectônica - Exemplos Nas Bacias Brasileiras [in Portuguese]. Editora Beca, São Paulo, pp. 18–41.

Mohriak, W.U., Leroy, S., 2012. Architecture of rifted continental margins and break-up evolution: Insights from the South Atlantic, North Atlantic and Red Sea-Gulf of aden conjugate margins, in: Mohriak, W.U., Danforth, A., Post,

P.J., Brown, D.E., Tari, G.C., Nemcok, M., Sinha, S.T. (Eds.), *Conjugate Divergent Margins*. Geological Society, London, pp. 497–535. <https://doi.org/10.1144/SP369.17>

Montaron, B., 2008. Confronting carbonates. *Oil Rev. Middle East* 132–135.

Mraz, D., Rothenburg, L., Dusseault, M.B., 1991. Design of mines in salt and potash, in: 7th ISRM Congress. pp. 1837–1845.

Muhammad, N., Spiers, C.J., Peach, C.J., De Bresser, J.H.P., 2015. Permeability of layered rock salt at different stresses and geometries, in: Roberts, Mellegard, H. (Ed.), *The Mechanical Behavior of Salt VIII Conference (Salt Mech 8)*. Taylor & Francis Group/CRC Press/Balkema, Rapid City, pp. 23–31.

Muñoz, L.F.P., Roehl, D., 2017. An analytical solution for displacements due to reservoir compaction under arbitrary pressure changes. *Appl. Math. Model.* 52, 145–159. <https://doi.org/10.1016/j.apm.2017.06.023>

Munson, D.E., 2004. M-D constitutive model parameters defined for gulf coast salt domes and structures, in: 6th North America Rock Mechanics Symposium (NARMS). Houston.

Munson, D.E., 1999. Multimechanism-deformation parameters of domal salts using transient creep analysis. Sandia National Laboratories (SAND99-2104). Albuquerque.

Munson, D.E., 1979. Preliminary deformation-mechanism map for salt (with application to WIPP). Sandia National Laboratories (SAND79-0076). Albuquerque.

Munson, D.E., Dawson, P.R., 1979. Constitutive model for the low temperature creep of salt (with application to WIPP). Sandia National Laboratories (SAND79-1853). Albuquerque.

Myrseth, V., Perez-Valdes, G.A., Bakker, S.J., Midthun, K.T., Torsæter, M., 2017. Development of a norwegian open-source plug-and-abandonment database with applications. *SPE Econ. Manag.* 9, 27–31. <https://doi.org/10.2118/180027-pa>

Nagel, N.B., 2001. Compaction and subsidence issues within the petroleum industry: From Wilmington to Ekofisk and beyond. *Phys. Chem. Earth, Part A Solid Earth Geod.* 26, 3–14. [https://doi.org/10.1016/S1464-1895\(01\)00015-1](https://doi.org/10.1016/S1464-1895(01)00015-1)

- Nelson, J.F., Jorpeland, J.T., Schwartz, C., 2018. Case history: A new approach to section milling: Leaving the swarf behind!, in: Offshore Technology Conference. Offshore Technology Conference (OTC). <https://doi.org/10.4043/28757-ms>
- Nieland, J.D., Mellegard, K.D., Schalge, R.S., Kaiser, H.D., 2001. Storage of chilled natural gas in bedded salt storage caverns. RESPEC. Rapid City.
- Njå, N.O.B., 2012. P&A of Valhall DP wells. MSc. Thesis - Faculty of Science and Technology, University of Stavanger.
- Norton, F.H., 1929. The creep of steel at high temperatures. McGraw-Hill, Inc., London.
- Odqvist, F.K., 1974. Mathematical theory of creep and creep rupture. Clarendon Press, Oxford.
- Oldenburg, C.M., 2007. Joule-Thomson cooling due to CO<sub>2</sub> injection into natural gas reservoirs. Energy Convers. Manag. 48, 1808–1815. <https://doi.org/10.1016/j.enconman.2007.01.010>
- Oliveira, R., Pepin, A.H., Carvalho, M.S., 2014. Estimation for representative element area of a coquinas analogue using statistical and numerical methods, in: SPE Latin American and Caribbean Petroleum Engineering Conference Proceedings. Society of Petroleum Engineers (SPE), Maracaibo. <https://doi.org/10.2118/169441-ms>
- Orlic, B., Buijze, L., 2014. Numerical modeling of wellbore closure by the creep of rock salt caprocks, in: 48th US Rock Mechanics / Geomechanics Symposium. American Rock Mechanics Association (ARMA), Minneapolis.
- Orlic, B., Wollenweber, J., Geel, C.R., Vandeweyer, V.P., Meekes, J.A., Heerens, G.J., TerHeege, J.H., 2019. Formation of a sealing well barrier by the creep of rock salt: numerical investigations, in: 53rd U.S. Rock Mechanics/Geomechanics Symposium. American Rock Mechanics Association (ARMA), New York.
- Otto, C., Kempka, T., 2015. Thermo-mechanical simulations of rock behavior in underground coal gasification show negligible impact of temperature-dependent parameters on permeability changes. Energies 8, 5800–5827.
- Peach, C.J., 1991. Influence of deformation on the fluid transport properties of salt rocks. PhD. Dissertation - University of Utrecht.

- Peña, W.D.L., Pereira, F.L.G., Firme, P.A.L.P., Roehl, D., Pereira, L.C., 2019. Casing integrity assessment of a wellbore crossing a karst cavity in a carbonate reservoir, in: 53rd U.S. Rock Mechanics/Geomechanics Symposium. American Rock Mechanics Association (ARMA), New York.
- Pereira, F.L.G., Firme, P.A.L.P., Teófilo, F., Santos, A.L.C., Roehl, D., Pereira, L.C., 2018. A methodology for a wellbore casing integrity assessment in scenarios of salt rock dissolution, in: 52nd U.S. Rock Mechanics/Geomechanics Symposium. American Rock Mechanics Association (ARMA), Seattle.
- Pereira, L.C., Sánchez, M., Guimarães, L.J.N., 2016. Uncertainty quantification for reservoir geomechanics. *Geomech. Energy Environ.* 8, 76–84. <https://doi.org/10.1016/j.gete.2016.11.001>
- Plucenio, D., Dannenhauer, C., Folsta, M., Lomba, R., 2013. Modelagem numérica da perfuração em formações salinas com fluido a base de água, in: V Encontro Nacional de Hidráulica de Poços de Petróleo e Gás. Teresópolis [in Portuguese].
- Poiate Jr., E., 2012. Rock mechanics and computational mechanics for the design of oil wells in salt zones. DSc. Thesis - Civil Engineering Department, Pontifical Catholic University of Rio de Janeiro (PUC-Rio) [in Portuguese].
- Poiate Jr., E., Costa, A.M., Falcao, J.L., 2006. Well design for drilling through thick evaporite layers in Santos Basin - Brazil, in: IADC/SPE Drilling Conference. IADC/SPE Drilling Conference, Miami.
- Popov, I.Y., Lobanov, I.S., Popov, S.I., Popov, A.I., Gerya, T. V., 2014. Practical analytical solutions for benchmarking of 2-D and 3-D geodynamic Stokes problems with variable viscosity. *Solid Earth* 5, 461–476.
- Popp, T., Kern, H., Schulze, O., 2001. Evolution of dilatancy and permeability in rock salt during hydrostatic compaction and triaxial deformation. *J. Geophys. Res.* 106, 4061–4078.
- Potts, D.M., Zdravkovic, L., 1999. Finite element analysis in geotechnical engineering - theory. Thomas Telford Limited.
- Pouya, A., 2000. Micro-macro approach for the rock salt behaviour. *Eur. J. Mech. A/Solids* 19, 1015–1028. [https://doi.org/10.1016/S0997-7538\(00\)00204-7](https://doi.org/10.1016/S0997-7538(00)00204-7)
- Pratt, W.E., Johnson, D.W., 1926. Local subsidence of the Goose Creek oil field.

J. Geol. 7.

- Pudewills, A., Droste, J., 2003. Numerical modeling of the thermomechanical behavior of a large-scale underground experiment. *Comput. Struct.* 81, 911–918.
- Quevedo, R., Firme, P., Roehl, D., 2019. Integration schemes with substepping algorithms for creep analysis in geomaterials. *Int. J. Numer. Anal. Methods Geomech.* 43, 1467–1487. <https://doi.org/10.1002/nag.2910>
- Quevedo, R., Firme, P., Roehl, D., Paullo, L., Parotidis, M., Domingues, A., 2015. Assessment of stress changes in hydrocarbon reservoirs using analytical methods, in: *49th US Rock Mechanics / Geomechanics Symposium*. American Rock Mechanics Association (ARMA), San Francisco.
- Quevedo, R.J., 2012. Three-dimensional analysis of hydromechanical problems in partially saturated soils. DSc. Thesis - Department of Civil Engineering, Pontifical University Catholic of Rio de Janeiro (PUC-Rio) [in Portuguese].
- Rabelo, J.G., Silva, A.T., Bezerra, F.H.R., Moraes, A., 2015. Numerical modeling of deformation in carbonates and implications for the formation of karst. *Geol. USP - Ser. Cient.* 15, 99–110. <https://doi.org/10.11606/issn.2316-9095.v15i2p>
- Rauter, M., Barker, T., Fellin, W., 2020. Granular viscosity from plastic yield surfaces: The role of the deformation type in granular flows. *Comput. Geotech.* 122. <https://doi.org/10.1016/j.compgeo.2020.103492>
- Rentsch, H.C., Mes, M.J., 1988. Measurement of Ekofisk subsidence, in: *Offshore Technology Conference*. Offshore Technology Conference (OTC), Houston. <https://doi.org/10.4043/5619-ms>
- Ribeiro da Silva, S.F.C., Pereira, E., 2017. Tectono-stratigraphic evolution of Lapa field pre-salt section, Santos basin (SE Brazilian continental margin). *J. Sediment. Environ.* 2, 133–148. <https://doi.org/10.12957/jse.2017.30052>
- Risnes, R., 2001. Deformation and yield in high porosity outcrop chalk. *Phys. Chem. Earth, Part A Solid Earth Geod.* 26, 53–57. [https://doi.org/10.1016/S1464-1895\(01\)00022-9](https://doi.org/10.1016/S1464-1895(01)00022-9)
- Rocca, V., Cannata, A., Gotta, A., 2019. A critical assessment of the reliability of predicting subsidence phenomena induced by hydrocarbon production. *Geomech. Energy Environ.* 20. <https://doi.org/10.1016/j.gete.2019.100129>

- Rueda, J.A.C., Mejia Sanchez, E.C., Roehl, D., 2019. Integrated discrete fracture and dual porosity - Dual permeability models for fluid flow in deformable fractured media. *J. Pet. Sci. Eng.* 175, 644–653.
- Rueda, J.A.C., Mejia Sanchez, E.C., Roehl, D., 2018. Discrete and smeared fracture model to simulate fluid flow in naturally fractured reservoirs, in: 52nd U.S. Rock Mechanics/Geomechanics Symposium. American Rock Mechanics Association, Seattle.
- Ruiz, M.S.S., 2018. A study on well design and integrity for deepwater exploratory drilling in Brazilian Equatorial Margin. MSc. Thesis - Escola Politécnica, Universidade de São Paulo (USP).
- Rutqvist, J., 2012. The geomechanics of CO<sub>2</sub> storage in deep sedimentary formations. *Geotech. Geol. Eng.* 30, 525–551. <https://doi.org/10.1007/s10706-011-9491-0>
- Sanderson, C., Curtin, R., 2018. A user-friendly hybrid sparse matrix class in C++. *Lect. Notes Comput. Sci.* 10931, 422–430.
- Sanderson, C., Curtin, R., 2016. Armadillo: a template-based C++ library for linear algebra. *J. Open Source Softw.* 1.
- Santos, A.L.C., 2018. Wellbore integrity evaluation using artificial neural networks. MSc. Dissertation - Civil Engineering Department, Pontifical Catholic University of Rio de Janeiro (PUC-Rio) [in Portuguese].
- Santos, A.L.C., Pereira, F.L.G., Roehl, D.M., 2017. Predicting casing failure in Pre-salt wellbores using artificial neural networks, in: Faria, P.O., Lopez, R.H., Miguel, L.F.F., Gomes, W.J.S., Noronha, M. (Eds.), *Proceedings of the XXXVIII Iberian Latin-American Congress on Computational Methods in Engineering*. CILAMCE, Florianopolis.
- Schulze, O., Popp, T., Kern, H., 2001. Development of damage and permeability in deforming rock salt. *Eng. Geol.* 61, 163–180. [https://doi.org/10.1016/S0013-7952\(01\)00051-5](https://doi.org/10.1016/S0013-7952(01)00051-5)
- Sears, G.F., Jessen, F.W., 1966. Controlled solution mining in massive salt. *Soc. Pet. Eng. J.* 6, 115–125. <https://doi.org/10.2118/1336-pa>
- Shadravan, A., Amani, M., 2012. HPHT 101 - What every engineer or geoscientist should know about high pressure high temperature wells, in: *SPE Kuwait International Petroleum Conference and Exhibition*. Society of Petroleum

Engineers (SPE), Kuwait. <https://doi.org/10.2118/163376-ms>

Sicsic, P., Bérest, P., 2014. Thermal cracking following a blowout in a gas-storage cavern. *Int. J. Rock Mech. Min. Sci.* 71, 320–329. <https://doi.org/10.1016/j.ijrmms.2014.07.014>

Silva, B.F., Longhin, G.C., Waldmann, A.A.T.A., Martins, A.L., Lomba, R.F., 2017. Simultaneous effect of salt creep and dissolution in caliper prediction during drilling operations, in: *Offshore Technology Conference Brasil. Offshore Technology Conference (OTC)*, Rio de Janeiro. <https://doi.org/10.4043/28006-ms>

Silva, C.F., 2016. Geomechanical analysis of pre-salt carbonates in the Santos Basin. MSc. Dissertation - Department of Civil and Environmental Engineering, Pontifical Catholic University of Rio de Janeiro (PUC-Rio) [in Portuguese].

Simoës, M.C.C., 2010. Modelagem da transferência de massa, energia e momento em cavidades subterrâneas formadas através da técnica de mineração por dissolução. MSc. Dissertation - School of Engineering, Federal University of Minas Gerais [in Portuguese].

Skjerve, K.M., 2013. Evaluation of shale formations as barrier element for permanent plug and abandonment of wells. MSc. Dissertation - Department of Petroleum Engineering and Applied Geophysics, Norwegian University of Science and Technology.

Soares, L.N.A.C., 2017. Well abandonment: global practices and recommendations for the Brazilian scenario. Undergraduate Project - Federal University of Rio de Janeiro (UFRJ) [in Portuguese].

Sobolik, S.R., Lord, A.S., 2014. Case study of the impact of prior cavern abandonment on long-term oil storage at a strategic petroleum reserve site, in: *48th US Rock Mechanics/Geomechanics Symposium (ARMA Symposium)*. Minneapolis.

Souza, A., 2019. Vida longa aos campos maduros. *Petróleo Hoje*.

Souza Neto, E.A., Peric, D., Owen, D.R.J., 2008. *Computational methods for plasticity - theory and applications*. John Wiley & Sons, Ltd.

Spiers, C.J., Peach, C.J., Brzesowsky, R.H., Schutjens, P.M.T.M., Liezenberg, J.L., Zwart, H.J., 1989. Long-term rheological and transport properties of dry

and wet salt rocks.

- Sriapai, T., Chaowarinwalsri, W., Fuenkajorn, K., 2012. Effect of temperature on compressive and tensile strengths of salt. *ScienceAsia* 38, 166–174.
- Stavland, S.T., 2017. Thermal Stimulation of Shale Barriers. MSc. Thesis - Department of Geoscience and Petroleum, Norwegian University of Science and Technology.
- Stone, C.M., 1997. SANTOS - A two-dimensional finite element program for the quasistatic, large deformation, inelastic response of solids. Sandia National Laboratories. Albuquerque.
- Stormont, J.C., Daemen, J.J.K., 1992. Laboratory study of gas permeability changes in rock salt during deformation. *Int. J. Rock Mech. Min. Sci. Geomech. Abstr.* 29, 325–342. [https://doi.org/10.1016/0148-9062\(92\)90510-7](https://doi.org/10.1016/0148-9062(92)90510-7)
- Stormont, J.C., Howard, C.L., Daemen, J.J.K., 1991. Changes in rock salt permeability due to nearby excavation, in: Roegiers (Ed.), 32nd U.S. Symposium on Rock Mechanics (USRMS). Balkema, Rotterdam, pp. 899–907.
- Stormont, J.C., Lampe, B.L., Lynn, T.D., Bauer, S.J., 2017. Gas permeability of granular salt during consolidation, in: 51st US Rock Mechanics / Geomechanics Symposium. American Rock Mechanics Association (ARMA), San Francisco.
- Strand, G.O., Corina, A.N., 2019. On risk control in the well plug and abandonment phase: The case of the Norwegian Continental Shelf. *J. Pet. Sci. Eng.* 183, 106375. <https://doi.org/10.1016/j.petrol.2019.106375>
- Sylte, J.E., Thomas, L.K., Rhett, D.W., Bruning, D.D., Nagel, N.B., 1999. Water induced compaction in the Ekofisk Field, in: SPE Annual Technical Conference and Exhibition. Society of Petroleum Engineers (SPE), Houston. <https://doi.org/10.2118/56426-ms>
- Szatmari, P., Tibana, P., Simões, I.A., Carvalho, R.S., Leite, D.C., 2009. Atlas petrográfico dos evaporitos, in: Mohriak, W., Szatmari, P., Couto Anjos, S.M. (Eds.), *Sal - Geologia e Tectônica - Exemplos Nas Bacias Brasileiras* [in Portuguese]. Editora Beca, São Paulo, pp. 42–65.
- Tempone, P., Fjær, E., Landrø, M., 2010. Improved solution of displacements due

to a compacting reservoir over a rigid basement. *Appl. Math. Model.* 34, 3352–3362. <https://doi.org/10.1016/j.apm.2010.02.025>

Teófilo, F.A.F., Poiate Jr., E., Roehl, D., Martha, L.F., 2018. A numerical approach for investigation of stress states induced by salt structures. *Int. J. Rock Mech. Min. Sci.* 106, 223–233. <https://doi.org/10.1016/j.ijrmms.2018.02.009>

Thieulot, C., 2011. FANTOM: Two- and three-dimensional numerical modelling of creeping flows for the solution of geological problems. *Phys. Earth Planet. Inter.* 188, 47–68.

Thoms, R.L., Gehle, R.M., 2000. A brief history of salt cavern use, in: *Eighth Salt Symposium*. The Hague, pp. 207–214.

Thoraval, A., Lahaie, F., Brouard, B., Berest, P., 2015. A generic model for predicting long-term behavior of storage salt caverns after their abandonment as an aid to risk assessment. *Int. J. Rock Mech. Min. Sci.* 77, 44–59.

Treybal, R.E., 1980. *Mass-transfer operations*, 3rd ed. McGraw-Hill, Inc., Singapore.

Trudel, E., Bizhani, M., Zare, M., Frigaard, I.A., 2019. Plug and abandonment practices and trends: A British Columbia perspective. *J. Pet. Sci. Eng.* 183, 106417. <https://doi.org/10.1016/j.petrol.2019.106417>

U. S. Department of Energy, 2022. SPR Storage Sites [WWW Document]. URL <https://www.energy.gov/fe/services/petroleum-reserves/strategic-petroleum-reserve/spr-storage-sites> (accessed 3.6.22).

U.S. Energy Information Administration, 2022. U.S. to release 30 million barrels of crude oil from its Strategic Petroleum Reserve [WWW Document]. *Today in Energy*. URL <https://www.eia.gov/todayinenergy/detail.php?id=51538> (accessed 4.1.22).

Urai, J.L., Scheléder, Z., Spiers, C.J., Kukla, P.A., 2008. Flow and transport properties of salt rocks, in: Al., L. et (Ed.), *Dynamics of Complex Intracontinental Basins: The Central European Basin System*. Springer, Berlin-Heidelberg, pp. 277–290.

Urai, J.L., Spiers, C.J., 2007. The effect of grain boundary water on deformation mechanisms and rheology of rock salt during long-term deformation, in: Wallner (Ed.), *6th Conference on the Mechanical Behavior of Salt: Understanding of THMC Process in Salt Rocks (Salt Mech 6)*. Taylor &

Francis Group, Hannover, pp. 149–158.  
<https://doi.org/10.1201/9781315106502-17>

- Urai, J.L., Spiers, C.J., Zwart, H.J., Lister, G.S., 1986. Weakening of rock salt by water during long-term creep. *Nature* 324, 554–557.  
<https://doi.org/10.1038/324554a0>
- van Heekeren, H., Bakker, T., Duquesnoy, T., de Ruiter, V., Mulder, L., 2009. Abandonment of an extremely deep cavern at Frisia Salt, in: SMRI Spring 2009 Technical Conference. Solution Mining Research Institute (SMRI), Krakow, pp. 1–13.
- van Opstal, G.H.C., 1974. The effect of base-rock rigidity on subsidence due to reservoir compaction, in: Proceedings of the 3rd Congress of the International Society of Rock Mechanics. pp. 1102–1111.
- van Sambeek, L.L., Fossum, A.F., Callahan, G.D., Ratigan, J.L., 1993a. Salt mechanics: empirical and theoretical developments, in: Seventh Symposium on Salt. Kyoto, pp. 127–134.
- van Sambeek, L.L., Ratigan, J.L., Hansen, F.D., 1993b. Dilatancy of rock salt in laboratory tests. *Int. J. Rock Mech. Min. Sci. Geomech. Abstr.* 30, 735–738.  
[https://doi.org/10.1016/0148-9062\(93\)90015-6](https://doi.org/10.1016/0148-9062(93)90015-6)
- van Thienen-Visser, K., Breunese, J.N., Muntendam-Bos, A.G., 2015a. Subsidence due to gas production in the Wadden Sea: how to ensure no harm will be done to nature, in: 49th US Rock Mechanics / Geomechanics Symposium. American Rock Mechanics Association (ARMA), San Francisco.
- van Thienen-Visser, K., Pruiksmá, J.P., Breunese, J.N., 2015b. Compaction and subsidence of the Groningen gas field in the Netherlands, in: Proceedings of the International Association of Hydrological Sciences. International Association of Hydrological Sciences (IAHS). <https://doi.org/10.5194/piahs-372-367-2015>
- van Wees, J.D., Osinga, S., Van Thienen-Visser, K., Fokker, P.A., 2018. Reservoir creep and induced seismicity: Inferences from geomechanical modeling of gas depletion in the Groningen field. *Geophys. J. Int.* 212, 1487–1497.  
<https://doi.org/10.1093/gji/ggx452>
- Vassileva, M., Al-Halbouni, D., Motagh, M., Walter, T.R., Dahm, T., Wetzel, H.U., 2021. A decade-long silent ground subsidence hazard culminating in a

metropolitan disaster in Maceió, Brazil. *Sci. Rep.* 11, 1–13.  
<https://doi.org/10.1038/s41598-021-87033-0>

Verdoes, A., Boin, Arjen, 2021. Earthquakes in Groningen: organized suppression of a creeping crisis, in: Boin, A., Ekengren, M., Rhinard, M. (Eds.), *Understanding the Creeping Crisis*. Palgrave Macmillan - Springer Nature Switzerland AG, Cham. <https://doi.org/10.1007/978-3-030-70692-0>

Vignes, B., 2011. Qualification of well barrier elements - test medium, test temperatures and long-term integrity, in: *SPE European Health, Safety and Environmental Conference in Oil and Gas Exploration and Production*. Vienna.

Vrålstad, T., Saasen, A., Fjær, E., Øia, T., Ytrehus, J.D., Khalifeh, M., 2019. Plug & abandonment of offshore wells: Ensuring long-term well integrity and cost-efficiency. *J. Pet. Sci. Eng.* 173, 478–491.  
<https://doi.org/10.1016/j.petrol.2018.10.049>

Waal, J.A., van Thienen-Visser, K., Pruiksmá, J.P., 2015. Rate type isotach compaction of consolidated sandstone, in: *49th US Rock Mechanics / Geomechanics Symposium*. American Rock Mechanics Association (ARMA), San Francisco.

Waele, J.D., Piccini, L., Columbu, A., Madonia, G., Vattano, M., Calligaris, C., D'Angeli, I.M., Parise, M., Chiesi, M., Sivelli, M., Vigna, B., Zini, L., Chiarini, V., Sauro, F., Drysdale, R., Forti, P., 2017. Evaporite karst in Italy: A review. *Int. J. Speleol.* 46, 137–168. <https://doi.org/10.5038/1827-806X.46.2.2107>

Wang, L., Bérest, P., Brouard, B., 2015. Mechanical behavior of salt caverns: closed-form solutions vs numerical computations. *Rock Mech. Rock Eng.* 48, 2369–2382. <https://doi.org/10.1007/s00603-014-0699-1>

Wang, T., Yang, C., Chen, J., Daemen, J.J.K., 2018. Geomechanical investigation of roof failure of China's first gas storage salt cavern. *Eng. Geol.* 243, 59–69.  
<https://doi.org/10.1016/j.enggeo.2018.06.013>

Wang, T., Yang, C., Ma, H., Daemen, J.J.K., Wu, H., 2015. Safety evaluation of gas storage caverns located close to a tectonic fault. *J. Nat. Gas Sci. Eng.* 23, 281–293. <https://doi.org/10.1016/j.jngse.2015.02.005>

Wang, Y., Vos, M., Karimpour, A., Fearn, M., Den Besten, H., Stanko, T., Bain, J., Shen, Y., Stokes, D., Issa, A., Khan, Z., 2016. Integration of time-based

dynamics simulation with milling and underreaming system to implement reliable single trip solution in plug and abandonment operation, in: SPE/IADC Drilling Conference. IADC/SPE Drilling Conference and Exhibition, Fort Worth.

- Wangen, M., Halvorsen, G., Gasda, S.E., Bjørnarå, T., 2018. An analytical plane-strain solution for surface uplift due to pressurized reservoirs. *Geomech. Energy Environ.* 13, 25–34. <https://doi.org/10.1016/j.gete.2018.03.002>
- Wawersik, W.R., Hannum, D.W., Lauson, H.S., 1980. Compression and extension data from dome salt from West Hackberry, Louisiana. Sandia National Laboratories (SAND79-0668). Albuquerque.
- Weijermars, R., Jackson, M.P.A., 2014. Predicting the depth of viscous stress peaks in moving salt sheets: Conceptual framework and implications for drilling. *Am. Assoc. Pet. Geol. Bull.* 98, 911–945.
- Weijermars, R., Jackson, M.P.A., Dooley, T.P., 2014a. Quantifying drag on wellbore casings in moving salt sheets. *Geophys. J. Int.* 198, 965–977.
- Weijermars, R., Jackson, M.P.A., van Harmelen, A., 2014b. Closure of open wellbores in creeping salt sheets. *Geophys. J. Int.* 196, 279–290.
- Willson, S.M., Driscoll, P.M., Arnis, J., Black, A.D., Martin, J.W., Ehgartner, B.L., Hinkebein, T.E., 2004. Drilling salt formations offshore with seawater can significantly reduce well costs. *SPE Drill. Complet.* 19, 147–155.
- Willson, S.M., Fossum, A.F., Fredrich, J.T., 2003. Assessment of salt loading on well casings. *SPE Drill. Complet.* 18, 13–21. <https://doi.org/10.2118/81820-PA>
- Wollenweber, J., Vanderweijer, V., Meekes, S., Geel, K., Orlic, B., 2018. Public Summary: TKI “Downhole field lab” – Wellbore sealing by rock salt. TNO. Utrecht.
- Xie, X., Bauer, A., Stenebråten, J.F., Bakheim, S., Lavrov, A., Fjær, E., Kristiansen, T.G., 2020. Can heating induce borehole closure? *Rock Mech. Rock Eng.* 53, 5715–5744. <https://doi.org/10.1007/s00603-020-02238-5>
- Xing, W., Zhao, J., Hou, Z., Were, P., Li, M., Wang, G., 2015. Horizontal natural gas caverns in thin-bedded rock salt formations. *Environ. Earth Sci.* 73, 6973–6985. <https://doi.org/10.1007/s12665-015-4410-y>

- Yao, H.T., Xuan, F.Z., Wang, Z., Tu, S.T., 2007. A review of creep analysis and design under multi-axial stress states. *Nucl. Eng. Des.* 237, 1969–1986. <https://doi.org/10.1016/j.nucengdes.2007.02.003>
- Yin, S., Towler, B.F., Dusseault, M.B., Rothenburg, L., 2010. Fully coupled THMC modeling of wellbore stability with thermal and solute convection considered. *Transp. Porous Media* 84, 773–798.
- Zechner, E., Konz, M., Younes, A., Huggenberger, P., 2011. Effects of tectonic structures, salt solution mining, and density-driven groundwater hydraulics on evaporite dissolution (Switzerland). *Hydrogeol. J.* 19, 1323–1334. <https://doi.org/10.1007/s10040-011-0759-5>
- Zhu, C., Arson, C., 2014. A thermo-mechanical damage model for rock stiffness during anisotropic crack opening and closure. *Acta Geotech.* 9, 847–867. <https://doi.org/10.1007/s11440-013-0281-0>
- Zoback, M., 2010. *Reservoir geomechanics*. Cambridge University Press, Cambridge.
- Zoccarato, C., Ferronato, M., Teatini, P., 2018. Formation compaction vs land subsidence to constrain rock compressibility of hydrocarbon reservoirs. *Geomech. Energy Environ.* 13, 14–24. <https://doi.org/10.1016/j.gete.2017.12.002>